Surface and Interfacial Nanoscience of Titanium Dioxide

Author: Immad Muhammed Nadeem

Thesis Submitted for the degree of Doctor of Engineering

of University College London

CDT: Molecular Modelling and Materials Science
Faculty of Mathematical and Physical Sciences
University College London
2018

Declaration

I, *Immad M. Nadeem*, confirm that the work presented in this thesis is my own. Where information has been derived from other sources, I confirm that this has been indicated in the thesis.

To my grandparents….

Abstract

Surfaces and interfaces of titanium dioxide (TiO_2) are investigated with scanning probe microscopy and surface X-ray diffraction. A discussion on an experimental arrangement for *in situ* solid/liquid interface surface crystallography of UHV prepared samples is also presented.

Water splitting on TiO_2 is a promising candidate for photocatalytic H_2 fuel production. In ultra-high vacuum (UHV), our scanning tunneling microscopy (STM) investigation on anatase TiO_2 (101) (A_{101}) suggests that surface oxygen vacancies can dissociate H_2O by forming bridging OH species. Additionally, surface X-ray diffraction (SXRD) of the room temperature interface of A_{101} in contact with an ultra-thin water film or bulk water indicate that both interfaces contain a 25:75 mixture of molecular H_2O and terminal OH bound to titanium atoms along with bridging OH species. This is in striking contrast to the inert character of room temperature A_{101} in UHV.

An electrochemical surface science perspective of TiO_2 is largely lacking. We present *in situ* STM and SXRD investigations of the rutile TiO_2 (110) (R_{110}) and electrolyte solution interface - chiefly 0.1 M NaOH and 0.1 M HCl. Our findings indicate that Na adsorbs at the surface tetra-dentate site between four oxygen atoms and the Cl adsorbs at the surface mono-dentate site bound to a Ti atom. Additionally, preliminary electrochemical STM measurements of R_{110} gives rise to terrace resolution images. This is a promising result for future electrochemical surface science on TiO_2.

Although the anatase/rutile interface is understood to play an important role in photocatalysis, surface science of TiO_2 has largely been restricted to single crystal and thin film surfaces. In UHV, we present an STM tip manipulation procedure to form regions of rutile TiO_2 (100) (R_{100}) on A_{101} and thus create an anatase/rutile interface. Furthermore, UHV STM of photoactive carboxylic acid adsorption on R_{100} is presented for surface characterisation and to understand the photoactivity of R_{100}. Acetic acid adsorption gives rise to a partially ordered overlayer with a ($\times$2) periodicity in the [001] direction. Tri-methyl acetic adsorption is largely disordered.

Impact Statement

In ambient pressure conditions metals typically form an oxide overlayer. Hence, the study of metal oxide surfaces has received much attention. Additionally, metal oxide materials have also received widespread interest for numerous applications such as the use of titanium dioxide (TiO_2) for photocatalytic water splitting to generate H_2 fuel. Photocatalysis provides a means of harnessing solar energy to provide a portable H_2 fuel source that has the potential to reduce our dependence on fossil fuels and its impact on climate change. TiO_2 is widely used as a photocatalyst due to its low cost, high photostability, high catalytic efficiency and non-toxicity when compared to other light harvesting materials such as SnO_2, WO_3, Cu_2O or CdS. Over the last few decades, surface scientists have extensively probed a variety of TiO_2 single crystals and thin films (primarily rutile TiO_2 (110) (R_{110}), rutile TiO_2 (011) (R_{011}) and anatase TiO_2 (101) (A_{101})) in ultra-high vacuum (UHV) with limited research at near ambient pressure.

Recent issues of the journal *Surface Science* have been devoted to the topics '*surfaces under environmental conditions*' and '*surface science and electrochemistry - 20 years later*'. Such research aims to bridge the 'pressure gap' of our understanding of surfaces to more technologically pertinent conditions. Surface and interfacial studies of the aqueous interfaces of TiO_2 with water and electrolyte solutions are largely lacking. This thesis discusses the structure of aqueous TiO_2 interfaces with scanning tunnelling microscopy (STM) and surface x-ray diffraction (SXRD) to better understand surface adsorption sites. From an academic perspective, these results present a comprehensive structure of the solid/liquid interface illustrating the difference in interface structure from UHV to the ambient. Additionally, this work lays the groundwork for future more complex process to be investigated such as deciphering the surface evolution under electrochemical and photo-electrochemical control. Ultimately, this will allow for rational electrocatalyst and photo-electrocatalyst design to improve commercial activity.

The most potent TiO_2 photocatalyst consists of a 3:1 ratio of anatase and rutile nanoparticles - commercially available as Degussa P-25®. Although TiO_2 surface science has been largely limited to single crystals and thin films, the anatase/rutile interface is considered the focal point for photocatalysis. To this extent, we present a 'nano-engineering' method where an STM tip pulse on A_{101} can induce an anatase to rutile phase transition. This method creates regions of surface order that we assign to different terminations of rutile TiO_2 (100) (R_{100}). Thus, we present a method to create an anatase/rutile interface. This will allow for future STM measurements investigating the photoactivity at the anatase/rutile interface. To complement this, the adsorption of photoactive materials on R_{100} has also been probed. Our findings are key to understand the photoactivity of the anatase/rutile interface and single crystal R_{100}. Ultimately, with scanning tunnelling spectroscopy (STS), this will allow for an atomic scale microscopic and spectroscopic understanding of the anatase/rutile interface and thus allow for an improved design of mixed anatase/rutile photocatalyst to maximise efficiency and promote commercial success.

Table of Contents

Publications List

Publications derived from findings presented in this thesis are:

1) Bridging Hydroxyls on Anatase TiO_2 (101) by Water Dissociation in Oxygen Vacancies

Chapter 4

I. M. Nadeem, G. T. Harrison, A. Wilson, C. L. Pang, J. Zegenhagen and G. Thornton, *Journal of Physical Chemistry B*, 2018, **122**, 834-839.

2) Water Dissociates at the Aqueous Interface with Reduced Anatase TiO_2 (101)

Chapter 4

I. M. Nadeem, J. P. W. Treacy, S. Selcuk, X. Torrelles, H. Hussain, A. Wilson, D. C. Grinter, G. Cabailh, O. Bikondoa, C. Nicklin, A. Selloni, J. Zegenhagen, R. Lindsay and G. Thornton, *Journal of Physical Chemistry Letters*, 2018, **9**, 3131-3136.

In Preparation:

3) Photo-Electrochemical Droplet Cell for Interfacial Nanoscience

Chapter 3

A. Wilson, I. M. Nadeem, H. Hussain, X. Torrelles, G. Thornton, C. Nicklin and J. Zegenhagen.

4) Interfaces of Rutile TiO_2 (110) with Electrolyte Solutions

Chapter 5

I. M. Nadeem, C. Penscke, J. Chen, X. Torrelles, A. Wilson, H. Hussain, G. Cabailh, O. Bikondoa, C. Nicklin, R. Lindsay, J. Zegenhagen, A. Michaeledis and G. Thornton.

5) STM Nanoscale Engineering of Anatase / Rutile Interface and Acetate Adsorption on Rutile TiO_2 (100)

Chapter 6

I. M. Nadeem, G. T. Harrison, A. Wilson, C. L. Pang, J. Zegenhagen, H. Idriss and G. Thornton.

Acknowledgements

I am most grateful to the supervision of Prof. Geoff Thornton and Dr. Jörg Zegenhagen who made my doctoral project a thoroughly invigorating experience. I will forever be indebted to them for their unfaltering support and for giving me the opportunity to grow and develop in my professional and personal life. I also thank Dr. Matthew Blunt and Dr. Philippe Marcus who welcomed me into their research groups at University College London (UCL) and École Nationale Supérieure de Chimie de Paris (ENSCP), respectively, to perform solid/liquid interface scanning tunnelling microscopy measurements. Additionally, I would like to thank Dr. Xavier Torrelles who invited me to his research group at the Institut de Ciència de Materials de Barcelona (ICMAB) to learn the intricacies of surface X-ray diffraction data analysis.

I extend my gratitude towards all research group members and research collaborators at University College London and Diamond Light Source. I thank Mr. Michael Allan, Dr. George Harrison, Dr. Axel Wilson, Dr. Hadeel Hussain, Dr. Yu Zhang and Dr. Xavier Torrelles for their support and insightful discussions throughout the doctoral project and who made the difficult task of learning, building (and fixing!) ultra-high vacuum and surface science systems a relatively straight forward one. I also thank Dr. George Harrison, Dr. Axel Wilson and Dr. Matthew Blunt who taught me the intricacies required to perform successful scanning tunneling microscopy. A special thanks goes to Dr. Xavier Torrelles, who was tremendous in his support with data acquisition during beam times and the subsequent analysis for the surface x-ray diffraction experiments.

I would like to thank Prof. Annabella Selloni and Dr. Sencer Selcuk for providing the density functional theory calculations to complement findings presented in Chapter 4. Regarding the scanning tunnelling microscopy results presented in Chapter 6, I would like to thank Dr. George Harrison for his help and support during experiment planning and implementation and for laying the groundwork to perform these measurements. Regarding the droplet cell development and implementation (Chapters 3, 4 and 5) at Beamline I07 of Diamond Light Source, I would like to thank Dr. Axel Wilson and Dr.

Hadeel Hussain who were instrumental in the development process and Prof. Chris Nicklin for kindly funding the project.

I would also like to thank Dr. Jonathan Rawle, Dr. Gregory Cabailh, Dr. Oier Bikondoa, Dr. Jon Treacy and Dr. Robert Lindsay for their support during beam times and in general for being excellent collaborators and teachers. The Centre for Doctoral Training: Molecular Modelling and Materials Science (CDT: M3S) is acknowledged for enabling me to be in a position funded by the Engineering and Physical Sciences Research Council and Diamond Light Source. I would like to thank Dr. Zhimei Du who was an excellent CDT manager. I also thank the workshops at University College London and Diamond Light Source for providing the support required to maintain and operate instrumentation.

Finally, I would like to thank all my family and friends who supported me throughout the doctoral project.

Abbreviations

ΔH_{ad}	Enthalpy of Adsorption
χ_n^2	Normalised Chi-Square
2PPE	Two Photoemission Photoelectron Spectroscopy
$\mathbf{A_{001}}$	Anatase TiO_2 (001)
$\mathbf{A_{101}}$	Anatase TiO_2 (101)
AA	Acetic Acid
AES	Auger Electron Spectroscopy
AFM	Atomic Force Microscopy
AP	Ambient Pressure
Ar	Argon
c	Speed of Light
CB	Conduction Band
CTR	Crystal Truncation Rod
DFT	Density Functional Theory
$\mathbf{E_F}$	Fermi Level
EH	Experimental Hutch
ESRF	European Synchrotron Radiation Facility
eV	Electron Volt
$\mathbf{F_{calc}}$	Calculated Structure Factor
$\mathbf{F_{exp}}$	Experimental Structure Factor
HCl	Hydrochloride Acid
$\mathbf{I_t}$	Tunnelling Current
LDOS	Local Density of States
LEED	Low Energy Electron Diffraction
mbar	Millibar
MD	Molecular Dynamics
ML	Monolayer
NaOH	Sodium Hydroxide
NC-AFM	Non-Contact AFM

nm	Nanometer
O_{3c}/O_{2c}	Three Co-Ordinate Oxygen / Two Co-Ordinate Oxygen
OH_{br}	Bridging OH
OH_t	Terminal OH
PEEK	Polyether ether ketone
PES	Photoelectron Spectroscopy
PTFE	Polytetrafluoroethylene
R_{010}	Rutile TiO_2 (010)
R_{011}	Rutile TiO_2 (011)
R_{100}	Rutile TiO_2 (100)
R_{110}	Rutile TiO_2 (110)
RGA	Residual Gas Analyser
SPM	Scanning Probe Microscopy
STM	Scanning Tunnelling Microscopy
SXRD	Surface X-Ray Diffraction
Ta	Tantalum
TCO	Transparent Conducting Oxide
Ti_{6c}/Ti_{5c}	Six Co-Ordinate Titanium / Five Co-Ordinate Titanium
TiO_2	Titanium Dioxide
TMAA	Tri-Methyl Acetic Acid
UHV	Ultra-High Vacuum
UPS	UV Photoelectron Spectroscopy
V_b	Tunnelling Bias
V_o	Oxygen Vacancy
V_s	Sample Bias
VB	Valence Band
VT	Variable Temperature
WKB	Wentzel-Kramers-Brillouin
XPS	X-Ray Photoelectron Spectroscopy

List of Tables

List of Figures

Chapter 1

Introduction

1.1 Surface and Interfacial Nanoscience

The nano-scale world is a mainstay of modern day research endeavours with applications in many fields of science and technology such as energy, chemicals, electronics and healthcare to name but a few.[1] Surface and interfacial nanoscience presents an explanation of the chemistry and physics at the interface of two phases. Its importance lies in obtaining an atomic scale understanding of relevant surfaces and interfaces to improve material performance using rational design.

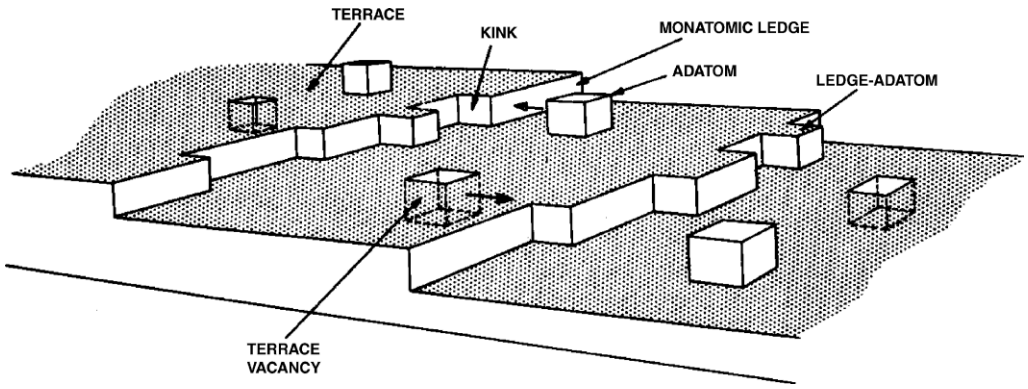

Figure 1.1: Schematic of surface step (monatomic ledge), kink, terrace, adatom and vacancy.[2] Reproduced with permission of the rights holder, *Elsevier*.

Investigating surfaces and interfaces on an atomic scale is an exceptionally complicated procedure. For this reason, a majority of research of this nature is performed on single crystal surfaces. Single crystals are cut to expose a specific crystal plane which is subsequently probed. Surface microscopy shows that surfaces consist of a variety of flat regions (terraces) and defects (steps / ledge, kinks and point defects) - see Figure 1.1. The local distribution of atoms around individual surface sites can be different depending on factors such as surface vacancies or adsorption. Hence, surface sites exhibit different surface chemical and physical phenomena.

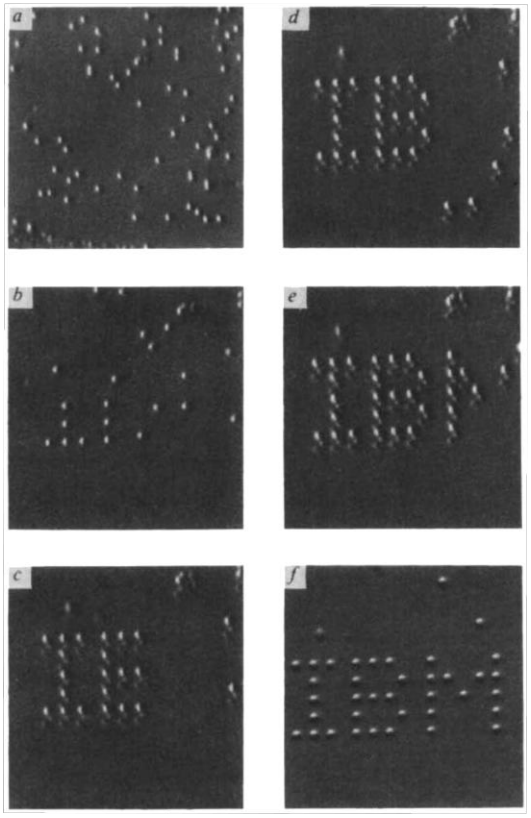

Figure 1.2: A sequence of STM images taken during the construction of a patterned array of xenon atoms on a nickel (110) surface. Grey scale is assigned according to the slope of the surface. The atomic structure of the nickel surface is not resolved. The [1$\bar{1}$0] direction runs vertically. (a) The surface after Xenon dosing. (b)-(f) Various stages during the construction. Each letter is 50 Å from top to bottom.[3] Reproduced with permission of the rights holder, *Springer Nature*.

The significance of surface and interfacial nanoscience is evidenced by the award of the 1986 Nobel Prize in Physics to Binnig and Rohrer[4-8] '*for their design of the scanning tunneling microscope'* and the 2007 Nobel Prize in Chemistry to Gerhard Ertl[9] *'for his studies of chemical processes on solid surfaces'*. The work of Binnig and Rohrer is considered a major breakthrough for surface science as scanning tunnelling microscopy (STM) (in parallel with atomic force microscopy (AFM)) enables real space imaging of surfaces. In conjunction with spectroscopic techniques and theoretical calculations, STM and AFM have been used to identify surface structure, point defects, adsorbate binding

sites and enable surface manipulation. Perhaps the most famous example of the latter is the iconic 'IBM' image - see Figure 1.2 - constructed by Eigler[3] and co-workers from xenon atoms on nickel. This event highlights the exceptional capability of STM to allow atomic level surface manipulation. Among Gerhard Ertl's work, his in-depth explanation of hydrogen adsorption sites on metal surfaces and the molecular mechanism of the Haber-Bosch process illustrate the role of surface and interfacial nanoscience research with respect to answering long-standing questions in heterogeneous catalysis.

Surface and interface studies of metals in ultra-high vacuum (UHV) has attracted an extensive amount of research interest, however in the ambient virtually every metal oxidises forming a thin oxide layer over the metal. Hence, for purposes of understanding the surfaces and interfaces, it is the metal oxide that demands greater attention rather than the metal. Metal oxides are among the most widely investigated materials which is reflected in the volume of research in this area, extending from applied studies of engineering materials to fundamental work on model surfaces.[10-14]

The complexity of obtaining a nano-scale understanding of surfaces and interfaces has resulted in a variety of different systems being investigated in UHV. To this extent, as an initial step a variety of different materials have been probed. UHV conditions are not representative of surface and interface behaviour under more technologically pertinent conditions, which has led to the emergence of the 'pressure gap'. To this extent, the past two decades has seen surface and interfacial nanoscience emerge from UHV towards ambient pressure investigations.[15-17] Recent issues of the journal *Surface Science* have been devoted to the topics '*surfaces under environmental conditions*'[18] and '*surface science and electrochemistry - 20 years later*'[19]. Such research aims to bridge the 'pressure gap' of our understanding of surfaces to more technologically pertinent conditions such as the solid/liquid interface.

1.2 Adsorption on Surfaces: Interface Formation

Surface adsorption refers to a process whereby an atom or molecule (adsorbate) forms a bond to a substrate. This adsorption process can either be associative (molecule adsorbs without fragmentation) or dissociative (molecule adsorbs with fragmentation) - see Figure 1.3 - and is the basis of an interface formation.

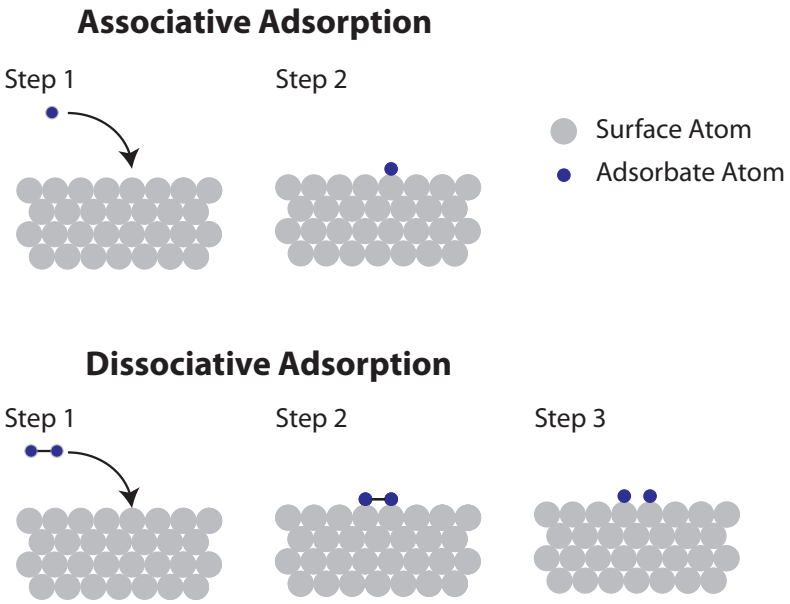

Figure 1.3: Schematic illustrating associative and dissociative adsorption on surfaces.

The fractional coverage (θ) of an adsorbate is given as,

$$\theta = \frac{N_S}{N} \qquad \textbf{Equation 1.1}$$

where N_s is the number of surface sites occupied by the adsorbate whilst N is the total number of surface adsorption sites. When θ = 1, the adsorbate ensemble is referred to as a monolayer. The bonding of adsorbate molecules to surfaces is divided into two categories: physisorption and chemisorption. In physisorption, the bonding is

characterised by a redistribution of electron density within the adsorbate and substrate separately. The adsorbate-substrate interaction is weak (van der Waals-type) with negligible exchange of electrons. The attractive force is provided by instantaneous dipoles. Quantitatively, the enthalpy of adsorptions (ΔH_{ad}) is less than 35 kJ mol^{-1}. A typical example of physisorption would be the interaction of noble gases with metal surfaces.[20] In chemisorption, the bonding is characterised by an exchange of electrons between the adsorbate and adsorbent with the formation of a chemical bond. Quantitatively, the ΔH_{ad} is greater than 35 kJ mol^{-1}. A typical example of chemisorption would be the interaction of water with the rutile TiO_2 (110) (R_{110}) surface. The R_{110} surface possesses oxygen vacancies, which facilitate water splitting to form two surface hydroxyls per water molecule.[13]

1.3 Titanium Dioxide (TiO_2)

The surface and materials science of titanium dioxide (TiO_2) is amongst the most widely investigated research fields.[11, 13] Since Honda and Fujishima[21] first demonstrated the water splitting (to generate H_2 fuel) capability of TiO_2, it has been widely investigated for purposes of heterogeneous catalysis.[22] This is due to its low cost, high photostability, high catalytic efficiency and non-toxicity when compared to other light harvesting materials such as SnO_2, WO_3, Cu_2O or CdS.[11] TiO_2 exists in nature as one of three polymorphs: rutile, anatase and brookite - see Figure 1.4. Rutile is the most abundant polymorph of TiO_2 whereas brookite is the least abundant. Hence, TiO_2 research is largely focussed on rutile and anatase, where the latter is considered to be more photo-active.[23] Today, anatase and rutile are amongst the most studied TiO_2 polymorphs for photo-catalytic H_2 fuel generation where an optimum TiO_2 material is prepared with a 3:1 ratio of anatase and rutile nanoparticles - commercially available as Degussa P-25®.[24] This mixture has been shown to be a more potent material for H_2 fuel generation than its individual components.

Surface studies on TiO_2 have largely focussed on R_{110} due to the ready availability of high quality crystals and because (110) is the most abundant and stable face of rutile. This has led to R_{110} being regarded as a prototypical TiO_2 surface where a vast majority of TiO_2 surface studies are initiated on R_{110}.[12-14] However, recently surface studies on anatase TiO_2 (101) (A_{101}) (the most abundant and stable face of anatase) have started to gain more attention as high quality single crystals become more readily available.[25-27] To this extent, surface studies of R_{110} and A_{101} in conditions ranging from UHV to ambient pressure (AP) have been pivotal in obtaining an understanding of how these surfaces behave e.g. water adsorption and splitting on R_{110} and A_{101}.[16, 28-32]

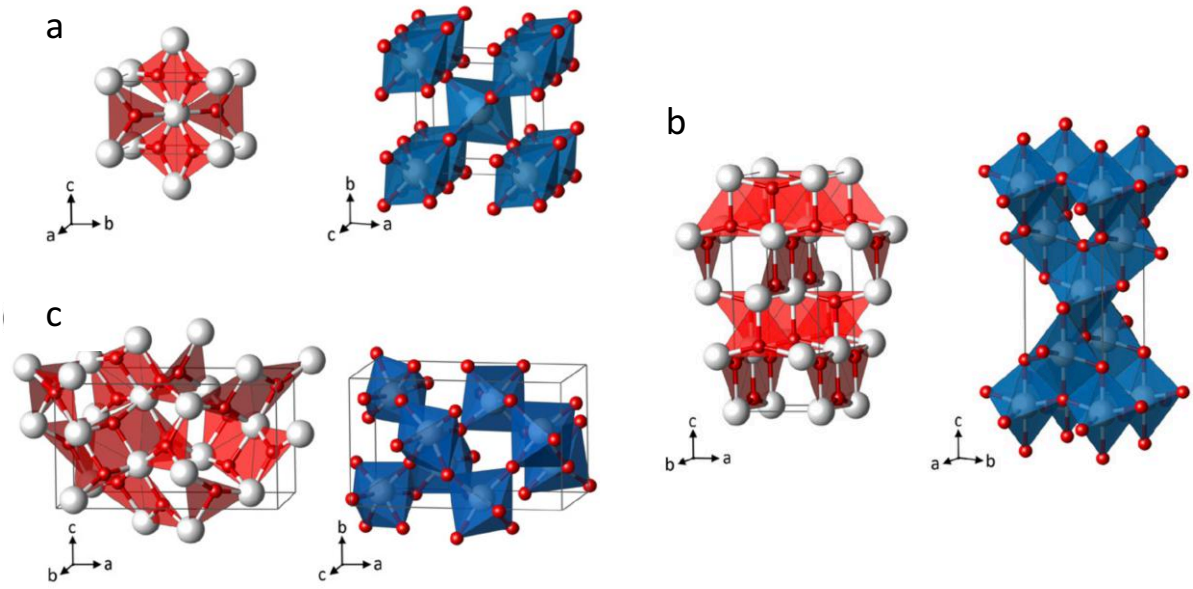

Figure 1.4: Planar Ti_3O building-block representation (left) and TiO_6 polyhedra (right) of TiO_2 - (a) rutile, (b) anatase and (c) brookite (Ti (white) & O (red)). Rutile has a tetragonal unit cell with lattice parameters a = b = 4.59 Å & c = 2.96 Å. Anatase has a tetragonal unit cell with lattice parameters a = b = 3.78 Å & c = 9.51 Å. Brookite has an orthorhombic unit cell with lattice parameters a = 9.16 Å, b = 5.43 Å & c = 5.13 Å.[33] Reproduced with permission of the rights holder, *IOP Publishing*.

A potential drawback of using TiO_2 for photocatalytic applications is its band gap of ~3.2 eV which limits light harvesting to UV light.[11] However, this issue can be alleviated by using TiO_2 in conjunction with materials that absorb visible light[34] or by doping[35] TiO_2 to improve visible light absorption. Additionally, noble metals and semi-conductors have been used with TiO_2 to improve exciton splitting efficiency.[36] Although TiO_2 exhibits numerous advantageous qualities for heterogeneous catalysis ranging from clean energy to water treatment, it has numerous other applications. The memristive switching in TiO_2 is a promising approach to data storage.[37] TiO_2-based transparent conducting oxides (TCO) have been shown to exhibit properties comparable to those of $In_{2-x}Sn_xO_3$ (ITO), the most widely used TCO.[38] Additionally, TiO_2 has a high refractive index making it appear bright whereby it is employed in paint, plastics and coatings.[39] It has also been used for corrosion protection[40] and medical implants (as oxidised Ti metal).[41]

1.4 Thesis Aim and Structure

TiO_2 exhibits advantageous properties for photocatalytic water splitting to generate H_2 fuel - chiefly its low cost, high photo-stability, high catalytic efficiency and non-toxicity when compared to other light harvesting materials.[11] This thesis aims to present a combined UHV and AP investigation probing the surfaces and interfaces of different TiO_2 polymorphs and terminations. Although the advantageous properties of TiO_2 have been commercially exploited, an atomic scale understanding of the relevant surfaces and interfaces (under typical working conditions) is lacking. The atomic/molecular interactions at the relevant surfaces and interfaces is of crucial importance to eventually unravel the atomic scale chemical and physical processes that occur at the interface relevant to photocatalysis. This will provide us with an explanation of the atomic scale processes (such as surface binding sites, surface evolution under different conditions and adsorption behaviour of specific adsorbates) behind photocatalysis and hence allow for a more rational nano-scale design of future TiO_2 based materials/products where advantageous properties can be rationally enhanced whilst disadvantageous properties associated with interface structure can be minimised. Essentially, an atomic scale understanding of the relevant photocatalytic surfaces/interface will allow for future nano-engineering of more efficient forms of TiO_2 photocatalysts which will in turn pave the way for a more efficient method of H_2 fuel generation (as an alternative to fossil fuels).

This thesis aims to explore a number of open research questions pertaining to the interfacial chemistry and physics surrounding TiO_2 photocatalytic interfaces with a focus on a) the A_{101}/H_2O interface, b) the R_{110}/Electrolyte interface and c) the anatase/rutile interface. Given below are the research questions that we are looking to explore:

a) A_{101}/H_2O interface: We aim to investigate the water splitting capabilities of A_{101}. Studies of this interface in relation to water splitting at defect sites and the interface structure in ambient conditions is lacking. Understanding water adsorption on A_{101} is a fundamental prerequisite to determining photocatalytic water splitting on A_{101}. The fundamental research question we ask is whether water adsorbs in an associative or dissociative manner depending on the surface structure and environment?

b) R_{110}/Electrolyte interface: We aim to investigate the structure and stability of R_{110} under electrolyte solutions to determine whether R_{110} can maintain its structural integrity under electrolyte solutions. The long term aim being to pursue electrochemical surface science so that we may obtain a nano-scale understanding of the photo-electrochemical water splitting process to generate hydrogen fuel. The fundamental research questions we ask is whether electrolyte exposure to as-prepared R_{110} results in the formation of an ordered or disordered interface? And whether electrochemical surface science is a field worthy of being explored?

c) Anatase/rutile interface: We aim to utilise STM tip manipulation on A_{101} to induce an anatase to rutile phase transition (where the latter polymorph is more thermodynamically stable) and thus create an anatase/rutile interface. This is expected to create an anatase/rutile interface which is widely reported to being the focal point for photocatalysis in TiO_2 due to improved exciton splitting efficiency in this region.[11] The fundamental research questions we ask here is to validate what form of rutile structures (if any) we can create on A_{101} via STM tip manipulation? If so, then how does the anatase/rutile interface react to photo-active illumination after the adsorption of photo-active molecules at the interface. We assign our rutile structures (created via STM tip manipulation) as R_{100} which eventually gives rise to a complementary research question which focusses on deciphering the manner in which photoactive carboxylic acids bind to R_{100}?

This thesis negotiates the above discussed research questions in Chapters 4, 5 and 6, respectively. A brief discussion of our results and answers to our research questions are provided below. Before discussing Chapter 4, 5 and 6, let us first discuss Chapters 1, 2 and 3 which provide an overall thesis introduction followed by a discussion of the research instrumentation and its theoretical aspects. Chapter 1 introduces the field of surface and interface nanoscience and provides an overview of surface adsorption and TiO_2. Chapter 2 presents the theoretical aspects of the instrumentation used to conduct the experiments discussed within this thesis. This includes scanning tunnelling microscopy (STM), surface X-ray diffraction (SXRD), photo-electron spectroscopy (PES), low energy electron diffraction (LEED) and Auger electron spectroscopy (AES). Chapter 3 details the experimental set up used to perform STM, SXRD, PES, LEED and AES measurements. This involves a description of the UHV and AP instruments as well as the sample preparation methodology. Additionally, the set-up of Beamline I07: Surface and Interface Diffraction at Diamond Light Source is presented followed by a discussion detailing the development and implementation of an experimental arrangement for *in situ* solid/liquid interface surface crystallography of UHV prepared samples.

Chapter 4 discusses the A_{101} interface with water and utilises STM and SXRD to elucidate the interface structure. Water is among the most pervasive substances on earth and understanding its interface with TiO_2 is a necessary step towards exploring the nano-scale behaviour of water splitting on TiO_2. Initially, we electron irradiate A_{101} to induce meta-stable surface oxygen vacancies (V_o) and use STM to probe if H_2O from the residual vacuum is able to quench the V_o to form bridging hydroxyl (OH_{br}) species. Our STM findings highlight features on the surface that we assign to OH_{br} with spectroscopic evidence from our previous work.[31, 32] Next, we present two separate *in-situ* SXRD measurements of as-prepared A_{101} exposed to $H_2O_{(g)}$ at 23 mbar (relative humidity (RH)

= 100%) and as-prepared A_{101} exposed to $H_2O_{(l)}$. Our findings indicate that in both cases the A_{101}/H_2O interface results in surface atoms adopting bulk-like positioning whilst the contact layer consists of mixed associatively and dissociatively adsorbed water in a 1:3 ratio. The main difference between the structure of the two interface is that in the $A_{101}/H_2O_{(l)}$ interface structure, a second ordered water layer (at 50% coverage) exists. To conclude and answer our research question, we observe that water splitting does not occur on as-prepared A_{101} in UHV, however defect mediated water splitting in UHV can be induced. In terms of pressure dependence, our findings show that although water splitting does not occur on the as prepared surface in UHV, water can split on A_{101} when exposed to $H_2O_{(g)}$ (23 mbar) or $H_2O_{(l)}$. We observe interface structure to be pressure dependant.

Chapter 5 describes a complementary *in-situ* STM and SXRD study of the R_{110} interface with electrolyte solutions. Understanding the TiO_2 and electrolyte interface is of fundamental importance to achieve an atomic scale understanding of electrochemical interfaces. To this end, a liquid cell STM has been employed to measure R_{110} submerged in 0.1 M NaOH (pH 13) or 0.1 M HCl (pH 1). Our findings indicate that the substrate maintains its periodicity evidenced with 'row-resolution' STM images. Next, we present a complementary *in-situ* SXRD study which probes the R_{110} interface with the same electrolytes as above. As was seen with the liquid cell STM measurements, our findings indicate that the substrate maintains order. At the 0.1 M NaOH interface, we propose a uniform coverage of terminal O^-/OH species at the Ti_{5c} site with the Na adsorbing preferentially at the surface tetra-dentate site (i.e. between two terminal O^-/OH species and two surface bridging O). This is coupled with an ordered hydration layer above it. At the 0.1 M HCl interface, we propose a uniform coverage of Cl adsorbing at the surface Ti_{5c} site. Lastly, preliminary electrochemical STM measurements of TiO_2 under 0.1 M NaOH yield terrace resolution images indicating a degree of order under electrochemical

control which is a promising sign for future work. To conclude and answer our research question, our combined STM and SXRD gives evidence that R_{110} is able to maintain order under both the chosen electrolytes that we explored. As such this is a significant step forward in exploring R_{110} under electrolyte solutions indicating electrochemical surface studies on R_{110} are potentially plausible. To this extent, our preliminary electrochemical STM findings are a promising step forward.

Chapter 6 discusses STM tip manipulation of electron irradiated A_{101} to create rutile TiO_2 (100) (R_{100}) patches and thus create an anatase/rutile interface that has been predicted to be the focal point of numerous TiO_2 chemical reactions. Our findings highlight that this tip manipulation method possesses the capability to create ordered regions with row spacing of ~4.5 Å, ~9.0 Å and ~13.5 Å which we assign to R_{100} (1 × 1), R_{100} (1 × 2) and R_{100} (1 × 3). In connection with the above, an STM study of single crystal R_{100} is presented to better understand the surface structure in UHV and its interface with photoactive carboxylic acids such as acetic acid and tri-methyl acetic acid (dosed in gas phase). Acetic acid adsorption gives rise to an ordered overlayer with a (×2) periodicity in the [001] direction. Tri-methyl acetic adsorption is largely disordered. These measurements are central to future experiments pertaining to the dosing of photo-active molecules at the R_{100} / A_{101} interface followed by illuminating the surface with UV light to probe photo-activity at the rutile/anatase interface. To conclude and answer our research question, we give evidence of the formation of numerous R_{100} terminations on A_{101} and have thus successfully created an anatase/rutile interface and characterised it on an atomic scale with STM. We have also successfully characterised the adsorption of photo-active carboxylic acids on R_{100} which was absent in the literature.

Lastly, Chapter 7 summarises the work presented in this thesis and provides a general outlook for future work.

1.5 References

1. F. Allhoff, P. Lin and D. Moore, *What Is Nanotechnology and Why Does It Matter?: From Science to Ethics*, Wiley-Blackwell, 2010.
2. H. P. Bonzel, *Physics Reports-Review Section of Physics Letters*, 2003, **385**, 1-67.
3. D. M. Eigler and E. K. Schweizer, *Nature*, 1990, **344**, 524-526.
4. G. Binnig and H. Rohrer, *Helvetica Physica Acta*, 1982, **55**, 726-735.
5. G. Binnig, H. Rohrer, C. Gerber and E. Weibel, *Applied Physics Letters*, 1982, **40**, 178-180.
6. G. Binnig and H. Rohrer, *Surface Science*, 1983, **126**, 236-244.
7. G. Binnig and H. Rohrer, *Ibm Journal of Research and Development*, 1986, **30**, 355-369.
8. G. Binnig and H. Rohrer, *Reviews of Modern Physics*, 1987, **59**, 615-625.
9. M. Bowker, *Acs Nano*, 2007, **1**, 253-257.
10. M. Setvin, M. Wagner, M. Schmid, G. S. Parkinson and U. Diebold, *Chemical Society Reviews*, 2017, **46**, 1772-1784.
11. H. J. Zhang, G. H. Chen and D. W. Bahnemann, *Journal of Materials Chemistry*, 2009, **19**, 5089-5121.
12. C. L. Pang, R. Lindsay and G. Thornton, *Chemical Society Reviews*, 2008, **37**, 2328-2353.
13. C. L. Pang, R. Lindsay and G. Thornton, *Chemical Reviews*, 2013, **113**, 3887-3948.
14. U. Diebold, *Surface Science Reports*, 2003, **48**, 53-229.
15. H. Hussain, Eng. D. Thesis, University College London, 2013.
16. H. Hussain, G. Tocci, T. Woolcot, X. Torrelles, C. L. Pang, D. S. Humphrey, C. M. Yim, D. C. Grinter, G. Cabailh, O. Bikondoa, R. Lindsay, J. Zegenhagen, A. Michaelides and G. Thornton, *Nature Materials*, 2017, **16**, 461-467.
17. M. J. Jackman, A. G. Thomas and C. Muryn, *Journal of Physical Chemistry C*, 2015, **119**, 13682-13690.
18. A. Ciszewski, R. Kucharczyk and K. Wandelt, *Surface Science*, 2013, **607**, 1-1.
19. A. Gross and K. Wandelt, *Surface Science*, 2015, **631**, 1-1.
20. K. T. Tang and J. P. Toennies, *Surface Science*, 1992, **279**, L203-L206.
21. A. Fujishima and K. Honda, *Nature*, 1972, **238**, 37-38.
22. M. Gratzel, *Nature*, 2001, **414**, 338-344.
23. F. Zhang, J. Evertsson, F. Bertram, L. Rullik, F. Carla, M. Langberg, E. Lundgren and J. S. Pan, *Electrochimica Acta*, 2017, **241**, 299-308.
24. T. Ohno, K. Sarukawa, K. Tokieda and M. Matsumura, *Journal of Catalysis*, 2001, **203**, 82-86.
25. M. Setvin, B. Daniel, U. Aschauer, W. Hou, Y. F. Li, M. Schmid, A. Selloni and U. Diebold, *Physical Chemistry Chemical Physics*, 2014, **16**, 21524-21530.
26. M. Setvin, B. Daniel, V. Mansfeldova, L. Kavan, P. Scheiber, M. Fidler, M. Schmid and U. Diebold, *Surface Science*, 2014, **626**, 61-67.
27. J. P. W. Treacy, H. Hussain, X. Torrelles, D. C. Grinter, G. Cabailh, O. Bikondoa, C. Nicklin, S. Selcuk, A. Selloni, R. Lindsay and G. Thornton, *Physical Review B*, 2017, **95**, 075416.
28. O. Bikondoa, C. L. Pang, R. Ithnin, C. A. Muryn, H. Onishi and G. Thornton, *Nature Materials*, 2006, **5**, 189-192.
29. Y. B. He, A. Tilocca, O. Dulub, A. Selloni and U. Diebold, *Nature Materials*, 2009, **8**, 585-589.
30. I. M. Nadeem, G. T. Harrison, A. Wilson, C. L. Pang, J. Zegenhagen and G. Thornton, *Journal of Physical Chemistry B*, 2018, **122**, 834–839.
31. D. T. Payne, Y. Zhang, C. L. Pang, H. H. Fielding and G. Thornton, *Topics in Catalysis*, 2017, **60**, 392-400.

32. S. Selcuk and A. Selloni, *Nature Materials*, 2016, **15**, 1107-1113.
33. M. Landmann, E. Rauls and W. G. Schmidt, *Journal of Physics-Condensed Matter*, 2012, **24**, 195503.
34. J. Georgieva, E. Valova, S. Armyanov, N. Philippidis, I. Poulios and S. Sotiropoulos, *Journal of Hazardous Materials*, 2012, **211**, 30-46.
35. R. Asahi, T. Morikawa, H. Irie and T. Ohwaki, *Chemical Reviews*, 2014, **114**, 9824-9852.
36. A. Paracchino, V. Laporte, K. Sivula, M. Gratzel and E. Thimsen, *Nature Materials*, 2011, **10**, 456-461.
37. K. Szot, M. Rogala, W. Speier, Z. Klusek, A. Besmehn and R. Waser, *Nanotechnology*, 2011, **22**, 254001.
38. Y. Furubayashi, T. Hitosugi, Y. Yamamoto, K. Inaba, G. Kinoda, Y. Hirose, T. Shimada and T. Hasegawa, *Applied Physics Letters*, 2005, **86**, 252101.
39. N. Nakayama and T. Hayashi, *Journal of Applied Polymer Science*, 2007, **105**, 3662-3672.
40. G. X. Shen, Y. C. Chen and C. J. Lin, *Thin Solid Films*, 2005, **489**, 130-136.
41. K. S. Brammer, C. J. Frandsen and S. Jin, *Trends in Biotechnology*, 2012, **30**, 315-322.

Chapter 2

Theoretical Aspects of Instrumentation

2.1 Introduction

An extensive effort to determine the nano-scale structure and behaviour of the surfaces and interfaces of technologically important materials has given rise to numerous research techniques that allow surface and interface investigations under a range of conditions such as pressure and temperature.[1-3] These techniques can be broadly placed in four categories – microscopy, diffraction, spectroscopy and theory. Microscopy is a particularly powerful method to probe the local morphology and topography of a surface or interface.[4] Alternatively, diffraction based techniques allow for a detailed understanding of surface geometry of well-ordered crystals.[5, 6] Spectroscopy is distinct from microscopy and diffraction as it provides extensive information on the chemical composition and electronic density of states of a system.[7, 8] Lastly, a theoretical approach allows for a simulated understanding of a system in question.[9] Together, these techniques provide a rigorous surface and interface investigation to better understand the atomic-scale structure and behaviour of technologically important materials.

This chapter reviews the theoretical aspects of the instrumentation used in this thesis – scanning tunnelling microscopy (STM), surface X-ray diffraction (SXRD), low energy electron diffraction (LEED), auger electron spectroscopy (AES) and photo-electron spectroscopy (PES).

2.2 Scanning Tunnelling Microscopy (STM)

2.2.1 Introduction and Basic Principles

Scanning Tunnelling Microscopy (STM) was developed by Binnig and Röhrer.[10-14] For their efforts, they shared the 1986 Nobel Prize in Physics. Today, STM is a mainstay of modern surface science investigations providing real-space imaging and atomic manipulation of surfaces.

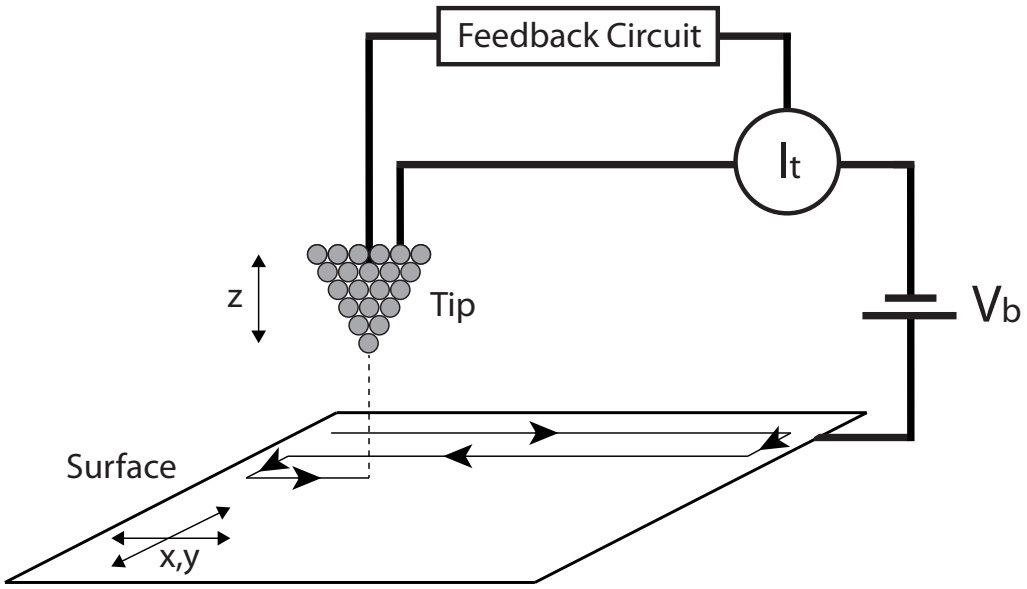

Figure 2.1: Schematic of STM operation where a tip moves over a surface to probe the local density of states.

In principle, STM operates by allowing electrons to flow from an atomically sharp conductive tip to a conducting sample (or vice versa) through a small gap (potential barrier). This phenomenon is known as the tunnelling effect. From a classical perspective, particles that do not have enough energy to overcome a potential barrier are not able to cross it. However, quantum mechanics postulates that there is a small, finite transmission

probability. If an infinite potential barrier exists between a tip and substrate, then the electron wave function amplitude would decay to zero outside the tip or sample. However, if the tip-substrate distance is lowered to around a few Å, then the tip and sample wave function can overlap in the potential barrier between them and emerge either side of the barrier with reduced amplitude. Hence, there is a finite probability of finding the electron in the potential barrier. The application of a bias induces the flow of electrons whereby a tunnelling current (I_t) can be measured. The basic principle of STM is shown in Figure 2.1. Two modes of STM exist which are discussed in section 3.3.2.

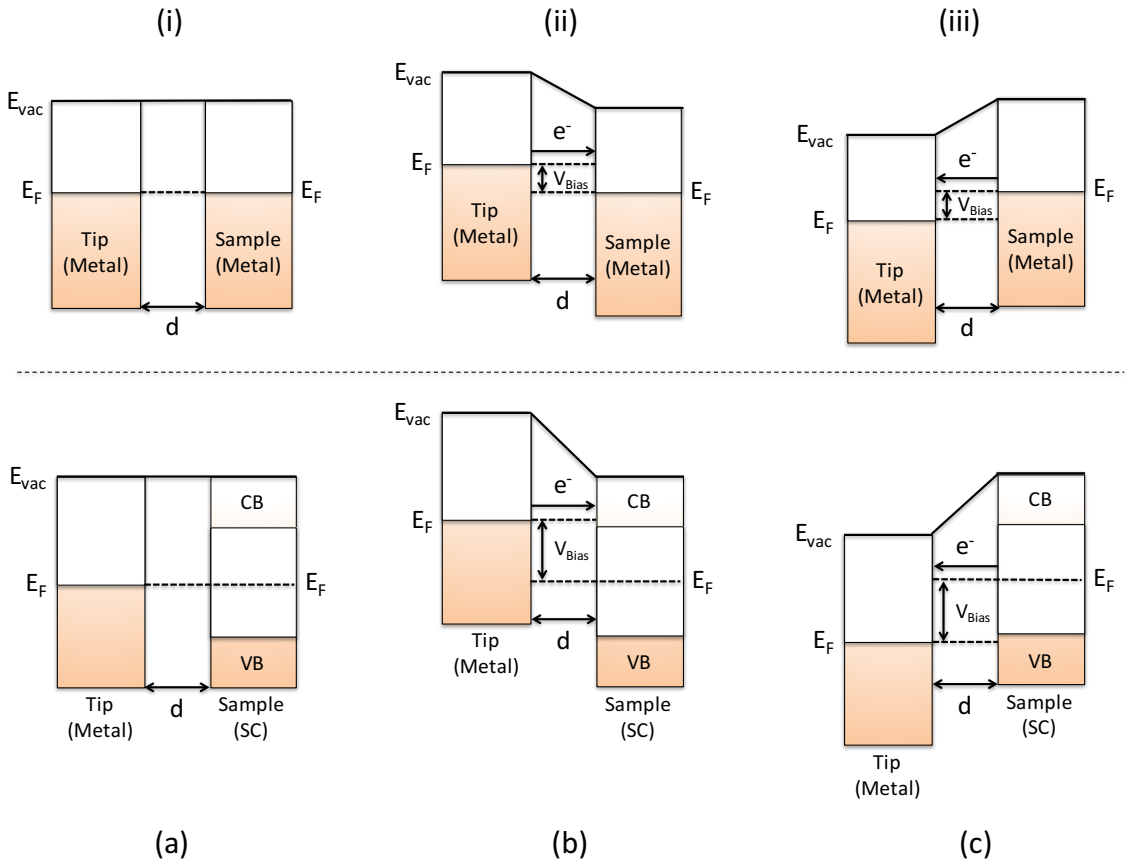

Figure 2.2: Band diagram showing the tunnelling junction between a metal tip and sample surface, which is either a metal (i, ii & iii) or a semiconductor (a, b & c) - 'a' and 'i' are at zero bias, 'ii' and 'b' are at a positive tip bias and 'iii' and 'c' are at a negative tip bias. E_{vac} is the vacuum level, E_F is the Fermi level, SC is semiconductor, CB is conduction band, VB is valence band and d is tip-surface distance.

Figure 2.2 shows a band diagram of the tunnelling junction illustrating the tunnelling phenomena in metals and semiconductors. In STM, the application of a bias induces electrons to flow from occupied to unoccupied states. Hence, STM images represent a convolution of the local density of states (LDOS) of occupied and unoccupied electronic states between a tip and surface. Assuming the use of a metal tip, metal surfaces require lower biases when compared to semiconductors. When the tip approaches tunnelling conditions with the metal or semiconductor surface, the tip and sample Fermi level (E_F) equilibrate. In metals, a small bias is required to offset this equilibration and induce a I_t. In semiconductors, E_F lies within the band gap. Hence, tunnelling must occur from the filled states of the tip to the empty states of the conduction band. Alternatively, tunnelling can occur from the valence band to the empty states in the tip. Therefore, there is a need to apply a higher bias when compared with metals.

2.2.2 Theory of STM

Figure 2.3 provides a model representation of the tunnelling process in one dimension. In the presence of a one-dimensional rectangular barrier which exists between a < *x* < b, the corresponding Schrödinger equation has the form,

$$\psi(x) \propto e^{-\kappa d}, \qquad \textbf{Equation 2.1}$$

where

$$\kappa = \frac{\sqrt{2m\,(V_H - E)}}{\hbar}. \qquad \textbf{Equation 2.2}$$

Here, d is the barrier width (tip-substrate distance), κ is the decay constant, m is the electron mass, V_H is the barrier height and E is the energy of the state from which

tunnelling occurs. The probability of the electron to tunnel is given by the transmission probability (T_p),

$$T_p = [1 + \frac{V_H^2 sinh^2(\kappa d)}{4E(V_H - E)}]^{-1}. \quad \textbf{Equation 2.3}$$

In this equation $sinh^2(\kappa d)$ can be rewritten as:

$$(\frac{e^{\kappa d} - e^{-\kappa d}}{2})^2. \quad \textbf{Equation 2.4}$$

In the regime of low transmission, it can be assumed that $\kappa d \gg 1$. Under this assumption, T_p can be reduced to:

$$T_p \propto e^{-2\kappa d}. \quad \textbf{Equation 2.5}$$

Subsequently, I_t can be given as:

$$I_t \propto e^{-2\kappa d}. \quad \textbf{Equation 2.6}$$

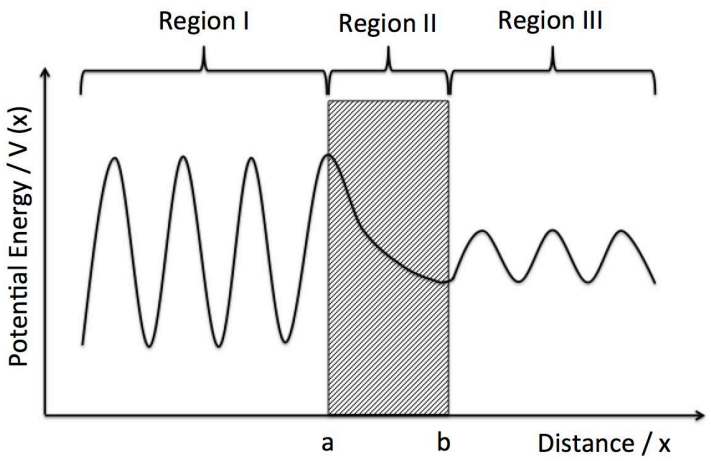

Figure 2.3: A model representation of the tunnelling effect in one-dimension. Region II represents the one-dimensional gap (barrier). Region I represents the incoming electron wave. Region III represents the electron wave after the tunnelling event. A reduction in amplitude is observed between Region I and II after the exponential decaying tunnelling event in Region II.

I_t is recorded on the order of nA and is extremely sensitive to changes in tip-substrate distances. κ is on the order of 1 $Å^{-1}$ whereby a change in tip substrate separation of 1 Å can lead to an order of magnitude change in I_t.[15] This relationship explains the extreme sensitivity of the STM. To better understand the theoretical aspects of the STM, a discussion into theoretical STM is necessary: Tersoff & Hamann[16-18], Lang[19-21], Chen[22, 23] and the Wentzel-Kramers-Brillouin[24, 25] (WKB) Approximation.

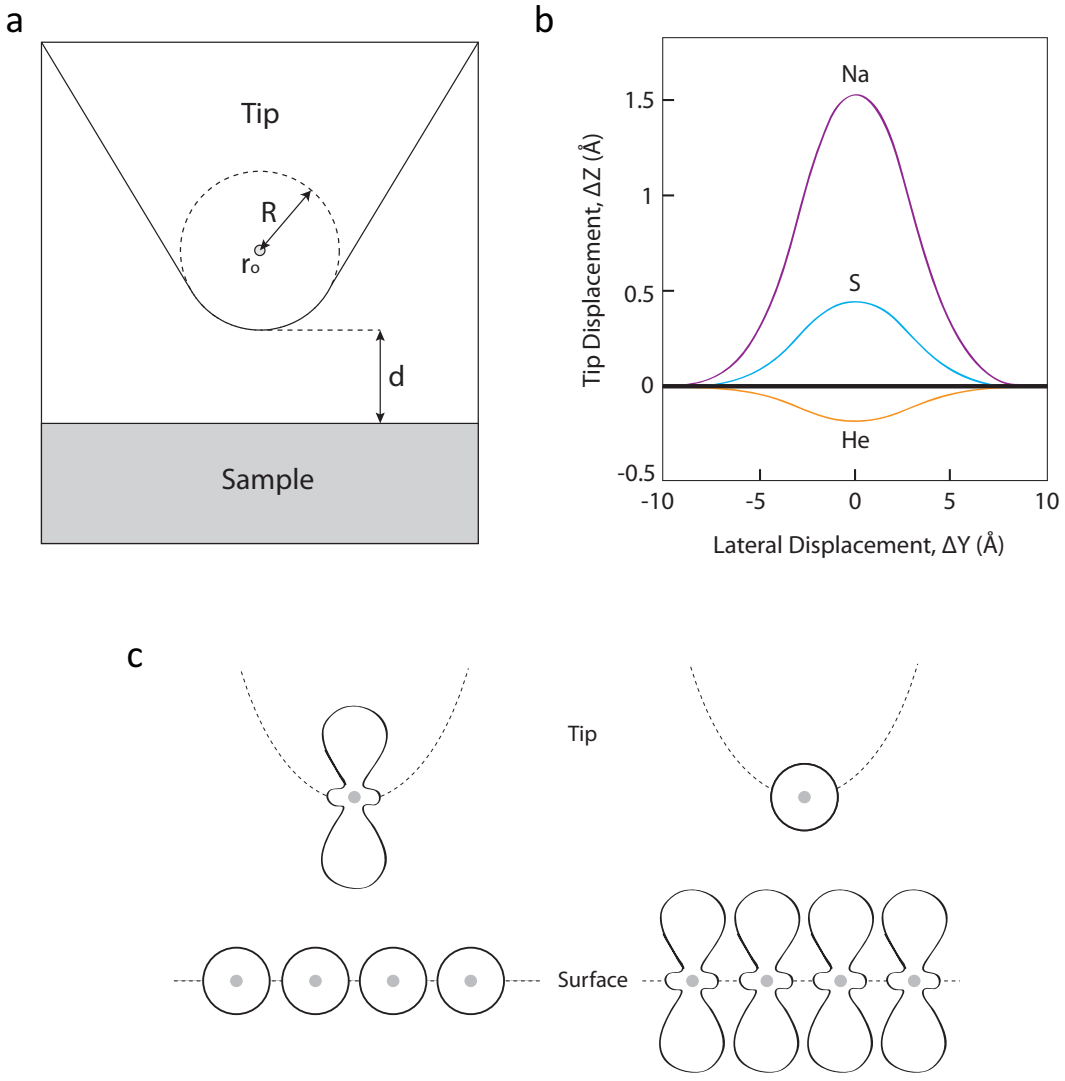

Figure 2.4: (a) Schematic of the spherically symmetric s-wave tip wavefunction model presented by Tersoff and Hamann.[17] (b) Change in tip displacement vs lateral separation at a constant I_t. Tip atom is Na. Sample adatoms are Na, S and He.[21] (c) Schematic illustrating Chen's reciprocity principle.[22]

Tersoff & Hamann[16, 17] define I_t by considering the overlap of the spherically symmetric s-wave tip wave function and sample wave function - see 2.4 (a). In Bardeen's perturbation theory of tunnelling[18], I_t is given in Equation 2.7.

$$I_t = \frac{2\pi e}{\hbar} \sum_{\mu,\nu} f\left(E_\mu\right)[1 - f(E_\nu + eV)]\left|M_{\mu\nu}\right|^2 \delta(E_\mu - E_\nu), \quad \textbf{Equation 2.7}$$

where *f(E)* is the Fermi function, *V* is the applied voltage, $M_{\mu\nu}$ is the tunnelling matrix element and E_μ and E_ν are the energy of the two states in the absence of tunnelling. In the low voltage and temperature limit, Equation 2.7 reduces to Equation 2.8:

$$I_t = \frac{2\pi e}{\hbar}\ e^2 V \sum_{\mu,\nu}\left|M_{\mu\nu}\right|^2\ \delta(E_\nu - E_F)\delta(E_\mu - E_F), \qquad \textbf{Equation 2.8}$$

where E_F is the Fermi level. Bardeen[18] demonstrated that $M_{\mu\nu}$ can be expressed as Equation 2.9.

$$M_{\mu\nu} = \frac{\hbar^2}{2m} \int d\vec{S}\ (\psi_\mu^* \vec{\nabla}\psi_\nu - \ \psi_\nu \vec{\nabla}\psi_\mu^*), \qquad \textbf{Equation 2.9}$$

where ψ_μ is the tip wavefunction and $\psi_\nu$is the sample wavefunction. The sample was given a general expression in the form of a Bloch wavefunction. Tersoff & Hamann assume that the tip is a single point probe, which yields the maximum possible resolution. They introduced an s-wave model for the tip wavefunction - Equation 2.10:

$$\psi_\mu = \ \Omega_t^{-\frac{1}{2}} c_t \kappa R e^{\kappa R} (\kappa|\vec{r} - \vec{r}_0|)^{-1} e^{-\kappa|\vec{r} - \vec{r}_0|}, \qquad \textbf{Equation 2.10}$$

where Ω_t is the tip probe volume. This leads to a matrix element which is proportional to the amplitude of ψ_ν at the position $\overrightarrow{r_0}$ of the tip. This gives the relationship for I_t in Equation 2.11:

$$I_t \ \propto \ \sum_\upsilon |\psi_\nu \overrightarrow{r_0}|^2\ \delta(E_\nu - E_F)\ \equiv\ \rho\ (\overrightarrow{r_0}, E_F). \qquad \textbf{Equation 2.11}$$

This relationship makes the approximation that I_t is proportional to the surface LDOS at E_F, which assumes a low bias voltage (10meV). This may be acceptable for metals but higher voltages are needed for semiconductors. Equation 2.11 can be approximated to Equation 2.12 for higher voltages where $T(E, eV)$ is the transmission probability:

$$I_t \sim \int_{E_f}^{E_f+V} \rho\left(\overrightarrow{r_0}, E_f\right) T(E, eV)\, \partial \mathrm{E}. \qquad \textbf{Equation 2.12}$$

The presence of adsorbates on a surface will affect the surface LDOS. As discussed above, STM measures the LDOS of a surface. Hence, the presence of adsorbates will affect the obtained STM images. Lang[19-21] used *ab initio* calculations in the Tersoff & Hamann formalism to investigate the effect of adsorbates on LDOS by modelling the tip and surface as two flat electrodes. The system consisted of a tip with a Na atom termination and a jellium model for the metal surface with adsorbates: Na, S and He. This work (see Figure 2.4 (a)) illustrated how the presence of adsorbates can increase (Na, S) or decrease (He) the LDOS. In an STM image, an increase in LDOS will appear as a protrusion whilst a decrease in LDOS will appear as depressions. Scanning over Na and S gave a positive tip displacement. This positive tip displacement was greater for Na than S as the Na atom sits higher on the surface and has a greater LDOS at E_F than S. Even though the actual height of He is positive, He has a closed valence shell, which causes a reduction in DOS at E_F by polarising the metal states away from E_F. This illustrates the difficulty in STM image analysis, where adsorbates can appear as depressions. Hence, theoretical STM images are often necessary for analysis.

Tersoff & Hamann and Lang treat the tip electrons as spherically symmetric s-wave functions. Experimentally, STM has resolved individual surface atoms with distances of 2.5-3 Å. This contradicts the resolution limits of 6-9 Å predicted by spherically symmetric s-wave functions. Chen[22] states that the assumption of an s-wave function is not suitable

as tips are typically made of d band metals (Pt or W), whose LDOS at E_F comes from d states. W is a commonly used tip material and is composed of highly localised d_z^2 dangling bonds, which are believed to partake in tunnelling. Chen introduced the reciprocity principle, which demonstrates that an s-wave tip scanning a d_z^2 surface is equivalent to a d_z^2 tip scanning an s-wave surface - see Figure 2.4 (c). This is due to the presence of a symmetric tunnelling gap. By scanning an s-wave tip over a d_z^2 wave surface, Chen showed results comparable to experiments. This illustrated the importance of knowing the nature of the tip apex atom.

The improved model presented by Chen shows that the tip-surface distance is between 4-6 Å.[23] In this regime, an attractive atomic force between the tip and surface exists due to the movement of electrons back and forth (partial covalent bond). The application of a bias (for imaging) moves electrons in one specific direction and involves covalent bonds forming and breaking. Hence, tip manipulation (voltage pulses) can be used to induce chemical reactions (H adtom desorption on rutile TiO_2 (110) (R_{110}))[26] or atom movement (Si atomic manipulation on Si surfaces).[27]

STM imaging of semiconductors (such as TiO_2) typically requires voltages in excess of 0.5 V. Under these conditions, the Tersoff & Hamann theory fails as it holds in the low bias regime (10 meV) where I_t is proportional to the LDOS at the E_F. To take the higher bias for semiconductors into consideration, the Wentzel-Kramers-Brillouin[24, 25] (WKB) approximation is used to represent I_t. At zero temperature, I_t is calculated with a given tunnelling probability between two electrodes. In the WKB approximation, I_t can be expressed as an integral over the initial filled and final empty energy states for tunnelling - Equation 2.13.

$$I_t = \int_0^{eV} \rho_s(r,E)\rho_t(r,-eV+E)T(E,eV,\ r)\delta E \qquad \textbf{Equation 2.13}$$

where ρ_s and ρ_t are the densities of state of the sample and tip, respectively, at location r and energy E, measured with respect to their individual E_F. The tunnelling transmission probability $T(E, eV,\ r)$ for electrons with energy E, applied bias voltage V, tip-surface separation (Z) and surface / tip work function ($\Phi_s\ /\ \Phi_t$) is given by Equation 2.14.

$$T(E, eV) = e^{-\frac{2Z\sqrt{2m}}{\hbar}\sqrt{\frac{\Phi_S + \Phi_t}{2} + \frac{eV}{2} - E}} \qquad \textbf{Equation 2.14}$$

If eV < 0 (negative sample bias), T is largest for E = 0. This corresponds to the electrons from the sample E_F. If eV > 0 (positive sample bias), T is largest for E = eV. This corresponds to the electrons from tip E_F. Thus, the tunnelling probability is highest for the electrons at E_F.

Today, the discussed theoretical insights into STM have been further built upon to simulate STM images and are used in conjunction with experimental STM to better elucidate structures on the nanoscale. For example, experimental and simulated STM image have been used to examine the R_{110} surface and defect structure.[28]

2.3 Surface X-Ray Diffraction (SXRD)

2.3.1 Introduction and Basic Principles

The discovery of X-rays by Röntgen[29] yielded him the inaugural Nobel Prize in Physics. In the following years, the 1914 Nobel Prize in Physics was awarded to Laue[30] '*for his discovery of the diffraction of X-rays by crystals*' and the 1915 Nobel Prize in Physics was awarded to the father-son Bragg[31, 32] duo '*for their services in the analysis of crystal structure by means of X-rays*'. Since then, X-ray diffraction has been a powerful tool for crystallographers where the density of electrons around atoms in a crystalline material gives rise to specific diffraction patterns. Bragg's law provides an effective description of diffraction conditions. As a wave impinges on a crystal with spacing *d*, constructive interference occurs when the optical path length difference between the scattered waves from successive atomic layers is an integer number, *n*, of wavelengths - mathematically and schematically shown in Equation 2.15 and Figure 2.5, respectively.

$$n\lambda = 2d\,sin\,\theta \qquad \textbf{Equation 2.15}$$

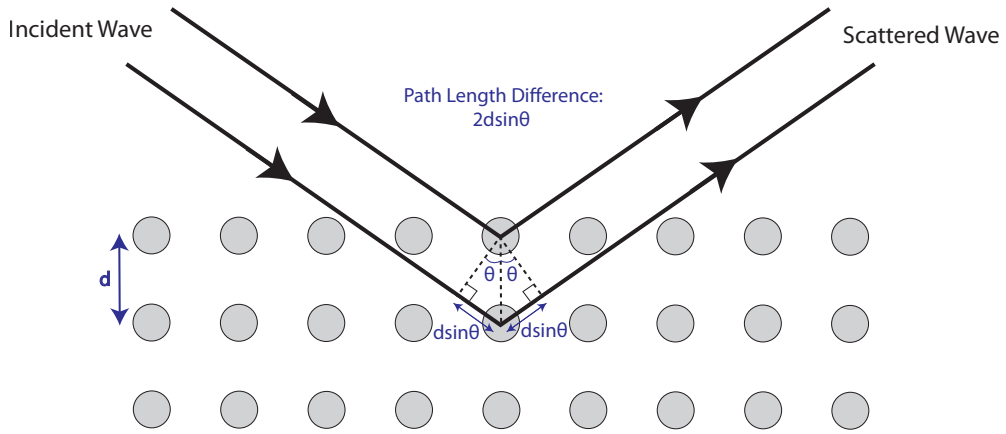

Figure 2.5: Schematic illustrating Bragg's law illustrating the wave path length difference of $2d\,sin\,\theta$.

X-ray crystallography has long been utilised to determine bulk crystal structures, however, its use in determining the crystal structure of surfaces and interfaces is relatively more recent.[33] Equation 2.16 depicts the equation for de Broglie wavelengths:

$$\lambda = {}^{h}/_{p} = {}^{h}/_{mv}\,, \qquad \textbf{Equation 2.16}$$

where λ is the wavelength, h is Planck's constant, p is the particle momentum, m is the particle mass and v is the particle velocity. In its current state, Equation 2.16 is unable to define a photon wavelength from a photon energy as photons do not possess a rest mass. However, considering Equation 2.17 and that $v = c$ for a photon where c is the speed of light, allows for Equation 2.16 to be re-arranged to equation 2.18:

$$\mathrm{E} = c^{2}\,, \qquad \textbf{Equation 2.17}$$

$$\lambda = {}^{h}/_{((E/c^{2})c)} = {}^{hc}/_{E}\,, \qquad \textbf{Equation 2.18}$$

where E is the photon energy. Utilising Equation 2.18, hard X-rays in the range of 10 to 30 keV will have wavelengths in the range of 1.2 to 0.4 Å. These wavelengths are similar to atomic distances within crystals making them ideal probes with which to probe periodically arranged surfaces.

X-ray diffraction is typically described by the kinematical or dynamical scattering theory.[34] The former assumes that the incident beam is only scattered once without a change in energy such that the intensity remains the same for each successive atomic plane in a periodic crystal.[34] In contrast, the latter considers multiple scattering events where the intensity for each successive atomic plane does not remain the same.[34] The kinematic approximation is typically used for X-ray diffraction measurements as X-rays interact weakly with matter resulting in minimal multiple scattering events.

Surface X-Ray Diffraction (SXRD) employs X-rays to probe surfaces and interfaces and is able to provide a comprehensive structural understanding of a given system. In comparison to utilising electrons as probes, X-rays interact very weakly with matter with minimal surface deterioration. This capability of X-rays makes it an excellent probe to investigate surfaces and interfaces - in particular buried interfaces such as the solid/liquid and solid/gas interface.

As X-rays interact weakly with matter, it can penetrate deeply into a crystal allowing for suitable bulk X-ray diffraction. However, surfaces are typically described as the first few atomic layers of a crystal resulting in SXRD requiring grazing incident X-rays (with respect to the surface plane) to improve surface sensitivity. Nonetheless, the corresponding diffraction intensities continues to be bulk dominated due to the low surface to bulk ratio. This necessitates a high photon flux in order to further improve surface sensitivity. Typically, this requires the use of synchrotron radiation facility that can supply sufficient levels of photon flux to perform successful SXRD measurements.

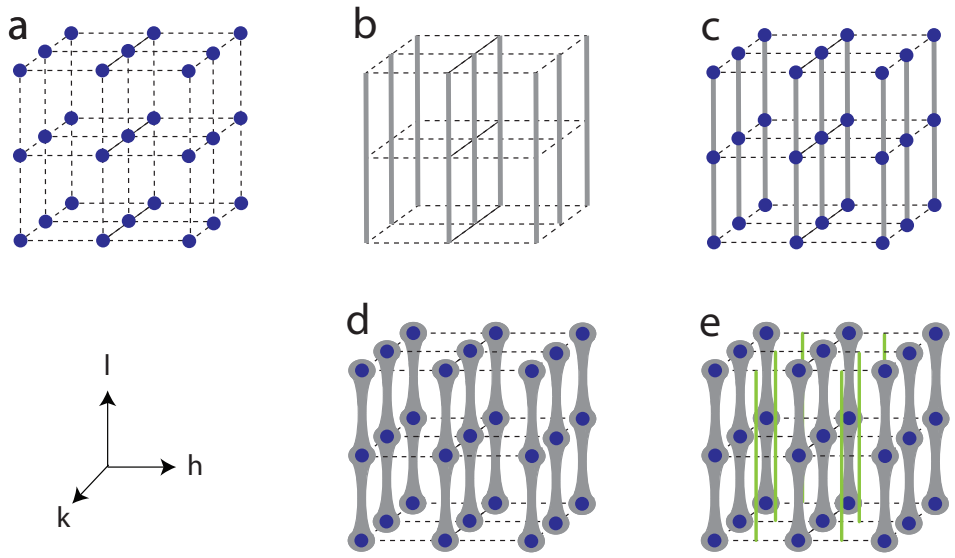

Figure 2.6: Schematic of reciprocal space diffraction features observed for (a) 3D bulk crystal, (b) a 2D monolayer, (c) 2D monolayer on a 3D bulk crystal (summation), (d) a surface yielding CTRs and (e) a reconstructed surface with FORs highlighted in orange.

Crystals possess infinite periodicity in the in-plane and out-of-plane directions. Upon the creation of a surface, the surface atoms undergo a re-arrangement to minimise surface energy where surface atoms can undergo relaxation[5, 35] and/or reconstruction[36]. A surface structure is distinct with respect to the bulk where moving from the surface towards the bulk results in each atomic layer becoming increasingly more bulk-like until it adopts the bulk structure. Additionally, the formation of a surface gives rise to a system that possesses infinite periodicity in the in-plane direction, however, the out-of-plane periodicity is semi-infinite resulting in non-isotropic scattering. This gives rise to surface crystal truncation rods (CTRs) where surface specific diffuse intensity can be observed between the bulk diffraction (Bragg) peaks perpendicular to the surface at integer reciprocal space *h* and *k* values. In the event of a surface reconstruction, fractional order rods (FORs) are observed where surface reconstruction specific diffuse intensity is observed perpendicular to the surface at non-integer reciprocal space *h* and/or *k* values. Figure 2.6 gives a schematic of reciprocal space lattices highlighting CTRs and FORs.

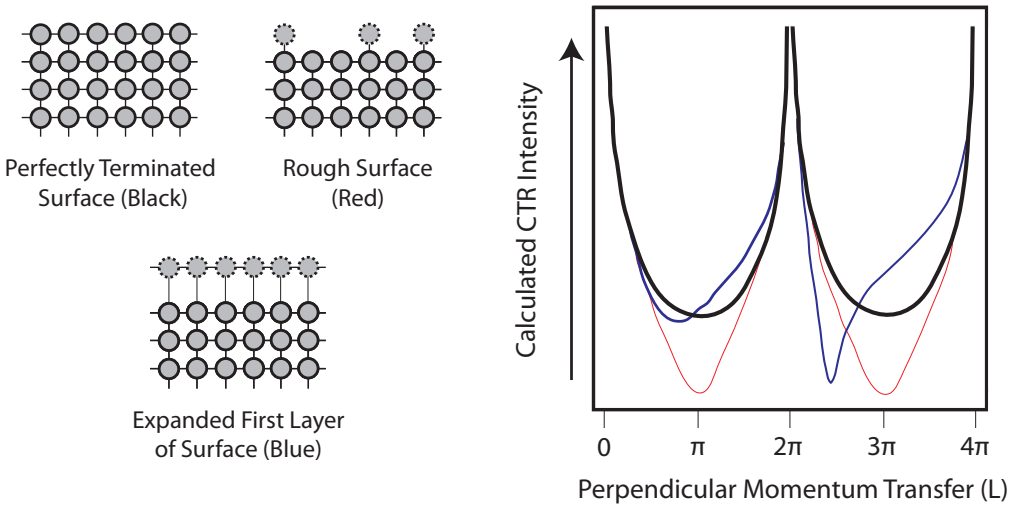

Figure 2.7: Calculated CTR intensity plotted against the perpendicular momentum transfer (L) for a simple structure ending abruptly. F_{calc} for a perfectly terminated, rough and expanded first layer surface are shown with black, red and blue lines, respectively.[37]

The intensity distribution of a CTR is highly sensitive to surface structure. Figure 2.7 shows a typical CTR for a surface and highlights how surface changes can alter the shape of the CTR. It can be observed that surface relaxation and roughness phenomena can result in drastic changes in intensity distribution in between the bulk diffraction (Bragg) peaks. In Figure 2.7, surface relaxation is shown to induce asymmetry in the intensity distribution between bulk diffraction (Bragg) peaks. Alternatively, surface roughness causes a decrease in intensity between the bulk diffraction (Bragg) peaks caused by destructive interference associated with loss of surface order.

In this thesis, all SXRD measurements were performed at Beamline I07: Surface and Interface Diffraction[38] at Diamond Light Source (see section 3.5.2) on a 2+3 diffractometer with a Pilatus100K 2D detector. Intensities obtained from measurements undergo a background subtraction followed by geometric corrections for a 2+3 detector as has been discussed by Vlieg[39, 40] and shown in Equation 2.19:

$$F_{exp} = Scaling\ Factor \times \sqrt{I_{BC} \times \frac{C_{Pol} \times C_{Int} \times C_{Lor}}{C_{Area} \times T_D}} \quad , \qquad \textbf{Equation 2.19}$$

where I_{BC} is the background corrected intensity, C_{Pol} is the polarisation correction factor, C_{Int} is the interception correction factor, C_{Lor} is the Lorentz correction factor, C_{Area} is active area correction factor, T_D is the dwell time and F_{exp} is the experimental structure factor. In this thesis, a macro in IGOR Pro developed at Beamline I07: Surface and Interface Diffraction[38] at Diamond Light Source (see section 3.5) by Prof. Chris Nicklin (Principal Beamline Scientist at I07) and Dr. Jon Treacy was used to perform the necessary background and geometric corrections.[41] This macro has been previously used for publications[35, 42] with measurements performed at Beamline I07. The macro operates by defining a region of interest (ROI) in the pilatus100K detector images where the main ROI highlights the CTR intensity whereas a background ROI represents the background

signal. Subsequently, after background subtraction, intensities are integrated and extracted followed by the necessary geometric corrections being applied.

The F_{exp} is a Fourier transform of the spatial distribution of the electron density where it is not possible to obtain the inverse Fourier transform to determine the surface / interface structure. This is known as the phase problem where experimentally the intensity of a wave can be measured whereas the phase is not recorded. To overcome this issue, F_{exp} can be compared with calculated structure factors (F_{calc}) to obtain a surface / interface structure. In this thesis, structure determination is performed with ROD (a manual for which is provided in reference[43]), a program developed by Vlieg. The program utilises a '.dat' file that contains the F_{exp}, a '.bul' file that contains information relating to the bulk structure of the crystal and a '.fit' file that contains information relating to the surface / interface structure. Next, iteratively, the '.fit' file is altered and varied with the atoms in the '.fit' file allowed to displace with specific occupancies and thermal atomic vibrations (Debye-Waller parameters) in an attempt to obtain a F_{calc} that best matches the F_{exp}. In ROD, the structure optimisation and structure refinement is performed via a least squares refinement process where the goodness-of-fit is reported via the normalised χ^2 (χ^2_n)[33, 43, 44] - see Equation 2.20. A χ^2_n of ~1 can be considered a good fit between F_{exp} and F_{calc} and thus a surface / interface structure can be determined.

$$\chi_n^2 = \frac{1}{N-P} \sum_{i=1}^{N} \left(\frac{|F_{exp(i)}| - |F_{calc(i)}|}{\sigma_{\exp(i)}} \right)^2 , \qquad \textbf{Equation 2.20}$$

where N is the number of measured structure factors, P is the number of parameters optimised during fitting and σ_{exp} is the uncertainty associated with F_{exp}. The reported precision of each fitted parameter is determined systematically by varying the parameter about its optimal value whilst optimising the remaining parameters until the χ^2_n increases by 1/(N-P) from its minimum value.[44]

As is shown in Figure 2.7, structure roughness can play an important role in a CTRs (and FORs) intensity. For this purpose, numerous 'roughness models' exist to effectively model surface roughness such as the ß-roughness model[45] or the terraced roughness model[46]. The former is incorporated into ROD as the approximate ß model[43] (see Equation 2.21) and is usually utilised until proven inappropriate.

$$R_{ß} = \frac{1-ß}{\sqrt{(1-ß)^2 + 4ß\sin^2\left(\frac{\pi\left(l-l_{bragg}\right)}{N_{layers}}\right)}}, \qquad \textbf{Equation 2.21}$$

where l_{bragg} is the l-value for the nearest Bragg peak, N_{layers} is the number of equidistant layers within the unit cell and $R_ß$ is the roughness factor that is multiplied by the F_{calc} so as to obtain a roughness adjusted F_{calc} ($F_{calc}^{ß}$). In essence, the approximate ß model varies the occupancy of the surface layers where surface layers furthest from the bulk exhibit the greatest degree of roughness. A ß value of 0 suggests no surface roughness whereas a ß value of 1 indicates a completely rough surface.

2.3.2 Theory of SXRD

The theoretical considerations and structure determination perspectives of SXRD have been discussed in great detail in the works of Robinson[33, 45], Feidenhans'l[44], Renaud[47] and Vlieg[39, 43]. The principles of SXRD are rooted in X-ray diffraction from periodic surfaces. Let us first consider the phenomena of X-ray diffraction from a single electron as is given by the Thomson scattering formula[33, 44]:

$$A_e\, e^{i\overrightarrow{k_f}\cdot\overrightarrow{r_e}} = A_0 \left(\frac{e^2}{mc^2R}\right) P^{1/2}\, e^{i\overrightarrow{k_i}\cdot\overrightarrow{r_e}}, \qquad \textbf{Equation 2.22}$$

where A_e is the amplitude of the scattered wave from a single electron, A_0 is the incident beam amplitude, e is the electron charge, m is the electron mass, c is the speed of light, R

is the distance at which the scattered wave is observed, r_e represents the electron position and P is the polarisation factor. $\overrightarrow{k_\iota}$ and $\overrightarrow{k_f}$ represent the incident and scattered wave vectors, respectively, where under elastic scattering conditions $\left|\overrightarrow{k_\iota}\right|$ equals $\left|\overrightarrow{k_f}\right|$. The difference between these two wave vectors is referred to as the scattering vector ($\vec{\mathrm{Q}}$), otherwise referred to as the momentum transfer. This allows for Equation 2.22 to be re-written as:

$$A_e = A_0 \left(\frac{e^2}{mc^2 R}\right) P^{1/2}\, e^{i\vec{\mathrm{Q}}\cdot\overrightarrow{r_e}} . \qquad \textbf{Equation 2.23}$$

Moving on to scattering from an atom, the electrons are distributed around the nucleus with an atomic electron density around the atomic nucleus of $\rho(r')$. The sum of the scattering amplitudes from each electron in the atom necessitates that electrons be represented by their density distribution. The summation is given as an integration: $\int A_e\, \rho\left(\overrightarrow{\mathrm{r}'}\right)\, d^3\overrightarrow{\mathrm{r}'}$. The amplitude of a wave scattered from a single atom (A_a) is given as:

$$A_a = A_0 \left(\frac{e^2}{mc^2 R}\right) P^{1/2} f_a(\vec{\mathrm{Q}})\, e^{i\vec{\mathrm{Q}}\cdot\overrightarrow{r_a}} , \qquad \textbf{Equation 2.24}$$

where r_a is the position of the atom and $f_a(\vec{Q})$ is the atomic form or scattering factor which describes the Fourier transform of the electron distribution in an atom and is given as:

$$f_a(Q) = \int \rho\left(\overrightarrow{\mathrm{r}'}\right) e^{i\vec{\mathrm{Q}}\cdot\overrightarrow{\mathrm{r}'}}\, d^3\overrightarrow{\mathrm{r}'} . \qquad \textbf{Equation 2.25}$$

When considering the scattering amplitude of a unit cell, this requires a summation of the scattering amplitudes of the atoms within the unit cell. The amplitude of a wave scattered from a unit cell (A_u) is given as:

$$A_u = A_0 \left(\frac{e^2}{mc^2 R}\right) P^{1/2}\, F(\vec{\mathrm{Q}}) , \qquad \textbf{Equation 2.26}$$

$$F(Q) = \sum f_a(\vec{Q})\, e^{i\vec{Q}\cdot\vec{r_a}}\,, \qquad \textbf{Equation 2.27}$$

where $F(\vec{Q})$ is referred to as the structure factor which defines the sum of the scattering contribution of the atoms in the unit cell (i.e. lattice sum). Considering a unit cell with lattice vectors $\vec{a}$, $\vec{b}$ and $\vec{c}$ where unit cell expansions in each direction are given by N_1, N_2 and N_3, the amplitude of a scattered wave from a crystal (A_c) can be given as:

$$A_c = A_0 \left(\frac{e^2}{mc^2R}\right) P^{\frac{1}{2}} F(\vec{Q}) \sum_{a_1}^{N_1-1} \sum_{a_2}^{N_2-1} \sum_{a_3}^{N_3-1} e^{i\vec{Q}\cdot(a_1\vec{a} + a_2\vec{b} + a_3\vec{c})}\,. \qquad \textbf{Equation 2.28}$$

The expression of the lattice sum as a geometric series and given that the intensity of a scattered wave (I_c) equals the square of the scattered wave amplitude from a crystal (A_c):

$$I_c = I_0 \frac{e^4}{m^2c^4R^2} P \left|F(\vec{Q})\right|^2 \cdot \frac{\sin^2(\frac{1}{2}N_1\vec{Q}\cdot\vec{a})}{\sin^2(\frac{1}{2}\vec{Q}\cdot\vec{a})} \cdot \frac{\sin^2(\frac{1}{2}N_2\vec{Q}\cdot\vec{b})}{\sin^2(\frac{1}{2}\vec{Q}\cdot\vec{b})} \cdot \frac{\sin^2(\frac{1}{2}N_3\vec{Q}\cdot\vec{c})}{\sin^2(\frac{1}{2}\vec{Q}\cdot\vec{c})}\,. \qquad \textbf{Equation 2.29}$$

Given a 3D crystal, peaks in intensity are observed when the Miller indices adopt integer values and satisfy the Laue conditions (Equation 2.30-2.32). The Laue conditions reduce to Bragg's law:

$$\vec{Q}\cdot\vec{a} = 2\pi h\,, \qquad \textbf{Equation 2.30}$$

$$\vec{Q}\cdot\vec{b} = 2\pi k\,, \qquad \textbf{Equation 2.31}$$

$$\vec{Q}\cdot\vec{c} = 2\pi l\,, \qquad \textbf{Equation 2.32}$$

where:

$$\vec{Q} = h\vec{a'} + k\vec{b'} + l\vec{c'}\,, \qquad \textbf{Equation 2.33}$$

and $\overrightarrow{a'}$, $\overrightarrow{b'}$ and $\overrightarrow{c'}$ represent reciprocal space vectors. When the Laue condition is satisfied Equation 2.29 can be reduced to:

$$I_c = I_0 \frac{e^4}{m^2 c^4 R^2} P \left|F\left(h\overrightarrow{a'} + k\overrightarrow{b'} + l\overrightarrow{c'}\right)\right|^2 (N_1)^2 (N_2)^2 (N_3)^2. \quad \textbf{Equation 2.34}$$

Thus far, the $F(\vec{Q})$ is considered to be a perfect crystal, however, in reality crystals undergo thermal atomic vibrations and maintain partial occupancies. To compensate for this, $F(\vec{Q})$ maintains an atomic Debye-Waller factor (B_a) and an atom occupancy factor (θ_a), respectively:

$$F(\vec{Q}) = \sum \theta_a \, f_a(\vec{Q}) \, e^{i\vec{Q}\cdot\vec{r_a}} \, e^{-B_a(\frac{\vec{Q}}{4\pi})^2} , \quad \textbf{Equation 2.35}$$

where:

$$B_a = \frac{8\pi^2}{3}\langle \mu_a^2 \rangle , \quad \textbf{Equation 2.36}$$

and $\langle \mu_a^2 \rangle$ is the mean square thermal vibration amplitude.

Let us now consider the case for X-ray diffraction of surfaces which in the first instance can be considered as a 2D monolayer where only two Laue conditions (Equation 2.30 and 2.31) can be met. As the constraint applied by Equation 2.32 is no longer considered, diffraction patterns consist of lines along the surface normal - a schematic for which is shown in Figure 2.6 (b). The amplitude of a scattered wave from a 2D monolayer (A_{ML}) can be given as:

$$A_{ML} = A_0 \left(\frac{e^2}{mc^2 R}\right) P^{\frac{1}{2}} F_{hk}(\vec{Q}_z) \, N_1 \, N_2 , \quad \textbf{Equation 2.37}$$

and:

$$I_{ML} = I_0 \frac{e^4}{m^2 c^4 R^2} P \left|F_{hk}(\vec{Q}_z)\right|^2 (N_1)^2 (N_2)^2 \ . \qquad \textbf{Equation 2.38}$$

As is discussed earlier, the definition of a surface is not restricted to a monolayer on a bulk crystal as this would lead to diffraction features portrayed in Figure 2.6 (c), where intensity associated with the 2D monolayer gives rise to intensity between the bulk diffraction (Bragg) peaks. SXRD yields CTRs and FORs as is portrayed in Figure 2.6 (d) and (e), where the CTR maintains intensity that is a summation of the several surface layers and the bulk. To consider the formation of a CTR, we must consider that a surface consists of several layers where the outermost (first) layer is least like the bulk and each layer below the first layer becomes increasingly more like the bulk until a point where the layers adopt the geometry of the bulk lattice. Robinson[33] presented an expression discussing the intensity distribution in a CTR where the scattered amplitude from each successive mono-layer is summed:

$$I_{CTR}(\vec{\mathrm{Q}}) = I_{ML}(\vec{\mathrm{Q}}) \left(\sum e^{i\vec{\mathrm{Q}}_z\vec{c}}\right)^2 = \frac{I_{ML}(\vec{\mathrm{Q}})}{(1 - e^{i\vec{\mathrm{Q}}_z\vec{c}})^2} \ . \qquad \textbf{Equation 2.39}$$

Taking equation 2.32 into consideration:

$$I_{CTR}(\vec{\mathrm{Q}}) = \frac{I_{ML}(\vec{\mathrm{Q}})}{(1 - e^{i2\pi l})^2} = \frac{I_{ML}(\vec{\mathrm{Q}})}{2\,sin^2(\pi l)} \ . \qquad \textbf{Equation 2.40}$$

From Equation 2.28 and 2.29, considering the N_3 constraint:

$$|A\left(\vec{Q}\cdot\vec{c}\right)|^2 = \frac{\sin^2(\frac{1}{2}N_3\vec{Q}\cdot\vec{c})}{\sin^2(\frac{1}{2}\vec{Q}\cdot\vec{c})}, \qquad \textbf{Equation 2.41}$$

which for N_3 >>:

$$\sin^2(\frac{1}{2}N_3\vec{Q}\cdot\vec{c}) \approx 1/2 \ . \qquad \textbf{Equation 2.42}$$

Hence:

$$|A\left(\vec{Q}\cdot\vec{c}\right)|^2 = \frac{1}{2\sin^2(\frac{1}{2}\vec{Q}\cdot\vec{c})} = \frac{1}{2\sin^2(\pi l)}. \qquad \textbf{Equation 2.43}$$

The intensity between the diffraction (Bragg) peaks along the l-direction is continuous, takes a non-zero value and is independent of the number of layers integrating the surface slab. Equivalently, the intensity variation along the CTR can also be constructed from the diffraction amplitude (see Equation 2.28) coming from a semi-infinite crystal with absorption (Ɛ) from one layer to the next:

$$A\left(\vec{Q}\cdot\vec{c}\right) \approx \sum e^{(i\vec{Q}\cdot\vec{c}+\varepsilon)} \approx 1/(1-e^{(i\vec{Q}\cdot\vec{c}-\varepsilon)}) \qquad \textbf{Equation 2.44}$$

In the limit of Ɛ tending to 0, $|A\left(\vec{Q}\cdot\vec{c}\right)|^2$ tends to the form given by Equation 2.43. When Ɛ is small, real case for a crystal, Equation 2.44 is different from the ideal case given in Equation 2.43. Equation 2.43 is incorrect for real crystals because it gives infinite intensities for diffraction (Bragg) peaks, but takes realistic values when l-values are between diffraction (Bragg) peaks.

Figure 2.8 shows an Ewald's sphere reconstruction which can be used to geometrically illustrate scattering. Considering that an incoming wave (that maintains a wave vector $\overrightarrow{k_i}$) is scattered elastically, the scattered wave will have the wave vector $\overrightarrow{k_f}$ such that $\overrightarrow{k_i} = \overrightarrow{k_f}$. In this case, an Ewald's sphere can be drawn up where the radius equals $\overrightarrow{k_i}$ which equals $\overrightarrow{k_f}$ where the origin is determined by the point where $\overrightarrow{k_i}$ intercepts the Ewald's sphere - see Figure 2.8. The diffraction conditions are only satisfied on the Ewald's sphere surface. In essence, a particular *hkl* reflection will only be observed when it lies on the Ewald's sphere surface.

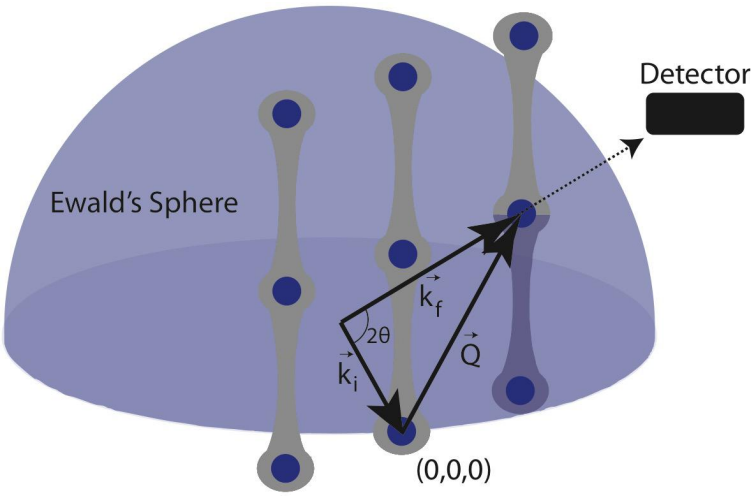

Figure 2.8: 3D representations of Ewald's sphere with respect to a reciprocal lattice. Diffraction conditions are only satisfied at the edge of the Ewald's sphere.

As a particular *hkl* reflection is observed when it lies on the Ewald's sphere surface, movement of the detector and sample/hexapod motors (see section 3.5.2), will allow for intensity to be recorded from another region of the reciprocal lattice. With the advent of the 2D detector, reciprocal lattice scans can be made at fixed *h* and *k* values with *l* being varied as intensity is recorded for a given CTR or FOR. This form of data acquisition is otherwise known as the stationary mode or l-scan.[48]

2.4 Low Energy Electron Diffraction (LEED)

The theoretical basis of electron diffraction emerged when de Broglie proposed the wave-like nature of particles. Low Energy Electron Diffraction (LEED) was independently experimentally demonstrated by Davisson & Germer[49] and Thomson & Reid[50]. This resulted in de Broglie being awarded the 1929 Nobel Prize in Physics whilst Davisson and Thomson were jointly awarded the 1937 Nobel Prize in Physics for their experimental efforts.

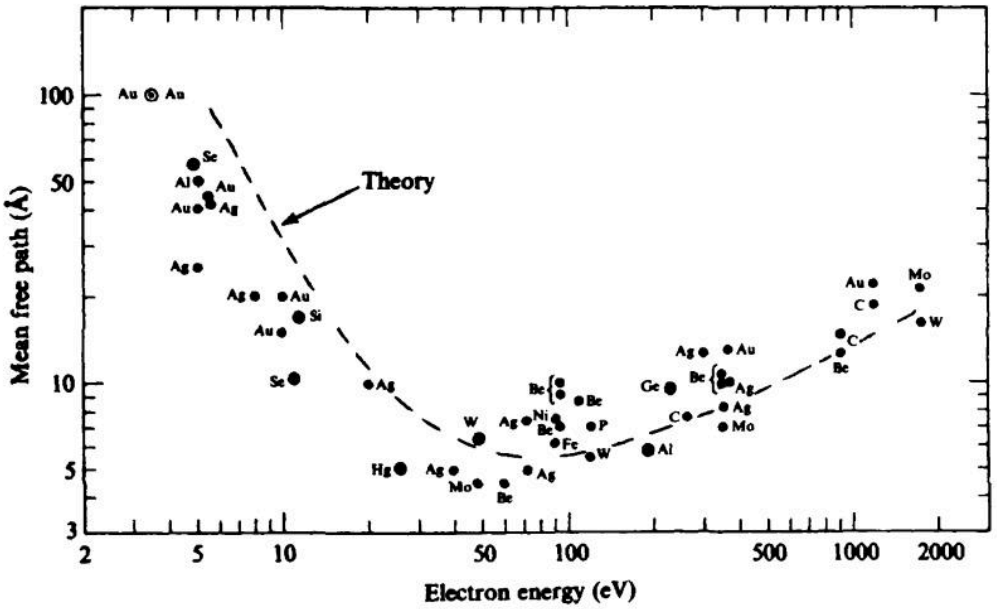

Figure 2.9: Plot depicting the electron mean free paths against electron energy for a variety of elements. The dashed line has been calculated from theory. Adapted from reference.[51]

LEED operates on the principle of analysing elastically back-scattered electrons. A monochromatic electron gun creates incident electrons in the energy range of 20 - 150 eV. Their mean free paths give a penetration depth of a few atomic layers into a surface - see Figure 2.9.[51] Electrons in this energy range possess de Broglie wavelengths

(Equation 2.47) of the same order as the interatomic spacing between surface atoms at ~2.7 to ~1.0 Å. This makes electrons excellent probes for surfaces as they undergo diffraction for periodically arranged surfaces. The de Broglie wavelength can be determined using the previously discussed Equation 2.16 where using Equation 2.45, Equation 2.15 can be converted to Equation 2.46 that can subsequently be reduced to Equation 2.47:

$$E = \frac{mv^2}{2}, \qquad \textbf{Equation 2.45}$$

$$\lambda = \sqrt{\frac{h^2}{2\,m\,E}}, \qquad \textbf{Equation 2.46}$$

$$\lambda(\text{Å}) = \sqrt{\frac{150.6}{E\,(eV)}}. \qquad \textbf{Equation 2.47}$$

As is shown in Figure 2.10, the electron diffraction process involves an incident electron perpendicular to the surface. In a one-dimensional atom chain (lattice parameter *a*), the path length difference is given as '$asin\theta_a$', which for constructive interference must be equal to '$n\lambda$' (where 'n' is an integer). This yields the relationship,

$$sin\theta_a = \frac{n\lambda}{a} \qquad \textbf{Equation 2.48}$$

which yields a diffraction pattern consisting of a series of equally spaced lines perpendicular to the one-dimensional lattice. Introducing periodicity in an orthogonal direction with lattice parameter *b* to the aforementioned one-dimensional chain will yield a two-dimensional system (i.e. a surface). As before, a one-dimensional chain of lattice parameter *b* will yield a diffraction pattern consisting of equally spaced lines perpendicular to the one-dimensional lattice with the relationship,

$$sin\theta_b = \frac{n\lambda}{b} \qquad \textbf{Equation 2.49}$$

In a two dimensional system (with lattice parameters *a* and *b*), a diffraction pattern is observed at the intersection of the diffraction lines associated with the two aforementioned parameters. This results in a series of diffraction spots that correspond to the reciprocal surface unit cell - see Figure 2.11.

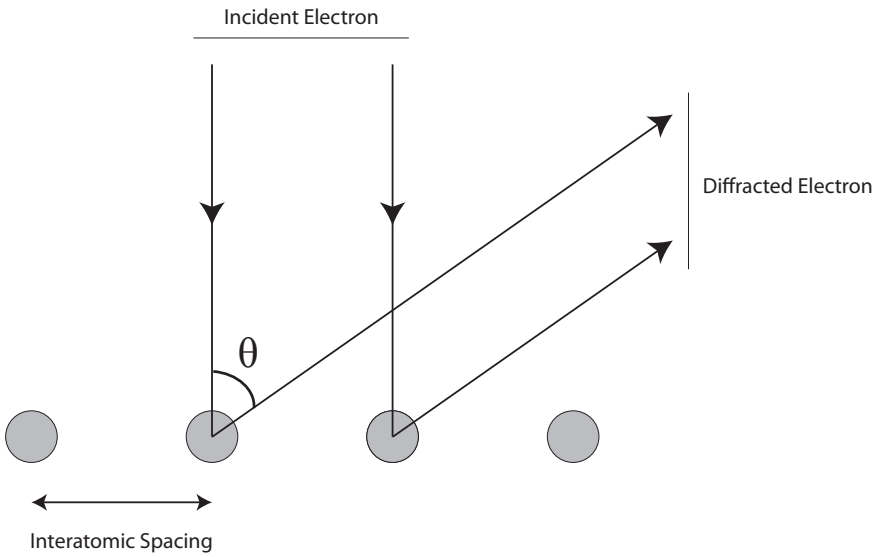

Figure 2.10: A schematic illustrating electron diffraction in one dimension with the incident electron perpendicular to the surface.

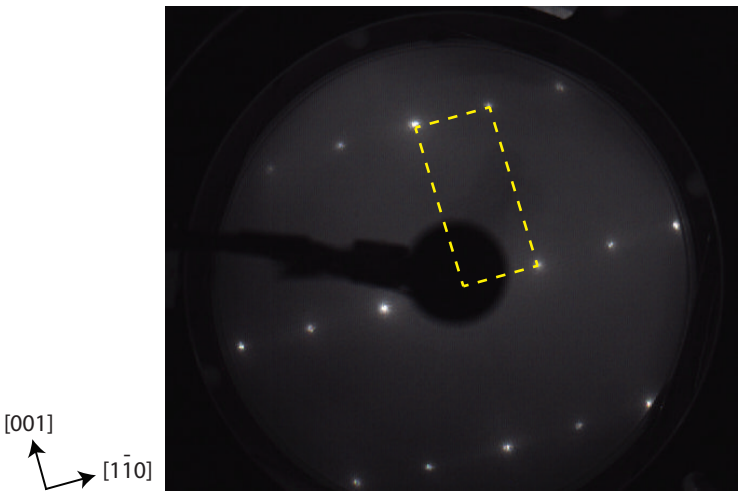

Figure 2.11: A typical LEED observed for R_{110} where the surface unit cell in reciprocal space is highlighted in a dashed yellow rectangle.

2.5 Auger Electron Spectroscopy (AES)

The Auger effect was independently reported by Meitner[52] and Auger[53]. Auger Electron Spectroscopy (AES) is widely used for surface spectroscopy where its surface specificity arises due to incident and emitted electrons having a mean free path of a few atomic layers - see Figure 2.9.

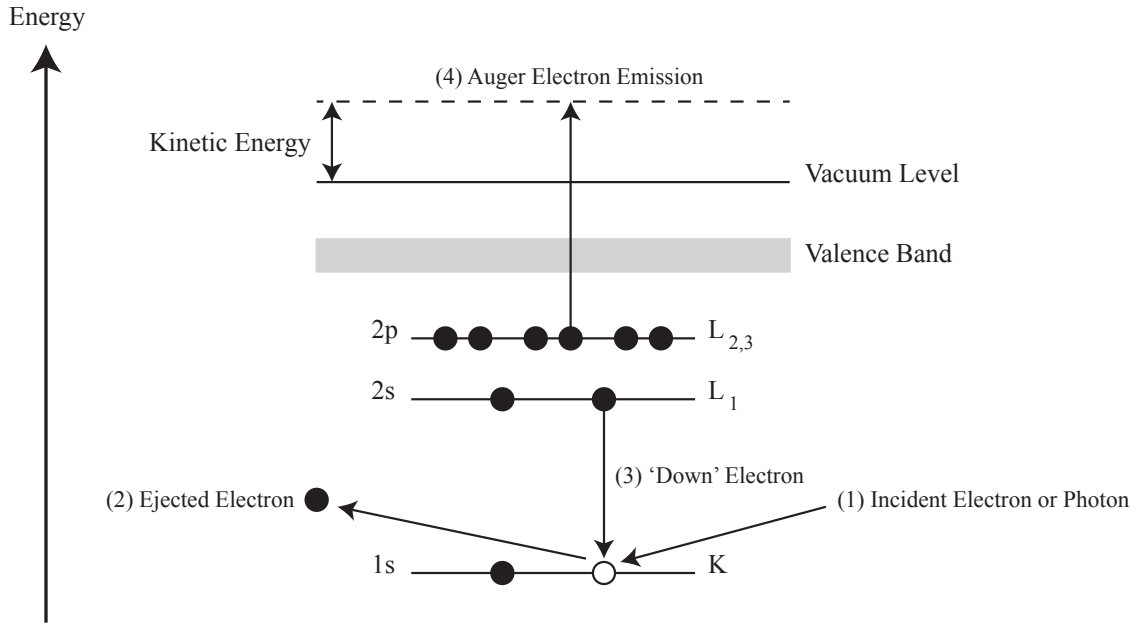

Figure 2.12: An energy level diagram depicting the process by which an Auger electron is emitted. The kinetic energy of the emitted electron conveys elemental specificity and hence allows for chemical identification of surface atoms and/or adsorbates.

In AES, see Figure 2.12, an incident electron or photon causes the emission of a core electron resulting in the formation of a hole. This induces an autoionization process whereby the hole is neutralised by a 'down' electron. This electron transition results in a quantum of energy equivalent to the difference in binding energy between the core hole and 'down' electron which is released in the form of an electron. The electron (termed

the Auger electron) escapes into the vacuum with a given kinetic energy as is given in Equation 2.50 for the processes shown in Figure 2.12. Auger peaks are often observed in Photoelectron Spectroscopy (PES) measurements - see Figure 2.15.

$$E_{kin} = E_K - E_{L1} - E_{L2,3}. \qquad \textbf{Equation 2.50}$$

In AES spectra, the number of electrons of a given kinetic energy, *N*, is measured against a given kinetic energy. This results in Auger peaks occurring with a relatively larger secondary electron background. This is overcome by the electronic differentiation of *N* to yield a *dN/dE* spectra where the small Auger peaks are more readily visible. Peak labelling in AES spectra is done with three letters: core level with hole, 'down' electron level and Auger electron emission level. In the example given in Figure 2.12, this equates to $KL_1L_{2,3}$. Figure 2.13 depicts an AES spectra taken of R_{110}.

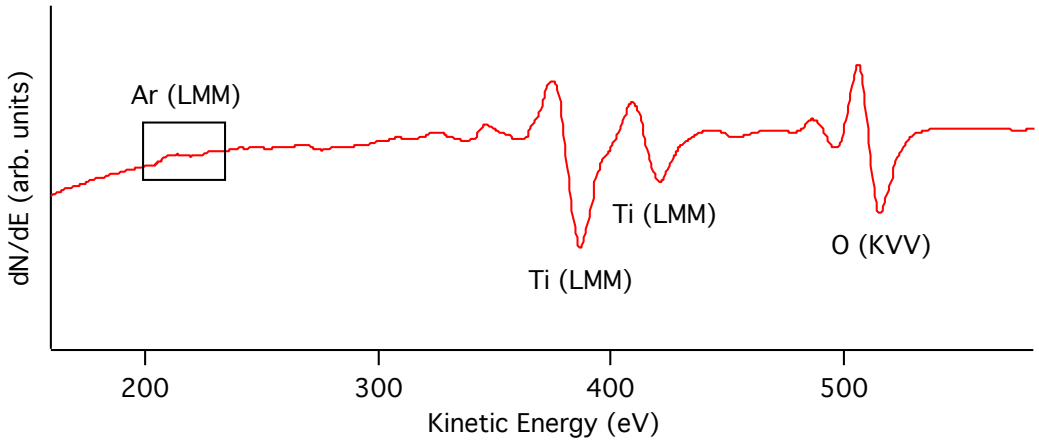

Figure 2.13: An AES spectra taken of R_{110} which highlights the presence of surface Ti and O atoms

2.6 X-Ray Photoelectron Spectroscopy (XPS)

The photoelectric effect was introduced by Hertz[54] and explained by Einstein[55]. The latter was awarded the 1921 Nobel Prize in Physics for his efforts. The basis of X-Ray Photoelectron Spectroscopy (XPS) lies in the photoelectric effect (see Figure 2.14) whereby photons can induce electron ejection from a solid. Siegbahn[56] was awarded one half of the 1981 Nobel Prize in Physics for his efforts in the development of this technique.

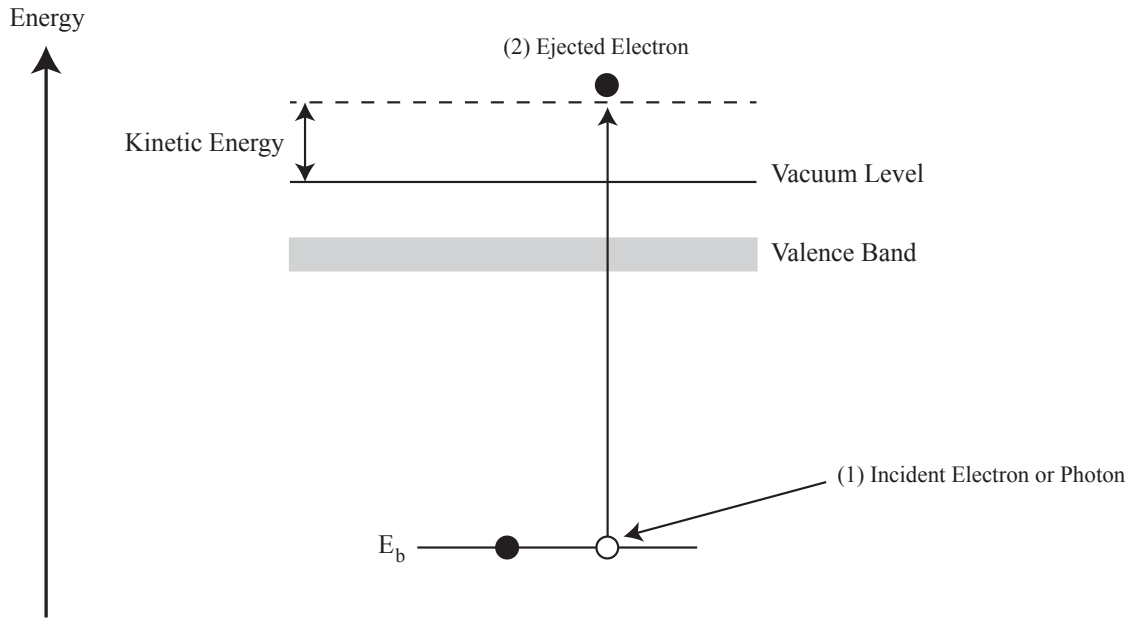

Figure 2.14: An energy level diagram depicting the photoelectric effect. An incoming photon or electron provides an electron with sufficient energy to overcome the binding energy (E_b). The emitted electron has elemental specificity and hence allows for surface chemical identification.

In XPS, a monochromatic beam of X-rays is incident on a surface whereby core and valence electrons are ejected from the solid. The surface sensitivity of XPS arises from the ejected free electrons that have a mean free path of a few atomic layers. Under the

principle of energy conservation, the kinetic energy of the emitted photoelectron is given in Equation 2.51 where '$h\nu$' is the photon energy, 'E_b' is the binding energy and 'ϕ' is the work function of the electron energy analyser. Figure 2.15 depicts an XPS spectra taken of R_{110}.

$$E_{kin} = h\nu - E_b - \phi \qquad \textbf{Equation 2.51}$$

Other than XPS, the photoelectric effect can be exploited utilising UV photons to probe valence energy levels and chemical bonding via a technique referred to as UV Photoelectron Spectroscopy (UPS).

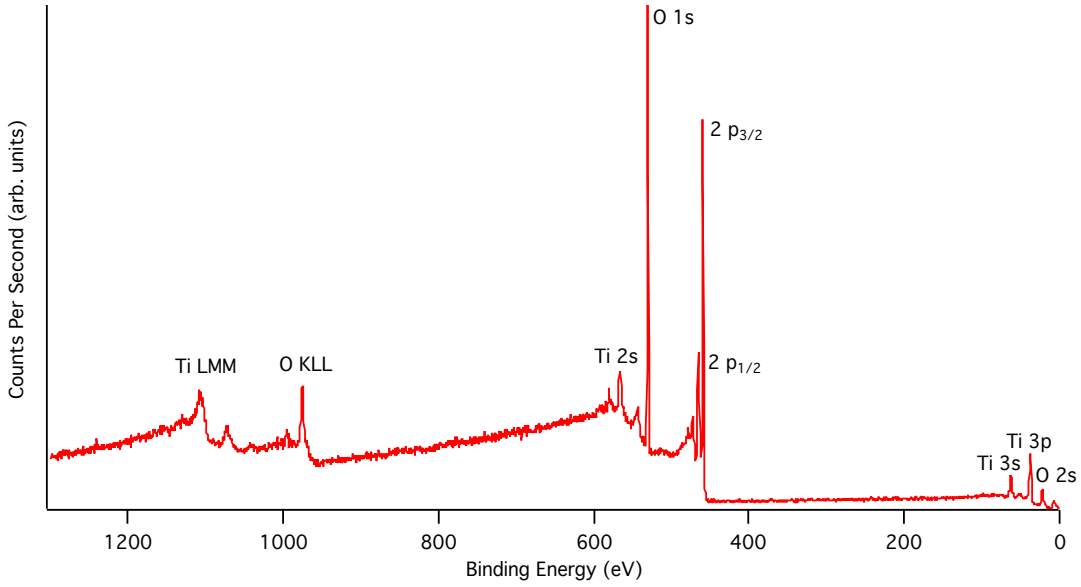

Figure 2.15: A XPS spectra taken of R_{110} which highlights the presence of surface Ti and O atoms with photoelectrons and Auger electrons being detected.

2.7 References

1. C. L. Pang, R. Lindsay and G. Thornton, *Chemical Society Reviews*, 2008, **37**, 2328-2353.
2. C. L. Pang, R. Lindsay and G. Thornton, *Chemical Reviews*, 2013, **113**, 3887-3948.
3. U. Diebold, *Surface Science Reports*, 2003, **48**, 53-229.
4. C. L. Pang, O. Bikondoa, D. S. Humphrey, A. C. Papageorgiou, G. Cabailh, R. Ithnin, Q. Chen, C. A. Muryn, H. Onishi and G. Thornton, *Nanotechnology*, 2006, **17**, 5397-5405.
5. G. Cabailh, X. Torrelles, R. Lindsay, O. Bikondoa, I. Joumard, J. Zegenhagen and G. Thornton, *Physical Review B*, 2007, **75**, 241403.
6. H. Hussain, G. Tocci, T. Woolcot, X. Torrelles, C. L. Pang, D. S. Humphrey, C. M. Yim, D. C. Grinter, G. Cabailh, O. Bikondoa, R. Lindsay, J. Zegenhagen, A. Michaelides and G. Thornton, *Nature Materials*, 2017, **16**, 461-467.
7. D. T. Payne, Y. Zhang, C. L. Pang, H. H. Fielding and G. Thornton, *Surface Science*, 2016, **652**, 189-194.
8. D. T. Payne, Y. Zhang, C. L. Pang, H. H. Fielding and G. Thornton, *Topics in Catalysis*, 2017, **60**, 392-400.
9. S. Selcuk and A. Selloni, *Nature Materials*, 2016, **15**, 1107-1113.
10. G. Binnig and H. Rohrer, *Helvetica Physica Acta*, 1982, **55**, 726-735.
11. G. Binnig, H. Rohrer, C. Gerber and E. Weibel, *Applied Physics Letters*, 1982, **40**, 178-180.
12. G. Binnig and H. Rohrer, *Surface Science*, 1983, **126**, 236-244.
13. G. Binnig and H. Rohrer, *IBM Journal of Research and Development*, 1986, **30**, 355-369.
14. G. Binnig and H. Rohrer, *Reviews of Modern Physics*, 1987, **59**, 615-625.
15. K. W. Kolasinski, *Surface Science: Foundations of Catalysis and Nanoscience*, Wiley, 2012.
16. J. Tersoff and D. R. Hamann, *Physical Review Letters*, 1983, **50**, 1998-2001.
17. J. Tersoff and D. R. Hamann, *Physical Review B*, 1985, **31**, 805-813.
18. J. Bardeen, *Physical Review Letters*, 1961, **6**, 57-59.
19. N. D. Lang, *Physical Review Letters*, 1985, **55**, 230-233.
20. N. D. Lang, *Physical Review B*, 1986, **34**, 5947-5950.
21. N. D. Lang, *Physical Review Letters*, 1986, **56**, 1164-1167.
22. C. J. Chen, *Physical Review Letters*, 1990, **65**, 448-451.
23. C. J. Chen, *Scanning Microscopy*, 1993, **7**, 793-804.
24. J. A. Kubby and J. J. Boland, *Surface Science Reports*, 1996, **26**, 61-204.
25. R. J. Hamers, *Scanning Tunneling Microscopy I*, Springer Series, 1992.
26. O. Bikondoa, C. L. Pang, R. Ithnin, C. A. Muryn, H. Onishi and G. Thornton, *Nature Materials*, 2006, **5**, 189-192.
27. I. W. Lyo and P. Avouris, *Science*, 1991, **253**, 173-176.
28. R. Schaub, P. Thostrup, N. Lopez, E. Laegsgaard, I. Stensgaard, J. K. Norskov and F. Besenbacher, *Physical Review Letters*, 2001, **87**, 266104.
29. W. C. Rontgen, *Radiology*, 1945, **45**, 428-435.
30. M. Eckert, *Annalen Der Physik*, 2012, **524**, A83-A85.
31. J. Jenkin, *Minerva*, 2001, **39**, 373-392.
32. W. H. Bragg and W. L. Bragg, *Proceedings of the Royal Society of London Series a-Containing Papers of a Mathematical and Physical Character*, 1913, **88**, 428-438.
33. I. K. Robinson and D. J. Tweet, *Reports on Progress in Physics*, 1992, **55**, 599-651.
34. B. E. Warren, *X-Ray Diffraction*, Dover Publications, 1969.

35. J. P. W. Treacy, H. Hussain, X. Torrelles, D. C. Grinter, G. Cabailh, O. Bikondoa, C. Nicklin, S. Selcuk, A. Selloni, R. Lindsay and G. Thornton, *Physical Review B*, 2017, **95**, 075416.
36. X. Torrelles, G. Cabailh, R. Lindsay, O. Bikondoa, J. Roy, J. Zegenhagen, G. Teobaldi, W. A. Hofer and G. Thornton, *Physical Review Letters*, 2008, **101**, 185501.
37. I. K. Robinson, *Acta Crystallographica Section A*, 1998, **54**, 772-778.
38. C. Nicklin, T. Arnold, J. Rawle and A. Warne, *Journal of Synchrotron Radiation*, 2016, **23**, 1245-1253.
39. E. Vlieg, *Journal of Applied Crystallography*, 1998, **31**, 198-203.
40. E. Vlieg, *From beam time to structure factors: Including a concise guide to ANA and AVE*, 2012.
41. J. Treacy and C. Nicklin, unpublished work.
42. M. H. M. Ahmed, X. Torrelles, J. P. W. Treacy, H. Hussain, C. Nicklin, P. L. Wincott, D. J. Vaughan, G. Thornton and R. Lindsay, *Journal of Physical Chemistry C*, 2015, **119**, 21426-21433.
43. E. Vlieg, *Journal of Applied Crystallography*, 2000, **33**, 401-405.
44. R. Feidenhansl, *Surface Science Reports*, 1989, **10**, 105-188.
45. I. K. Robinson, *Physical Review B*, 1986, **33**, 3830-3836.
46. U. Magdans, H. Gies, X. Torrelles and J. Rius, *European Journal of Mineralogy*, 2006, **18**, 83-91.
47. G. Renaud, *Surface Science Reports*, 1998, **32**, 5-90.
48. X. Torrelles and J. Rius, *Journal of Applied Crystallography*, 2004, **37**, 395-398.
49. C. Davisson and L. H. Germer, *Physical Review*, 1927, **30**, 705-740.
50. G. P. Thomson and A. Reid, *Nature*, 1927, **119**, 890-890.
51. A. Zangwill, *Physics at Surfaces*, 1988.
52. L. Meitner, *Zeitschrift Fur Physik*, 1923, **17**, 54-66.
53. P. Auger, *Journal De Physique Et Le Radium*, 1925, **6**, 205-U212.
54. H. Hertz, *Annalen der Physik*, 1887, **267**, 983-1000.
55. A. Einstein, *Annalen Der Physik*, 1905, **17**, 132-148.
56. J. M. Hollander and D. A. Shirley, *Science*, 1981, **214**, 629-631.

Chapter 3

Instrumentation and Instrumentation Development

3.1 Ultra-High Vacuum (UHV) and Ambient Pressure (AP) Instruments

3.1.1 Generating a UHV Environment

Vacuum science and technology has been a mainstay of fundamental research. Since the advent of surface and interfacial nano-science, research has largely been performed at pressures of ~10^{-8} mbar and below. This is for purposes of controlling the surface environment and because surface and interface nano-science techniques traditionally utilise probes, such as electrons and X-rays, that are best suited to UHV. To achieve the mandated pressures, numerous measures and equipment are employed.

Achieving UHV necessitates a cost-effective material that maintains the capability to achieve and maintain the necessary pressures. To this extent, UHV research is largely performed in stainless steel chambers consisting of numerous different sized flanges that allow for various pieces of equipment to be attached to the chamber whilst simultaneously maintaining UHV pressures. When attaching a piece of equipment to the chamber, it is necessary to create a vacuum seal otherwise 'leaks' will compromise the integrity of the chamber vacuum. For this purpose, flanges consist of a knife-edge where a gasket (typically a malleable metal such as copper) is placed in between two flanges. When the two flanges are bolted together and compressed, the knife-edge cuts into the gasket and creates a vacuum seal. Although malleable metals are ideal, they are not re-usable and are widely used to attach components that will remain on the chamber over a long period. In the event where a flange is regularly opened (such as a load lock) re-usable rubber (Viton^{TM}) gaskets may be employed, however, these gaskets are less reliable at increasingly lower pressures and create a comparatively weaker vacuum seal when compared to malleable metal gaskets.

The evacuation of air from inside the chamber and the generation of a UHV environment is a process that is performed by using a series of pumps. Initially, a chamber is pumped down via a roughing pump (such as a rotary pump) which allow for rough vacuum with pressures in the range of ~10^{-2} to ~10^{-3} mbar. Its principle of operation is based on a repeated motion where air is trapped and removed. After achieving rough vacuum, a turbo-molecular pump is utilised to lower the pressure further to high vacuum (HV) conditions of ~10^{-6} to ~10^{-7} mbar where the roughing pumps now act as pumps used to back the turbo-molecular pump. A turbo-molecular pump operates on the principle of a series of alternating rows of angled stator and rotor blades such that gas molecules are driven out of the chamber. The expelled air is subsequently pumped away by the roughing pumps that act as backing pumps to the turbo-molecular pump. Gas molecules entering the turbo molecular pump hit the spinning angled rotor blades such that the mechanical energy of the blades directs the gas molecules towards the outlet. The gas molecule subsequently passes through the static stator blades and are then exposed to another spinning angled rotor blade. Thus gases are successively compressed and eventually expelled and pumped away by the backing pump.

Achieving UHV conditions requires the additional use of an ion pump and a titanium sublimation pump which are typically operational at pressures at or below ~10^{-9} mbar. However, after a chamber is exposed to atmosphere, the combined pumping of a turbo-molecular and roughing pump is unlikely to achieve pressures of below ~10^{-9} mbar as these pumps are unable to effectively remove sufficient levels of residual gases (with high sticking co-efficients) in the chamber. Hence, before the introduction of these pumps, the set-up is baked at 100 to 150 ºC for a period of time (depending on the size of the chamber) such that residual gas expulsion can be accelerated.

After achieving pressures of ~10^{-9} mbar, an ion pump and titanium sublimation pump are used to achieve and maintain UHV pressure in the absence of a turbo-molecular and roughing pump where both operate on the principle of trapping residual UHV gases. In a stainless steel casing and under vacuum, an ion pump consists of electrically isolated cylindrical stainless steel anodes and grounded titanium cathodes. Outside the stainless steel casing, in ambient pressure, exists a magnet such that the magnetic field is parallel to the anodes. This configuration generates a magnetic field that penetrates through the casing, anode and cathode. Under UHV conditions, 3 - 7 kV is applied to the set up such that free electrons are drawn towards the anode where the magnetic field induces the electrons to spin within the cylindrical anodes (i.e. magnetron motion). Subsequently, as gases diffuse towards the anodes, the electrons collide with gas molecules inducing an ionisation reaction which ultimately generates a positively charged ion within the positively charged anode. This positively charged ion is subsequently expelled from the anode and accelerates towards the grounded titanium cathode where the impact results in the titanium chemically reacting with the positive ion and 'traps' it. Additionally, the impact induces the 'sputtering' of titanium atoms that chemically react with gas molecules which serves to lower the pressure of the chamber. A major advantage of an ion pump is its lack of vibration inducing mechanical components (when compared to a turbo-molecular pump) such that it can be used in parallel with vibration sensitive techniques such as STM.

A titanium sublimation pump can complement an ion pump or turbo-molecular pump and is used periodically to further reduce and maintain chamber pressures. A titanium sublimation pump consists of a titanium filament through which a current (in the range of 40 to 50 A) is passed such that the filament reaches the sublimation temperature for titanium and results in the surrounding regions within the chamber being coated in a thin

film of reactive titanium. Residual UHV gases subsequently react with the titanium and are 'trapped'. Ultimately this serves to further lower the pressure of the chamber. Overtime, the titanium film gets covered with reacted residual gases such that the titanium sublimation pump will need to be operated again to deposit a new film of titanium.

Measuring pressures requires different types of gauges depending on the pressure. Pirani gauges are commonly used to measure pressures associated with roughing pumps. It operates on the principles of exposing a metal filament (usually platinum) to a region under vacuum where the pressure is probed as a function of the filament resistivity. A constant current is applied through the metal filament such that it heats up and registers a resistance. At higher pressures, the gas molecules collide with the metal filament and enable heat dissipation. In other words, decreasing concentrations of gaseous species result in less heat dissipation and an increase in resistivity.

At and beyond ~10^{-3} mbar, filament cooling is largely radiative, therefore monitoring pressures in the ~10^{-4} to ~10^{-12} mbar regimes necessitates the use of an ionisation gauge such as a hot cathode gauge that measures pressure as a function of current induced by ionic species. Typically, it consists of a metal filament (cathode) and a collector electrode separated by a gridded anode. A current is passed through the cathode which induces resistive heating and the emission of electrons towards the gridded anode where a certain number of electron pass through the gridded anode. Gas molecules between the gridded anode and collector collide with the electrons and induce an ionisation reaction resulting in the formation of a positively charged ion. As the collector is held at a potential more negative to that of the gridded anode, the positively charged ions accelerate towards the collector where its collision with the collector can be used to determine a current that in turn can be used to determine a pressure. Hence, ionic current can be used to determine chamber pressure where increasingly lower currents represent a decrease in

pressure. Gauges are largely utilised to determine the pressure of a chamber but are chemically insensitive. To obtain a chemical understanding of the residual gases in UHV, a quadrupole mass spectrometer can be utilised to perform residual gas analysis. In UHV, typical residual gases observed are for H_2 (m/z = 2), C (m/z = 12), N (m/z = 14), H_2O (m/z = 18), CO/N_2 (m/z = 28) and CO_2 (m/z = 44).

3.1.2 The UHV Instruments

The UHV instruments used within this work are compatible with *Omicron* sample holders. Samples are mounted onto standard *Omicron* Ta plates with spot-welded Ta strips to hold the sample in position - see Figure 3.1. Figure 3.2 and 3.3 give a pictorial and schematic representation of the UHV instruments used within the present work i.e. the *Omicron* AFM/STM Instrument at University College London (base pressure: ~10^{-10} to ~10^{-11} mbar) and the *Omicron* Variable Temperature (VT) AFM/STM Instrument at Diamond Light Source (base pressure: ~10^{-10} to ~10^{-11} mbar).

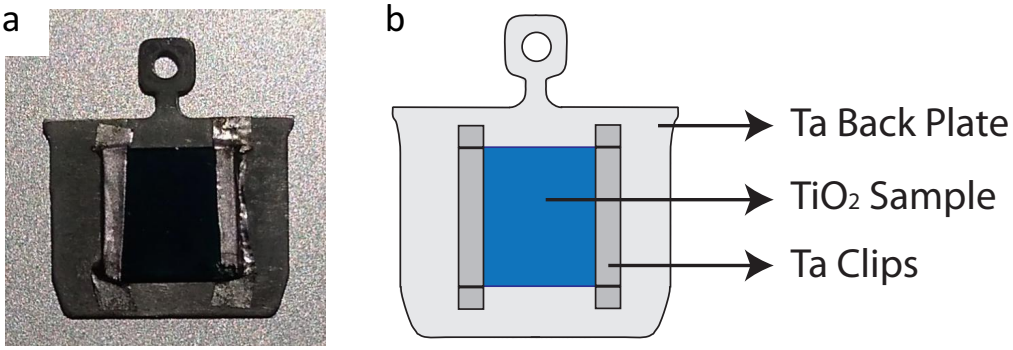

Figure 3.1: (a) Photograph of a sample on an Omicron Ta plate where the sample is held in place by spot welding Ta strips over the sides of the sample.

The instruments maintain capabilities of Ar^+ sputtering and electron irradiation annealing so as to prepare high quality surfaces (see section 3.2.1 and 3.2.2). Prepared surfaces

are subsequently transferred to the microscopy stage where scanning tunnelling microscopy (STM) or atomic force microscopy (AFM) investigations (with vibration isolation) can be performed. For purposes of preliminary surface characterisation low energy electron diffraction (LEED), Auger electron spectroscopy (AES) and/or X-ray photoelectron spectroscopy (XPS) are available.

As is discussed in section 3.1.1, the chamber is initially pumped down with a roughing pump to ~10^{-2} to ~10^{-3} mbar followed by a turbo-molecular pump to ~10^{-7} mbar. Subsequently, the setup is baked to ~130 ^{o}C for a period of 24 hours to accelerate removal of gas molecules from the chamber. To achieve pressures in the ~10^{-10} to ~10^{-11} mbar range, an ion pump and a titanium sublimation pump are introduced. Lastly, residual gas analysis is performed to affirm the integrity of the chamber. Each chamber in the instruments is equipped with a hot cathode gauge which allows for continuous pressure determination. The backing pumps possess pirani gauges to affirm that the turbo-molecular pumps have sufficient backing pressures to be operated.

Both instruments maintain a 'load-lock' that allows for fast entry and removal of samples and STM tips without the need to vent the entire chamber. The load lock is separated from the instrument via a UHV gate valve. Its small volume ensures that venting and subsequent pumping down is fast such that samples and STM tips can be manoeuvred in and out of the instrument on the scale of a few hours without compromising the pressure in the preparation and analysis chambers. The preparation and analysis chamber in both instruments consist of sample manipulators that allow x, y and z translational movements and 360º rotation. Samples can be manoeuvred from the preparation to analysis chambers (and vice-versa) with transfer arms fitted with an *Omicron* manipulation head. In the analysis chamber, both instruments maintain a pincer 'wobble stick' which allows for sample transfer from the manipulator to the STM/AFM stage.

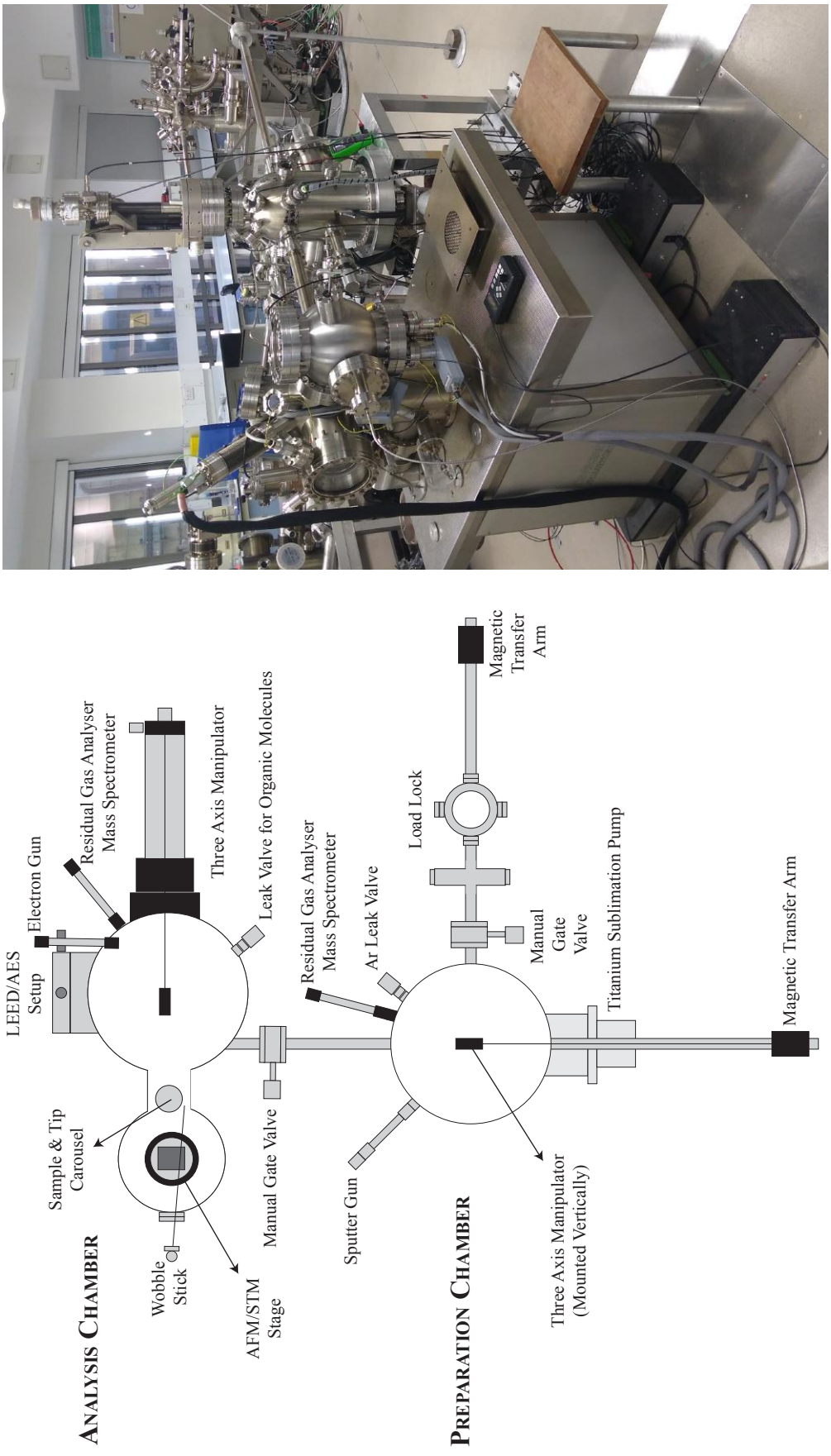

Figure 3.2: Photograph (right) and schematic (left) of the *Omicron* STM/AFM Instrument at University College London.

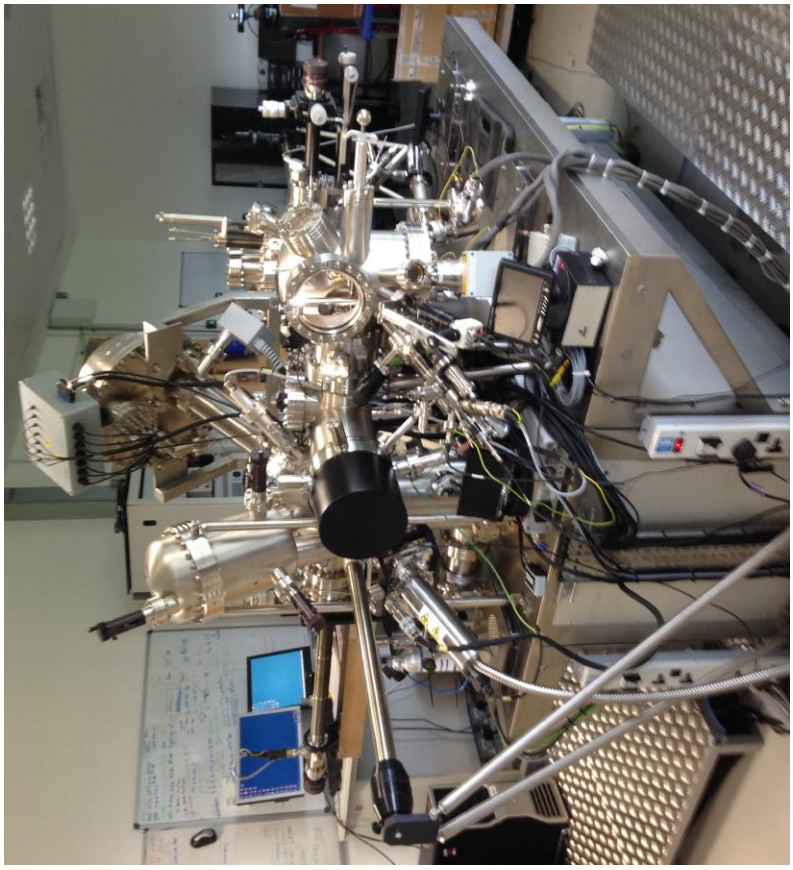

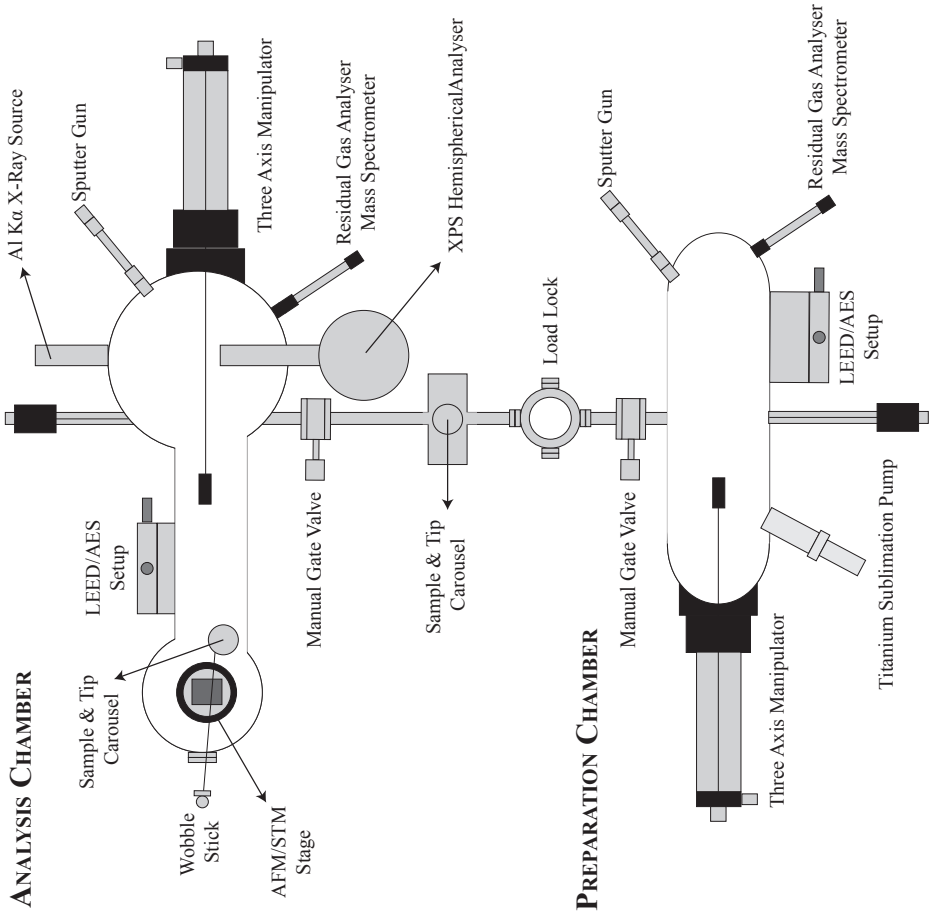

Figure 3.3: Photograph (right) and schematic (left) of the *Omicron* VT STM/AFM Instrument at Diamond Light Source.

3.1.3 The AP Instruments

Figure 3.4 gives a pictorial and schematic representation of the AP instruments used within the presented work i.e. the *Agilent 5500* Liquid Cell STM at University College London and the *Pico-Scan* Electrochemical STM at ParisTech (ENSCP). In this work, samples were prepared and characterised in UHV prior to experimentation on the AP instruments.

The sample mounting mechanism is identical for both instruments. As is seen in Figure 3.4 (c), samples are placed on a conducting plate with a Viton^{TM} 'o'-ring placed on the sample. Subsequently, the 'liquid cell' (made of an inert material such as PTFE or PEEK) is placed on top of the 'o'-ring and bound in place with clips. The compressed 'o'-ring allows for a seal to be created such that the cell can be filled with a desired liquid (50 to 100 μL). As is seen in Figure 3.4 (f), the sample plate mounts onto the STM stage and is held in place via three magnetic posts with the STM tip submerged in the liquid at which point a tip approach can be initiated to achieve tunnelling conditions.

All STM measurements are performed inside an environmental chamber filled with nitrogen. A beaker of water is placed inside the environmental chamber so as to achieve vapour saturation and hence ensure little or negligible levels of liquid evaporation during measurements. Both instruments are operated on top of a vibration isolation pad to minimise noise. In addition to the liquid cell set up, the electrochemical STM setup consists of two platinum electrodes submerged in solution where one behaves as the reference electrode and the other as a quasi-reference electrode.

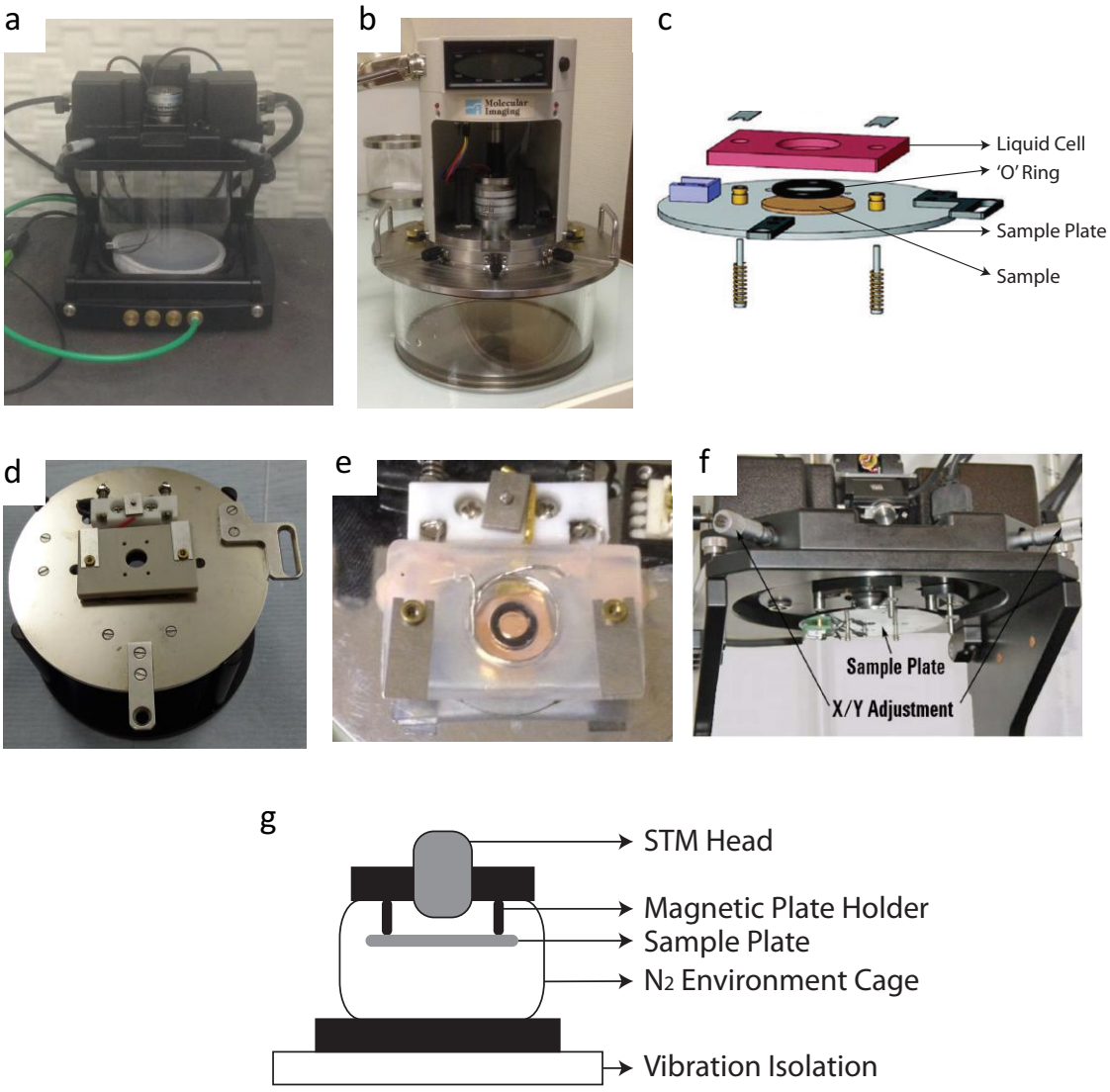

Figure 3.4: (a) Photograph of *Agilent 5500* Liquid Cell STM at University College London. (b) Photograph of *Pico-Scan* Electrochemical STM at ParisTech (ENSCP). (c)[1] Schematic of mounting liquid cell on sample. (d) Sample mounted on the sample plate with the liquid cell for measurements on the *Agilent 5500* Liquid Cell STM. (e) Sample mounted on the sample plate with the liquid cell, with electrodes, for measurements on the *Pico-Scan* Electrochemical STM. (f)[1] Photograph of sample plate being mounted onto the STM with the tip submerged in the liquid cell solution. (g) Schematic illustrating the makeup of the *Agilent 5500* Liquid Cell STM and Pico-Scan Electrochemical STM.

3.2 Sample Preparation

3.2.1 Argon Ion Sputtering

Sample preparation is performed by bombarding the sample with an inert gas ion for purposes of removing surface contaminants.[2, 3] A common inert gas employed is Ar where samples are prepared via an 'Ar^+ sputtering' process. The Ar^+ ion beam is incident on to the surface at an angle of 45° with respect to the surface normal. This allows for the surface to be sputtered without embedding an unnecessarily large amount of Ar atoms into the surface. A sputter gun consists of a filament and a high voltage grid where the filament emits electrons that are accelerated towards the positively biased (~1 kV) grid. These electrons possess sufficient energies to ionise gaseous species and create a plasma of Ar^+ ions under Ar partial pressures of ~10^{-5} mbar. The Ar^+ ions are subsequently expelled from the sputter gun towards the sample surface where its kinetic energy is transferred to surface atoms and adsorbed species which effectively removes them and leaves a roughened surface with embedded Ar. The density of Ar^+ sputtering can be measured from the sample drain current that can be varied depending on the angle of sputtering, the filament emission, the grid bias and the partial pressure of Ar.

3.2.2 Sample Annealing

The Ar^+ sputtering process gives rise to a rough surface that can be ordered by annealing in UHV conditions. This process can be performed by electron irradiating the back of the Ta sample plate. The sample plate is positively biased (~1 kV) with respect to a hot filament that emits electrons. The emitted electrons accelerate towards the back of the Ta sample plate which gives rise to an increase in temperature of the Ta sample

plate and in turn the sample mounted on it. The sample temperature can be monitored via a pyrometer and/or a thermocouple. Annealing temperatures can be varied by altering the electron flux. This is achieved by altering the sample bias or the filament current.

3.2.3 Sample Electron Irradiation

In this work, electron irradiation of surfaces has been performed to alter surface structure. All work was performed on the *Omicron* AFM/STM instrument at University College London (see Figure 3.2). For electron irradiation at 50 - 500 eV, an outgassed manipulator filament (three axis manipulator in analysis chamber - see Figure 3.2) was used where the filament was held at a negative bias with respect to the grounded sample. The front face of the sample was ~2 cm from the filament and the drain current from the sample was used to monitor the electron flux. Electron energy and flux can be varied by changing the bias and filament current, respectively. For electron irradiation at 3keV, a commercial UHV high energy electron gun (*Thermo LEG62*) (see analysis chamber on Figure 3.2) was utilised at an electron gun aperture to sample distance of 10 cm and a beam spot of diameter 3 mm. The drain current was measured from the sample to ground and registered at up to 100 μA. The electron gun operates on the principle of electrons being emitted from a tungsten filament that are focussed via a series of lens and then ejected. The electron gun maintains capabilities of electron irradiating at 2 - 5 keV where the electron flux can be altered by changing the bias and/or the filament current.

3.2.4 Dosing Gas Phase Molecules

Deliberate dosing of gas phase species on surfaces was performed to better understand molecular adsorption on surfaces. Surfaces were exposed to up to 10^{-8} mbar of a gas phase

molecule with measurements performed on the *Omicron* AFM/STM instrument at University College London (see Figure 3.2). A high precision leak valve was used to introduce gaseous species into the analysis chamber of the instrument. In liquid phase, the molecules to be dosed were placed inside a glass vial and connected to the leak valve and a roughing pump. Repeated freeze-pump-thaw cycles were performed to remove dissolved gases and to purify the solution. The freeze-pump-thaw methodology that is commonly used to remove dissolved gases in liquids. In this process, the liquid in the glass vial is frozen (with liquid nitrogen). This is followed by the pumping of the glass vial with the roughing pump for a short period of time such that static vacuum conditions can be generated above the frozen liquid in the glass vial. Next, the frozen liquid is allowed to melt and return to the liquid phase. During this process, dissolved gases within the liquid are expelled into the static vacuum region in the glass vial. This procedure is repeated several times till the liquid has been fully degassed.

3.3 Scanning Tunnelling Microscope

3.3.1 Microscope Operation

The instruments discussed in section 3.1.2 and 3.1.3 exhibit different forms of STM operation. In the *Omicron* STM/AFM instrument at University College London, the sample is placed vertically in the STM stage with the tip positioned opposite to it - see Figure 3.5 (a). STM is performed with a stationary tip and a moving sample where a bias is applied to the sample to induce tunnelling. In the *Omicron* VT AFM/STM instrument at Diamond Light Source, the sample is placed horizontally facing downwards in the STM stage with the tip facing upwards - see Figure 3.5 (b). STM is performed with a bias applied to the mobile tip whilst the sample is stationary. The high precision movement of the tip or sample is achieved by a piezoelectric drive that permits motion in the z (towards/away from surface), x and y directions as the tip manoeuvres over the surface.

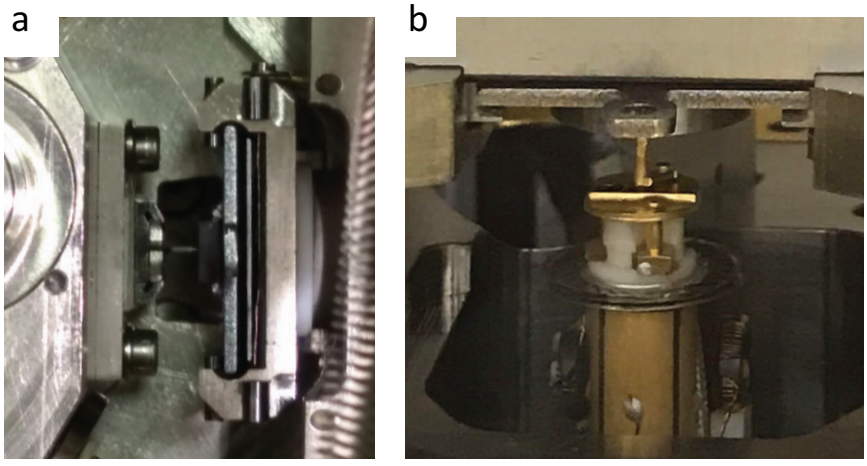

Figure 3.5: (a) Aerial view photograph of the STM stage in the *Omicron* STM/AFM instrument at University College London with the tip on the left and the sample (on an *Omicron* sample plate) to the right. (b) Side view photograph of the STM stage in the *Omicron* VT STM/AFM instrument at Diamond Light Source with the tip at the bottom and the sample (on an *Omicron* sample plate) on the top.

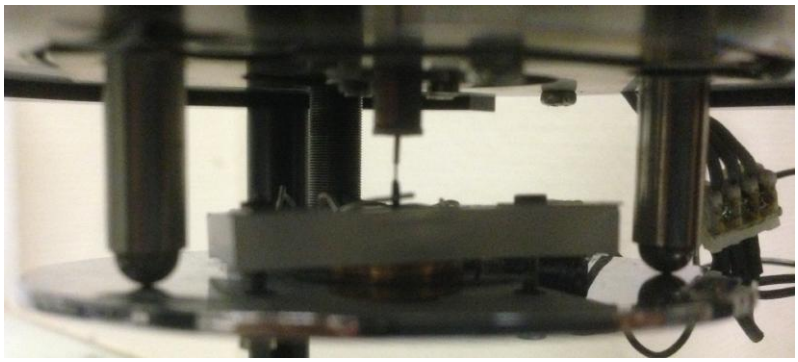

Figure 3.6: Photograph of a typical STM stage in the AP STM instruments i.e. the *Agilent 5500* Liquid Cell STM at University College London and the *Pico-Scan* Electrochemical STM at ParisTech (ENSCP). Three magnetic arms hold the sample plate which houses the liquid cell. Tip (from above) enters the liquid cell and is submerged in solution.

In the *Agilent 5500* Liquid Cell STM at University College London and the *Pico-Scan* Electrochemical STM at ParisTech (ENSCP), the sample is placed horizontally facing upwards with the tip facing downwards - see Figure 3.6. Imaging in the former is performed with a mobile tip and a stationary sample where the bias is applied to the sample. Imaging in the latter is performed with a mobile tip and a stationary sample where the stationary sample is placed at a specific electrochemical potential and the tip is biased (with respect to the sample) to induce tunnelling. As is the case with the UHV instruments, the high precision movement of the tip is achieved by a piezoelectric drive that permits motion in the z direction (towards and away from the surface) and the x and y directions as the tip manoeuvres over the surface.

3.3.2 STM Imaging Modes

STM measurements can be performed either in constant current mode or in constant height mode - see Figure 3.7. In constant current scanning mode, the tip-substrate distance is varied (by adjusting the z-piezo) to ensure that the tunneling current (I_t)

remains constant. The movement of the tip in the z-direction gives a map of the surface. Operating in constant current mode requires the use of a feedback loop that allows for a specific user defined current (set point) to be maintained by altering the voltage applied to the z-piezo. Alternatively, in constant height mode the tip does not move in the z direction. As the tip probes the surface, the change in I_t is used to record the surface electronic structure.

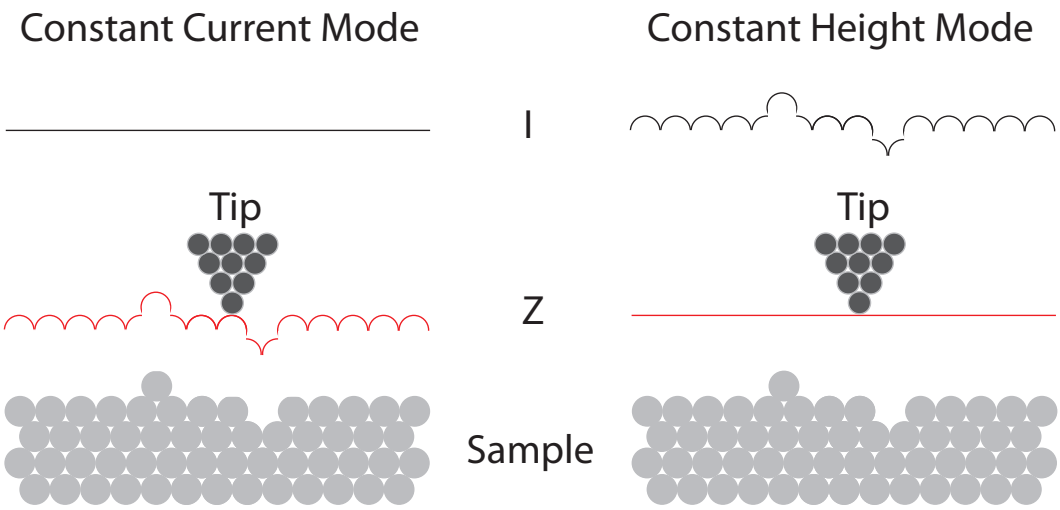

Figure 3.7: Schematic of constant current and constant height imaging modes in STM.

As constant height mode does not require the use of a feedback loop, measurements may be obtained at a faster rate than in constant current mode. However, constant height mode is largely suited to extremely flat surfaces where the risk of 'tip crashing' is minimal. In this thesis, STM measurements are performed in constant current mode where the risk of 'tip crashing' is relatively less severe than in constant height mode. TiO_2 surfaces (the focus of this work) have been more commonly imaged in constant current mode.[4, 5]

3.3.3 STM Tips

Successful STM necessitates the preparation of an atomically sharp and robust tip. The STM tungsten tips were prepared via an electrochemical etching process. Two methods of tungsten tip making were pursued: the plate method and the dip method - see Figure 3.8.

The plate method consists of a metallic plate (cathode) with a hole through which a 0.5 - 1 mm diameter tungsten wire (anode) is passed - see Figure 3.8 (a and c). Subsequently, a small volume of electrolyte (such as 2 M NaOH) is placed in the hole between the tungsten wire and metallic plate that is held in place by surface tension. Upon the application of a voltage, the tungsten starts to etch away (see Equation 3.1) at the region where tungsten is in contact with the 2 M NaOH. As the tungsten wire etches, it gets thinner with the weight of the wire below the plate continuously pulling downwards. Eventually, the tungsten wire breaks leaving behind two tips suitable for STM. All tips used in the *Omicron* AFM/STM instrument at University College London were prepared using the plate method.

$$W_{(s)} + 2OH^-_{(aq)} + H_2O_{(l)} \rightarrow WO_4^{2-}{}_{(aq)} + 3H_{2(g)} \qquad \textbf{Equation 3.1}$$

The dip method consists of placing a tungsten wire (anode) and a platinum wire (cathode) into an electrolyte (such as 2 M NaOH) filled beaker - see Figure 3.8 (b and d). Due to capillary action, the electrolyte solution rises around the tungsten wire (0.5 - 1 mm diameter). As in the plate method, upon the application of a voltage, the tungsten submerged in solution starts to etch away (see Equation 3.1). Over time, the tungsten submerged in solution fractures such that the tungsten wire in air can be used as a tip. All tips used in the *Omicron* VT AFM/STM instrument at Diamond Light Source were prepared using the dip method.

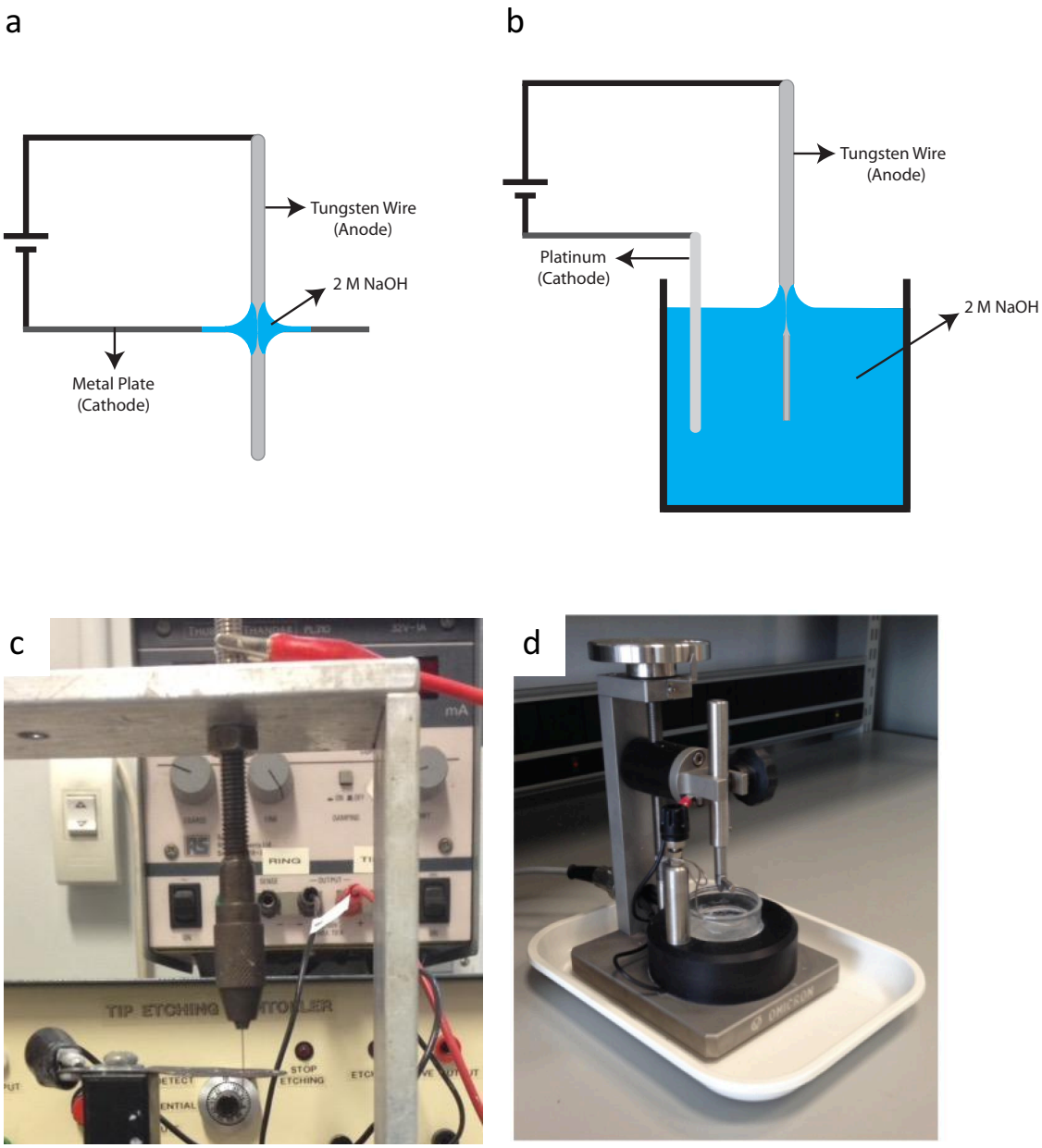

Figure 3.8: Schematic of the (a) plate method and (b) dip method used to prepare tips for UHV STM. Photograph of set ups used for (c) plate method and (d) dip method.

For purposes of performing STM of surface / electrolyte interfaces, STM tips need to be coated in an insulating substance with only the tip apex exposed. This ensures that the 'leakage' current associated with the metallic tip in contact with the electrolyte solution is kept at < 10 pA and thus allows STM to be performed with I_t in the nA range. All tips

used in the *Agilent 5500* Liquid Cell STM instrument at University College London and *Pico-Scan* Electrochemical STM instrument at ParisTech (ENSCP) were commercial[6] , wax coated 0.25 mm diameter, Pt (80%) / Ir (20%) STM tips with 10 pA maximum leakage current purchased from Keysight Technologies. Figure 3.9 gives a pictorial and schematic representation of a Pt/Ir tip coated in wax. These tips are prepared by electrochemically etching Pt/Ir wires and subsequently coating the tips with hot Apiezon™ wax. This wax is widely used and suited to aqueous interfaces and electrochemical work. As the wax cools and hardens, the coated tip is exposed to mild heat to melt a fraction of the wax off of the tip apex such that only the tip apex is exposed whilst the remainder of the tip continues to be coated in the inert wax.

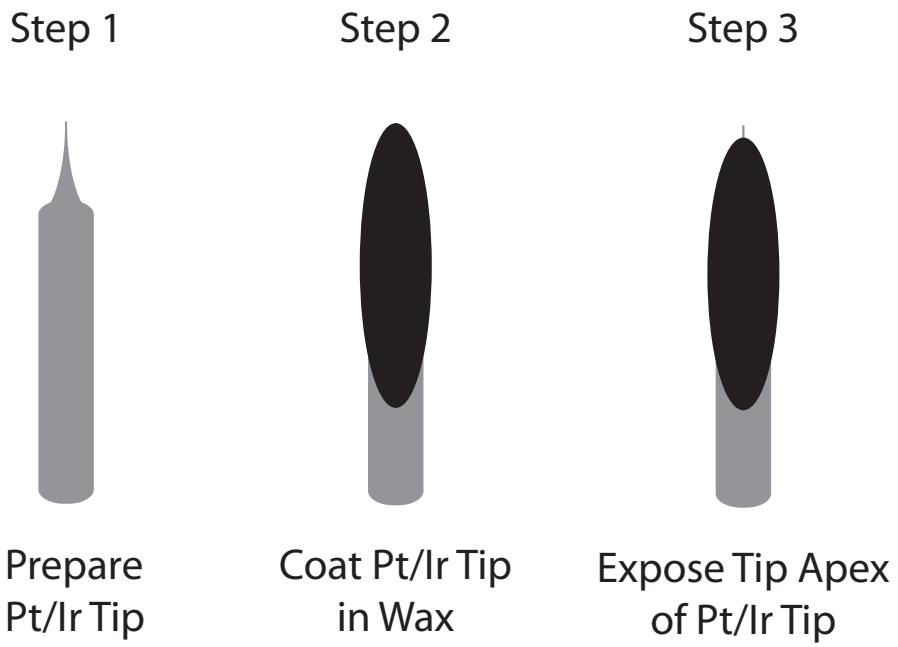

Figure 3.9: Steps involved in the preparation of wax coated STM tips for STM under electrolyte solutions.

3.4 Auxiliary Analytical Techniques

3.4.1 LEED and AES Optics

LEED and AES were common auxiliary analytical techniques used to confirm the long range order of the surface and to determine the chemical nature of the surface. Both UHV instruments discussed in section 3.1.2 possess an *Omicron* rear-view LEED / AES set up that consists of four grids and an electron gun - see Figure 3.10. AES operates with the LEED optics set up in the retarding field analysis arrangement.

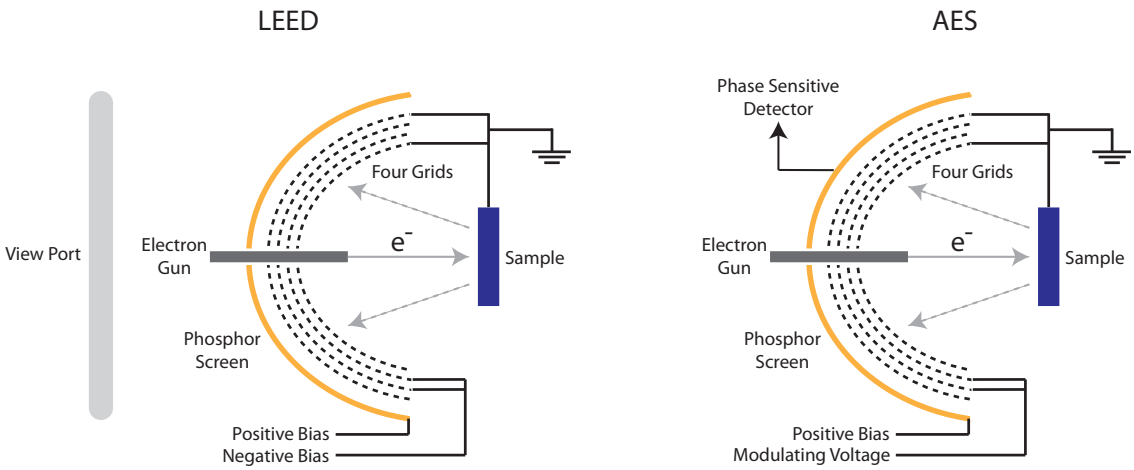

Figure 3.10: Schematic of the LEED and AES optics of the *Omicron* rear-view LEED / AES set up in the *Omicron* AFM/STM instrument at University College London and the *Omicron* VT AFM/STM instrument at Diamond Light Source.

In LEED, an electron beam impinges on the surface along the surface-normal direction whereby the elastically backscattered electrons give an intensity pattern that represents the reciprocal lattice of the surface. Upon diffraction, electrons are back scattered towards a series of four grids (G1 to G4). The outer grids (G1 and G4) are earthed to ensure that the electrons travel in a field free region. The inner grids (G2 and G3) are held at a negative

potential whereby only elastically scattered electrons reach the detector, which is biased at a high positive voltage (approx. 7 kV). This accelerates the transmitted electrons to a sufficient kinetic energy to enable light emission from the coated fluorescent glass screen. The diffracted electrons give rise to a pattern, which consists of bright spots on a dark background.

In AES, as for LEED, the outer grids (G1 and G4) are earthed to ensure that the electrons flow in a field free region. The inner grids (G2 and G3) act as a high pass filter with an alternating voltage. The phosphor screen acts as an electron collector and measures the current with respect to the filter voltage. The use of a lock-in amplifier allows for phase-sensitive detection and produces a differentiated signal.

3.4.2 X-Ray Source and Hemispherical Analyser

In this work, XPS has been used as an auxiliary technique to obtain chemically sensitive information from the surface. XPS is available in the *Omicron* VT AFM/STM instrument at Diamond Light Source - see Figure 3.3. The XPS (Al Kα source) set up employs an *Omicron* X-ray source - see Figure 3.11. Electron irradiation of the aluminium anodes is induced by electron emission from grounded filaments to the positively biased (up to 10 to 15 kV) anodes. This results in X-rays of energy 1486 eV being emitted from the anode out of the slits and towards the sample. The aperture through which the X-rays escape is covered with an aluminium window. Its purpose it to protect the sample from being exposed to X-ray source related contaminants whilst simultaneously being permeable to X-rays. Due to the continuous electron irradiation of the anodes, the X-ray source is water cooled to prevent overheating.

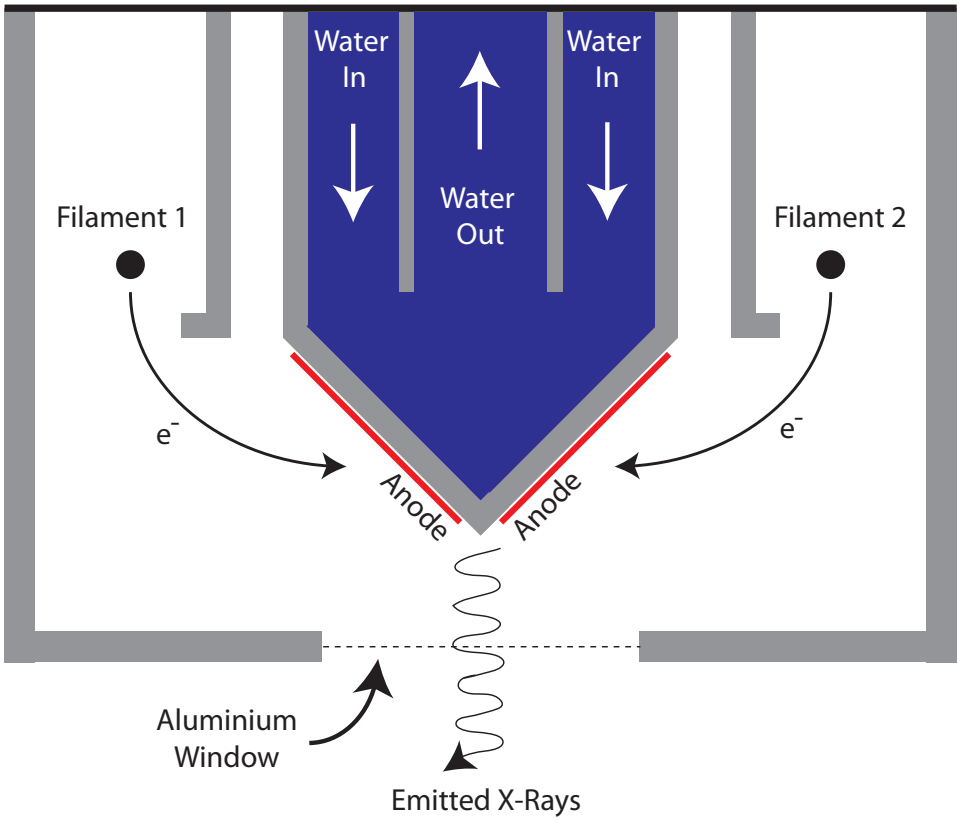

Figure 3.11: Schematic of the X-ray source for the XPS on the Omicron VT AFM/STM instrument at Diamond Light Source.

XPS detectors measure the number of electrons at a given kinetic energy. This is typically done with a hemispherical analyser (see Figure 3.12), which consists of two (inner and outer) concentric hemispheres with a potential difference across them. The chosen potential difference separates electrons whilst specifically allowing a chosen electron kinetic energy (see Equation 3.2) to pass to the detector. In Equation 3.2, 'e' is the electron charge, 'V' is the potential difference and 'R1' and 'R2' are the radii of the inner and outer hemispheres, respectively.

$$E = e\Delta V \frac{R_1 R_2}{R_2^2 - R_1^2} \qquad \textbf{Equation 3.2}$$

Electrons with a kinetic energy higher or lower than the chosen kinetic energy follow a path whose radius is higher or lower than the mean radius of the analyser. Electrons with the selected kinetic energy reach the electron detector.

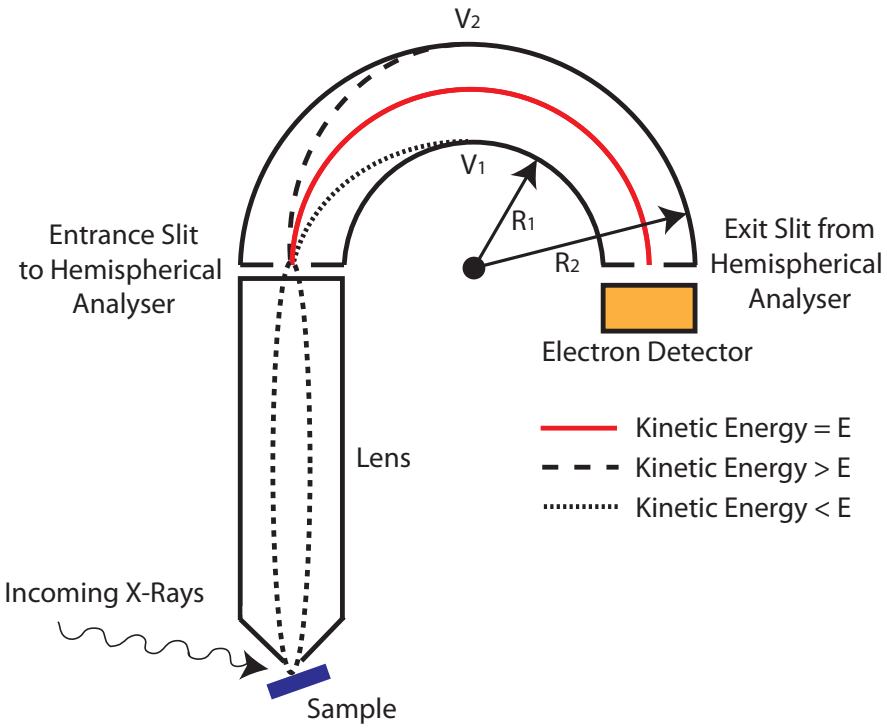

Figure 3.12: Schematic of a hemispherical analyser for the XPS on the *Omicron* VT AFM/STM instrument at Diamond Light Source.

3.5 Beamline I07: Surface and Interface Diffraction

3.5.1 Diamond Light Source: Synchrotron Radiation Facility

Figure 3.13 shows a photograph and structure of Diamond Light Source with numerous components labelled. A hot cathode electron source generates electrons (via thermionic emission from a hot filament) that are accelerated to 100 MeV by a linear accelerator (linac). The electron gun provides a steady supply of electrons to replace the lost electron via collisions with residual vacuum gas particles. Next, the electrons enter a booster ring where electrons are accelerated to the required operational velocity before being periodically injected into the storage ring such that a specific storage ring current (300 mA at Diamond Light Source) is maintained.

The storage ring consists of a series of straight and bend sections where electrons are maintained in a closed path, in a circular trajectory via a series of magnets. The electrons maintain a velocity near the speed of light and a kinetic energy on the GeV scale (3 GeV at Diamond Light Source). Under these conditions, electromagnetic (synchrotron) radiation is emitted tangential to the circular trajectory of the electron. The storage ring further consists of radio frequency devices that replenishes electron energy loss associated with synchrotron radiation emission.

Beamlines are set up tangentially to the storage ring where the photon beam is supplied via a bending magnet or an insertion device (undulator or wiggler). The latter lie in straight sections of the storage ring. At the beamline, the photon beam is subsequently focussed and/or monochromated before illuminating a sample in the experimental hutch where users can control the experiment from the control room.

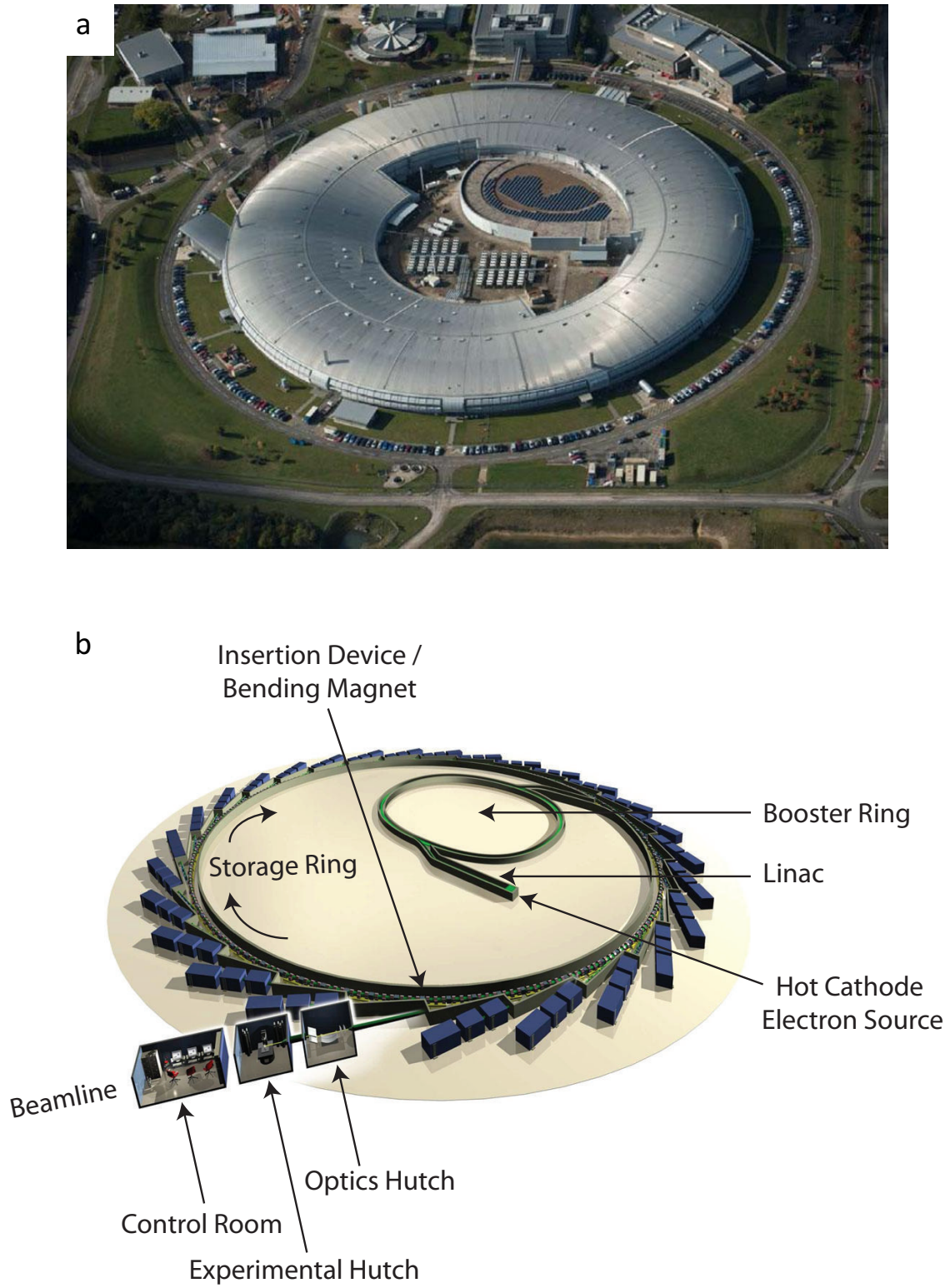

Figure 3.13: (a) Aerial photograph of Diamond Light Source. (b) Schematic of Diamond Light Source synchrotron machine and beamline layout. Adapted from reference.[7]

3.5.2 Beamline Layout

Beamline I07 is a dedicated beamline for surface and interface diffraction at Diamond Light Source. A general layout of the beamline is given in Figure 3.14. It highlights the position of the insertion device (undulator), the major optical components of the beamline and two-hutch in-line design - experimental hutch 1 (EH1) and experimental hutch 2 (EH2).

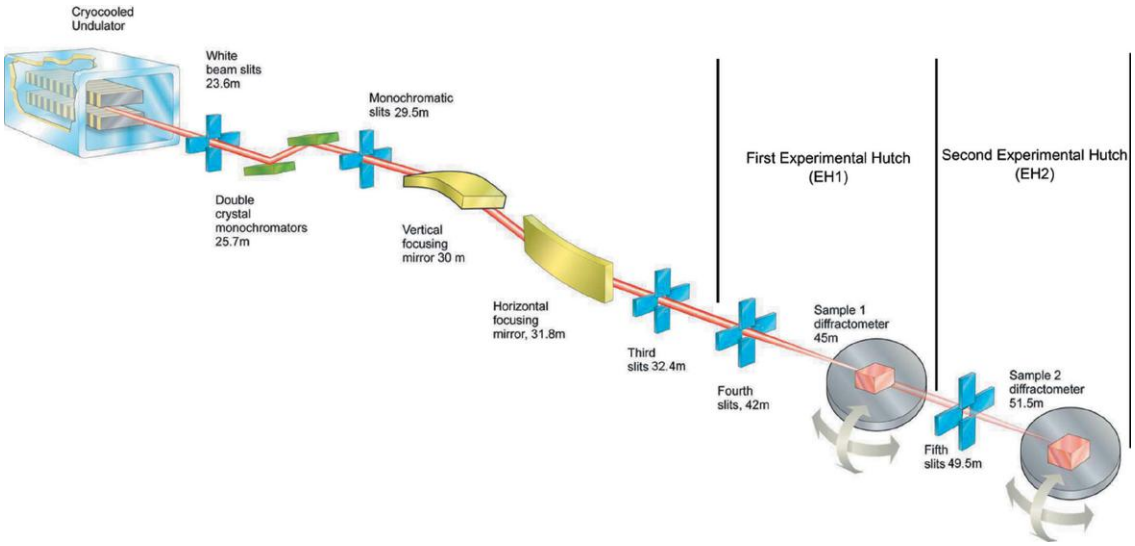

Figure 3.14: Schematic layout of beamline I07 showing some key components with distance from the source. Adapted from reference.[8]

The beamline is positioned at the centre of a 5 m long straight section of the storage ring where it is sourced by a cryogenic permanent-magnet undulator that maintains a liquid nitrogen cryocooler capable of achieving temperatures of ~150 K. The use of a cryocooler was implemented at I07 as temperature reduction is understood to increase the magnetic field and coercivity of specific permanent magnets.[9] At I07, this allows for a photon flux increase of up to a factor three when compared to

without cooling. I07 employs a commercial double crystal monochromator (*Accel*) which utilises two cryocooled Si (111) crystals on an in-vacuum rotation stage to allow for the desired X-ray energy to be extracted for experimentation. Beam focussing is achieved by using a pair of bimorph mirrors mounted in a Kirkpatrick-Baez geometry that allow for control over the vertical and horizontal beam size.

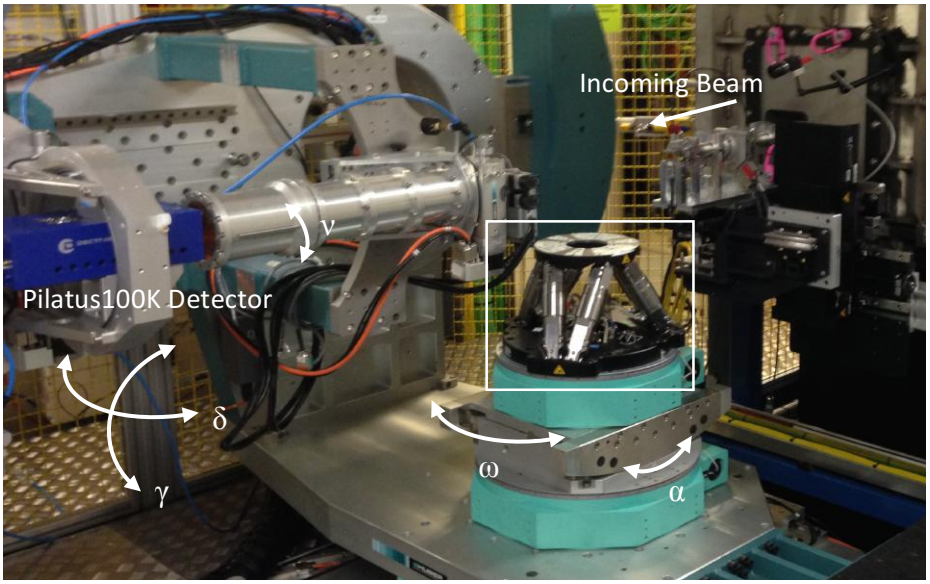

Figure 3.15: Photograph of Experimental Hutch 1 (2 + 3 diffractometer)[10] with a hexapod (white box) and motors labelled. Custom built chamber housing the sample are mounted on the hexapod. α determines the angle of incidence. γ represents detector movement parallel to surface normal. δ represents detector movement parallel to the surface plane. ω represents sample rotation around surface normal. ν represents axial detector rotation.

Photons travel in UHV conditions up to EH1 (see Figure 3.15) or EH2. EH1 and EH2 both contain a Huber (2 + 3) diffractometer.[10] EH1 behaves as a versatile experimental hutch where users may employ custom built set ups (mounted on the hexapod) to perform a variety of different forms of experiments ranging from UHV to ambient pressures.

3.5.3 Development and Implementation of Droplet Cell at I07

a. Introduction

Part of my research project involved the development of a cell for solid/liquid, photo-chemical, electrochemical and photo-electrochemical interface research on Beamline I07. The design is based on a cell developed at the European Synchrotron Radiation Facility (ESRF).[11] Although a myriad of solid/liquid and electrochemical cells have been developed for surface science investigations[12-16], the droplet cell maintains the unique distinction of being UHV compatible and hence allows for samples to be prepared, characterised and transferred to the beamline in UHV conditions. This enables characterisation of the surface in UHV prior to the introduction of the liquid delivery system under controlled conditions of inert gases such as N_2, Ar or He.

b. Portable UHV Chamber

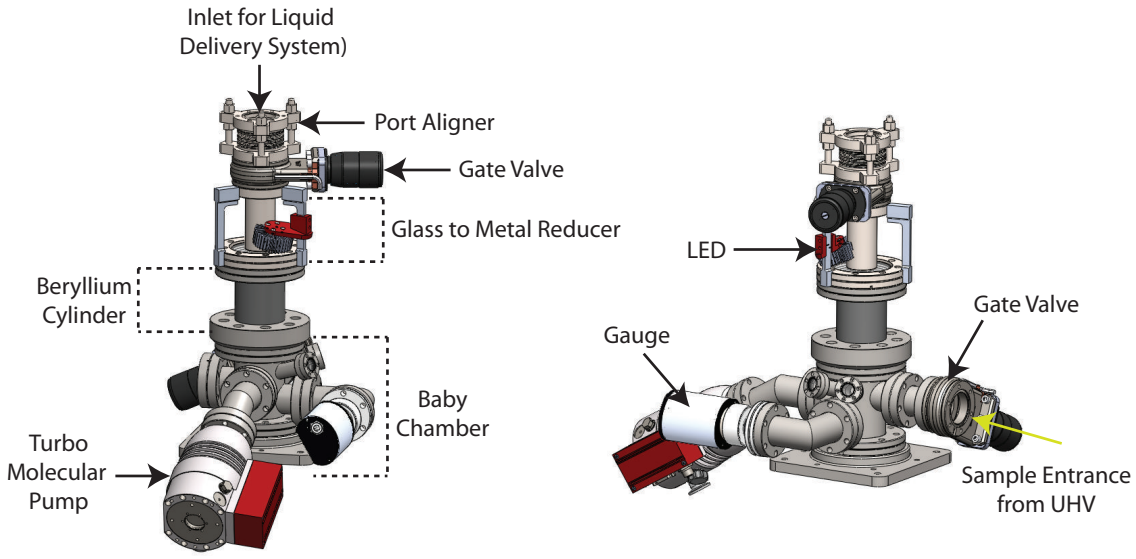

Figure 3.16: Schematic illustrations of the portable UHV chamber.

Let us begin by discussing the portable UHV chamber of the droplet cell that is schematically illustrated in Figure 3.16. Engineering drawings by Diamond Light Source of the baby chamber, beryllium cylinder and sample stage are shown in Appendix 3.1 - 3.3, respectively. The set-up can be mounted on the hexapod in EH2 of beamline I07. With the use of a suitable adaptor it can be mounted on the hexapod of other beamlines.

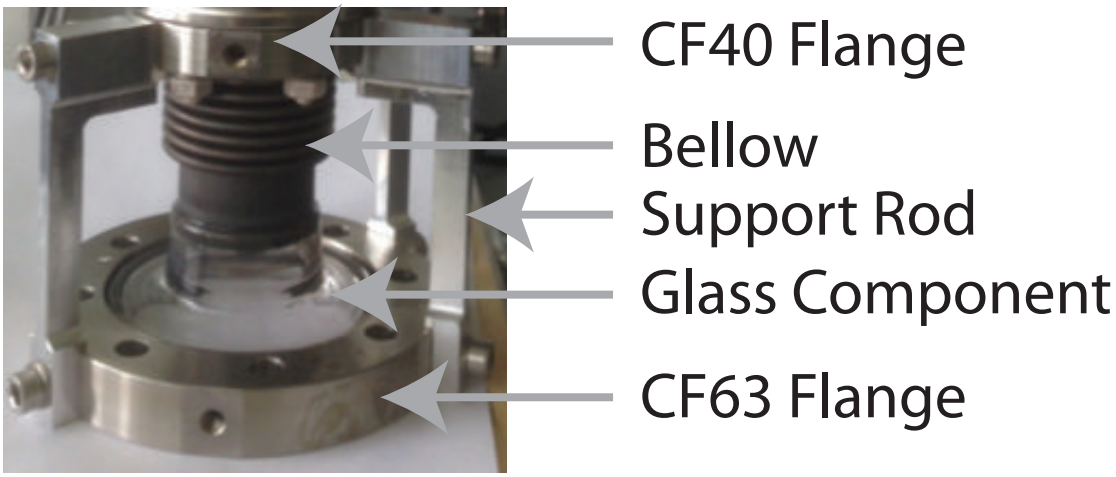

Figure 3.17: Photograph of custom built UHV compatible glass-to-metal reducer.

The portable UHV chamber consists of a custom-built baby chamber that houses a sample stage on a linear z-drive. The baby chamber also contains a turbo-molecular pump to achieve a base pressure of 1×10^{-9} mbar as well as a pressure gauge. Mounted on top of the baby chamber is a beryllium cylinder that consists of a 10 cm long beryllium cylinder (with 1 mm thick walls) that has stainless steel CF63 flanges on either end. This cylinder was purchased from *Materion*. To provide the beryllium cylinder with support whilst the cylinder (and components above it) are being mounted, support rods (see Figure A.3.2 in Appendix) were developed to prevent damage to the beryllium. A custom built UHV compatible glass-to-metal reducer (see Figure 3.17) was mounted on top of the beryllium cylinder that served numerous purposes. Firstly, the reducer converts the CF63

flange of the beryllium cylinder to a CF40 flange for purposes of mounting the remaining set up components. Secondly, via the glass, the reducer provides a direct view of the sample to allow for the subsequent mounting of the liquid delivery system (see section 3.5.2.c for more details). Thirdly, via the glass, the sample can be exposed to photo-active illumination for purposes of probing photo-chemical and photo-electrochemical interfaces (see section 3.5.2.c for more details). Figure, 3.17 provides a photograph and schematic of the custom built glass-to-metal reducer (CF63 to CF40). The CF63 flange is directly welded to the glass component. However, between the CF40 flange and the glass component, exists a welded Kovar® rigid bellow which acts as a support to the glass component. Additionally, three stainless steel rods are incorporated around the glass-to-metal reducer as a support. The glass-to-metal reducer was purchased from *Larson Electronic Glass*. A gate valve (purchased from *VAT*) is positioned above the reducer and when shut allows for the creation of a closed environment that can be pumped to UHV conditions. Lastly, a CF40 port aligner (purchased from *Kurt J. Lesker*) is positioned above the gate valve and is intended for use with the liquid delivery system (see section 3.5.2.c for more details).

Sample transfer into the portable UHV chamber occurs via the route highlighted in green in Figure 3.16. The portable UHV chamber can be attached to any UHV instrument using a CF40 stainless steel flange through which the sample (on a sample plate) enters the portable chamber (highlighted in green in Figure 3.16). Figure 3.18 shows the portable UHV chamber attached to the *Omicron* VT AFM/STM instrument at Diamond Light Source (see Figure 3.3). Samples can be prepared in the UHV instrument and subsequently characterised with STM, AFM, LEED and/or XPS. Next the sample can be placed in the carousel (see Figure 3.18 (b)) nearest to the load lock (base pressure: $\sim 5 \times 10^{-10}$ mbar). Lastly, by installing a temporary transfer arm (see Figure 3.18 (b)) to the UHV

instrument, samples can be transferred from the carousel directly into the portable UHV chamber by positioning the sample stage in the portable UHV chamber at a suitable height with the linear z-drive. The portable UHV chamber can then be transferred and mounted to the hexapod in EH2 (beamline I07). The linear z-drive can be used to move the sample upwards such that it is at the same height as the beryllium cylinder. In its current setup, diffraction measurements can be performed on the sample in UHV conditions. The sample can also be exposed to controlled ambient pressures with inert gases such as N_2, He or Ar. To this extent, the portable UHV chamber allows for UHV prepared and characterised samples to be measured with SXRD in UHV and under controlled conditions with pressures ranging from ~1 $\times 10^{-9}$ mbar to ambient pressure.

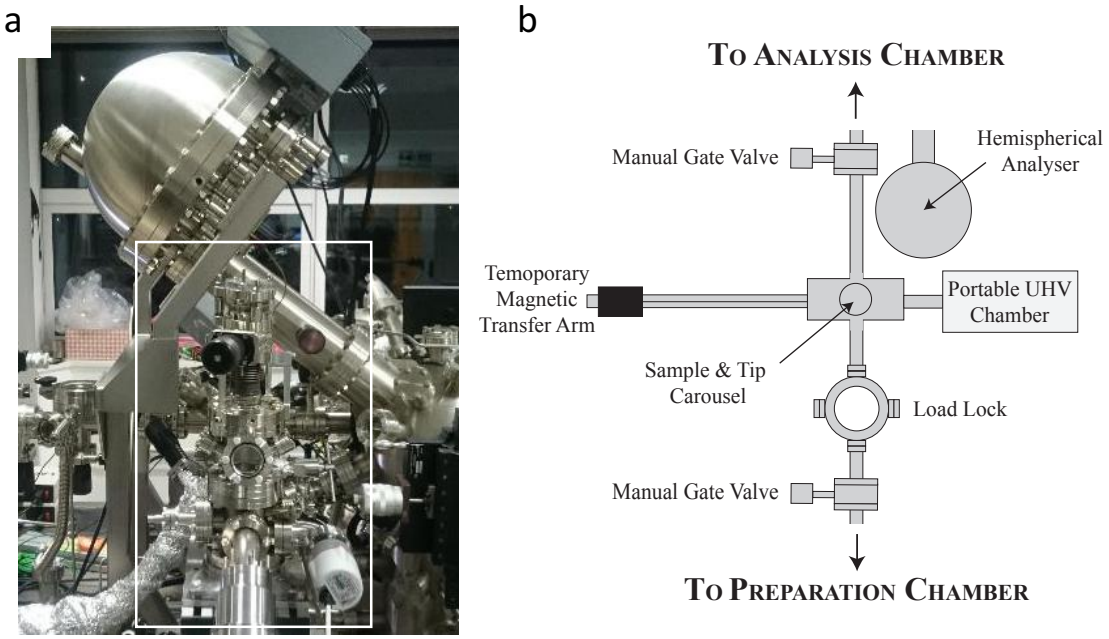

Figure 3.18: (a) Photograph of the portable UHV chamber attached to the Omicron VT AFM/STM instrument at Diamond Light Source (see Figure 3.3). The white box highlights the portable UHV chamber. (b) Schematic of modifications made to Omicron VT AFM/STM instrument at Diamond Light Source (see Figure 3.3) to allow for sample transfer to the portable UHV chamber. In this photograph, the beryllium cylinder is replaced with a stainless steel cylinder for offline testing purposes.

c. Liquid Delivery System and LED

The liquid delivery system (see Figure 3.19) utilises capillary action to allow a liquid droplet to be formed and maintained on the surface. The liquid flow is controlled with a syringe pump (*Hamilton MicroLab500 series*) for which a python script was written and developed to allow for syringe control from the control room. The set up was initially developed to perform solid/liquid interface measurements and was next upgraded to allow for electrochemical / photoelectrochemical measurements. For the solid / liquid interface set up (see Figure 3.19), liquid is expelled from the 'inlet' syringe that passes through a PTFE inner tubing and expels liquid out towards the substrate. The 'outlet' syringe pumps liquid out of the system. The liquid expelled from the 'inlet' tube onto the surface is pulled via the outer capillary (glass) into the cross piece and subsequently into the outlet PTFE tubing. When the liquid delivery system is filled with a chosen liquid, it is approached to around 2 mm away from the sample with no droplet at the end of the outer capillary. Next, liquid is expelled to form an increasingly large droplet at the end of the outer capillary until it make contact with the substrate surface. The syringe system can then be utilised to maintain the droplet on the surface.

For the electrochemical interface set up (see Figure 3.19), the system is largely identical to the solid/liquid interface set up with a few changes. For electrochemical measurements, a reference electrode (Ag/AgCl - Sigma Aldrich) is incorporated into the cross piece. Additionally, a platinum counter electrode (Sigma Aldrich) is introduced via the inner PTFE capillary where the electrically isolated sample (working electrode) is connected to a UHV feedthrough. When a droplet forms on the substrate surface, this system operates as a typical three electrode electrochemical cell. A current flowing between the substrate (working electrode) and the Pt (counter electrode) can be measured with respect to an applied potential that is measured against a reference.

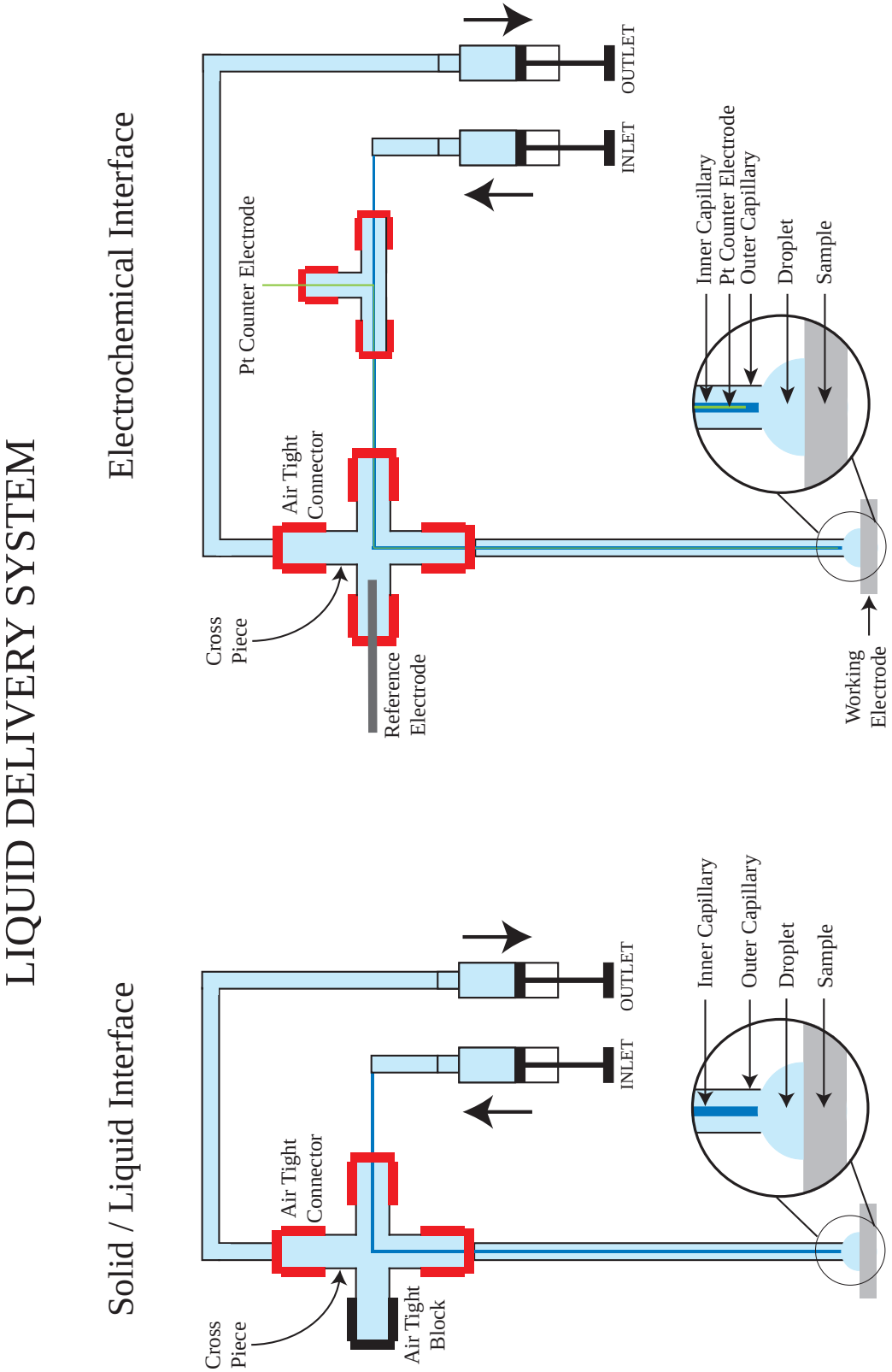

Figure 3.19: Schematic of liquid delivery system for the solid / liquid interface and electrochemical interface set up.

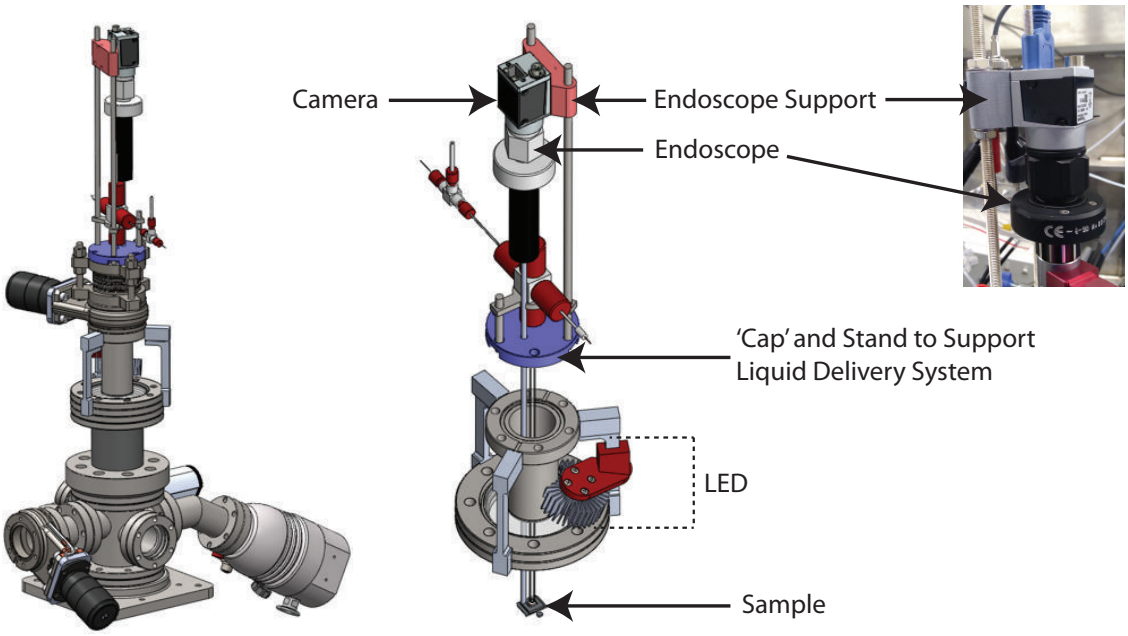

Figure 3.20: Schematic of liquid delivery system installed on the portable UHV chamber with a photograph of the endoscope support on the top right.

A schematic for the liquid delivery system mounted on the portable UHV chamber is shown in Figure 3.20. A 'cap' with a tripod stand (see Figure 3.21), for the liquid delivery system and endoscope (*EverestVIT*), is placed on top of the port-aligner. After the portable UHV chamber is vented to ambient pressure with an inert gas (such as N_2, Ar or He), under an overpressure of gas, the liquid delivery system and endoscope is installed on the portable UHV chamber via the 'cap' and is locked into place with the tripod stand. When lowering the liquid delivery system and the endoscope into the portable UHV chamber, great care is taken and the end of both appliances are viewed via the glass-to-metal reducer to ensure that neither crash into the substrate. The port-aligner (above the gate valve) is subsequently used to do the final 'fine' approach to ensure that the end of the liquid delivery system is ideally centred on the sample and is at a suitable distance of a few mm away from the surface. The endoscope has a camera attached on the outside and allows for droplet visibility from the control room.

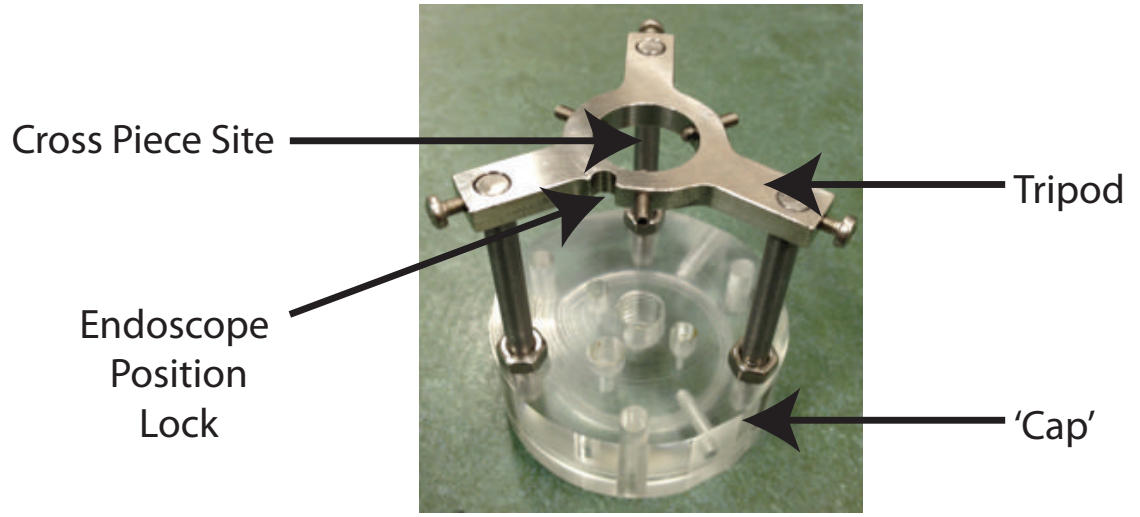

Figure 3.21: Photograph of PTFE 'cap' and stainless steel tripod stand to position and firmly hold the liquid delivery system and endoscope on the portable UHV chamber.

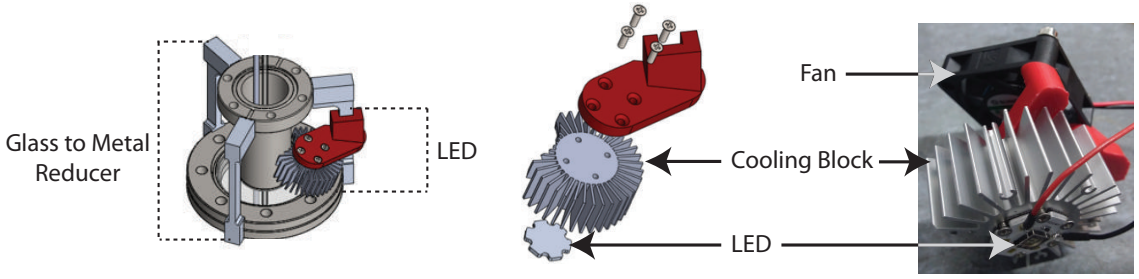

Figure 3.22: Schematic of LED illumination system mounted on the glass to metal reducer of the portable UHV chamber.

For purposes of photo-chemical and photo-electrochemical interface measurements, an LED illuminating system was incorporated into the set up (see Figure 3.22). The system clamps onto one of the rods supporting the glass-to-metal reducer. Subsequently, via the glass component of the reducer, the surface (with or without liquid contact) can be illuminated to investigate the behaviour of interfaces under photo-active conditions. For example, the photo-activity of the surface under photo-active illumination (such as TiO_2 under UV illumination) can be measured with SXRD following adsorption of photo-

active adsorbates from the gas phase. Alternatively, SXRD measurements can be made of interfaces under photo-electrochemical control. A cooling block is positioned immediately behind the LED (see Figure 3.22) such that the LED is prevented from over-heating. Regarding the components associated with the liquid delivery system, i.e. tubing, cross piece, air tight connectors for cross piece and tubing connectors (see Figure 3.23), these can be readily purchased from *Bola* and are general 'off the shelf' products suitable for electrochemical research.

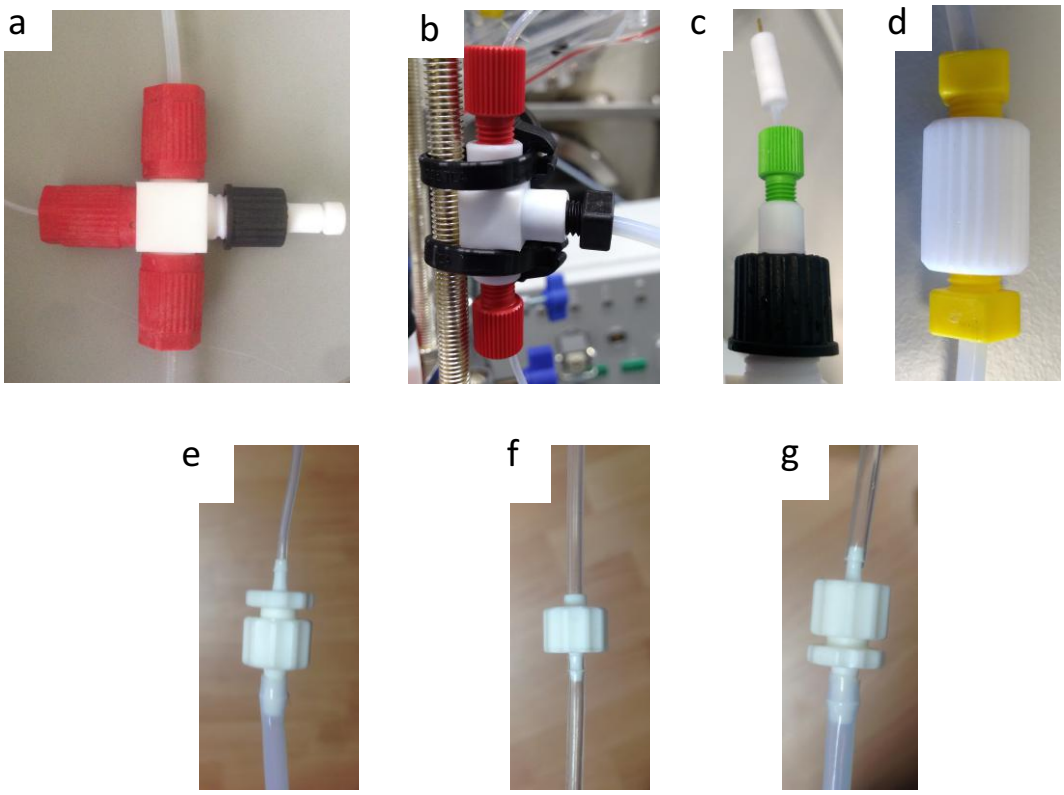

Figure 3.23: A few photographs showing (a) a cross piece and air tight connectors to connect tubing of various sizes to the cross piece (b) a 'T' piece and air tight connectors to connect tubing of various sizes to the 'T' piece (c) an 'air-tight' reference electrode and adaptor (d-g) adaptors for purposes of converting or connecting tubes of different sizes. All are readily available from *Bola*.

d. Summary and Future

Figure 3.24 illustrates the droplet cell set up (portable UHV chamber and liquid delivery system) mounted on the hexapod in EH1 of I07. After mounting the cell, the syringe pump of the liquid delivery system, the potentiostat for the electrochemical set up, the live droplet view via the endoscope/camera and the LED light can all be controlled from the control room (see Figure 3.24) and as such this provides users with an 'all-in-one' package to remotely control the operation of the set up during measurements with X-rays. In its current state, the droplet cell set up allows users to prepare (Ar^+ sputter and annealing) and characterise (STM, AFM, LEED and/or XPS) surfaces using traditional surface science techniques and subsequently transfer the sample (in UHV) to EH1 of beamline I07 for characterisation of surfaces in UHV. Next samples can be exposed to a variety of different partial pressures of a chosen substance with or without photo-active illumination. Thus this allows users to perform experiments that would otherwise not be suited to the UHV instrument in EH2 of I07 which is strictly designed for UHV experiments. Alternatively, the portable UHV chamber is compatible with the liquid delivery system that allows for solid/liquid interface, photo-chemical interface, electrochemical interface and photo-electrochemical interface measurements in controlled environments of inert gases such as N_2, Ar and He.

The main advantages of the cell over the 'ESRF design' are:

1) In the ESRF design, aligning the liquid delivery system above the surface was not user-friendly as alignment was based on partial visibility (via the endoscope) of the surface and liquid delivery system. In the upgraded design, a custom-built UHV compatible glass-to-metal reducer (see Figure 3.17) is incorporated. This enables sufficient visibility of the liquid delivery system and the surface to easily align

the liquid delivery system above the surface, where final ‘fine’ adjustments can be easily made with the port aligner.

2) The ESRF design was only capable of solid/liquid interface and electrochemical interface research. In the new design, we have incorporated an LED (see Figure 3.22), which enables surface illumination to investigate surfaces under photo-active conditions i.e enables photo-chemical and photo-electrochemical interface research.

3) The ESRF design did not possess a port-aligner to allow for a ‘fine’ approach of the liquid delivery system capillary to the surface. In the new design, a port-aligner (see Figure 3.16 and 3.20) is present to allow for a ‘fine’ approach of the liquid delivery system capillary to the sample surface to within a few mm where the port-aligner also aids in centring the liquid delivery system capillary on the surface.

4) In the ESRF design during measurements the liquid delivery system cross-piece and endoscope are held in place with zip ties attached to stainless steel threads. This caused problems associated with structural stability during data acquisition when the hexapod moved. In the new design, a stainless steel tripod stand has been incorporated into the ‘cap’ (see Figure 3.21). This allows for a strong grip and support of the liquid delivery system and endoscope which ensures a sturdier set up during measurements.

5) The ESRF design was only compatible with samples mounted on *Omicron* sample plates. The portable UHV chamber in this upgraded model consists of a ‘clip on / clip off’ sample stage on top of the linear z-drive (see Figure A.3.3). This allows for other stages to be ‘clipped on’ to the linear z-drive thus permitting samples mounted on other forms of sample plate.

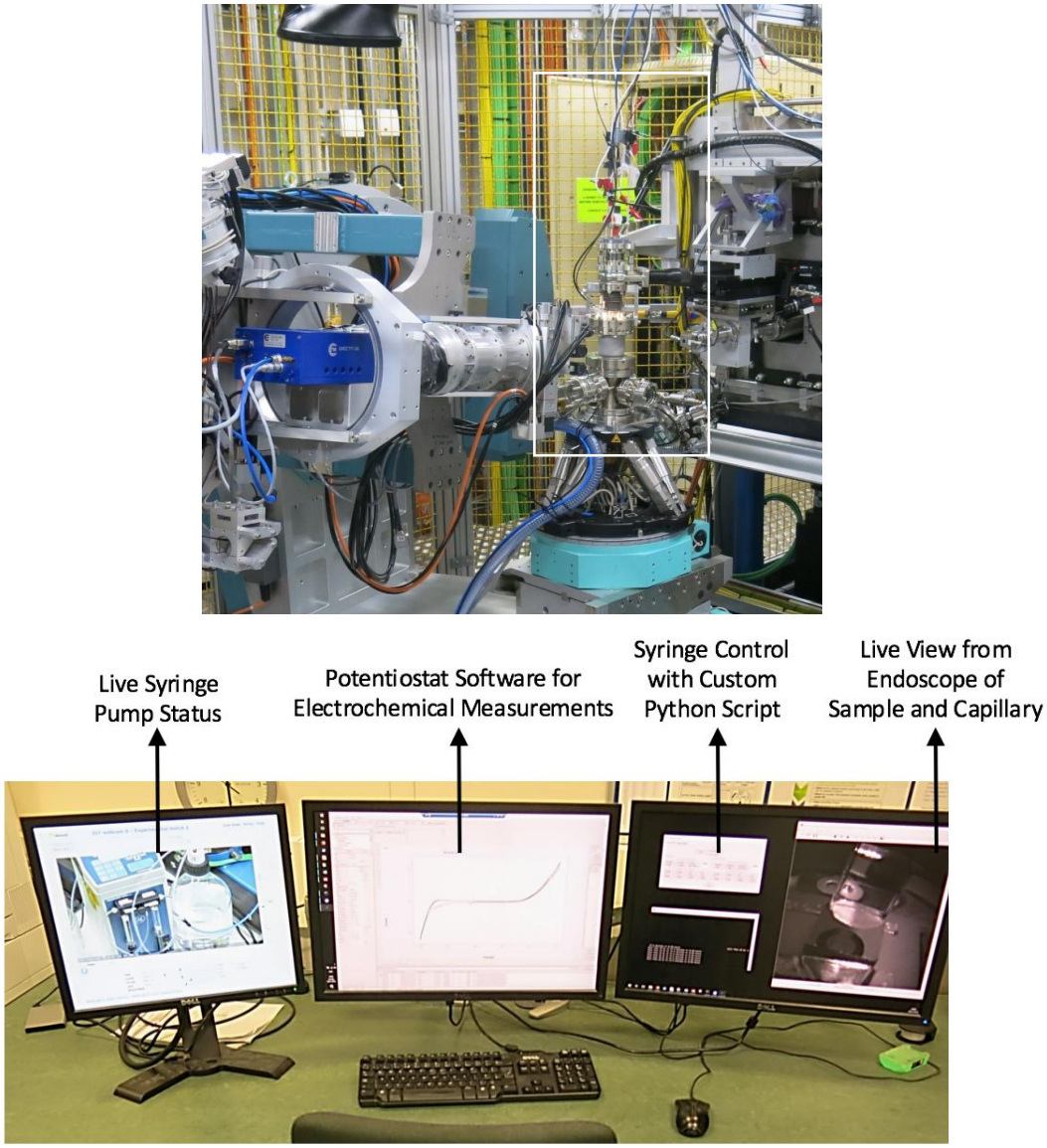

Figure 3.24: Top: Photograph of droplet cell setup (portable UHV chamber and liquid delivery system) mounted on the hexapod in EH1 of I07. Bottom: An 'all in one' display system set up a I07 such that users can control the syringe pump, Potentiostat (for electrochemistry) and have a live view of the endoscope/camera and the syringe pump.

Looking to the future:

1) A resistive heater and cooling unit are expected to be incorporated underneath the sample stage that will allow for variable temperature measurements.

2) A mass spectrometer will be incorporated into the baby chamber allowing for analysis of gas phase products produced by chemical reactions.

3) A small ion pump is expected to be incorporated into the system to allow for an increased reduction in pressures into the $\times 10^{-11}$ mbar regime.

4) Currently, the portable UHV chamber permits one sample to be measured per experiment. In the future, a 'sample storage' section is expected to be incorporated into the linear z-drive underneath the sample stage. This would allow for an exchange of samples during experimentation without the need to re-attach the portable UHV chamber to the *Omicron* VT AFM/STM instrument at Diamond Light Source (see Figure 3.18).

5) Currently, the liquid delivery system approach to the surface is performed largely manually with the 'fine' approach being performed with the port-aligner. In the future, the entire approach set up is expected to be motorised and thus ease the approach process.

6) The liquid delivery system is expected to be upgraded to allow for a relatively more compact design - see Figure 3.25.

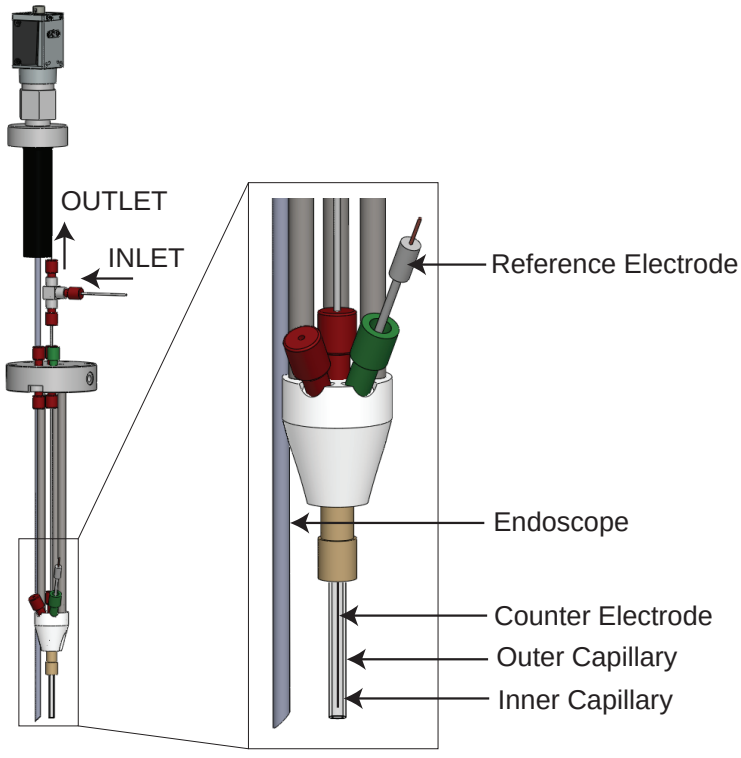

Figure 3.25: Planned new liquid delivery system with a relatively more compact design.

3.6 References

1. *Agilent Technologies 5500 Scanning Probe Microscope: User's Guide*, Agilent Technologies.
2. D. P. Woodruff and T. A. Delchar, *Modern Techniques of Surface Science*, Cambridge University Press, 1994.
3. J. A. Venables, *Introduction to Surface and Thin Film Processes*, Cambridge University Press, 2000.
4. C. L. Pang, R. Lindsay and G. Thornton, *Chemical Society Reviews*, 2008, **37**, 2328-2353.
5. C. L. Pang, R. Lindsay and G. Thornton, *Chemical Reviews*, 2013, **113**, 3887-3948.
6. https://www.keysight.com/en/pd-1709786-pn-N9803A/stm-tips-electrochemically-etched-wax-coated-10pa-max-leakage?nid=-33981.914296&cc=GB&lc=eng.
7. G. Materlik, T. Rayment and D. I. Stuart, *Philosophical Transactions of the Royal Society a-Mathematical Physical and Engineering Sciences*, 2015, **373**, 20130161.
8. C. Nicklin, T. Arnold, J. Rawle and A. Warne, *Journal of Synchrotron Radiation*, 2016, **23**, 1245-1253.
9. T. Hara, T. Tanaka, H. Kitamura, T. Bizen, X. Marechal, T. Seike, T. Kohda and Y. Matsuura, *Physical Review Special Topics-Accelerators and Beams*, 2004, **7**, 050702.
10. E. Vlieg, *Journal of Applied Crystallography*, 1998, **31**, 198-203.
11. F. U. Renner, Y. Gruender and J. Zegenhagen, *Review of Scientific Instruments*, 2007, **78**, 033903.
12. F. U. Renner, Y. Grunder, P. F. Lyman and J. Zegenhagen, *Thin Solid Films*, 2007, **515**, 5574-5580.
13. T. Koop, W. Schindler, A. Kazimirov, G. Scherb, J. Zegenhagen, T. Schulz, R. Feidenhans'l and J. Kirschner, *Review of Scientific Instruments*, 1998, **69**, 1840-1843.
14. O. M. Magnussen, K. Krug, A. H. Ayyad and J. Stettner, *Electrochimica Acta*, 2008, **53**, 3449-3458.
15. F. Carla, F. Loglio, A. Resta, R. Felici, E. Lastraioli, M. Innocenti and M. L. Foresti, *Journal of Physical Chemistry C*, 2014, **118**, 6132-6139.
16. F. Zhang, J. Evertsson, F. Bertram, L. Rullik, F. Carla, M. Langberg, E. Lundgren and J. S. Pan, *Electrochimica Acta*, 2017, **241**, 299-308.

3.7 Appendix

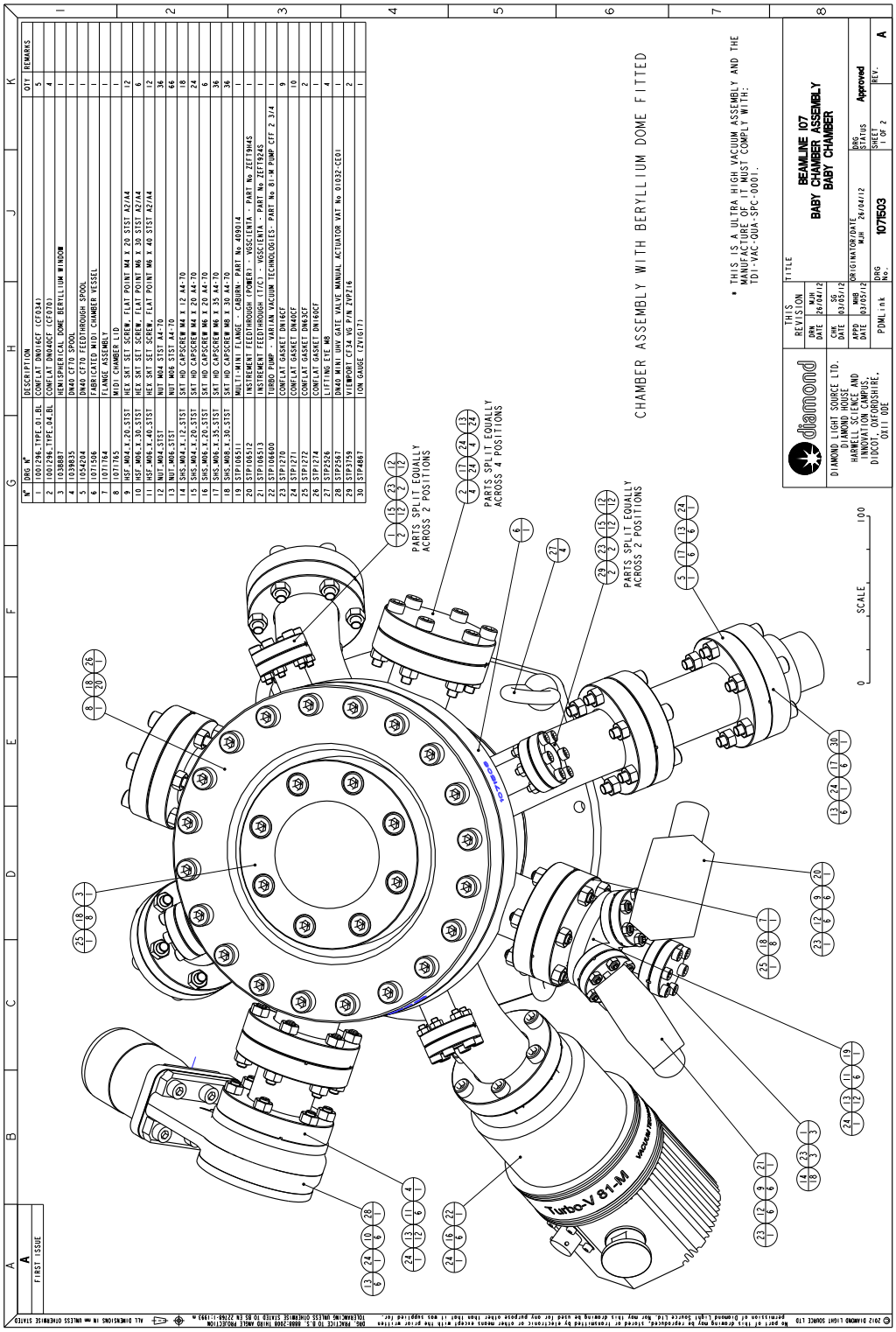

Figure A.3.1: Engineer Diagram by Diamond Light Source of the baby chamber.

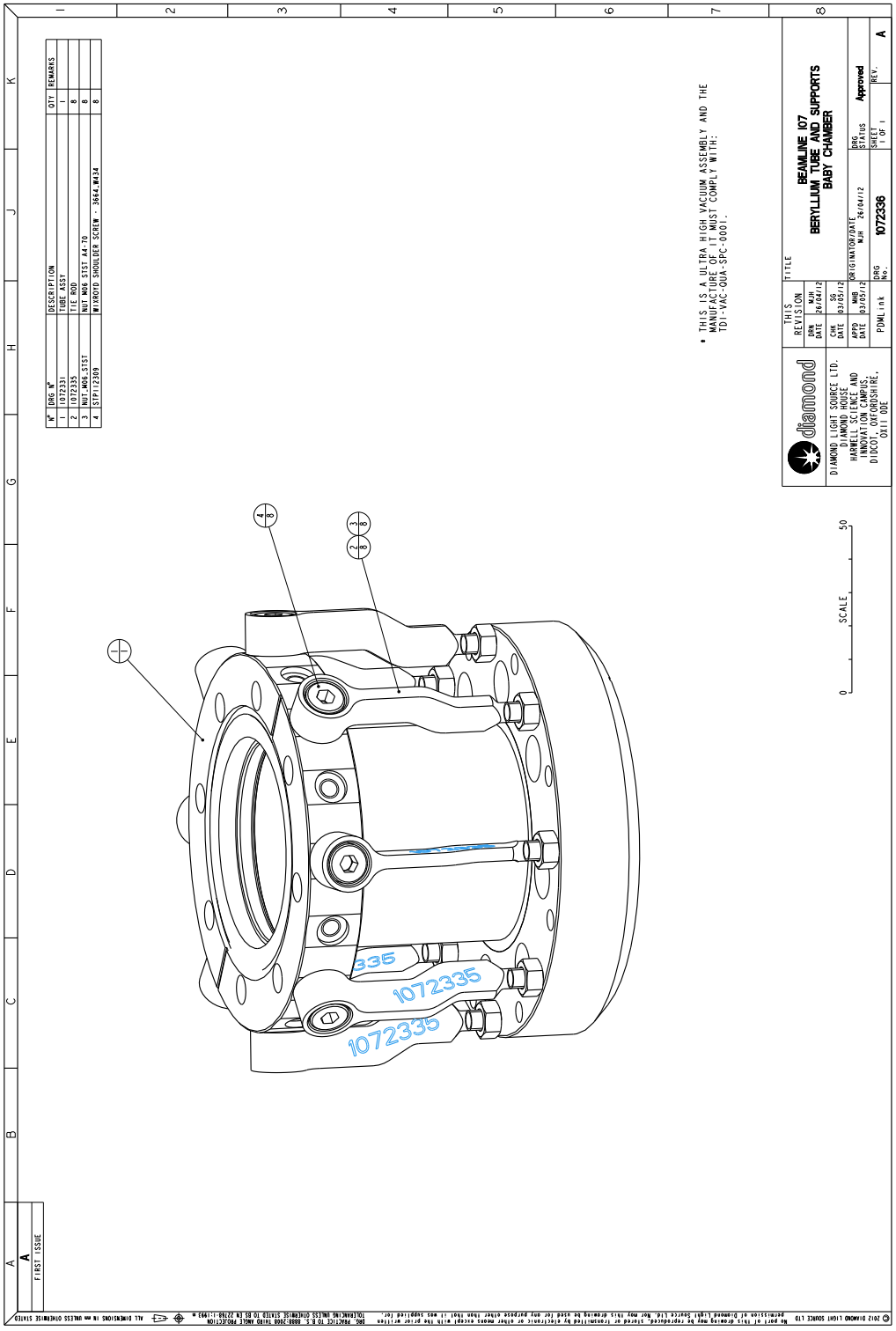

Figure A.3.2: Engineer Diagram by Diamond Light Source of the beryllium cylinder and supports.

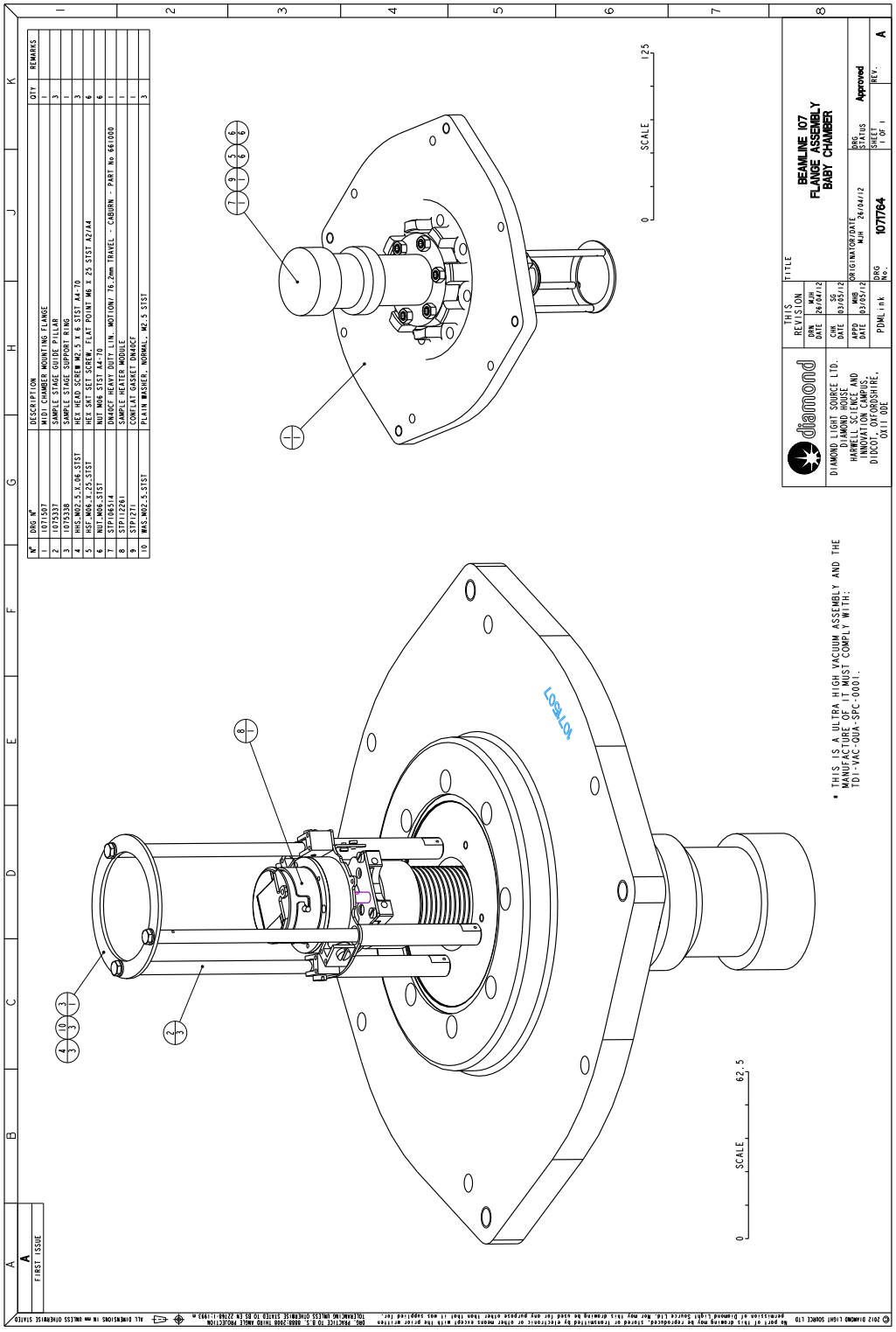

FigureA.3.3: Engineer Diagram by Diamond Light Source of the clip on/clip off sample stage and linear translator in baby chamber.

Chapter 4

The Anatase TiO_2 (101) and Water Interface

4.1 Introduction

4.1.1 Aims and Objectives

Anatase is considered the most active polymorph of titanium dioxide (TiO_2), however, surface/interface studies on rutile single crystals[1-3] are more wide spread due to the ready availability of high quality single crystals and relatively better understood preparation methods. However, over the last decade research on anatase surfaces[4-19], in particular for anatase TiO_2 (101) (A_{101}), has been initiated due to a relatively better availability of natural single crystals from suppliers and due to the publication[20] of successful surface preparation practices. The (101) face of anatase is considered the most stable and abundant and is considered the prototypical anatase surface to probe. The A_{101} and H_2O interface has largely been probed in ultra-high vacuum (UHV) (see Section 4.1.3). In this chapter, we present a UHV, near-ambient pressure (NAP) and ambient pressure (AP) perspective of the A_{101} and H_2O interface. In UHV, we aim to utilise scanning tunnelling microscopy (STM) to investigate the dissociation of H_2O from the residual vacuum at oxygen vacancy (V_o) sites on the A_{101} surface to form OH species (see Section 4.3.1). In NAP and AP we aim to utilise surface X-ray diffraction (SXRD) to probe the interface structure under $H_2O_{(g)}$ (23 mbar) (i.e. ultra-thin film) and $H_2O_{(l)}$ (i.e. bulk water) (see Section 4.3.2). The main motivation behind the work presented in this chapter is to better understand the water adsorption and splitting phenomena on A_{101}.

4.1.2 Structure of Anatase TiO_2 (101)

The A_{101} surface consists of 5 (Ti_{5c}) and 6 (Ti_{6c}) coordinated Ti atoms and 2 (O_{2c}) and 3 (O_{3c}) coordinated O atoms in a saw-tooth geometry[6, 21] - see Figure 4.1. Molecular H_2O

is understood to adsorb at the Ti_{5c} site.[10] In principle, surface OH adsorption is suggested to occur as terminal OH (OH_t)[16, 19] (i.e. OH adsorbed to Ti_{5c}) or bridging OH (OH_{br})[22, 23] (i.e. H adsorbed to O_{2c}) species.

4.1.3 The Literature: Water on Anatase TiO_2 (101)

The interface of A_{101} with H_2O is of great importance to understand the behaviour of this surface under conditions closer to those in technological applications. The temperature and pressure dependence of H_2O adsorption on A_{101} has been realised[4, 10, 11, 16, 19, 24-27] largely in UHV conditions. In UHV, there is little or no evidence of H_2O adsorption at room temperature, although adsorption is increasingly favoured below 298 K.[10] STM at 6 K indicates that H_2O adsorbs molecularly on the surface in a locally ordered (2×2) arrangement.[10] In UHV at 6 K, STM tip pulsing (a voltage pulse applied to the surface via the STM tip) can transform H_2O into features thought to be OH_t.[16] Co-dosing O_2 and H_2O on A_{101} at 105 K and subsequently annealing for 10 minutes at room temperature, followed by STM (at 6 K) also yields features thought to be OH_t.[19] In UHV at 120 K, water has been adsorbed on A_{101} with photoemission measurements collected at intervals from 160 - 400 K. The results indicate that water adsorbs in a mixed associative and dissociative state below 300 K.[4] At room temperature, photoemission measurements of A_{101} under exposure to water pressures of 0.6 to 6 mbar indicates mixed associative and dissociative adsorption of water.[11] In UHV, at 100 K and under UV illumination, H_2O adsorbed on A_{101} has been observed to generate gaseous OH species. This has been interpreted as the adsorbed H_2O dissociating into OH_{br} and OH_t where the latter leaves the surface.[28] As for theory, first principles molecular dynamics (MD) calculations predict that H_2O can dissociate in V_o[29, 30] to form OH_{br} and that the aqueous A_{101} interface (at 300 - 400 K) can maintain OH_t and OH_{br} species.[31, 32]

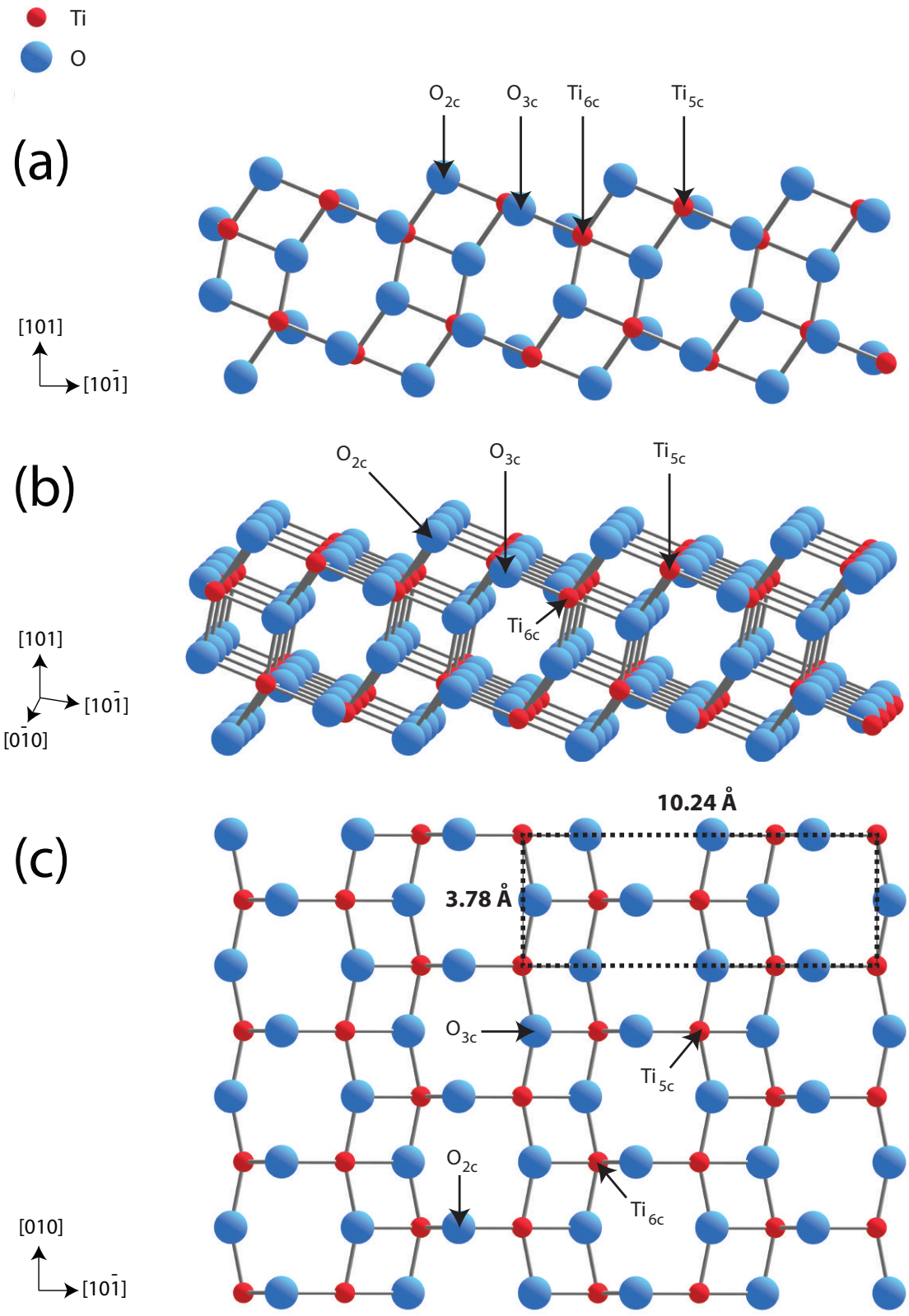

Figure 4.1: Ball and stick illustration depicting the A_{101} surface via different view-points with surface atoms Ti_{6c}, Ti_{5c}, O_{3c} and O_{2c} labelled. (a) Side view of surface. (b) Tilted view of surface with respect to (a). (c) Aerial view of surface with surface unit cell in black dashed box.

4.2 Experimental Procedure

For results presented in Section 4.3.1, a natural A_{101} single crystal (purchased from *Pi Kem*) was mounted onto a Ta plate with Ta strips. The sample was prepared in UHV with cycles of Ar^+ sputtering ($P_{Ar} = 5 \times 10^{-5}$ mbar, 1 kV, 10 μA cm^{-2}, 20 minutes) and annealing (T < 1023 K, 10 minutes).[20] Low energy electron diffraction (LEED) and Auger electron spectroscopy (AES) were used to ensure an ordered and contaminant free surface (below the detection limits of AES) for STM measurements. The STM used is an *Omicron* UHV AFM/STM instrument (see Figure 3.2) operated in constant current mode at room temperature using electrochemically etched tungsten tips, which were degassed in UHV and conditioned during scanning with voltage pulses of up to ±10 V. All STM imaging was carried out by tunneling into empty states using positive sample bias voltages in the range of 1 to 1.6 V. The base pressure of the instrument was 5×10^{-10} mbar. An outgassed filament was used for electron irradiation, with a negative bias with respect to the grounded sample. The front face of the sample was ~2 cm from the filament and the drain current from the sample was used to monitor the electron flux. During irradiation, the UHV chamber pressure increased up to the low 10^{-8} mbar range with an H_2O partial pressure up to the low 10^{-9} mbar region. Immediately after irradiation, the pressure returned to the 10^{-10} mbar region. The irradiation stimulated chamber pressure rise is largely attributed to residual UHV gases - H_2, H_2O, CO and CO_2. At room temperature, H_2O has been experimentally shown to react with V_o to form an OH_{br} defect site on A_{101}[23] and rutile TiO_2 (110) (R_{110})[1, 2]. However, at room temperature, there is no evidence to suggest that either CO or CO_2 react with V_o on A_{101}[23] or R_{110}[1, 2]. Therefore, the effect of H_2O on V_o can be investigated in the presence of CO and CO_2. During irradiation, the sample is expected to be mildly heated by electrons emitted from the filament. It takes at

least 15 minutes to transfer the sample from the electron irradiation position to the STM and achieve tunneling conditions. STM presented little or no thermal drift suggesting that the sample had returned to or was very close to room temperature. This indicates a mild increase in temperature during electron irradiation. The reactivity of the V_o created by electron-irradiation with residual H_2O in UHV (i.e. at the base pressure and during electron irradiation) was investigated with STM. We define a monolayer (ML) as corresponding to the number of surface Ti_{5c}-O_{2c} pairs (density: 5.17 nm^{-2}).

For results presented in Section 4.3.2, SXRD measurements were performed at room temperature on Beamline I07: Surface and Interface Diffraction[33] (see Section 3.5.2) at Diamond Light Source. Experimental Hutch 1 was employed with data acquisition performed using a (2 + 3) diffractometer and a PILATUS 100K area pixel detector. A natural (reduced) anatase TiO_2 (101) (A_{101}) single crystal (purchased from *Matek*) was prepared with repeated cycles of Ar^+ sputtering ($P_{Ar} = 6 \times 10^{-6}$ mbar, 1.5 kV, 2 μA cm^{-2}, 10 minutes) and annealing ($T \leq 1023$ K, 10 minutes) and characterized with STM, LEED and X-ray photoelectron spectroscopy (XPS). LEED and STM showed the surface to be well-ordered while XPS evidenced the absence of contaminants. Sample preparation was performed in an *Omicron* VT STM/AFM instrument (see Figure 3.3) with a base pressure of $\sim 1 \times 10^{-10}$ mbar. Samples were transferred, in UHV, to a baby chamber (base pressure: $\sim 1 \times 10^{-9}$ mbar) (see Section 3.5.3). SXRD measurements of the A_{101} interface with an ultra-thin water film were performed at 23 mbar $H_2O_{(g)}$ (relative humidity (RH) = 100%) by introducing water vapour from a vial of ultra-pure water (18.2 MΩ cm) into the UHV baby chamber via a leak valve after the liquid was further purified by several freeze/pump/thaw cycles. Water adsorption on various substrates shows that its adsorption in the first ML is substrate dependent whereas adsorption in the second and subsequent ML is dependent on the RH.[34] As a general trend RH 60% gives rise to ~5

ML of water irrespective of the substrate.[34] This commonality of behaviour (measured with NAP XPS) arises because the second and subsequent water layers are physisorbed and hence are simply a function of the RH rather than the substrate. This is further evidenced at 90% RH where different substrates[35-37] yield 6-7 water layers. On R_{110}, NAP XPS at 100% RH indicates 10 ±2 water layers.[35] Given the relationship between RH and number of water layers and considering that R_{110} and A_{101} are both polymorphs of TiO_2, we attribute the thickness of our ultra-thin water film at 100% RH to be 10 ±2 layers. In these conditions, 13 crystal truncation rods (CTRs) (2016 structure factors) were collected. SXRD measurements of the A_{101} / bulk water interface were performed by venting the baby chamber to N_2 and using a droplet cell (see Section 3.5.3) to form a water droplet on the surface. Ultra-pure water (18.2 MΩ cm) was again used, being bubbled with N_2 to remove dissolved gases. In these conditions, 15 CTRs (3910 structure factors) were collected. Reference reflections were acquired to ensure that the surface structure did not change during the course of the experiment. SXRD data were acquired in stationary scanning mode[38] at an incident photon energy of 17.7 keV and an incidence angle of 1^o. The goodness of fit of the SXRD model is given via the normalized χ^2 (χ^2_n).[39-41] Due to the low scattering factor of hydrogen, it has not been incorporated into our proposed models. SXRD modelling was performed using the ROD[39] software with a pseudo-orthorhombic surface cell of dimensions a = 10.23 Å, b = 3.71 Å, c = 24.60 Å, $\alpha = 90^o$, $\gamma = 90^o$ and $\beta = 88.98^o$.[21] The A_{101} interface with an ultra-thin water film SXRD measurements were performed and analysed by Dr. Jon Treacy, Dr. Xavier Torrelles, Prof. Geoff Thornton and co-workers.[42] My contribution to the A_{101}/ultra-thin film interface work was limited to partial analysis / re-analysis of the collected data and has been presented in this chapter as it was complementary to the A_{101}/bulk water findings. Findings for both conditions were published together.[43]

4.3 Results and Discussion

4.3.1 Bridging Hydroxyls on Anatase TiO_2 (101) by H_2O Dissociation in Oxygen Vacancies

The chemistry and physics of TiO_2 surfaces is known to be affected by surface defects sites.[1, 2] Defects such as V_o, OH_{br} and interstitial Ti act as excess electron traps generating preferred molecular adsorption sites for chemical reactions. The formation of OH_{br} (see Figure 4.2) on A_{101} is of interest to understand surface defect sites and to investigate water splitting on TiO_2. Scanning probe microscopy (SPM) of OH_t[16, 19] on A_{101} is reported whilst SPM of OH_{br}[44] is relatively briefly discussed. Similar to A_{101}, R_{110} consists of Ti_{5c}, Ti_{6c}, O_{2c} and O_{3c} species, with the two surfaces differing in their bond angles.[1-3] OH_{br} can form on R_{110} via dissociation of H_2O from the residual vacuum at V_o sites.[1, 2] Previous work in the Thornton group at University College London[23] presents spectroscopic evidence of OH formation on the A_{101} surface via H_2O dissociation in the meta stable V_o.[23] In this section, we describe an STM study that identifies the OH species as OH_{br} species. We propose that the OH_{br} are formed via water splitting in V_o through a mechanism where the oxygen in the H_2O occupies a V_o and proceeds to 'split' to create an OH_{br} species where the remaining H moves to an adjacent O_{2c} to form a second OH_{br}.

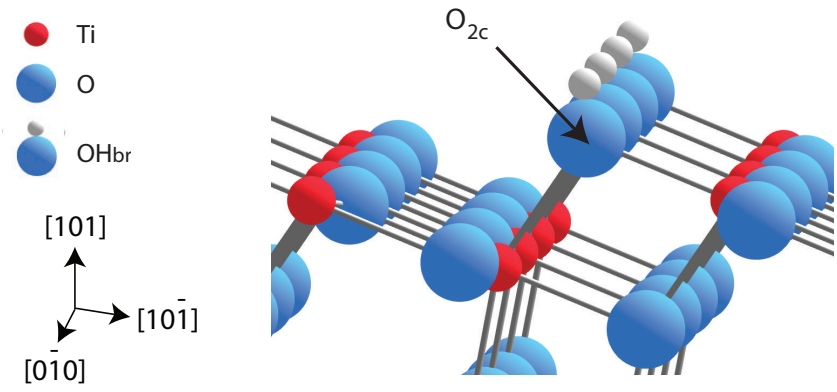

Figure 4.2: Ball and stick representation of OH_{br} on the A_{101} surface.

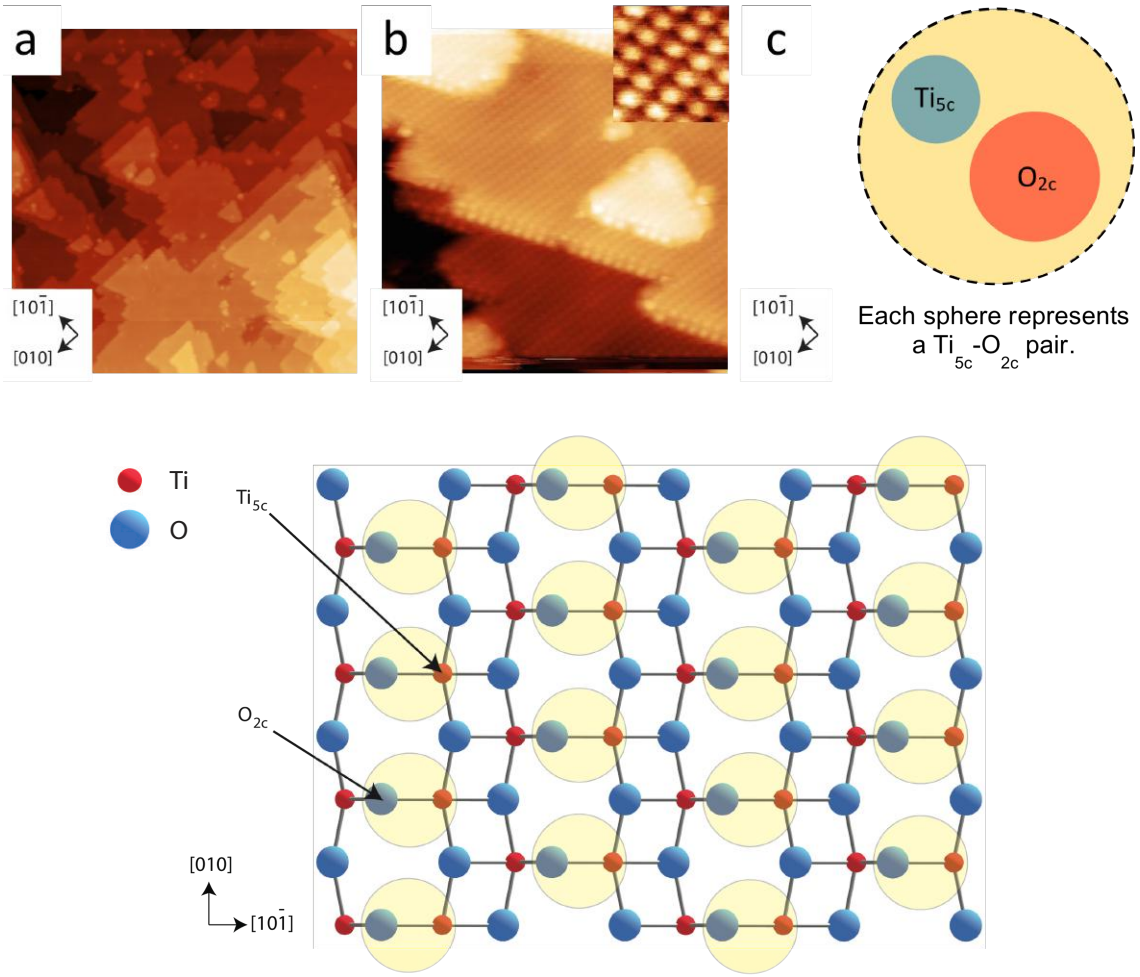

Figure 4.3: As-prepared A_{101}. (a) 100 × 100 nm^2 STM image of A_{101} (V_s = +1.6 V, I_t = 0.4 nA). (b) 15 × 15 nm^2 STM image of A_{101} (V_s = +1.1 V I_t = 0.6 nA) with the inset (2 × 2 nm^2) illustrating the sphere-like features observed with STM. (c) Illustration that each sphere-like feature in STM represents a Ti_{5c} - O_{2c} pair.[6] (d) Ball and stick model of an aerial view of the A_{101} surface where the light yellow circles represent the sphere-like features observed with STM.

STM of as-prepared A_{101} show trapezoidal shaped terraces (see Figure 4.3 (a)) where 'atomically resolved' images depict sphere-like features (see Figure 4.3 (b)). However, each sphere-like feature does not represent a single atom rather it represents a surface Ti_{5c}-O_{2c} pair[6] (see Figure 4.3 (c and d)). Electron irradiation of R_{110} and A_{101} has been shown to create V_o on R_{110} and A_{101} via O^+ ejection.[45, 46] On R_{110}, at room temperature, electron irradiation has been shown to create stable V_o that can be quenched by residual

H_2O in UHV to form OH_{br}.[1] As-prepared A_{101} surfaces are not known to exhibit stable V_o as these species are more stable in the sub-surface and bulk rather than the surface.[46] V_o migration from the surface to the sub-surface and bulk has been shown to begin at temperatures greater than 200 K. Thus, at room temperature, there is little or no evidence of V_o on A_{101}.

Figure 4.4 shows the A_{101} surface at room temperature after three electron irradiation events. Images of the electron irradiated surface contain a number of bright features (marked with white arrows in Figure 4.4) that we identify as OH_{br} groups formed via H_2O dissociation in V_o. The density of bright features in Figure 4.4 is reported in Table 1 and is ~0.05 ML, independent of the electron irradiation conditions. Theory and experiment suggest that A_{101} surface defects act as excess electron 'traps', where the excess electrons are loosely bound to the defect.[23, 31, 47] In particular, OH_{br} species on A_{101} are predicted to maintain trapped charge at the Ti_{5c} site adjacent to the OH_{br}.[31] Previously published two-photon photoelectron (2PPE) spectroscopy and UV photoelectron spectroscopy (UPS) work in the Thornton group[23] shows that electron irradiated A_{101} can maintain excess electrons beyond thermally equilibrated levels on the surface as OH species. While these earlier results indirectly support the electron irradiation induced formation of OH_{br} (via H_2O reacting with the V_o), STM allows us to image the position of the OH species. A high-resolution image of part of the surface imaged in Figure 4.4 (b) is shown in Figure 4.5. The positioning of the bright feature is above the sphere-like feature of the as-prepared surface. This is consistent with the formation of OH_{br} with H bound to the O_{2c} (see Figure 4.5 (b)). On A_{101}, OH_t[16, 19] appear as dimer-like features. Additionally, the appearance of the bright features is reminiscent of OH_{br} observed on R_{110}.[1, 2] This suggests

that the bright features are surface OH_{br} on A_{101} formed via the dissociation of H_2O in a V_o.

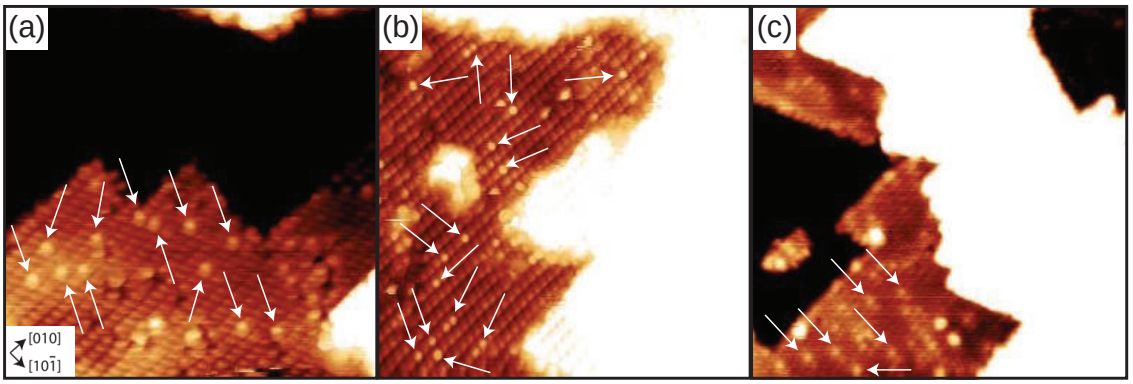

Figure 4.4: (a) 13 × 13 nm^2 STM image (V_s = +1.6 V, I_t = 0.5 nA) of A_{101} after electron irradiation at 500 eV, for 30 s and at a density of 37 μA cm^{-2}. (b) 15 × 15 nm^2 STM image (V_s = +1.03 V, I_t = 0.3 nA) of A_{101} after electron irradiation at 500 eV, for 60 s and at a density of 37 μA cm^{-2}. (c) 23 × 23 nm^2 STM image (V_s = +1.5 V, I_t = 0.4 nA) of A_{101} after electron irradiation at 50 eV, for 30 s and at a density of 74 μA cm^{-2}.

Theory predicts that H_2O dissociation in V_o on A_{101} forms a pair of adjacent OH_{br}.[29, 30] On R_{110}, this type of behaviour is observed experimentally, with OH_{br} forming in adjacent pairs.[1, 2] The OH_{br} subsequently diffuse (i.e. H adatom diffusion) in the [001] and [1$\bar{1}$0] direction through thermally activated pathways, where diffusion in the latter direction can be promoted by H_2O.[48, 49] Our STM results for A_{101} show that the OH related bright features are largely immobile on the surface. Hence, the bright features should exist as adjacent pairs representing two OH_{br}. In contrast, the data in Figure 4.4 show that the bright features are well dispersed. This discrepancy could arise from thermally activated OH_{br} migration caused by heating from the filament during electron irradiation or could be due to H_2O induced mobility when the H_2O partial pressure increases during electron irradiation.[48, 49] An alternative perspective could be that the bright features are not paired as, during electron irradiation, OH_{br} are being formed and desorbed simultaneously – as is the case on R_{110}.[45] Additionally, there may be a complex series of steps where paired

OH_{br} initially move quickly away from each other and subsequently over time this movement could slow down and stop after the species are spread over the surface in the most energetically favourable distribution.

Electron Energy (eV)	Current Density (μA cm^{-2})	Duration (s)	ML Coverage
500	37	30	0.05 ±0.01
500	37	60	0.05 ±0.01
50	74	30	0.04 ±0.01

Table 4.1: Surface ML coverages of the electron irradiated A_{101} presented in Figure 4.4.

On R_{110}, the H adatom (associated with OH_{br} species) can be removed (pulsed off) with approximately +3 V STM tip pulses.[1, 2, 50] On A_{101}, STM tip pulsing (in the range +2.7 to +3.5 V) has been reported to convert OH_t to O_2.[16, 19] However, the bright features under discussion do not pulse off or convert with +3 to +4 V pulses suggesting that OH_{br} species on A_{101} are energetically more stable than on R_{110}. This could result in less mobility and greater resistance to STM tip pulsing. Although R_{110} and A_{101} can maintain defects/adsorbates at similar sites, the behaviour of these species has been shown to be different e.g. at room temperature, V_o can exist on the R_{110} surface whereas on A_{101}, V_o migrate towards the bulk.[46, 50] Hence, it is reasonable to suggest that other defects (such as OH_{br}) also exhibit different characteristics. Therefore, on R_{110} pulsing can remove OH_{br} whereas this would not necessarily be the case with A_{101}. STM tip pulsing beyond +4 V resulted in a 'tip-change' which prevented high-resolution, atomically-resolved STM images from being recorded.

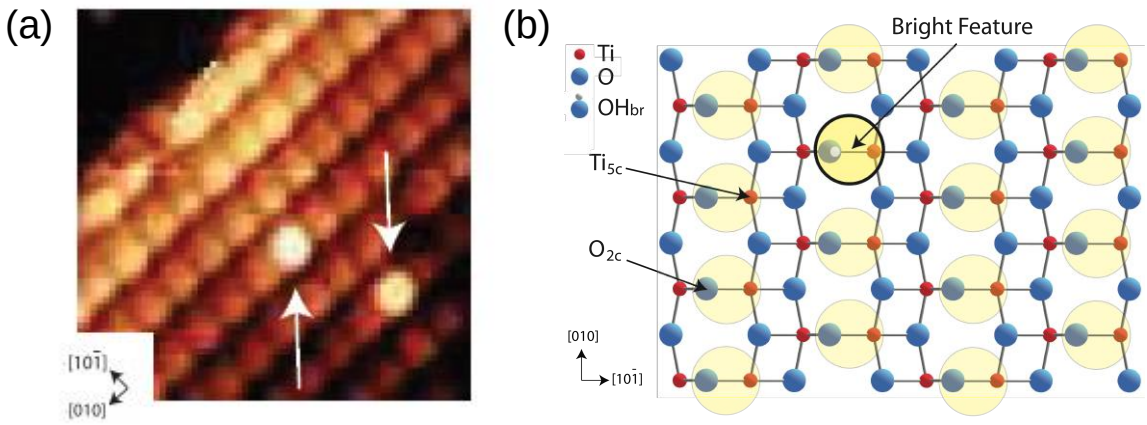

Figure 4.5: Left: 3.5 × 3.5 nm^2 STM image (V_s = +1.2 V, I_t = 0.4 nA) of A_{101} surface after electron irradiation conditions given for Figure 4.4 (b). STM image showing that the bright feature exists above the sphere-like feature on A_{101} where each sphere-like feature represents a surface Ti_{5c}-O_{2c} pair. Right: Ball and stick model showing that the positioning of the bright feature is above the sphere-like feature of the as-prepared surface which is consistent with the formation of OH_{br} with H bound to the O_{2c}

To further probe the origin of the bright features created by electron irradiation, the surface imaged in Figure 4.4 (a) was subjected to progressive electron irradiation without surface re-preparation (see Figure 4.6 and Table 2). Each successive electron irradiation condition consists of an increase in density of electrons irradiating the surface whereas the electron energy and duration of irradiation were fixed at 500 eV and 30 s, respectively. As is shown in Table 2, this resulted in an increase in bright feature density as the electron density was increased. This likely arises from an increase in the density of electrons irradiating the surface that would increase the number of V_o being created and subsequently result in more H_2O molecules quenching them to form OH_{br}. Another point of interest - see Figure 4.6 (b) and (c) - is that the bright features appear to begin to cluster. This clustering phenomenon may be associated with OH_{br} stabilization at higher coverages. V_o have been reported to form sub-surface vacancy clusters,[46] presumably due to favourable energetics and stabilization. A high resolution image of clustered bright

features is shown in Figure 4.7. Here we see that the clustered bright features are essentially the same as the bright features discussed in Figure 4.5 i.e. the bright feature exists above an individual sphere-like feature (Ti_{5c}-O_{2c} pair) of the surface.

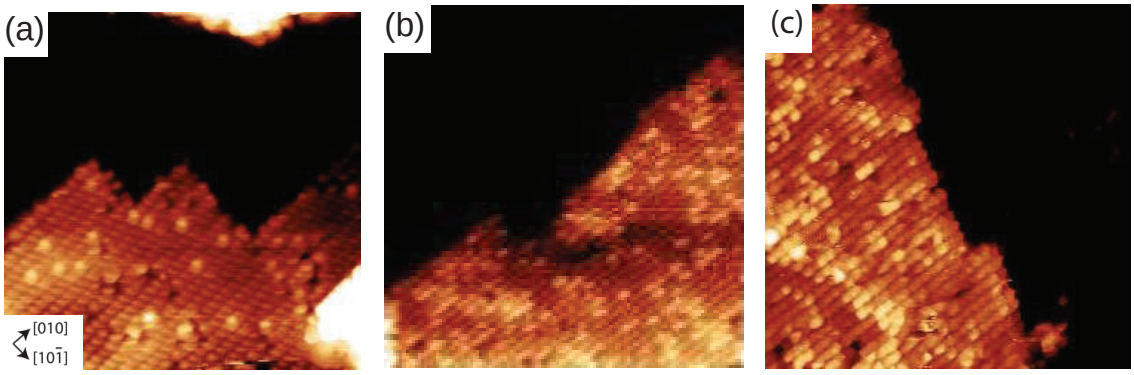

Figure 4.6: STM images obtained after A_{101} has been progressively electron irradiated (without surface re-preparation). (a) 13 × 13 nm^2 STM image (V_s = +1.6 V, I_t = 0.5 nA) of A_{101} after electron irradiation at 500 eV, for 30 s and at a density of 37 µA cm^{-2}. This image is identical to Figure 4.6 (a). (b) 15 × 15 nm^2 STM image (V_s = +1.6 V, I_t = 0.4 nA) after surface in Figure 4.6 (a) was electron irradiated at 500 eV, for 30 s and at a density of 74 µA cm^{-2}. (c) 15 × 15 nm^2 STM image (V_s = +1.0 V, I_t = 0.3 nA) after surface in Figure 4.6 (b) was electron irradiated at 500 eV, for 30 s and at a density of 150 µA cm^{-2}.

Let us now consider other possible origins of the bright features observed in Figures 4.4 - 4.7. Post-electron irradiation, we do not expect to observe V_o on A_{101}. In our experiment, we operate at room temperature where the sample is heated by the filament during electron irradiation followed by at least 15 min required to transfer the sample from the electron irradiation position to tunneling conditions for STM. Subsequently, a further duration of time is necessary to obtain high resolution 'atomic-resolved' STM images. Given that V_o start to move towards the bulk at temperatures as low as 200 K[46], little or no V_o will exist on the surface with our experimental procedure. STM at 78 K, of electron irradiated A_{101} shows features assigned as V_o that upon annealing for 10 minutes at 326

K result in what is described as sub-surface oxygen vacancy clusters[46] - a phenomenon not observed in our work. This may be because heating could allow the V_o to diffuse along thermally activated pathways into the sub-surface and then bulk such that it is not possible to probe with STM. Previous STM studies have investigated the adsorption of H_2O[10, 16, 19], OH_t[16, 19], CO[16, 17] and O_2[12, 16, 19] on A_{101}. The findings are unlike the bright features observed here with a number of tips.

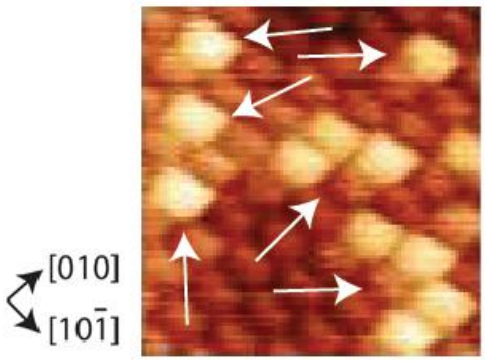

Figure 4.7: 3×3 nm^2 STM image (V_s = +1.6 V, I_t = 0.5 nA) of A_{101} surface after electron irradiation conditions given for Figure 4.6 (b). STM image shows clustered bright features (pointed to with white arrows) that that exist above the sphere-like feature on A_{101} where each sphere-like feature represents a surface Ti_{5c}-O_{2c} pair.

As single atomic defects on A_{101}, the STM appearance of OH_{br} assigned bright feature and V_o are very similar (i.e. bright feature above a sphere-like feature) making it difficult to differentiate the two species with STM alone. Low temperature STM shows that the adsorption of di-atomic species on A_{101}, such as CO, O_2 and OH_t, presents 'dimer-like' features where species are differentiated effectively by their behaviour.[16] Similarly, OH_{br} and V_o can be differentiated by their behaviour. In our STM, at room temperature, OH_{br} has been shown to be stable on the surface whereas V_o stability on the surface is restricted to temperatures below 200 K.[46] Above 200 K, V_o are increasingly mobile resulting in sub-surface vacancy cluster formation or V_o migration to the bulk. The temperature

dependent behaviour of OH_{br} and V_o can be effectively used to differentiate the two species.

Electron Energy (eV)	Current Density (μA cm^{-2})	Duration (s)	ML Coverage
500	37	30	0.05 ±0.01
500	74	30	0.20 ±0.06
500	150	30	0.22 ±0.08

Table 4.2: Surface ML coverages of the electron irradiated A_{101} presented in Figure 4.6.

Previous STM studies of electron irradiated A_{101} have been performed at 6 - 78 K, where V_o are observed.[18, 19, 46] In these publications,[18, 19, 46] there is no report of OH_{br} formation, which can be attributed to the low levels of residual H_2O in the respective UHV chamber (base pressure at $\times 10^{-11}$ to $\times 10^{-12}$ mbar). Alternatively, an activation barrier to water dissociation may prevent OH_{br} formation, as is the case on R_{110}.[51] At room temperature, STM[8] of electron irradiated A_{101} has been pursued to understand Au and Pt nanoparticle interaction with V_o. Post-electron irradiation STM shows some features which are similar to the bright features shown in Figures 4.4 - 4.7, which were tentatively assigned to V_o. However, it has since become apparent that V_o are unstable on the surface at room temperature.[46] Hence, it is reasonable to suppose that the previously observed features arise from OH_{br} species, similar to the bright features observed in our work.

To conclude, we have electron irradiated A_{101} to probe if the residual H_2O in UHV is sufficient to quench the resulting V_o and form OH_{br} groups. Our STM images show that this results in the formation of bright features on the surface, which we assign as OH_{br} species. This claim is supported by theoretical calculations[29, 30] and our previously published spectroscopic measurements.[23]

4.3.2 Water Dissociates at the Aqueous Interface with Reduced Anatase TiO_2 (101)

Determining the interface structures of well-defined TiO_2 surfaces and water is a crucial step towards understanding this process on an atomic scale. While the structure of the R_{110}/H_2O interface has been studied in a number of environments[1, 52], studies of A_{101} have so far been largely restricted to UHV.[4, 10, 16, 19, 22, 23, 28, 31, 32] Water does not adsorb on A_{101} in UHV conditions at room temperature, although it adsorbs molecularly on Ti_{5c} at 6 K.[10] Dissociative adsorption to form OH_t[16, 19] and/or OH_{br}[22, 23] (see Section 4.3.1 for latter) has been reported following electron[22, 23] and photon excitation[28] as well as co-adsorption with O_2[16, 19] at low temperature. There is evidence from photoemission spectroscopy of mixed molecular-dissociative adsorption at room temperature at a higher pressure of water (0.6 - 6.0 mbar).[11]

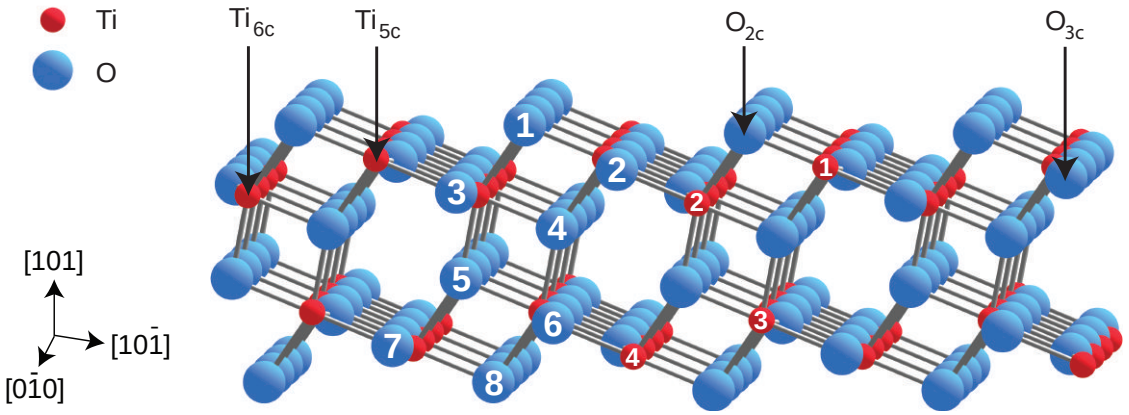

Figure 4.8: Ball and stick model of A_{101} (1 × 1). The numerical labelling of the atoms serves as identification for the atomic displacements shown in Table 4.3. The indicated azimuth defines the x, y and z directions along which the atomic co-ordinates are defined as positive.

The reduced room temperature reactivity of A_{101} to water in UHV compared with R_{110} is thought to be due to the lack of V_o.[46] These vacancies, which promote dissociation on R_{110}[50], are absent on A_{101} because they are more stable in subsurface sites.[46] However, the unreactive character of reduced A_{101} in UHV is predicted to be modified when a liquid interface is formed by trapping excess electrons at bound hydroxyl complexes.[31] Here we test this idea through a quantitative structure determination of the A_{101} surface covered by an ultra-thin water film or bulk water, complemented with density functional theory (DFT) calculations (performed by the Selloni Group at Princeton University). We find that a mixture of molecular and dissociated water is present in the contact layer, pointing to a significantly enhanced reactivity of the substrate compared with that observed in UHV.

The interface structures for A_{101} with an ultra-thin film and bulk water were obtained from SXRD data in comparison with DFT calculations. SXRD data recorded from the clean surface in UHV prior to the interface measurements are essentially identical to those published previously.[21] Labelling of titanium and oxygen atoms used is given in Figure 4.8. The atomic displacements on the as-prepared surface, given in Table 4.3, indicate a relaxation of atoms away from the bulk, a phenomenon previously observed on R_{110} in UHV.[53] As discussed in our previous work[21], surface roughness has been modelled with a 'terraced roughness'[54] approach which allows better simulation of the step-related surface roughness. Modelling is performed with two surface domains with identical terminations that differ in the relative height from the bulk at which the termination occurs. Occupancy of the two domains is in a 1:3 ratio as is reported in previous work.[21]

Atom Label	Displacements (Å)					
	A_{101} / UHV (As-Prepared)		A_{101} / Ultra-Thin Water Film		A_{101} / Bulk Water	
	$\Delta\,[10\bar{1}]$ [^{a}SXRD^{21} : ^{b}SXRD : ^{c}DFT]	$\Delta\,[101]$ [^{a}SXRD^{21} : ^{b}SXRD : ^{c}DFT]	$\Delta\,[10\bar{1}]$ [SXRD : ^{c}DFT]	$\Delta\,[101]$ [SXRD : ^{c}DFT]	$\Delta\,[10\bar{1}]$ [SXRD : ^{c}DFT]	$\Delta\,[101]$ [SXRD : ^{c}DFT]
O - 1	0.11 : 0.14 : 0.23	0.07 : 0.10 : 0.02	0.05 : -0.01	-0.01 : 0.08	-0.03 : -0.05	0.03 : 0.05
Ti - 1	0.03 : 0.02 : -0.01	0.01 : -0.01 : -0.12	0.02 : 0.00	0.07 : 0.15	-0.02 : -0.06	0.11 : 0.13
O - 2	0.11 : 0.13 : 0.14	0.15 : 0.14 : 0.25	-0.08 : -0.02	0.12 : 0.16	-0.03 : -0.04	0.09 : 0.17
O - 3	0.18 : 0.16 : 0.11	0.08 : 0.05 : 0.06	-0.08 : -0.04	0.10 : 0.00	-0.04 : -0.09	0.04 : 0.01
Ti - 2	0.12 : 0.11: 0.12	0.15 : 0.16 : 0.21	0.08 : -0.03	0.09 : 0.01	0.02 : -0.07	0.06 : 0.03
O - 4	-0.01 : 0.01 : 0.13	0.01 : 0.01 : -0.02	0.15 : -0.04	0.00 : 0.07	0.04 : -0.05	0.01 : 0.08
O - 5	-0.07 : -0.04 : 0.05	0.06 : 0.06 : 0.06	-0.03 : -0.03	-0.03 : 0.04	0.05 : -0.04	0.04 : 0.04
Ti - 3	0.01 : -0.01 : -0.05	0.04 : 0.03 : -0.05	0.06 : -0.02	0.06 : 0.07	0.05 : -0.03	0.05 : 0.07
O - 6	-0.06 : -0.05 : -0.01	0.05 : 0.07 : 0.02	-0.13 : -0.03	0.07 : 0.06	-0.04 : -0.03	0.05 : 0.07
O - 7	0.13 : 0.14 : 0.01	0.08 : 0.05 : 0.04	0.01 : -0.03	0.04 : 0.05	0.05 : -0.04	0.02 : 0.05
Ti - 4	0.06 : 0.08 : 0.01	0.08 : 0.09 : 0.10	0.07 : -0.03	0.07 : 0.03	0.03 : -0.04	0.03 : 0.04
O - 8	-0.05 : -0.04 : -0.01	0.00 : 0.04 : 0.02	0.03 : -0.03	0.00 : 0.04	0.01 : -0.03	0.01 : 0.05

Table 4.3: Experimental (SXRD) and theoretical (DFT) surface atomic displacements away from the bulk terminated structure of A_{101}. Positive or negative displacements indicate those parallel or anti-parallel to the directions of the coordinate axis defined in Figure 4.8. Experimental errors correspond to ± 0.01 Å as obtained from the fitting procedure. [a]Represents as-prepared surface before formation of the ultra-thin water film interface (10 ± 2 layers). [b]Represents as-prepared surface before formation of the bulk water interface. [c]Performed by Selloni Group (Princeton University).

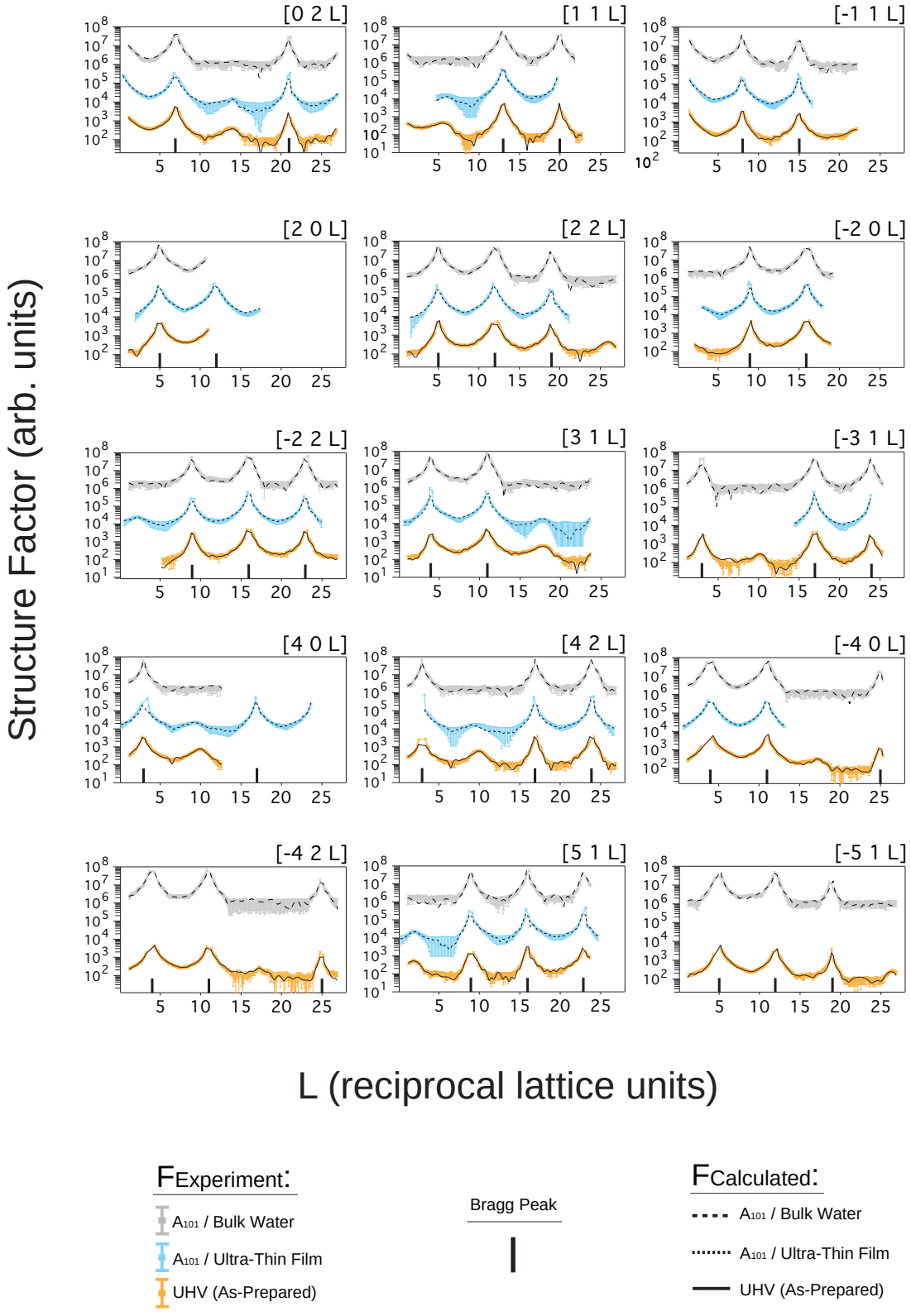

Figure 4.9: Experimental CTRs for as-prepared A_{101} in UHV (orange), and for the A_{101} interface with an ultra-thin water film (blue) and bulk water (grey). CTRs are offset for clarity. $F_{Experiment}$: experimental structure factor. $F_{Calculated}$: calculated structure factor.

CTRs and the best fits for A_{101} covered with a water film and bulk water are shown in Figure 4.9. Table 4.3 gives the surface atomic displacements before and after formation of the water interface. These optimized atomic displacements indicate mixed associative and dissociative water adsorption with a χ^2_n of 1.12 and 1.05 for the water film and bulk water, respectively. The non-uniform agreement between certain experimental and DFT displacements is largely attributed to calculation limitations such that they are limited to indicating trends. In this respect, our experimental and DFT displacements are in good agreement where in UHV the general trend follows surface atoms relaxing away from the bulk whilst after water exposure the surface atoms adopt a more bulk-like appearance.

The best-fit SXRD model for the A_{101} interface with the ultra-thin water film suggests ordering in the contact layer only, with a complete coverage of adsorbed H_2O/OH species on Ti_{5c} (Ti-1). There are two distinct Ti_{5c}-OH_2/OH species with 25% and 75% coverage and bond lengths of 2.21 ± 0.04 Å and 1.94 ± 0.01 Å, respectively (see Figure 4.10 and see Figure 4.11 (a) for a graph of χ^2_n against a change in surface adsorbate coverage). The best-fit SXRD model for the interface with bulk water has an additional ordered layer above the contact layer. Similar to the ultra-thin case, the contact layer contains two distinct Ti_{5c}-OH_2/OH species with 25% and 75% surface coverage and bond lengths of 2.18 ± 0.03 Å and 1.95 ± 0.01 Å, respectively (see Figure 4.10 and see Figure 4.11 (a) for a graph of χ^2_n against a change in surface adsorbate coverage). The second layer appears to consist of H_2O molecules that are hydrogen bonded to molecules in the contact layer based on the bond distances (see Figure 4.10). Interestingly, as is shown in Figure 4.10, the bond angle of the H_2O and OH_t species on Ti_{5c} (Ti-1) varies depending on whether the surface is contacted with the ultra-thin film or bulk water. This can be attributed to the presence of the ordered second layer in the case of the bulk water interface (see Figure 4.11 (b) for a graph of χ^2_n against a change in second monolayer coverage).

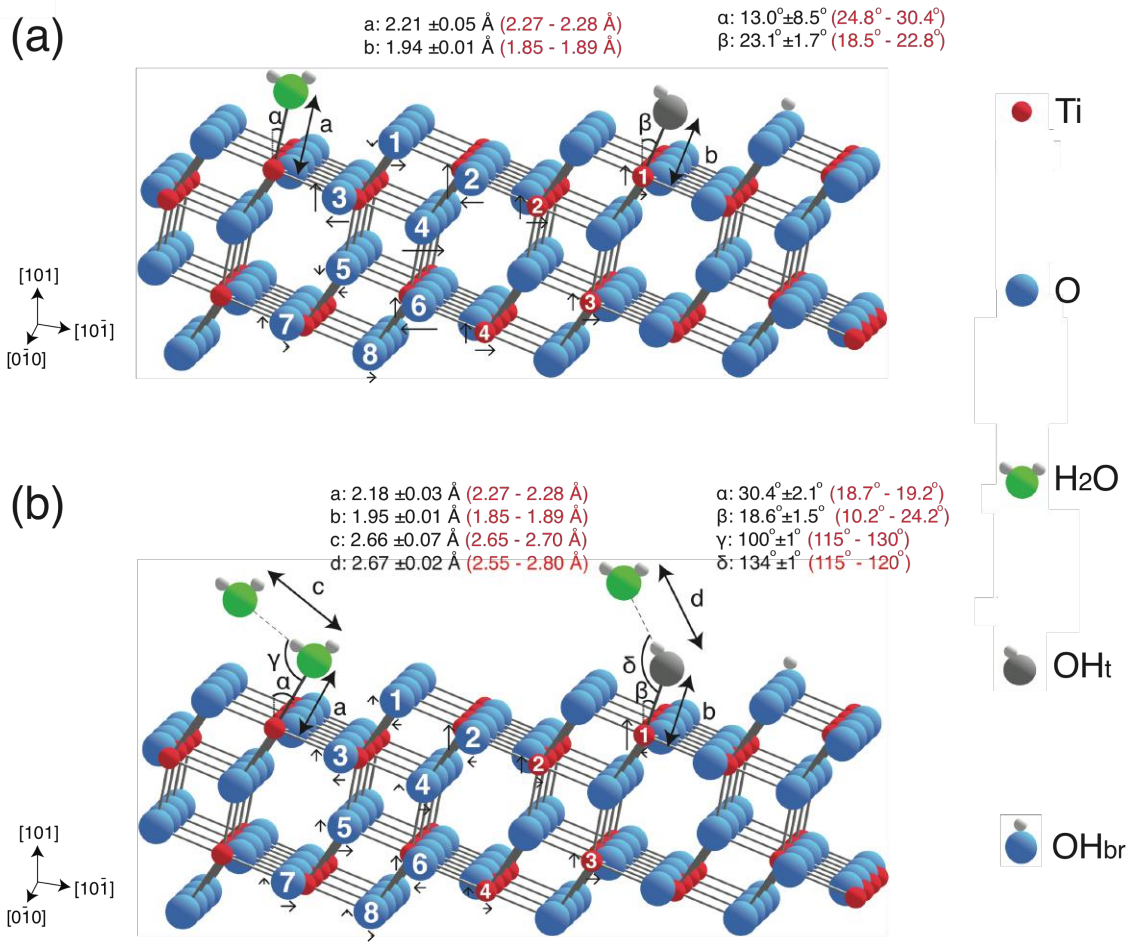

Figure 4.10: Ball and stick model of the proposed A_{101} interface with (a) an ultra-thin water film and (b) bulk water. Experimental (SXRD) bond lengths and angles are presented in black, with DFT calculations (Performed by Selloni Group (Princeton University)) denoted in red. The black arrows represent the relative magnitude and direction of atom displacements with respect to bulk lattice positions. Hydrogen atoms were not included in the experimental fitting procedure due to their small X-ray scattering strength, and so are only displayed for illustrative purposes. A complete coverage of adsorbed H_2O/OH on Ti_{5c} is proposed. However, for presentation purposes this figure shows only one adsorbed H_2O and OH_t.

Previous DFT and MD simulations[7, 30, 55-62] predict a Ti_{5c}-O_{H2O} bond length in the range 2.15 - 2.30 Å, while the Ti_{5c}-O_{OH} bond length is predicted to be 1.80 - 1.90 Å. Our current DFT calculations predict the Ti_{5c}-OH_2 bond length to be 2.27 - 2.28 Å and the Ti_{5c}-OH_t bond length to be 1.85 - 1.89 Å (see Figure 4.10). Experimental measurements of the $R_{110}/H_2O_{(l)}$ interface show a Ti_{5c}-OH_t bond length at 1.95 ± 0.03 Å.[52] On this basis, the

Ti_{5c}-O bond lengths of 2.21 ± 0.05 Å (ultra-thin film) and 2.18 ± 0.03 Å (bulk water) can be attributed to associative H_2O surface adsorption on Ti_{5c}, while the bond lengths of 1.94 ± 0.01 Å (ultra-thin film) and 1.95 ± 0.01 Å (bulk water) correspond to dissociative adsorption to form Ti_{5c}-OH_t. A 25% occupation of Ti_{5c} sites by molecular water was also found in UHV scanning tunneling microscopy (STM) images following exposure of A_{101} to water vapour at 6 K.[10] At low temperature this forms a locally ordered (2 × 2) overlayer, which could in principle be present at the ultra-thin water film and bulk water interface. The small domain size would prevent fractional order rods (FORs) from being observed.

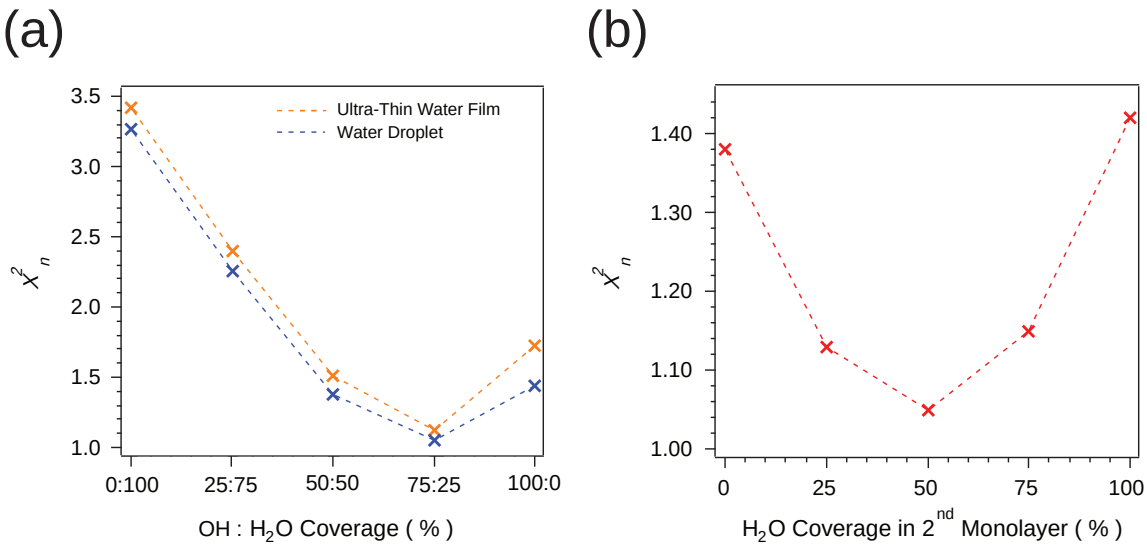

Figure 4.11: (a) Change in χ^2_n as a function of the OH:H_2O ratio for the A_{101} interface with an ultra-thin film of water and the A_{101} interface with bulk water. (b) Change in χ^2_n as a function of H_2O coverage in the second monolayer at the A_{101} / bulk water interface where the first monolayer consists of 75% OH and 25% H_2O adsorption.

The surface atomic displacements after formation of the aqueous interfaces are in general close to zero. In other words, the expansion of the surface observed in UHV is reversed with the formation of the interface. This behaviour has been previously observed at the R_{110}/H_2O interface[52] and is well reproduced by our DFT calculations. Interestingly,

experiment and theory suggest an expansion away from the bulk for the Ti_{5c} (Ti-1) atom. This movement is attributed to the formation of Ti_{5c} (Ti-1) bonds to OH_2/OH in the contact layer. DFT[7, 30, 55-62] calculations of water on TiO_2 has consistently predicted adsorbate bond lengths that are in good agreement with experiment. This trend is also observed in our findings (see Figure 4.10) indicating the accurate predictive capabilities of DFT in this respect. We utilise the optb88-vdw DFT functional which has been shown to simulate the aqueous environment better than the Perdew, Burke and Ernzerhof (PBE) functional[63, 64] and has been used to describe several semiconductor/water interfaces accurately. The experimental bond angles associated with molecules in the contact layer (see Figure 4.10) are reproduced reasonably well by our theoretical calculations. Any discrepancies are attributed to limitations associated with the optb88-vdw DFT functional where its suitability to reproduce bond angles is as yet unclear due to a lack of bond angle comparison between a variety of experimental and theoretical work.[63-66]

Previous calculations of the A_{101}/water interface predict that the formation of OH_t species from water dissociation is coupled with the formation of OH_{br} species that trap excess electrons from the selvedge.[31] In principle, this can be probed experimentally by the position of the O_{2c} to which a H atom is bound to form OH_{br}.[59] Our SXRD results indicate that, after H_2O exposure, the Ti_{5c}-O_{2c} bond length increases from 1.90 ± 0.02 Å to 1.95 ± 0.01 Å and 1.88 ± 0.01 Å to 1.95 ± 0.01 Å, respectively for the ultra-thin water film and bulk water interfaces. Earlier calculations[59] predict that the Ti_{5c}-O_{2c} bond length is 1.86 Å for the clean surface, which can increase up to 1.88 Å in the presence of OH_t and H_2O species at the Ti_{5c} (Ti-1) site. However, in the presence of both OH_{br} and OH_t species the Ti_{5c}-O_{2c} bond length can increase up to 2.01 Å. This is supported by our current DFT calculations, which show that the presence of OH_{br} species can result in a Ti_{5c}-O_{2c} bond length of ~2 Å whereas in the absence of OH_{br} and with only H_2O or OH_t adsorption at

the Ti_{5c} site, the Ti_{5c}-O_{2c} bond length is ~1.85 Å. Given that our experimental findings indicate an expansion of the Ti_{5c}-O_{2c} bond length after aqueous interface formation, it can be inferred that the interface consists of OH_{br} species formed via H_2O dissociation to form OH_t and OH_{br} species.

The influence of the water layer thickness on the contact layer structure has been discussed by numerous research groups however there is a lack of experimental evidence.[67] In our work, we observe that our ultra-thin water film and bulk water on A_{101} induces a similar interface structure i.e. the surface atoms adopt a bulk-like positioning with water adsorbing in a dissociative (Ti_{5c}-OH_t) and associative (Ti_{5c}-OH_2) manner in a 3:1 ratio. The main difference between the two interface is the existence of an ordered second ML (at 50% coverage) at the bulk water interface that does not occur at the ultra-thin film interface. This indicates that the ultra-thin water film thickness of 10 ±2 ML[35] is below that required for it to behave as bulk water. This interesting phenomenon can be explained in terms of the sensitivity to water adsorption that A_{101} (and R_{110}[1,2,52]) exhibit with respect to varying temperature and/or pressures. This difference can be attributed to the change in environmental pressure from near-ambient (23 mbar) to the ambient such that the latter is required to form an ordered second ML. Essentially, there is a pressure dependence that dictates the structure of A_{101} interfaces. This highlights the importance of investigating A_{101} at the appropriate pressure such that near-ambient pressures are close but not entirely representative of the ambient.

The activation of A_{101} to induce water dissociation at the aqueous interface while being inert in UHV can be explained in terms of the interplay between excess electrons and adsorbed water. Although little electron trapping is observed at the surface of as-prepared A_{101} in UHV, an excess electron at the aqueous interface can trigger water dissociation to form surface OH species.[31] The catalytic activation of A_{101} under aqueous conditions can

be explained by the interaction of excess electrons with multiple water layers and the subsequent electron trapping at the resultant OH species.

In conclusion, this study has shown that room temperature aqueous interfaces with reduced A_{101} have a mixture of molecular H_2O (25%) and OH_t (75%) bound to Ti_{5c} in the contact layer. OH_t formation from water dissociation is accompanied by the formation of OH_{br}. On the basis of previous calculations[31], the reduced state of the anatase will play a crucial role in the formation of this contact layer since it provides the excess electrons needed for dissociation. Upon water exposure to the as-prepared surface, the surface atoms contract towards the bulk and adopt a relatively more bulk-like appearance when compared to the as-prepared surface. This study highlights the importance of the substrate environment in determining its reactivity. For A_{101}, the aqueous interface is reactive, whereas the UHV substrate is inert at room temperature. Since the aqueous interface is relevant in photo-catalysis, it also highlights the importance of studies in realistic environments. This behaviour of A_{101} is likely to be observed on other reducible metal oxides, however this will depend on its surface electronic structure. For instance, in contrast to the (101) termination, the (001) termination of anatase does not trap electrons.[31]

4.4 Conclusions and Future Work

In this chapter, we discuss (a) the formation of OH_{br} species on A_{101} in UHV and (b) the nature of the aqueous interface of A_{101}. Regarding the formation of OH_{br} species on A_{101} in UHV, we electron irradiate the surface at room temperature and probe the effectiveness of residual H_2O in vacuum to quench these vacancies to create OH_{br} species. Our STM findings (supported by theoretical and spectroscopic research) point towards the formation of OH_{br} that quench the meta-stable V_o species. This research presents evidence of defect mediated water splitting on A_{101}. Regarding the nature of the aqueous interface of A_{101}, our SXRD findings suggest that the interface consists of a mixed H_2O/OH_t overlayer in a 25:75 ratio with indirect evidence of OH_{br} species. As A_{101} in UHV is largely inert, this work highlights the importance of investigating A_{101} in more realistic conditions.

In light of our findings and since the aqueous interface is relevant to photo-catalysis, an interesting future experiments would consist of further probing the aqueous interface of A_{101}. This would involve experiments where the aqueous interface of A_{101} is exposed to photo-active illumination. Alternatively, probing the interface of A_{101} with electrolyte solution is also a promising avenue to pursue to better understand various electrochemical and photo-electrochemical process on A_{101}.

4.5 References

1. C. L. Pang, R. Lindsay and G. Thornton, *Chemical Society Reviews*, 2008, **37**, 2328-2353.
2. C. L. Pang, R. Lindsay and G. Thornton, *Chemical Reviews*, 2013, **113**, 3887-3948.
3. U. Diebold, *Surface Science Reports*, 2003, **48**, 53-229.
4. L. E. Walle, A. Borg, E. M. J. Johansson, S. Plogmaker, H. Rensmo, P. Uvdal and A. Sandell, *Journal of Physical Chemistry C*, 2011, **115**, 9545-9550.
5. D. C. Grinter, M. Nicotra and G. Thornton, *Journal of Physical Chemistry C*, 2012, **116**, 11643-11651.
6. W. Hebenstreit, N. Ruzycki, G. S. Herman, Y. Gao and U. Diebold, *Physical Review B*, 2000, **62**, R16334-R16336.
7. X. Q. Gong, A. Selloni, M. Batzill and U. Diebold, *Nature Materials*, 2006, **5**, 665-670.
8. X. Q. Gong, A. Selloni, O. Dulub, P. Jacobson and U. Diebold, *Journal of the American Chemical Society*, 2008, **130**, 370-381.
9. Y. B. He, O. Dulub, H. Z. Cheng, A. Selloni and U. Diebold, *Physical Review Letters*, 2009, **102**, 106015.
10. Y. B. He, A. Tilocca, O. Dulub, A. Selloni and U. Diebold, *Nature Materials*, 2009, **8**, 585-589.
11. M. J. Jackman, A. G. Thomas and C. Muryn, *Journal of Physical Chemistry C*, 2015, **119**, 13682-13690.
12. M. Setvin, U. Aschauer, P. Scheiber, Y. F. Li, W. Y. Hou, M. Schmid, A. Selloni and U. Diebold, *Science*, 2013, **341**, 988-991.
13. M. Setvin, P. Scheiber, B. Daniel, M. Fidler, M. Schmid and U. Diebold, *Abstracts of Papers of the American Chemical Society*, 2013, **246**.
14. M. Setvin, X. F. Hao, B. Daniel, J. Pavelec, Z. Novotny, G. S. Parkinson, M. Schmid, G. Kresse, C. Franchini and U. Diebold, *Angewandte Chemie-International Edition*, 2014, **53**, 4714-4716.
15. M. Setvin, C. Franchini, X. F. Hao, M. Schmid, A. Janotti, M. Kaltak, C. G. Van de Walle, G. Kresse and U. Diebold, *Physical Review Letters*, 2014, **113**, 086402.
16. M. Setvin, B. Daniel, U. Aschauer, W. Hou, Y. F. Li, M. Schmid, A. Selloni and U. Diebold, *Physical Chemistry Chemical Physics*, 2014, **16**, 21524-21530.
17. M. Setvin, M. Buchholz, W. Y. Hou, C. Zhang, B. Stoger, J. Hulva, T. Simschitz, X. Shi, J. Pavelec, G. S. Parkinson, M. C. Xu, Y. M. Wang, M. Schmid, C. Woll, A. Selloni and U. Diebold, *Journal of Physical Chemistry C*, 2015, **119**, 21044-21052.
18. M. Setvin, M. Schmid and U. Diebold, *Physical Review B*, 2015, **91**, 195403.
19. M. Setvin, U. Aschauer, J. Hulva, T. Simschitz, B. Daniel, M. Schmid, A. Selloni and U. Diebold, *Journal of the American Chemical Society*, 2016, **138**, 9565-9571.
20. M. Setvin, B. Daniel, V. Mansfeldova, L. Kavan, P. Scheiber, M. Fidler, M. Schmid and U. Diebold, *Surface Science*, 2014, **626**, 61-67.
21. J. P. W. Treacy, H. Hussain, X. Torrelles, D. C. Grinter, G. Cabailh, O. Bikondoa, C. Nicklin, S. Selcuk, A. Selloni, R. Lindsay and G. Thornton, *Physical Review B*, 2017, **95**, 075416.
22. I. M. Nadeem, G. T. Harrison, A. Wilson, C. L. Pang, J. Zegenhagen and G. Thornton, *Journal of Physical Chemistry B*, 2018, **122**, 834–839.
23. D. T. Payne, Y. Zhang, C. L. Pang, H. H. Fielding and G. Thornton, *Topics in Catalysis*, 2017, **60**, 392-400.
24. G. S. Herman, Z. Dohnalek, N. Ruzycki and U. Diebold, *Journal of Physical Chemistry B*, 2003, **107**, 2788-2795.
25. A. Dahal and Z. Dohnalek, *Journal of Physical Chemistry C*, 2017, **121**, 20413-20418.
26. C. Dette, M. A. Perez-Osorio, S. Mange, F. Giustino, S. J. Jung and K. Kern, *Journal of Physical Chemistry C*, 2018, **122**, 11954-11960.

27. A. Schaefer, V. Lanzilotto, U. Cappel, P. Uvdal, A. Borg and A. Sandell, *Surface Science*, 2018, **674**, 25-31.
28. Z. H. Geng, X. Chen, W. S. Yang, Q. Guo, C. B. Xu, D. X. Dai and X. M. Yang, *Journal of Physical Chemistry C*, 2016, **120**, 26807-26813.
29. A. Tilocca and A. Selloni, *Journal of Chemical Physics*, 2003, **119**, 7445-7450.
30. A. Tilocca and A. Selloni, *Journal of Physical Chemistry B*, 2004, **108**, 4743-4751.
31. S. Selcuk and A. Selloni, *Nature Materials*, 2016, **15**, 1107-1113.
32. Z. Futera and N. J. English, *Journal of Physical Chemistry C*, 2017, **121**, 6701-6711.
33. C. Nicklin, T. Arnold, J. Rawle and A. Warne, *Journal of Synchrotron Radiation*, 2016, **23**, 1245-1253.
34. A. Verdaguer, G. M. Sacha, H. Bluhm and M. Salmeron, *Chemical Reviews*, 2006, **106**, 1478-1510.
35. G. Ketteler, S. Yamamoto, H. Bluhm, K. Andersson, D. E. Starr, D. F. Ogletree, H. Ogasawara, A. Nilsson and M. Salmeron, *Journal of Physical Chemistry C*, 2007, **111**, 8278-8282.
36. X. Deng, T. Herranz, C. Weis, H. Bluhm and M. Salmeron, *Journal of Physical Chemistry C*, 2008, **112**, 9668-9672.
37. A. Verdaguer, C. Weis, G. Oncins, G. Ketteler, H. Bluhm and M. Salmeron, *Langmuir*, 2007, **23**, 9699-9703.
38. X. Torrelles and J. Rius, *Journal of Applied Crystallography*, 2004, **37**, 395-398.
39. E. Vlieg, *Journal of Applied Crystallography*, 2000, **33**, 401-405.
40. R. Feidenhansl, *Surface Science Reports*, 1989, **10**, 105-188.
41. I. K. Robinson and D. J. Tweet, *Reports on Progress in Physics*, 1992, **55**, 599-651.
42. J. Treacy, PhD Thesis, University of Manchester, 2015.
43. I. M. Nadeem, J. P. W. Treacy, S. Selcuk, X. Torrelles, H. Hussain, A. Wilson, D. C. Grinter, G. Cabailh, O. Bikondoa, C. Nicklin, A. Selloni, J. Zegenhagen, R. Lindsay and G. Thornton, *Journal of Physical Chemistry Letters*, 2018, **9**, 3131-3136.
44. O. Stetsovych, M. Todorovic, T. K. Shimizu, C. Moreno, J. W. Ryan, C. P. Leon, K. Sagisaka, E. Palomares, V. Matolin, D. Fujita, R. Perez and O. Custance, *Nature Communications*, 2015, **6**, 7265.
45. C. L. Pang, O. Bikondoa, D. S. Humphrey, A. C. Papageorgiou, G. Cabailh, R. Ithnin, Q. Chen, C. A. Muryn, H. Onishi and G. Thornton, *Nanotechnology*, 2006, **17**, 5397-5405.
46. P. Scheiber, M. Fidler, O. Dulub, M. Schmid, U. Diebold, W. Y. Hou, U. Aschauer and A. Selloni, *Physical Review Letters*, 2012, **109**, 136103.
47. M. Setvin, C. Franchini, X. F. Hao, M. Schmid, A. Janotti, M. Kaltak, C. G. Van de Walle, G. Kresse and U. Diebold, *Physical Review Letters*, 2014, **113**, 086402.
48. S. Wendt, J. Matthiesen, R. Schaub, E. K. Vestergaard, E. Laegsgaard, F. Besenbacher and B. Hammer, *Physical Review Letters*, 2006, **96**, 066107.
49. Z. Zhang, O. Bondarchuk, B. D. Kay, J. M. White and Z. Dohnalek, *Journal of Physical Chemistry B*, 2006, **110**, 21840-21845.
50. O. Bikondoa, C. L. Pang, R. Ithnin, C. A. Muryn, H. Onishi and G. Thornton, *Nature Materials*, 2006, **5**, 189-192.
51. I. M. Brookes, C. A. Muryn and G. Thornton, *Physical Review Letters*, 2001, **87**.
52. H. Hussain, G. Tocci, T. Woolcot, X. Torrelles, C. L. Pang, D. S. Humphrey, C. M. Yim, D. C. Grinter, G. Cabailh, O. Bikondoa, R. Lindsay, J. Zegenhagen, A. Michaelides and G. Thornton, *Nature Materials*, 2017, **16**, 461-467.
53. G. Cabailh, X. Torrelles, R. Lindsay, O. Bikondoa, I. Joumard, J. Zegenhagen and G. Thornton, *Physical Review B*, 2007, **75**, 241403.
54. U. Magdans, H. Gies, X. Torrelles and J. Rius, *European Journal of Mineralogy*, 2006, **18**, 83-91.
55. U. J. Aschauer, A. Tilocca and A. Selloni, *International Journal of Quantum Chemistry*, 2015, **115**, 1250-1257.
56. C. E. Patrick and F. Giustino, *Physical Review Applied*, 2014, **2**, 014001.

57. Z. Y. Zhao, Z. S. Li and Z. G. Zou, *Journal of Physical Chemistry C*, 2012, **116**, 7430-7441.
58. U. Aschauer, Y. B. He, H. Z. Cheng, S. C. Li, U. Diebold and A. Selloni, *Journal of Physical Chemistry C*, 2010, **114**, 1278-1284.
59. A. Vittadini, A. Selloni, F. P. Rotzinger and M. Gratzel, *Physical Review Letters*, 1998, **81**, 2954-2957.
60. M. Sumita, C. P. Hu and Y. Tateyama, *Journal of Physical Chemistry C*, 2010, **114**, 18529-18537.
61. X. Q. Gong and A. Selloni, *Journal of Catalysis*, 2007, **249**, 134-139.
62. Z. Y. Zhao, Z. S. Li and Z. G. Zou, *Physics Letters A*, 2011, **375**, 2939-2945.
63. N. Kharche, M. S. Hybertsen and J. T. Muckerman, *Physical Chemistry Chemical Physics*, 2014, **16**, 12057-12066.
64. H. H. Kristoffersen, J. E. Shea and H. Metiu, *Journal of Physical Chemistry Letters*, 2015, **6**, 2277-2281.
65. M. Z. Ertem, N. Kharche, V. S. Batista, M. S. Hybertsen, J. C. Tully and J. T. Muckerman, *Acs Catalysis*, 2015, **5**, 2317-2323.
66. N. Kharche, J. T. Muckerman and M. S. Hybertsen, *Physical Review Letters*, 2014, **113**, 176802.
67. E. Bjornehohn, M. H. Hansen, A. Hodgson, L. M. Liu, D. T. Limmer, A. Michaelides, P. Pedevilla, J. Rossmeisl, H. Shen, G. Tocci, E. Tyrode, M. M. Walz, J. Werner and H. Bluhm, *Chemical Reviews*, 2016, **116**, 7698-7726.

Chapter 5

Interfaces of Rutile TiO_2 (110) with Electrolyte Solutions

5.1 Introduction

5.1.1 Aims and Objectives

Surface science of rutile single crystals forms the majority of research presented on TiO_2 surfaces.[1] In particular, rutile TiO_2 (110) (R_{110}) has been widely investigated due to the abundance of high quality single crystals available.[2] The (110) face is the most common and stable face of rutile which has led to this surface being extensively explored at various temperatures and pressures.[1] In particular, the surface structure of R_{110} has been probed extensively with liquids - in particular $H_2O_{(l)}$[3, 4] and carboxylic acids[5, 6].

Semi-conductor electrodes have been widely utilised in electrochemical cells[7, 8] where the electrochemical set up naturally favours the use of oxide based electrodes due to their stability against oxidation. The ground breaking research of Honda and Fujishima first demonstrated the electrochemical capabilities of TiO_2.[9] A recent issue of the journal *Surface Science* has been devoted to electrochemical surface science - *Surface Science and Electrochemistry - 20 Years Later*[10] - indicating the ever increasing importance of this subject. However, there is limited research presented on the surface and interface studies of TiO_2 and electrolyte solutions for purposes of instigating research into electrochemical surface and interfacial science.[4]

In this chapter an *in situ* scanning tunnelling microscopy (STM) (see Section 5.3.1) and *in situ* surface X-ray diffraction (SXRD) (see Section 5.3.2) investigations of R_{110} and its interface with aqueous sodium hydroxide (NaOH) and hydrochloric acid (HCl) are presented. Additionally, preliminary findings of the electrochemical interface of R_{110} under aqueous NaOH is also presented (see Section 5.3.3). We aim to present an understanding of alkali metal (in this case Na) and halogen (in this case Cl) adsorption at

the aqueous interface of R_{110}. Elucidating the adsorption site of these elements is of crucial importance towards understanding electrolysis mechanisms at the electrochemical interface of TiO_2. We hope that this work will encourage further research into the nano-scale interface of TiO_2 with electrolyte solutions and promote future electrochemical surface and interface research on TiO_2.

5.1.2 Structure of Rutile TiO_2 (110)

The rutile TiO_2 (110) surface consists of 5 (Ti_{5c}) and 6 (Ti_{6c}) co-ordinate Ti atoms and 2 (O_{2c}) and 3 (O_{3c}) co-ordinate O atoms - see Figure 5.1.[1, 2, 11] In principle, the surface forms two types of OH groups: bridging OH groups (OH_{br}) and terminal OH groups (OH_t). OH_t groups exist as Ti_{5c}-OH species whereas a OH_{br} group is an H adatom attached to an O_{2c}.

5.1.3 The Literature: Rutile TiO_2 (110) and Liquid Water Interface

R_{110} has been extensively investigated from ultra-high vacuum (UHV) to near-ambient pressure (NAP) conditions, however, its interface with liquids is less well documented.[1-6, 11] In UHV, R_{110} has been exposed to a wide variety of elements to better elucidate the respective interfaces.[1, 2, 11] Systematically, R_{110} has been exposed to $H_2O_{(g)}$ ranging from UHV to NAP.[1] In UHV, above 170 K, surface oxygen vacancies (V_o) have been explained to be 'water splitting' sites where an H_2O species dissociates to create a pair of OH_{br} species that are mobile at room temperature.[1, 2, 12] These species are stable on the surface upto 500 K at which point they desorb as H_2O leaving a V_o on the surface.[1, 2] The adsorption of H_2O and OH_t on R_{110} occurs exclusively at the Ti_{5c} site. [1, 2] Recently, the R_{110} and $H_2O_{(l)}$ interface has been presented as a first step towards understanding the interface of R_{110} with liquids. STM studies (*in situ*[13] and *ex situ* [3, 14]) suggest that after the

R_{110} surface is exposed to $H_2O_{(l)}$, a (2 × 1) overlayer is formed above a (1 × 1) surface termination. Theory predicts that this overlayer consists of H_2O molecules where the O forms a bond with a surface Ti_{5c} atom[13] or that this overlayer consists of OH_t species[3]. Alternatively, *ex situ* photoelectron spectroscopy (PES) measurements indicate that the overlayer consists of OH_t groups.[3] *in situ* SXRD measurements[4] of the R_{110} and $H_2O_{(l)}$ interface suggest that the surface maintains its (1 × 1) surface termination but does not maintain a (2 × 1) overlayer. This is in contradiction to the aforementioned STM work and may arise due to this surface undergoing non-UHV preparation without robust surface characterisation prior to measurements whereas the aforementioned STM and PES work investigates UHV prepared R_{110}. More recent SXRD measurements[3] (*in situ* and *ex situ*) have shown UHV prepared R_{110} to maintain a (2 × 1) overlayer which are claimed to be OH_t species where the *in situ* measurements present evidence of H_2O hydrogen bonded to the O_{2c}. Another recent SXRD study[15] indicates that the surface should only maintain a uniform coverage of associatively adsorbed H_2O when the substrate has undergone non-UHV preparation, although with AFM, LEED and AES characterisation so as to confirm high surface cleanliness and quality. Similarly, a separate SXRD study[16] also suggests a uniform coverage of adsorbed H_2O species at the Ti_{5c} site of wet chemically prepared R_{110}. Although, the interface of R_{110} with liquid water has received limited attention, numerous groups have attempted to better understand this interface structure. However, investigations of the R_{110} interface with electrolyte solutions are thus far largely lacking.[4, 17]

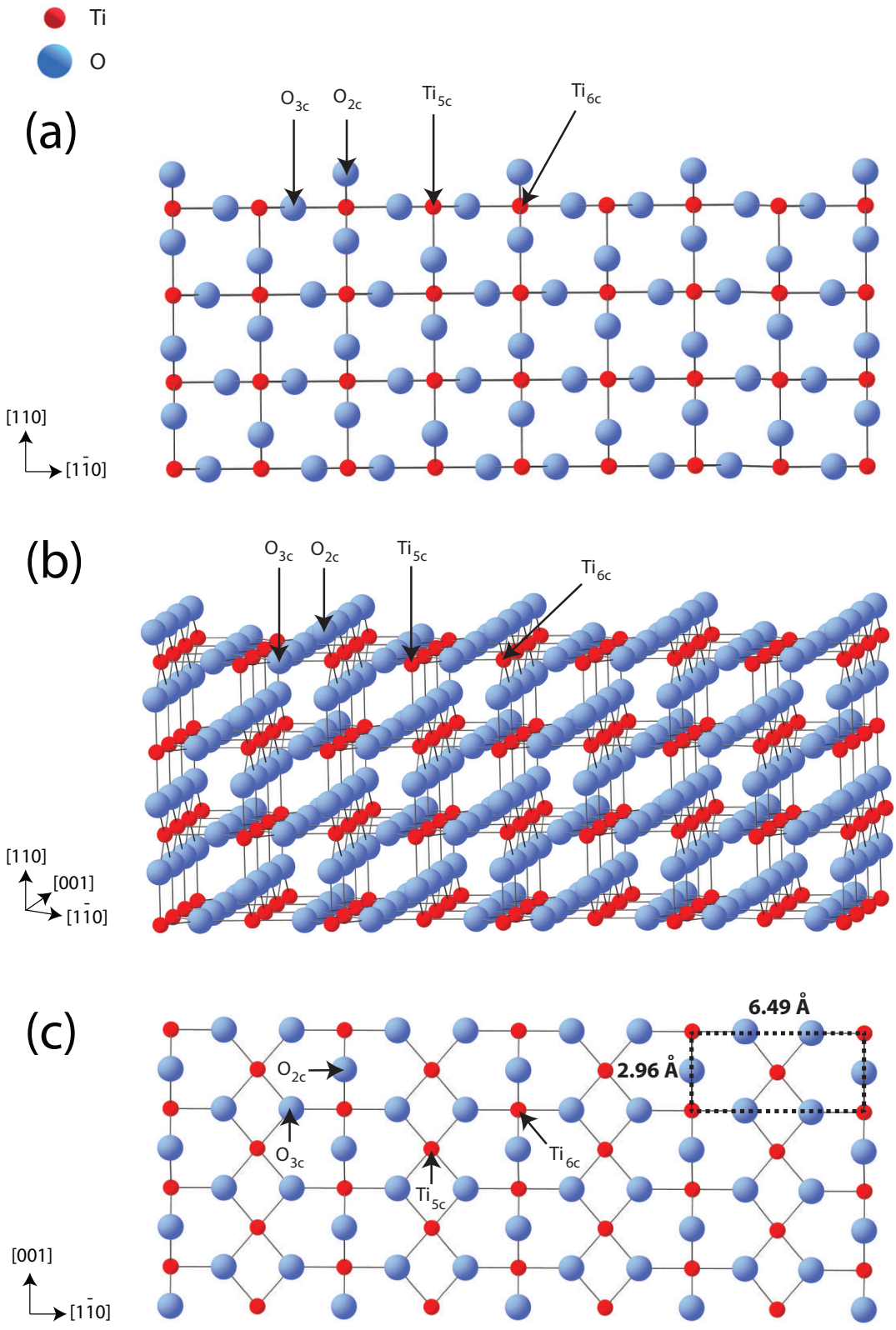

Figure 5.1: Ball and stick illustration depicting the R_{110} surface via different view-points with surface atoms Ti_{6c}, Ti_{5c}, O_{3c} and O_{2c} labelled. (a) Side view of surface. (b) Tilted view of surface with respect to (a). (c) Aerial view of surface with surface unit cell in black dashed box.

5.2 Experimental Procedure

Substrate preparation for the liquid cell STM measurements was performed on an *Omicron* AFM/STM instrument (see Figure 3.2) with a base pressure of 1×10^{-10} mbar. R_{110} single crystals (purchased from *Pi Kem*) were mounted onto a Ta plate with Ta strips. The sample was prepared in UHV with cycles of Ar^+ sputtering ($P_{AR} = 5 \times 10^{-5}$ mbar, 1kV, 10 μA cm^{-2}, 10 minutes) and annealing (T < 1023 K, 10 minutes). At room temperature, the prepared surface was characterised with STM, low energy electron diffraction (LEED) and Auger electron spectroscopy (AES) to ensure an ordered and contaminant free surface for the *in situ* liquid cell STM measurements. After UHV preparation and characterisation, the samples were transferred to a peripheral UHV chamber and vented to N_2. Subsequently, under a flow of N_2, the sample was unmounted from the Ta plate and transferred to a beaker containing the experiment specific electrolyte solution. Next, the sample was transferred to an *Agilent 5500 SPM* liquid cell STM (see Figure 3.4) that was then filled with the aqueous solution. The liquid cell STM images presented have been collected under constant current conditions with a negative sample bias voltage in the range of -0.1 to -0.6 V i.e. filled states imaging. Electrochemical STM measurements were performed on a *Pico-Scan* electrochemical STM set-up (see Figure 3.4) in constant current mode with negative tip bias voltages with respect to the sample. Commercial, wax coated 0.25 mm diameter, Pt/Ir STM tips with 10 pA maximum leakage current (Keysight Technologies) were used for the liquid cell and electrochemical STM measurements. The aqueous solutions (0.1 M NaOH and 0.1 M HCl) were prepared by dissolving NaOH pellets (*Fischer Scientific*) and diluting aqueous HCl (*Sigma Aldrich*) in ultra-pure water (18 MΩ cm).

SXRD measurements were performed at room temperature on Diamond Light Source Beamline I07: Surface and Interface Diffraction[18] (see Section 3.5.2). Experimental Hutch 1 (EH 1) was employed with data acquisition performed using a (2 + 3) diffractometer and a PILATUS 100K area pixel detector. Substrate preparation was performed on an *Omicron* VT STM instrument (see Figure 3.3) with a base pressure of 1 $\times 10^{-10}$ mbar. R_{110} single crystals (purchased from *Matek*) were mounted onto a Ta plate with Ta strips. The sample was prepared in UHV with cycles of Ar^+ sputtering (P_{AR} = 6 $\times 10^{-6}$ mbar, 1kV, 2 $\mu A\ cm^{-2}$, 10 minutes) and annealing (T < 1023 K, 10 minutes) and characterised with STM, LEED and X-ray photo-electron spectroscopy (XPS) to ensure an ordered and contaminant free surface for the SXRD measurements. After UHV preparation and characterisation, the samples were transferred, in UHV, to a baby chamber with a base pressure of 1 $\times 10^{-9}$ mbar. The baby chamber was subsequently mounted onto the diffractometer in EH 1. SXRD measurements of the R_{110} / electrolyte interface were performed by venting the baby chamber to N_2 and using a droplet cell (see Section 3.5.3) to form an electrolyte droplet on the surface. In these conditions, 15 CTRs (2465 structure factors) were collected for the R_{110}/0.1 M NaOH interface and 9 CTRs (1956 structure factors) were collected for the R_{110}/0.1 M HCl interface. SXRD data were acquired in stationary scanning mode[19] at an incident photon energy of 17.7 keV (R_{110} / 0.1 M NaOH measurements) or 23 keV (R_{110} / 0.1 M HCl measurements) at an incidence angle of 1^o. The goodness of fit of the SXRD model is given via the normalized χ^2 (χ^2_n).[20-22] Reference reflections were acquired to ensure that the surface structure did not change during the course of the experiment. Due to the low scattering factor of hydrogen, it has not been incorporated into our proposed models. SXRD modelling was performed using the ROD[20] software with an orthorhombic surface cell of dimensions a = 6.497 Å, b = 2.958 Å, c = 6.497 Å and $\alpha = \gamma = \beta = 90^o$.

5.3 Results and Discussion

5.3.1 STM of the Rutile TiO_2 (110) Aqueous Interface of NaOH and HCl

STM of R_{110} has been extensively reported.[1] Typically, STM images of R_{110} depict pseudo-hexagonal terraces with the surface consisting of a series of bright and dark rows in the [001] direction (see Figure 5.2 (a)). Additionally, the surface consists of defect regions which are usually either surface oxygen vacancies (O_{vac}), OH_{br} or TiO_x clusters. Figure (5.2 (b)) provides a ball and stick model that illustrates that the bright rows observed in STM correspond to surface Ti_{5c} rows whilst the dark rows correspond to O_{2c}. On UHV as-prepared R_{110}, O_{vac} are stable on the surface however these defects are typically quenched by residual H_2O in UHV to form OH_{br} species.

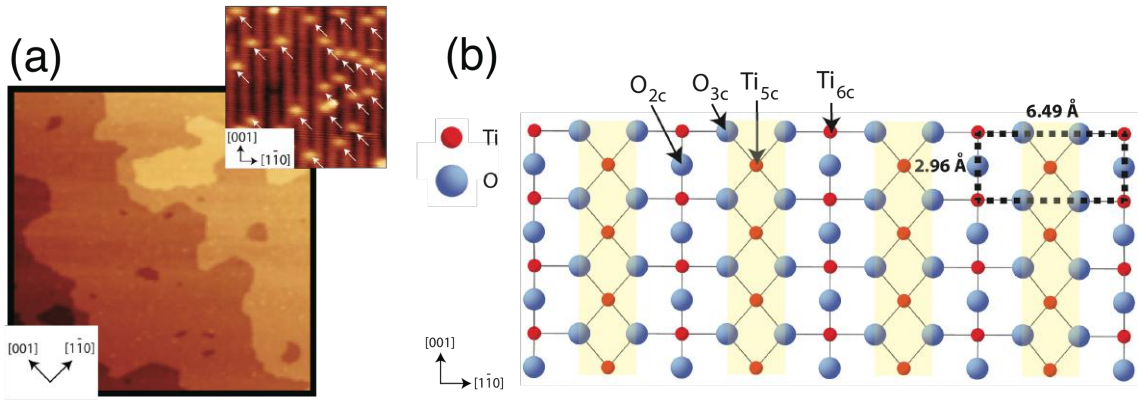

Figure 5.2: As-prepared R_{110}. (a) 300 × 300 nm^2 STM image of R_{110} (V_s = +1.6 V, I_t = 0.1 nA) with inset (7 × 7 nm^2 (V_s = +1.3 V I_t = 0.3 nA)) illustrating the bright and dark row features in the [001] direction observed with STM. The white arrows point to OH_{br} (defect) sites. (b) Ball and stick model of an aerial view of the R_{110} surface where the light yellow rows represent the bright rows seen in STM. The bright rows correspond to Ti_{5c} whereas the darks rows represent O_{2c}.

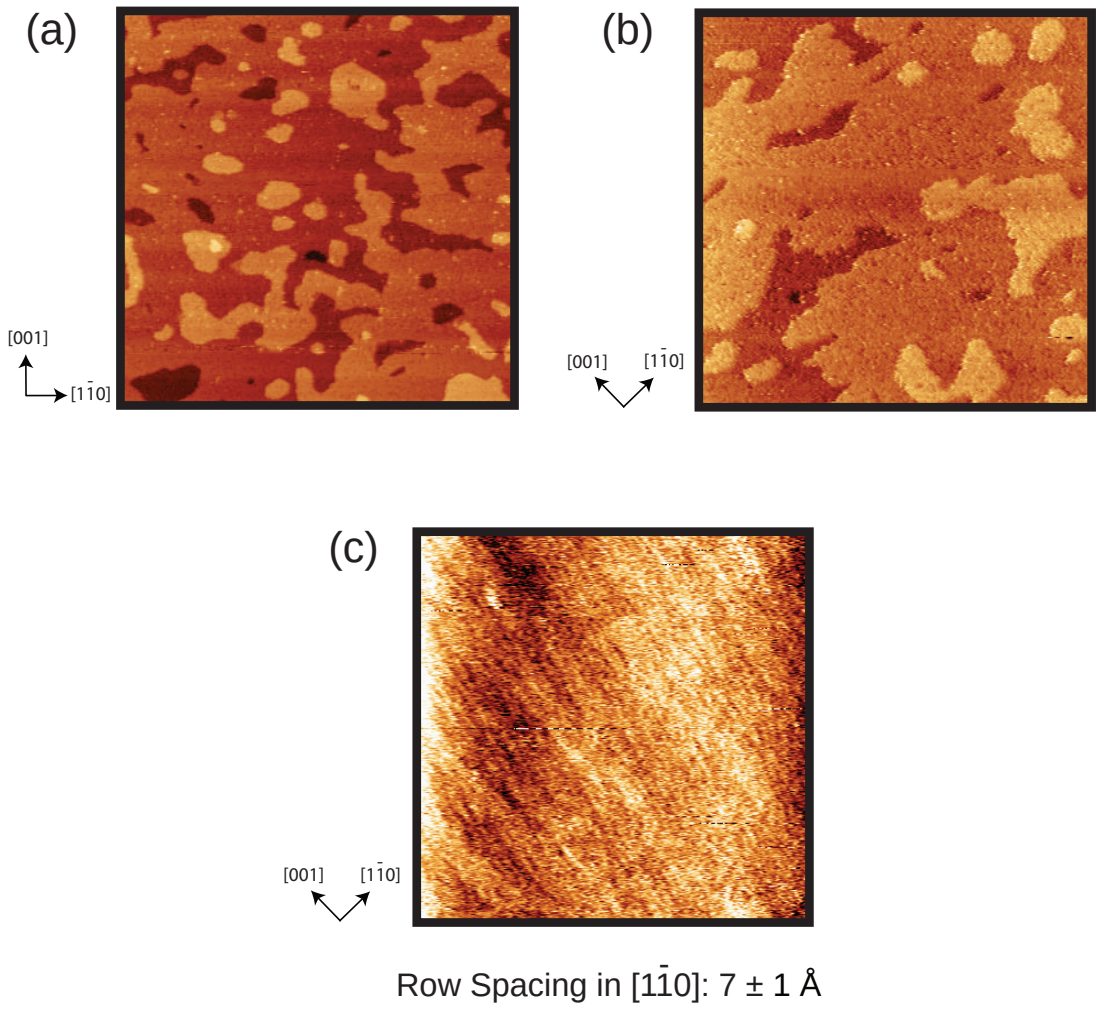

Figure 5.3: (a) 300 × 300 nm^2 UHV STM image of R_{110} (V_s = +1.6 V, I_t = 0.1 nA) prior to 0.1 M NaOH exposure. (b) 300 × 300 nm^2 Liquid Cell STM of R_{110} (V_s = -0.6 V, I_t = 3 nA) submerged in 0.1 M NaOH. (c) 25 × 25 nm^2 Liquid Cell STM of R_{110} (V_s = -0.6 V, I_t = 3 nA) submerged in 0.1 M NaOH.

Figures 5.3 and 5.4 present *in situ* STM images of R_{110} exposed to 0.1 M NaOH (pH 13) and 0.1 M HCl (pH 1), respectively. Figure 5.3 (a), shows a terrace resolution STM image obtained of the as prepared R_{110} in UHV prior to 0.1 M NaOH exposure. Figure 5.3 (b) shows an *in situ* terrace resolution STM image of the R_{110}/0.1 M NaOH interface. As is evidenced from the images, the surface under 0.1 M NaOH has maintained its terrace shape indicating that the large (terrace) scale integrity of the surface is maintained under 0.1 M NaOH.

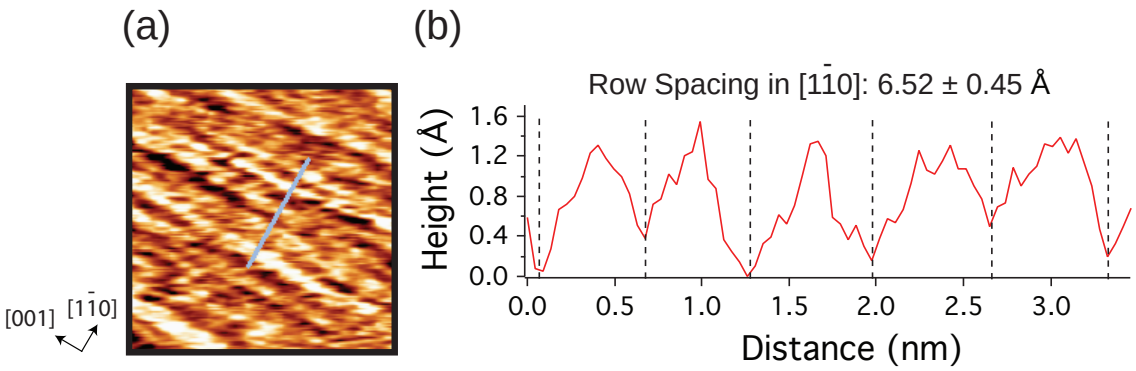

Figure 5.4: (a) 7.5 × 7.5 nm^2 Liquid Cell STM image of R_{110} (V_s = -0.6 V, I_t = 1.5 nA) submerged in 0.1 M HCl. (b) Line profile highlighting the row spacing in the [001] direction.

Figure 5.3 (c) shows a 'row-resolution' STM image obtained of R_{110} under 0.1 M NaOH. The surface maintains order with a row spacing of 7 ±1 Å in the [1$\bar{1}$0] direction. Figure 5.4 (a) shows a 'row resolution' STM image obtained of the surface under 0.1 M HCl with a row spacing of 6.52 ±0.45 Å (see Figure 5.4 (b)) in the [1$\bar{1}$0] direction. The R_{110} surface cell has dimensions of 6.49 Å in the [1$\bar{1}$0] direction - as is widely reported with UHV STM.[11] More recently, *in situ* AP STM of the R_{110} / $H_2O_{(l)}$ interface has reported a row-spacing of 7.0 ±0.5 Å, indicating that the surface maintains a similar row-spacing in the [1$\bar{1}$0] direction as is observed in UHV STM.[13] In our *in situ* STM of R_{110} under 0.1 M NaOH and 0. 1 M HCl, we observe a row spacing of 7 ±1 Å and 6.52 ±0.45 Å in the [1$\bar{1}$0] direction which is in good agreement with the surface cell dimensions of R_{110}.

In an attempt to ensure that the structure observed in Figure 5.3 and 5.4 are not an artefact, the scan angle was changed by 90°. This caused a corresponding rotation in the surface order by 90°, indicating that the observed surface order is associated with the R_{110}/electrolyte interface structure. In this study, we were able to obtain terrace and/or

row resolution images of the surface in contact with 0.1 M NaOH or 0.1 M HCl over a period of 36 hours with no evidence of severe surface dissolution or degradation.

In summary, this section provides the first *in situ* STM images taken of R_{110} exposed to electrolyte solutions. The obtained STM images indicate that the substrate maintains its periodicity. Although UHV STM of TiO_2 is widely reported, STM of TiO_2 in ambient conditions (in-particular the solid/liquid interface) are largely lacking. In the next section (Section 4.3.2), we present an *in situ* SXRD investigation of the R_{110} interface with 0.1 M NaOH and 0.1 M HCl. This will ultimately provide a quantitative structural analysis of the preferred surface adsorption sites and behaviour of surface atoms.

5.3.2 SXRD of the Rutile TiO_2 (110) Aqueous Interfaces with NaOH and HCl

In light of the liquid cell STM measurements presented in section 4.3.1, this section looks to provide an SXRD perspective of the R_{110}/0.1 M NaOH and R_{110}/0.1 M HCl interfaces. The labelling of the surface titanium and oxygen atoms used throughout this section is given in Figure 5.5. Table 5.1 presents the surface atomic displacements of as-prepared R_{110}. The atomic displacements for an as-prepared surface prior to electrolyte exposure are largely identical to that observed previously.[3, 23] Surface atoms displace away from the bulk, a phenomenon that has been previously observed on R_{110}[3, 23] and other TiO_2 surfaces such as anatase TiO_2 (101) (A_{101})[24] - see Table 4.3.

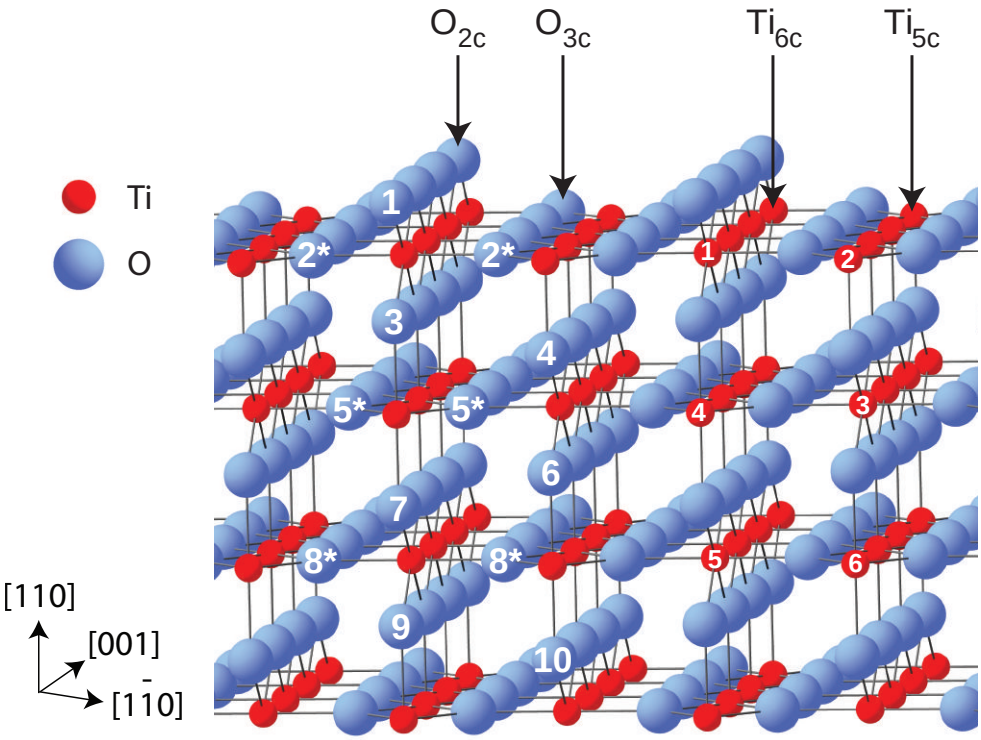

Figure 5.5: Ball and stick model of R_{110} (1 × 1). The numerical labelling of the atoms serves as identification for the atomic displacements shown in Table 5.1. The indicated azimuth defines the x, y and z directions along which the atomic co-ordinates are defined as positive. Symmetry paired atoms are denoted with a *.

Atom Label	Displacements (Å)			
	R_{110} / UHV (As-Prepared)		R_{110} / Liquid Interface	
	Δ [110] [Nadeem : Cabailh[23] : Hussain[3]]	Δ [1$\bar{1}$0] [Nadeem : Cabailh[23] : Hussain[3]]	Δ [110] [$H_2O_{(l)}$[3] : 0.1 M NaOH : 0.1 M HCl]	Δ [1$\bar{1}$0] [$H_2O_{(l)}$[3] : 0.1 M NaOH : 0.1 M HCl]
O - 1	0.10 ± 0.01 : 0.10 ±0.04 : 0.10 ± 0.04	-	0.08 ± 0.04 : 0.09 ± 0.01 : -0.08 ± 0.02	-
O - 2*	0.13 ± 0.01 : 0.17 ±0.03 : 0.13 ± 0.03	0.03 ± 0.00 : 0.01 ± 0.05 : 0.02 ± 0.04	0.08 ± 0.03 : 0.13 ± 0.01 : 0.05 ± 0.01	0.01 ± 0.05 : 0.12 ± 0.01 : -0.13 ± 0.03
Ti - 1	0.20 ± 0.01 : 0.25 ±0.01 : 0.17 ± 0.01	-	0.09 ± 0.01 : 0.08 ± 0.01 : 0.07 ± 0.01	-
Ti - 2	-0.11 ± 0.01 : -0.11 ±0.01 : -0.06 ± 0.01	-	0.03 ± 0.01 : 0.08 ± 0.01 : -0.01 ± 0.01	-
O - 3	0.08 ± 0.01 : 0.07 ±0.04 : 0.07 ± 0.04	-	0.07 ± 0.03 : 0.12 ± 0.01 : -0.08 ± 0.02	-
O - 4	0.04 ± 0.01 : 0.00 ±0.03 : 0.02 ± 0.03	-	0.05 ± 0.05 : 0.04 ± 0.01 : -0.06 ± 0.02	-
O - 5*	0.07 ± 0.01 : 0.04 ±0.03 : 0.03 ± 0.03	0.02 ± 0.00 : 0.05 ± 0.05 : 0.02 ± 0.03	0.06 ± 0.03 : 0.08 ± 0.01 : -0.10 ± 0.01	0.05 ± 0.05 : 0.05 ± 0.01 : 0.10 ± 0.02
Ti - 3	-0.01 ± 0.01 : -0.08 ±0.01 : -0.02 ± 0.01	-	0.06 ± 0.01 :0.07 ± 0.01 : 0.07 ± 0.01	-
Ti - 4	0.10 ± 0.01 : 0.19 ±0.01: 0.12 ± 0.01	-	0.04 ± 0.01 : 0.04 ± 0.01 : 0.02 ± 0.01	-
O - 6	0.06 ± 0.01 : 0.01 ±0.04 : 0.04 ± 0.04	-	0.08 ± 0.05 : 0.01 ± 0.01 : 0.13 ± 0.02	-
O - 7	0.01 ± 0.01 : 0.01 ±0.04 : 0.01 ± 0.04	-	0.06 ± 0.05 : 0.00 ± 0.01 : -0.01 ± 0.02	-
O - 8*	0.03 ± 0.01 : 0.01 ±0.03 : 0.01 ± 0.05	-0.02 ± 0.00 : -0.03 ± 0.05 : -0.02 ± 0.05	0.05 ± 0.03 : 0.04 ± 0.01 : -0.05 ± 0.01	-0.03 ± 0.02 : -0.05 ± 0.01 : -0.06 ± 0.02
Ti - 5	0.07 ± 0.01 : 0.08 ±0.01 : 0.05 ± 0.01	-	-0.04 ± 0.01 : 0.06 ± 0.01 : -0.01 ± 0.01	-
Ti - 6	0.00 ± 0.01 : -0.04 ±0.01 : -0.02 ± 0.01	-	0.08 ± 0.01 : 0.06 ± 0.01 : 0.07 ± 0.01	-
O - 9	0.05 ± 0.01 : 0.02 ±0.04 : 0.03 ± 0.03	-	0.04 ± 0.04 : 0.02 ± 0.01 : -0.06 ± 0.02	-
O - 10	-0.01 ± 0.01 : -0.02 ±0.04 : -0.01 ± 0.03	-	0.03 ± 0.03 : -0.01 ± 0.01 : -0.02 ± 0.02	-

Table 5.1: Surface atomic displacements away from the bulk terminated structure of R_{110} obtained via SXRD for an as-prepared surface and its interface with 0.1 M NaOH and 0.1 M HCl. Positive or negative displacements indicate those parallel or anti-parallel to the directions of the coordinate axis defined in Figure 5.5.

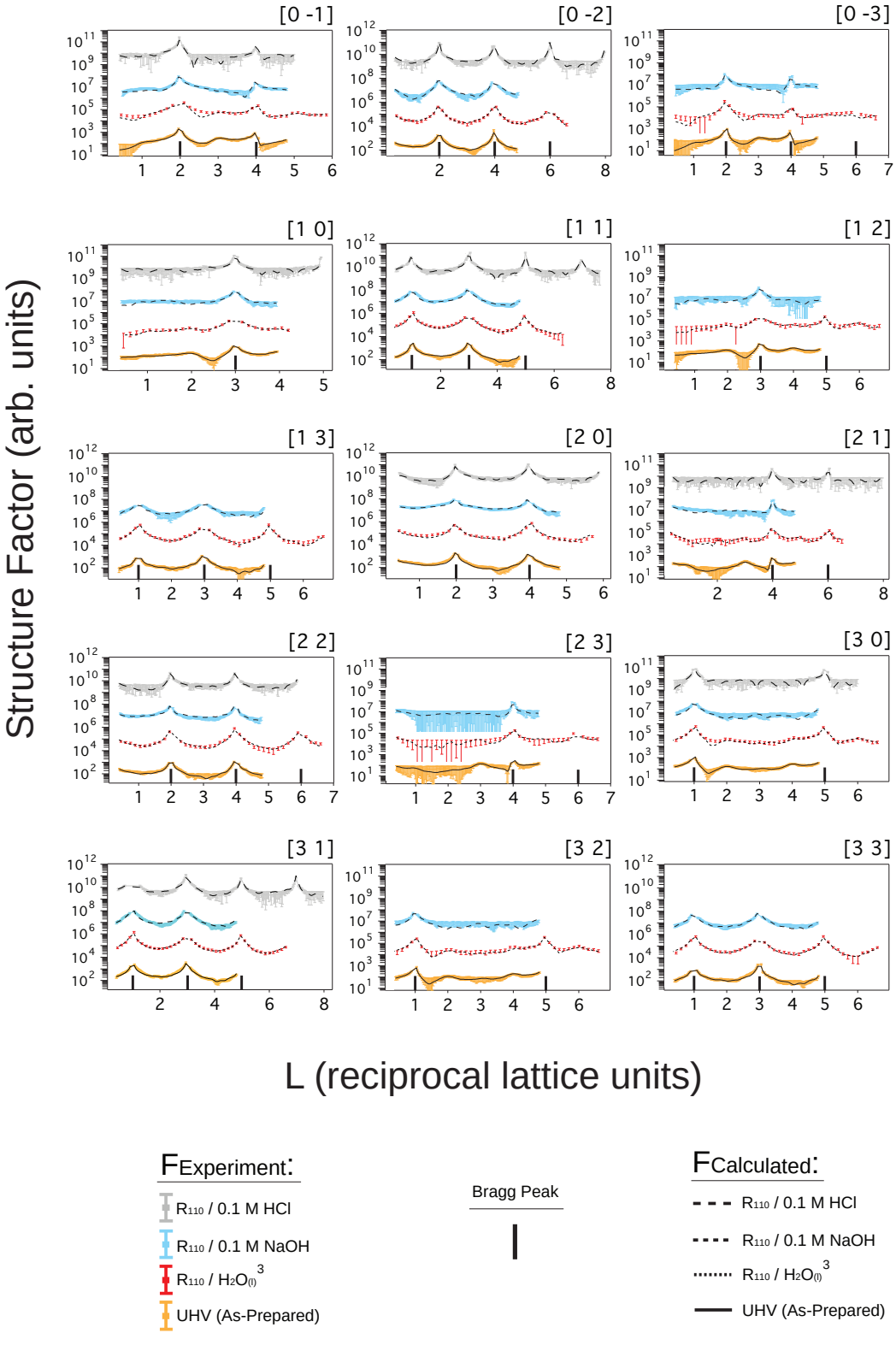

Figure 5.6: Comparison of experimental CTRs and best fit for as-prepared R_{110} in UHV (orange), and for the R_{110} interface with $H_2O_{(l)}$[3] (red),0.1 M NaOH (blue) and 0.1 M HCl (grey). CTRs are offset for clarity. $F_{Experiment}$: experimental structure factor. $F_{Calculated}$: calculated structure factor.

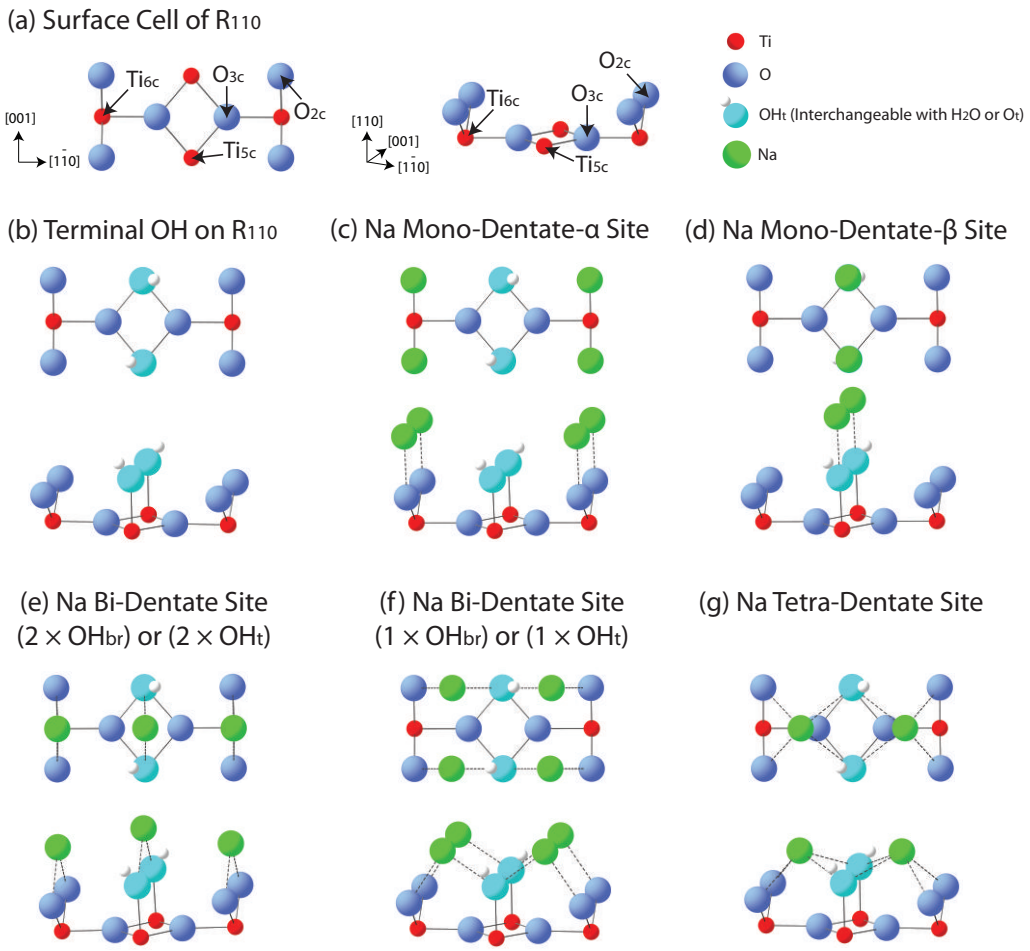

Figure 5.7: Ball and stick on top and side view models illustrating (a) the surface cell of R_{110} and (b-g) different adsorption sites for Na on R_{110}. The O species bound to Ti_{5c} is interchangeable with a one-coordinate terminal O (O_t), two-coordinate terminal OH (OH_t) or a three-coordinate H_2O species.

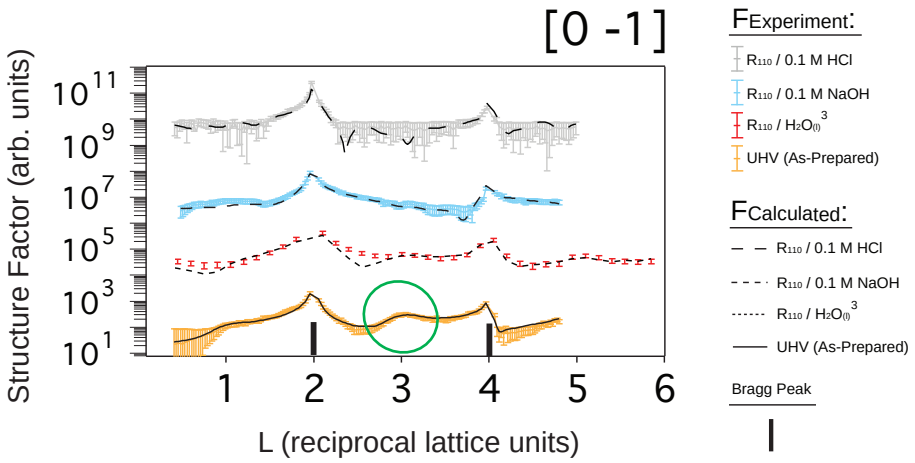

Figure 5.8: CTR [0 -1 L] from Figure 5.6 shown at a higher magnification. Green circle represents an 'anti-Bragg' modulation that is supressed upon liquid exposure.

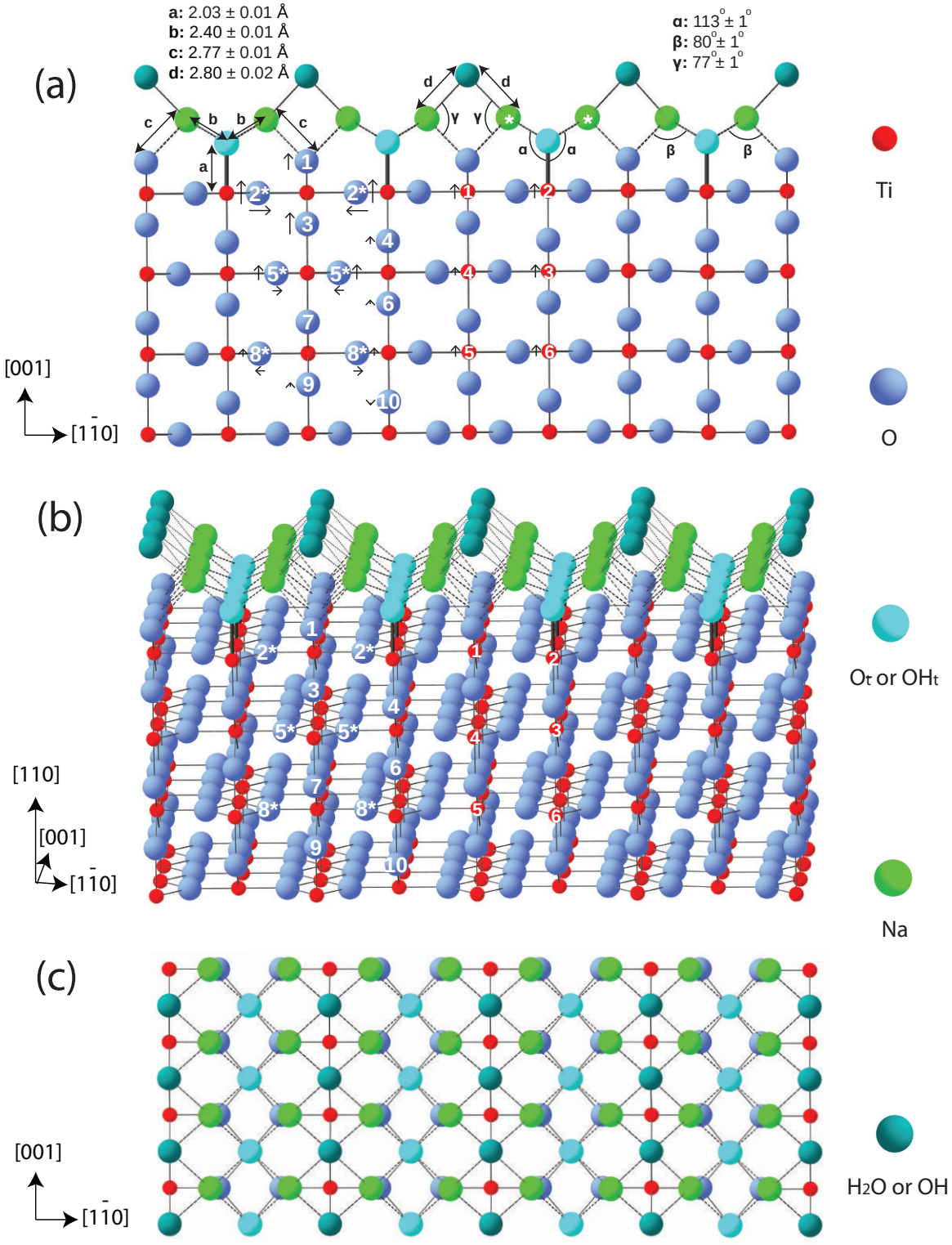

Figure 5.9: Ball and stick illustration depicting the R_{110} / 0.1 M NaOH interface structure obtained from SXRD. (a) Side view, (b) tilted view and (c) aerial view of the interface structure. The black arrows represent the relative magnitude and direction of atom displacements with respect to bulk lattice positions. Numerical labelling serves as identification for the atomic displacements shown in Table 5.1. Symmetry paired atoms are denoted with a *.

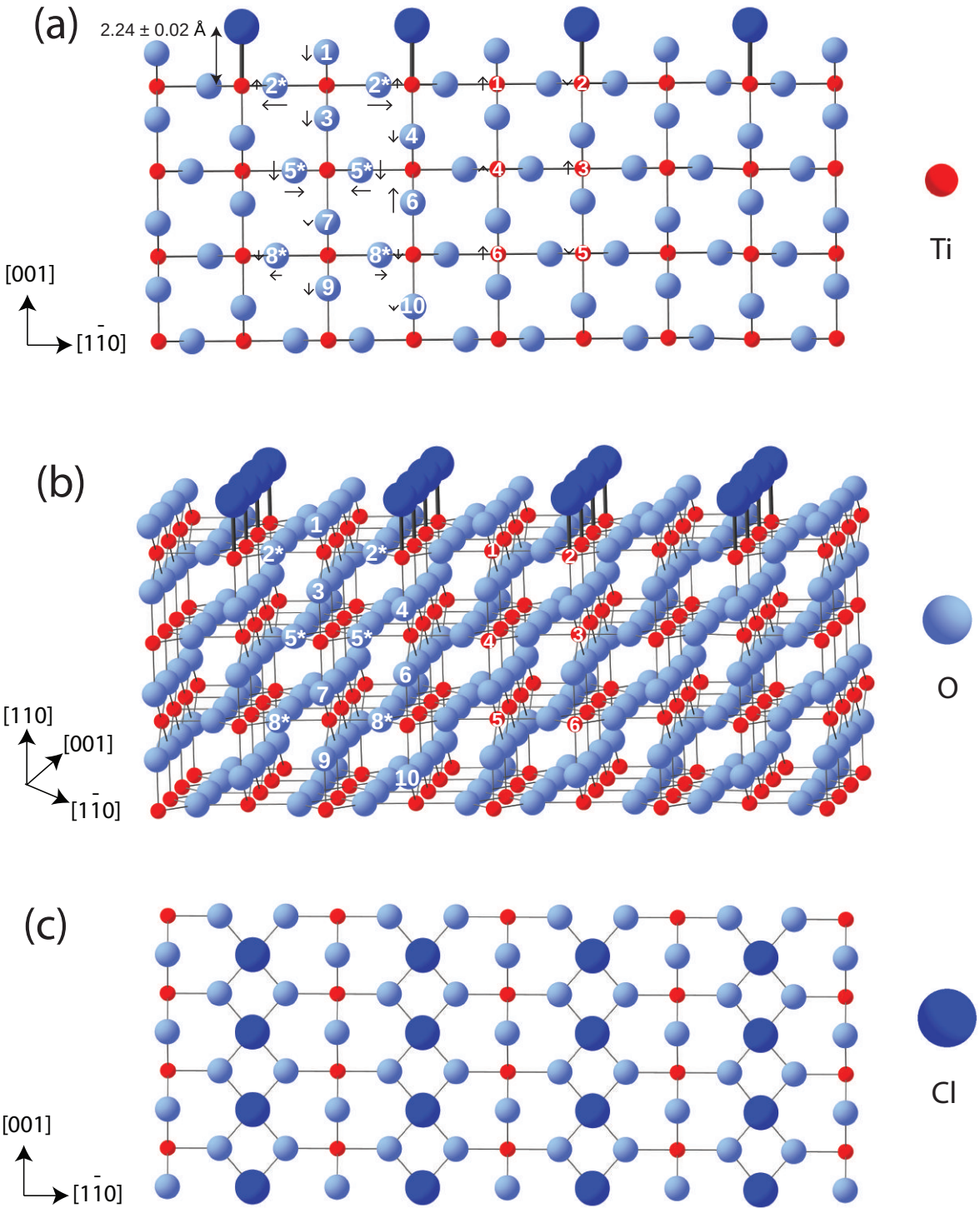

Figure 5.10: Ball and stick illustration depicting the R_{110} / 0.1 M HCl interface structure obtained from SXRD. (a) Side view, (b) tilted view and (c) aerial view of the interface structure. The black arrows represent the relative magnitude and direction of atom displacements with respect to bulk lattice positions. Numerical labelling serves as identification for the atomic displacements shown in Table 5.1. Symmetry paired atoms are denoted with a *.

CTRs and the best fits for R_{110} covered with 0.1 M NaOH or 0.1 M HCl are shown in Figure 5.6 with a χ^2_n of 1.16 and 1.06, respectively. The surface roughness has been modelled with the ß-roughness method[25] with an increase from 0.02 for the as-prepared surface to 0.17 and 0.19 for R_{110} covered with 0.1 M NaOH or 0.1 M HCl, respectively. This is due to electrolyte induced roughness at the solid/liquid interface with chemical reactions on the surface. Figure 5.7 shows that the adsorption of Na (or another alkali metal) on R_{110} can occur at several surface sites where a O species is bound to the Ti_{5c}. This terminal O species is interchangeable with a terminal O (O_t), terminal OH (OH_t) or a H_2O species. The surface atomic displacements of the best fit are given in Table 5.1. The optimized structure of the R_{110}/0.1 M NaOH interface indicates that the Na adsorbs at the tetra-dentate site (between two O_{2c} and two terminal O species bound to Ti_{5c}) with a H_2O/OH layer above the Na (see Figure 5.9). The optimized structure of the R_{110}/0.1 M HCl interface indicates Cl adsorption at the Ti_{5c} site (see Figure 5.10).

Figure 5.8 shows a zoom in of CTR [0 -1 L] which qualitatively illustrates the changes in the CTR intensity. Immediately obvious in Figure 5.8 is the suppression or loss of the circled (green) 'anti-Bragg' modulation once the as-prepared surface in UHV is exposed to a liquid. This is attributed to the surface Ti atoms adopting a more bulk-like position post liquid exposure and is also quantitatively observed in Table 5.1. Additionally, the intensity distribution comparison between R_{110}/0.1 M NaOH and R_{110}/0.1 M HCl is strikingly different especially in the L = 2 to 4 region. This suggests a significant effect of pH and/or electrolyte on the behaviour of surface atoms and surface adsorption. Lastly, Figure 5.8 shows that the CTR intensity distribution for $R_{110}/H_2O_{(l)}$ and R_{110}/0.1 M NaOH is similar with the major differences in intensity only observed at $L < 1$ and $L > 4$. This suggests that the two interfaces should exhibit some similarities which can be attributed to both systems possessing terminal O species bound to Ti_{5c}.

The best-fit SXRD model of the R_{110}/0.1 M NaOH interface suggests ordering in the contact layer with an additional adsorbed layer above this. At the contact layer, the Ti_{5c} site maintains an adsorbed O_x species (i.e. O_t, OH_t or OH_2) at a bond length of 2.03 ± 0.01 Å. The Na is adsorbed at the tetra-dentate site between two O_{2c} atoms and two O_x with an O_x-Na bond length of 2.40 ± 0.01 Å and O_{2c}-Na bond length of 2.77 ± 0.01 Å. Above the tetra-dentate Na (i.e. the second adsorbed layer) exists a layer of O_y (i.e. H_2O or OH^-) residing in a tetra-dentate site between four Na at a distance of 2.80 ± 0.01 Å. These O-Na bond lengths are in good agreement with O-Na bond lengths reported at 2.3 - 2.9 Å[26-28] (environment dependant). Alternative models with different adsorbate coverage and Na adsorbed at different surface sites was also attempted, however, this gave a relatively worse fit when compared to the optimized best-fit with a χ^2_n in excess of 1.5. Additionally, investigations[29] of alkali metal adsorption on R_{110} give evidence that the preferred adsorption site of alkali metals is at the tetra-dentate site.

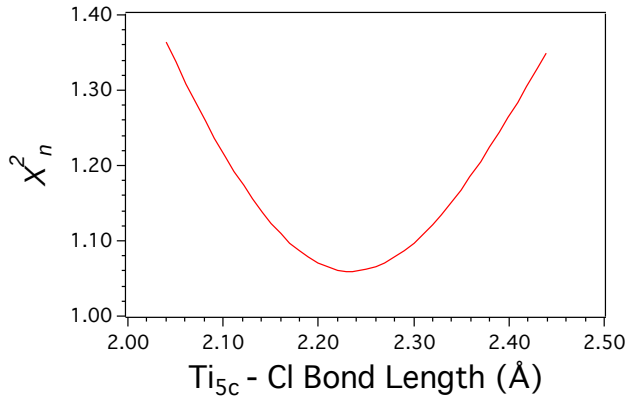

Figure 5.11: χ^2_n evolution against the Ti_{5c}-Cl bond length for R_{110}/0.1 M HCl interface.

The nature of the O species in the contact (O_x) and second (O_y) layer is difficult to ascertain from SXRD due to the small scattering strength of H. Previous experimental work on R_{110} reports the Ti_{5c}-OH bond length at 1.95 ± 0.03 Å[3] and the Ti_{5c}-OH_2 bond

length at 2.21 ± 0.02 Å[30]. Our obtained bond length for the adsorbed O_x species on the Ti_{5c} site is 2.03 ± 0.01 Å. This is in closer proximity to the bond length reported for Ti_{5c}-OH_t[3] suggesting that the existence of Ti_{5c}-OH_2 is unlikely. Additionally, Ti_{5c}-OH_2 species would presumably make the adsorption of the electro-positive Na at the tetra-dentate site relatively unfavourable when compared to an O_t or OH_t species. Hence, the adsorbed O_x species on the Ti_{5c} site is likely to be an O_t or OH_t species. The smaller O_x-Na bond length compared with O_{2c}-Na can provide some indirect evidence of the nature of the adsorbed O_x species. O_{2c} and OH_t are both two-coordinate such that the O-Na bond distance would presumably be similar. Alternatively, O_t is one-coordinate such that the O_t-Na bond length would be different to O_{2c}-Na. This would suggest that O_x is O_t (i.e. an O^-Na^+ species), however assigning O_x as O_t or OH_t is difficult to ascertain from SXRD alone as O-Na bond distances can also be affected by the local environment of the $OH_t/O_t/O_{2c}$. In the second layer, the nature of the O_y species can either be OH^- (pH 13 electrolyte solution) or H_2O. Again, due to the small scattering strength of H, the precise nature of the O_y species is difficult to assert. Theoretical calculations would be required to provide a more conclusive answer to the nature of the O_x and O_y species.

The best-fit SXRD model of the R_{110}/0.1 M HCl suggests uniform Cl adsorption on the Ti_{5c} site with a Ti_{5c}-Cl bond length of 2.24 ± 0.02 Å (see Figure 5.11 for a graph of χ^2_n against a change in Ti_{5c}-Cl bond length). This bond length is in good agreement with the calculated Ti_{5c}-Cl bond lengths on R_{110} which are reported at 2.2 Å.[31] Experimentally, Ti-Cl bond lengths are generally reported between 2.2 and 2.4 Å.[32-38] In UHV, Cl adsorption on R_{110} is suggested to occur at the Ti_{5c} site.[31, 39, 40] Alternative models including the adsorption of OH_t or OH_2 species at the Ti_{5c} site were also probed, however this gave a relatively worse fit with a χ^2_n of 1.68 and 1.39, respectively. The preference of Ti_{5c}-Cl formation can be considered in terms of the Ti_{5c}-Cl bond being stronger based on its

greater ionicity. Although Cl adsorption at surface O_{2c} vacancies (V_o) is also possible[31], this site is not available as when the baby chamber is vented to N_2 these sites will be healed by residual water dissociation. A hydration layer above the adsorbed Cl species was also probed to investigate the existence of H_2O molecule either hydrogen bonded to the O_{2c} or forming an electrostatic (dipole-dipole) interaction with the adsorbed Cl atoms, however, this was found not to be the case.

The surface atomic displacements for the R_{110}/0.1 M NaOH interface best fit (see Table 5.1) indicate significant changes in the displacements of the surface Ti atoms when compared to the as-prepared surface. Importantly, the significant differences in displacements of 'Ti-1 & Ti-2 pair', 'Ti-3 & Ti-4 pair' and 'Ti-5 & Ti-6 pair' are dampened with the surface adopting a relatively more 'bulk-like' appearance when compared to the as-prepared surface. This phenomenon has been previously observed at the $R_{110}/H_2O_{(l)}$ interface.[3] The surface O atoms largely adopt similar positions to the as-prepared surface with the exception of the O-2* atom in the $\Delta[1\bar{1}0]$ direction whose large displacement can be explained to accommodate the Na atom at the tetra-dentate site.

On the contrary, the surface atomic displacements for the R_{110}/0.1 M HCl interface best fit (see Table 5.1) indicates significant changes in surface atomic displacements when compared to an as-prepared surface. The Ti atoms behave in a manner similar to the R_{110}/0.1 M NaOH interface best-fit whilst the surface O atoms are largely displacing towards the bulk. The displacement of the surface O atoms can be explained by the adsorption of the electronegative Cl. At the R_{110} / 0.1 M NaOH interface, the adsorption of O species at the Ti_{5c} site is essentially an extension of the TiO_2 cell. However, at the R_{110}/0.1 M HCl interface, the adsorption of the larger (relative to O) Cl species results in surface O species being repelled and thus displace towards the bulk.

Let us now consider the existence of OH_{br} species at the R_{110}/0.1 M NaOH and R_{110}/0.1 M HCl interface. As an OH_{br} species is essentially a proton adsorbed on the O_{2c} atom, SXRD is an insensitive probe. Indirectly and complemented by theory, the Ti_{5c}-O_{2c} bond length can be used to infer the presence of OH_{br} species. For example, at the A_{101}/H_2O interface, as is discussed in section 4.3.2, in the presence of both OH_{br} and OH_t adsorbed species the Ti_{5c}-O_{2c} bond length can increase from ~1.85 Å for the as-prepared surface in UHV to ~2 Å. However, in the presence of solely OH_t and/or H_2O adsorbed species, the Ti_{5c}-O_{2c} bond length registers at ~1.85 Å. Currently, such theoretical calculations do not exist for the R_{110}/0.1 M NaOH and R_{110}/0.1 M HCl interfaces, making any assignment of OH_{br} species largely tentative. The Ti_{5c}-O_{2c} bond length at the R_{110}/0.1 M NaOH and R_{110}/0.1 M HCl interface is observed at 1.95 ± 0.01 Å and 1.85 ± 0.01 Å, respectively. As-prepared R_{110} in UHV possesses a Ti_{5c}-O_{2c} bond length of 1.88 ± 0.01 Å. Tentatively speaking, OH_{br} species are unlikely to exist at the R_{110}/0.1 M NaOH interface due to the O_{2c}-Na interaction. Alternatively, OH_{br} species can be speculated to exist at the R_{110}/0.1 M HCl interface. The protons in solution are well suited to adsorption at the O_{2c} site allowing for the formation of OH_{br} species.

The point of zero charge (PZC) of TiO_2 is widely reported in the range of pH 6.0 - 7.5 i.e. the surface has a net neutral charge.[41-44] Thus, pH variation can allow for control over the surface charge.[44] At 0.1 M NaOH (pH 13) the surface can be expected to be negatively charged and at 0.1 M HCl (pH 1) the surface can be expected to be positively charged.[44] At the R_{110}/0.1 M NaOH interface, positive ion adsorption will be favoured on the negatively charged surface. This is in agreement with our findings with Na^+ (the main cation in solution) adsorption on the tetra-dentate site. The adsorption of the terminal O_x species at the Ti_{5c} site of R_{110}/0.1 M NaOH is unlikely to be associated with OH^- (the main anion in solution) adsorption. Dissociation of molecular water at the Ti_{5c} site is

likely to be the origin of the terminal O_x species. At the R_{110}/0.1 M HCl interface, negative ion adsorption will be favoured on the positively charged surface. This is in agreement with our findings with Cl^- (the main anion in solution) adsorption at the Ti_{5c} site.

To conclude, this study presents an SXRD perspective of the R_{110}/0.1 M NaOH and R_{110}/0.1 M HCl interface at room temperature. Our findings indicate that Na adsorbs at the tetra-dentate site on R_{110} whilst Cl adsorbs at the Ti_{5c} site. The existence of OH_{br} species is largely unclear and requires theoretical calculations to elucidate its existence.

5.3.3 Electrochemical Interfaces of Rutile TiO_2 (110): Preliminary STM Findings

A surface science perspective of the electrochemical interfaces of R_{110} has received little or no attention. To this extent, we present some preliminary electrochemical STM measurements obtained for R_{110} under 0.1 M NaOH.

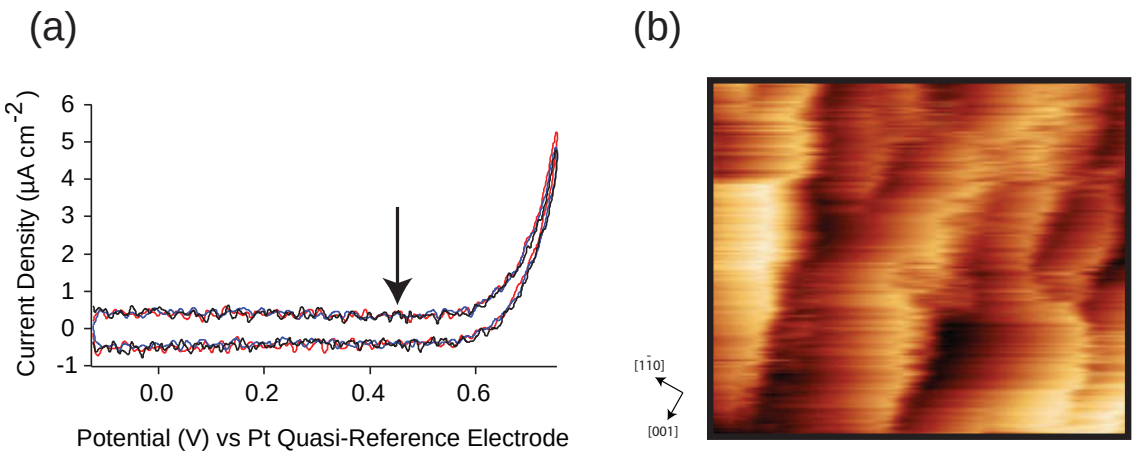

Figure 5.12: (a) Three successive CVs of R_{110} submerged in 0.1 M NaOH. The black arrow represents the potential at which the R_{110} sample was held during the electrochemical STM measurements. (b) 300 × 250 nm^2 Electrochemical STM image of R_{110} (V_t = -1.1 V, I_t = 2.5 nA) submerged in 0.1 M NaOH.

Figure 5.12 (a) illustrates cyclic voltammograms (CVs) taken of R_{110} under 0.1 M NaOH in the electrochemical STM set up. At just before the oxygen evolution potential (black arrow in Figure 5.12 (a)), Figure 5.12 (b) illustrates a 'terrace resolution' STM image taken of R_{110}. The observations of terraces are a significant step forward in the electrochemical surface science of TiO_2 as it indicates that the surface maintains a certain degree of 'order' under electrochemical control. Although atomically resolved STM images were not achievable, the observation of terraces is a promising sign for future work. The terrace shape at the step-edge appears rounded which could be associated with a certain degree of surface dissolution or alternatively be attributed to poor tip resolution. R_{110} surfaces exposed to electrochemical experiments were easily re-prepared with repeated Ar^+ sputtering and annealing cycles indicating that electrochemical exposure does not etch or corrode the surface beyond re-preparation.

To conclude, we present the first *in situ* STM image of R_{110} under electrochemical control and illustrate that the surface maintains terraces where a certain degree of surface dissolution can be inferred. From our preliminary electrochemical STM findings, we propose that electrochemical STM on R_{110} is a promising method to better understand the electrochemical behaviour of TiO_2 surfaces on a nano-scale.

5.4 Conclusions and Future Work

In this chapter, an STM and SXRD perspective of the R_{110}/0.1 M NaOH and R_{110}/0.1 M HCl interface is presented. Evidence is provided that these interfaces maintain order where Na is preferentially adsorbed at a surface tetra-dentate site whilst Cl preferentially adsorbs at the Ti_{5c} site. Our findings on UHV prepared and characterised R_{110} presents the first *in situ* measurements of this surface exposed to electrolyte solutions. Subsequently, we present electrochemical STM measurements of R_{110}/0.1 M NaOH, which indicates that R_{110} can at least maintain terrace resolution under electrochemical control. Our findings present the first *in situ* electrochemical STM measurements of TiO_2 surfaces.

In light of our findings, an interesting future direction to pursue would be to obtain an atomic scale surface science perspective of the electrochemical interfaces of TiO_2. This can be performed using a myriad of different techniques including STM and SXRD. Additionally, electrochemical XPS systems[45] are becoming increasingly popular at synchrotron facilities and would provide a much needed spectroscopic perspective of electrochemical interfaces. Complemented with theoretical calculations, these measurements will allow for an atomic scale surface science perspective of the electrochemical behaviour of TiO_2 surfaces and thus allow for improved material performance with rational design.

5.5 References

1. C. L. Pang, R. Lindsay and G. Thornton, *Chemical Reviews*, 2013, **113**, 3887-3948.
2. C. L. Pang, R. Lindsay and G. Thornton, *Chemical Society Reviews*, 2008, **37**, 2328-2353.
3. H. Hussain, G. Tocci, T. Woolcot, X. Torrelles, C. L. Pang, D. S. Humphrey, C. M. Yim, D. C. Grinter, G. Cabailh, O. Bikondoa, R. Lindsay, J. Zegenhagen, A. Michaelides and G. Thornton, *Nature Materials*, 2017, **16**, 461-467.
4. Z. Zhang, P. Fenter, N. C. Sturchio, M. J. Bedzyk, M. L. Machesky and D. J. Wesolowski, *Surface Science*, 2007, **601**, 1129-1143.
5. H. Hussain, X. Torrelles, G. Cabailh, P. Rajput, R. Lindsay, O. Bikondoa, M. Tillotson, R. Grau-Crespo, J. Zegenhagen and G. Thornton, *Journal of Physical Chemistry C*, 2016, **120**, 7586-7590.
6. D. C. Grinter, T. Woolcot, C. L. Pang and G. Thornton, *Journal of Physical Chemistry Letters*, 2014, **5**, 4265-4269.
7. H. J. Zhang, G. H. Chen and D. W. Bahnemann, *Journal of Materials Chemistry*, 2009, **19**, 5089-5121.
8. X. B. Chen, S. H. Shen, L. J. Guo and S. S. Mao, *Chemical Reviews*, 2010, **110**, 6503-6570.
9. A. Fujishima and K. Honda, *Nature*, 1972, **238**, 37-38.
10. A. Gross and K. Wandelt, *Surface Science*, 2015, **631**, 1-1.
11. U. Diebold, *Surface Science Reports*, 2003, **48**, 53-229.
12. O. Bikondoa, C. L. Pang, R. Ithnin, C. A. Muryn, H. Onishi and G. Thornton, *Nature Materials*, 2006, **5**, 189-192.
13. G. Serrano, B. Bonanni, M. Di Giovannantonio, T. Kosmala, M. Schmid, U. Diebold, A. Di Carlo, J. Cheng, J. VandeVondele, K. Wandelt and C. Goletti, *Advanced Materials Interfaces*, 2015, **2**, 1500246.
14. A. Sasahara and M. Tomitori, *Journal of Physical Chemistry C*, 2016, **120**, 21427-21435.
15. T. Shirasawa, W. Voegeli, E. Arakawa, T. Takahashi and T. Matsushita, *Journal of Physical Chemistry C*, 2016, **120**, 29107−29115.
16. J. Treacy, unpublished work.
17. Z. Zhang, P. Fenter, L. Cheng, N. C. Sturchio, M. J. Bedzyk, M. Predota, A. Bandura, J. D. Kubicki, S. N. Lvov, P. T. Cummings, A. A. Chialvo, M. K. Ridley, P. Benezeth, L. Anovitz, D. A. Palmer, M. L. Machesky and D. J. Wesolowski, *Langmuir*, 2004, **20**, 4954-4969.
18. C. Nicklin, T. Arnold, J. Rawle and A. Warne, *Journal of Synchrotron Radiation*, 2016, **23**, 1245-1253.
19. X. Torrelles and J. Rius, *Journal of Applied Crystallography*, 2004, **37**, 395-398.
20. E. Vlieg, *Journal of Applied Crystallography*, 2000, **33**, 401-405.
21. R. Feidenhansl, *Surface Science Reports*, 1989, **10**, 105-188.
22. I. K. Robinson and D. J. Tweet, *Reports on Progress in Physics*, 1992, **55**, 599-651.
23. G. Cabailh, X. Torrelles, R. Lindsay, O. Bikondoa, I. Joumard, J. Zegenhagen and G. Thornton, *Physical Review B*, 2007, **75**, 241403.
24. J. P. W. Treacy, H. Hussain, X. Torrelles, D. C. Grinter, G. Cabailh, O. Bikondoa, C. Nicklin, S. Selcuk, A. Selloni, R. Lindsay and G. Thornton, *Physical Review B*, 2017, **95**, 075416.
25. I. K. Robinson, *Physical Review B*, 1986, **33**, 3830-3836.
26. W. S. McDonald and D. W. Cruickshank, *Acta Crystallographica*, 1967, **22**, 37-43.
27. C. J. Brown, H. S. Peiser and A. Turnerjones, *Acta Crystallographica*, 1949, **2**, 167-174.
28. J. Krogh-Moe, *Acta Crystallographica*, 1974, **B30**, 578-582.

29. D. C. Grinter, E. R. Remesal, S. Luo, J. Evans, S. D. Senanayake, D. J. Stacchiola, J. Graciani, J. F. Sanz and J. A. Rodriguez, *Journal of Physical Chemistry Letters*, 2016, **7**, 3866-3872.
30. F. Allegretti, S. O'Brien, M. Polcik, D. I. Sayago and D. P. Woodruff, *Physical Review Letters*, 2005, **95**, 226104.
31. D. Vogtenhuber, R. Podloucky, J. Redinger, E. L. D. Hebenstreit, W. Hebenstreit and U. Diebold, *Physical Review B*, 2002, **65**, 125411.
32. W. P. Kretschmer, C. Dijkhuis, A. Meetsma, B. Hessen and J. H. Teuben, *Chemical Communications*, 2002, 608-609.
33. C. I. Branden and I. Lindqvist, *Acta Chemica Scandinavica*, 1960, **14**, 726-732.
34. L. Brun, *Acta Crystallographica*, 1966, **20**, 739-749.
35. S. C. Lawrence, M. E. G. Skinner, J. C. Green and P. Mountford, *Chemical Communications*, 2001, 705-706.
36. S. Tinkler, R. J. Deeth, D. J. Duncalf and A. McCamley, *Chemical Communications*, 1996, 2623-2624.
37. I. W. Bassi, M. Calcaterra and R. Intrito, *Journal of Organometallic Chemistry*, 1977, **127**, 305-313.
38. M. Mitani, R. Furuyama, J. Mohri, J. Saito, S. Ishii, H. Terao, N. Kashiwa and T. Fujita, *Journal of the American Chemical Society*, 2002, **124**, 7888-7889.
39. U. Diebold, W. Hebenstreit, G. Leonardelli, M. Schmid and P. Varga, *Physical Review Letters*, 1998, **81**, 405-408.
40. E. L. D. Hebenstreit, W. Hebenstreit, H. Geisler, C. A. Ventrice, D. A. Hite, P. T. Sprunger and U. Diebold, *Surface Science*, 2002, **505**, 336-348.
41. J. C. Chou and L. P. Liao, *Thin Solid Films*, 2005, **476**, 157-161.
42. M. Kosmulski, *Advances in Colloid and Interface Science*, 2002, **99**, 255-264.
43. M. Kosmulski, *Journal of Colloid and Interface Science*, 2004, **275**, 214-224.
44. J. Cheng and M. Sprik, *Journal of Physics-Condensed Matter*, 2014, **26**, 244108.
45. S. G. Booth, A. M. Tripathi, I. Strashnov, R. A. W. Dryfe and A. S. Walton, *Journal of Physics-Condensed Matter*, 2017, **29**, 454001.

Chapter 6

Surfaces and Interfaces of Anatase TiO_2 (101) and Rutile TiO_2 (100)

6.1 Introduction

6.1.1 Aims and Objectives

Surface and interfacial nanoscience of rutile and anatase has largely been restricted to work on single crystal and thin films of rutile TiO_2 (110) (R_{110}), rutile TiO_2 (011) (R_{011}) and anatase TiO_2 (101) (A_{101}).[1, 2] To this extent, in this chapter, we aim to investigate the formation and characteristic behaviour of less well investigated TiO_2 surfaces and interfaces. In the first instance (see Section 6.3.1) we aim to utilise scanning tunneling microscopy (STM) tip manipulation to form regions of rutile on anatase surfaces and thus create an anatase/rutile interface. Although, the anatase/rutile interface[3] is understood to play a leading role in photo-catalysis there is a lack of a surface science, in particular STM, perspective on this interface. R_{110}, R_{011} and R_{100} are understood to be the most stable terminations of rutile TiO_2 with surface stability order of (110) > (100) > (011).[4] R_{110} and R_{011} are the basis of most fundamental surface and interface studies whereas research pertaining to R_{100} is relatively lacking.[2, 5] This is largely attributed to the numerous and complex nature of possible terminations and due to the relative ease to prepare R_{110} and R_{011}. R_{100} has been reported to exhibit (1×1)[6-8], (1×2)[9], (1×3)[7, 10, 11], (1×5)[12], (1×7)[13] and $c(2 \times 2)$[14] terminations. To this extent, we also aim to perform STM measurements on R_{100} (1×1) and (1×3). In particular, we aim to discuss ideal preparation conditions for surface science investigations. Lastly, we aim to investigate the R_{100} interface with acetic acid (AA) and tri-methyl acetic acid (TMAA) in order to better understand the adsorption of carboxylic acids on this surface. The particular manner in which these molecules adsorb to the surface is important for purposes of surface characterisation and because these photo-active molecules are central to better understand the photo-activity of R_{100} under UV illumination.

6.1.2 The Literature

a. Mixed Anatase / Rutile TiO_2

Rutile is the most thermodynamically stable polymorph of TiO_2. Mixed phase rutile and anatase TiO_2 have been experimentally shown to exhibit greater photo-catalytic activity than single phase TiO_2. Indeed the most potent TiO_2 photo-catalyst consists of a 3:1 ratio of anatase and rutile nanoparticles - commercially available as Degussa P-25®.[15] This has been largely attributed to a more robust separation of photo-excited charge carriers between the two phases.[3, 16] Experimentally, the rutile/anatase interface is considered the active site for photocatalysis.[17, 18] Numerous experiments of mixed phase rutile/anatase conclude that under photo-active conditions, anatase maintains a greater affinity towards electrons such that electrons flow from the rutile to the anatase and the holes flows in the opposite direction.[19-22] Thus understanding the interface of rutile and anatase and the nucleation of rutile on anatase is of critical importance to decipher the photocatalytic mannerisms of TiO_2.

The nucleation of the thermodynamically stable rutile on meta-stable anatase surfaces (i.e. the phase transition from anatase to rutile) has received much attention.[23] This allows for nano-scale engineering to enhance and/or inhibit the anatase to rutile phase transition to optimise performance. Interestingly, although rutile is more thermodynamically stable than anatase, the latter is often the product in nano-particle or thin film synthesis due to its less constrained structure and lower surface energy whereas rutile is more stable as the bulk phase.[24-26] The conversion from anatase to rutile is thermally activated and can range between 500 - 800^{o}C depending on the nature and environment of the material during the annealing process where the polymorph conversion rate is considered to be exponentially related to the rise in temperature.[23] The anatase to rutile conversion can be enhanced by

the creation of oxygen vacancies that would destabilise the crystal and induce a phase transition.

A surface science perspective of ordered anatase / rutile terminations is invaluable towards elucidating the anatase / rutile interface structure and physical properties. Thin films of anatase and thin films of rutile grown on specific substrates have received much attention with STM[1, 2], however, STM studies of mixed anatase / rutile thin films are relatively lacking.[27] An STM, transmission electron microscopy (TEM) and photo-emission electron microscopy (PEEM) study of anatase TiO_2 (001) (A_{001}) thin films grown on $LaAlO_3$ (001) or $SrTiO_3$ (001) present evidence of R_{100} nucleation at surface defect sites.[27, 28] This highlights the formation of an A_{001} / R_{100} interface. Theoretically, a variety of density functional theory (DFT) and molecular dynamics (MD) calculations have been performed to better understand the anatase / rutile interface.[4, 29-31] These calculations largely predict the existence of a disordered layer (a few Å thick) between the anatase and rutile. This disordered interface exists as a bridge between the anatase and rutile regions where the disordered region exhibits a structure more reminiscent of the polymorph in greater proximity to it. Alternatively, intermediate species between the anatase to rutile phase transition are also predicted such as when the nucleation of rutile species occurs via the formation of meta-stable TiO_2 II or brookite layers in an anatase matrix.[32]

b. STM Tip Manipulation of TiO_2 Single Crystals

In STM, the tip-surface distance of between 4-6 Å enables an attractive atomic force between the tip and surface due to the movement of electrons back and forth (partial covalent bond). Hence, tip manipulation can be used to induce changes such as chemical reactions, atom/defect movement and even enable surface reconstructions. Depending on

the STM tip manipulation conditions, surface atomistic manipulation is largely attributed to the electric field induced with the tip, the injection of electrons at local sites, localised heating by electrons and/or mechanical contact between the surface and the tip.

On TiO_2 surfaces, STM tip manipulation has been largely performed on R_{110} and A_{101}. On R_{110}, STM tip pulsing (a voltage point pulse applied to the surface via the STM tip) in the range of V_s (sample bias) = +3 to +5 V can be utilised to remove surface bridging hydroxyls[1, 33, 34] and displace adsorbed Au atoms[35]. Additionally, STM tip pulsing at V_s = +5 to +10 V is reported to induce surface reconstructions on as-prepared[34, 36] and electron irradiated[36] R_{110}. Alternatively, high bias scanning[37] of R_{110} (V_s = ±5 V) has been reported to generate Ti_2O_3 structures on top of a (1 × 1) terminated surface. Similarly, high current scanning[38] (10 nA) has been reported to remove R_{110} (1 × 2) to unearth the underlying (1 × 1) termination. Lastly, STM tip pulsing on R_{110} surfaces using a variety of high voltages and currents has been shown to induce the formation of 'craters'[34, 36, 39] on the surface.

At room temperature, A_{101} surface oxygen vacancies are meta-stable and thus reside in the sub-surface and bulk regions. Low temperature (6 K) STM tip manipulation of as-prepared A_{101}, with scanning performed at 5 V, has been shown to draw sub-surface oxygen vacancies to the surface.[40] Additionally, chemical reactions on A_{101} surfaces have been shown to occur with 3 - 4 V tip pulses being utilised to convert adsorbed H_2O to species that are identified as terminal OH (OH_t).[41]

c. Rutile TiO_2 (100) Surfaces

R_{100} has been reported to exhibit a variety of different terminations based on preparation conditions: (1 × 1)[6-8], (1 × 2)[9], (1 × 3)[7, 10, 11], (1 × 5)[12], (1 × 7)[13] and c(2 × 2)[14]. The (1 × 1) and (1 × 3) terminations are the most common for R_{100} and are central to the work

presented in this chapter. To this extent, an overview of these terminations is provided. In addition, the (1 × 3) termination can be expressed in three forms - the thermodynamically most stable 'micro-facet' ($(1 \times 3)^{MF}$) form or the intermediate 'α' ($(1 \times 3)^{\alpha}$) and 'β' ($(1 \times 3)^{\beta}$) forms.[7, 42] These intermediate forms highlight the existence of a series of discrete bond breaking step involved in the transition from (1 × 1) to $(1\times3)^{MF}$.

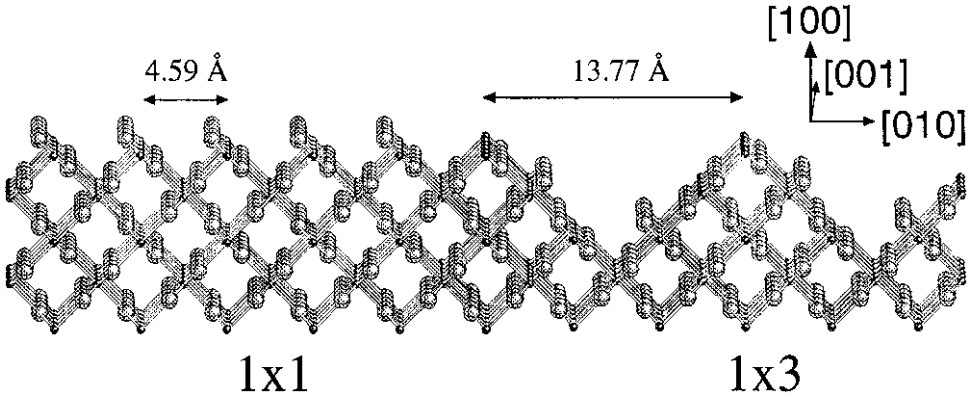

Figure 6.1: Ball and stick models of R_{100} (1 × 1) and $(1 \times 3)^{MF}$ illustrating spacing in [010] direction. Small spheres represent Ti atoms, while large spheres represent O atoms.[42] Reproduced with permission of the rights holder, *Elsevier*.

Figure 6.1 illustrates a ball and stick model highlighting the proposed structures of R_{100} (1 × 1) and $(1 \times 3)^{MF}$.[7, 42] The conversion of R_{100} (1 × 1) to $(1 \times 3)^{MF}$ (or $(1 \times 3)^{\alpha}$ and $(1 \times 3)^{\beta}$) results in an expansion of spacing in the [010] direction from 4.59 Å to 13.77Å. The periodicity in the [001] direction is maintained at 2.96 Å. Regarding the structure of R_{100} (1 × 1), there is a lack of research pertaining to its structure, however, using Tasker's rule the structure proposed in Figure 6.1 is widely accepted.[6-8] Regarding the structure of R_{100} $(1 \times 3)^{MF}$, STM[7, 10, 42, 43], surface X-ray diffraction (SXRD)[11] and photo-electron diffraction (PhD)[44] suggest the structure depicted in Figure 6.1.

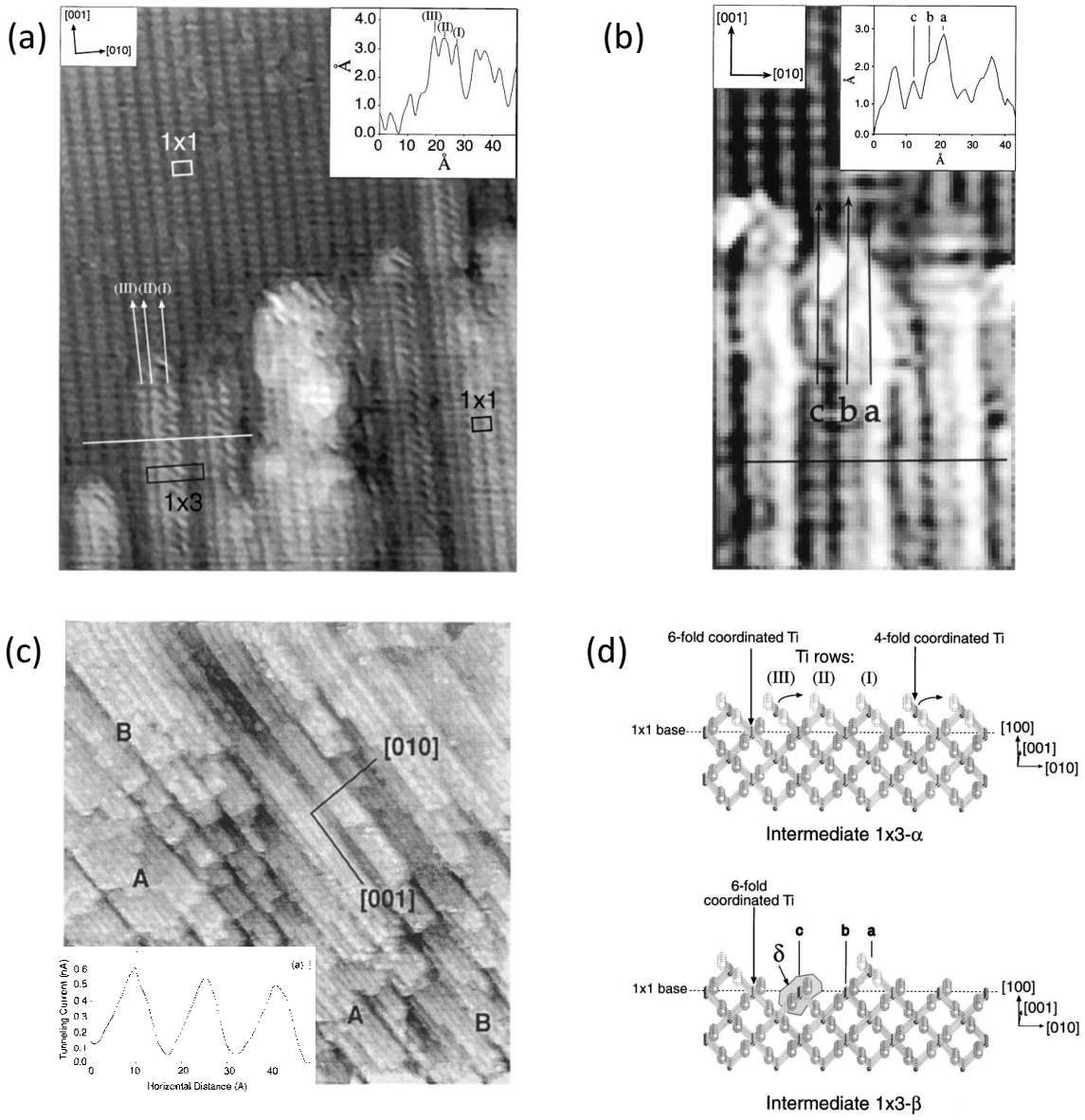

Figure 6.2: (a) 8 × 10 nm^2 STM image (V_s = +1 V, I_t = 0.8 nA) of a region highlighting R_{100} (1 × 1) and R_{100} (1 × 3)$^{\alpha}$ with a line profile inset.[7] Reproduced with permission of the rights holder, *American Physical Society*. (b) 5 × 7 nm^2 STM image (V_s = +1.1 V, I_t = 0.8 nA) of a region highlighting R_{100} (1 × 1) (lower terrace) and R_{100} (1 × 3)^{ß} with a line profile inset.[7] Reproduced with permission of the rights holder, *American Physical Society*. (c) 100 × 100 nm^2 STM image (V_s = +2 V, I_t = 0.2 nA in constant current) image of R_{100} (1 × 3)^{MF} with a line profile inset where features, contains irregularly spaced staircase steps (A) and regular steps in the [010] direction (B).[43] Reproduced with permission of the rights holder, *Elsevier*. (d) Proposed mechanism for the conversion of R_{100} (1 × 1) to the R_{100} (1 × 3)$^{\alpha}$ and R_{100} (1 × 3)^{ß}. The labels I, II and III on (d) correspond to that in (a). The labels a, b and c on (d) correspond to that in (b). Removal of the volume denoted ∂ transforms R_{100} (1 × 3)^{ß} to R_{100} (1 × 3)^{MF}. Small spheres represent Ti atoms, while large spheres represent O atoms. The O termination of the R_{100} (1 × 1) base terrace is indicated in (d).[7] Reproduced with permission of the rights holder, *American Physical Society*.

Figure 6.2 illustrates the three varieties of the R_{100} (1 × 3) termination. Of the three, R_{100} (1 × 3)^{MF} (see Figure 6.1 and 6.2 c) is the most thermodynamically stable whereas R_{100} (1 × 3)$^{\alpha}$ (see Figure 6.2 a and d) and R_{100} (1 × 3)^{ß} (see Figure 6.2 b and d) are intermediate species that exists between the transition from R_{100} (1 × 1) to R_{100} (1 × 3)^{MF}. As is the case with R_{110} (1 × 1) to R_{110} (1 × 2) conversion, the reconstruction of the surface from R_{100} (1 × 1) to R_{100} (1 × 3)^{MF} is driven by oxygen deficiency.

d. Acetic Acid and Tri-Methyl Acetic Acid Adsorption on TiO_2 Surfaces

Over the last few decades[45], the interaction of organic molecules with rutile[46-48] and anatase[49-51] TiO_2 surfaces has been the focus of numerous investigations as model systems to elucidate surface photo-activity and for purposes of understanding dye adsorption on surfaces.[1, 2, 5] The adsorption of AA (see Figure 6.3 (a)) and TMAA (see Figure 6.3 (b)) on R_{110} has received much attention.[1, 2]

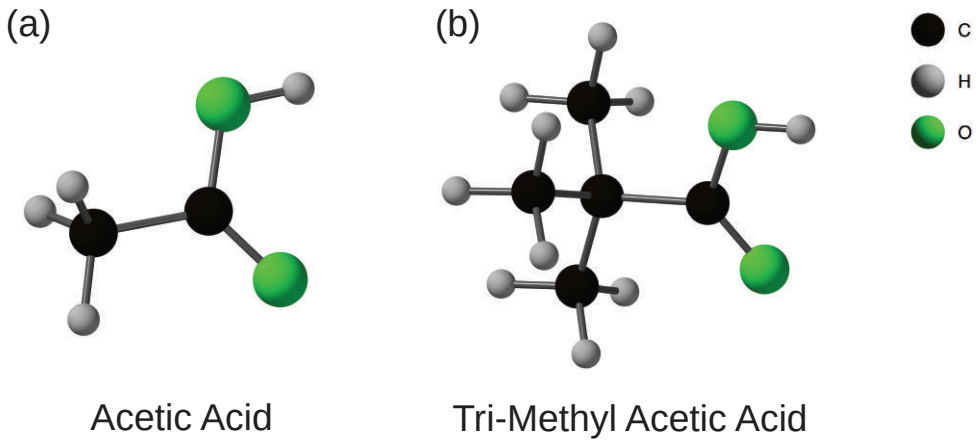

Figure 6.3: Ball and stick model of (a) acetic acid and (b) tri-methyl acetic acid.

Room temperature STM[47, 52], surface X-ray diffraction (SXRD)[52] and low energy electron diffraction (LEED)[45] measurements of R_{110} single crystal surfaces (see Figure 5.1) exposed to gaseous[47, 52] or aqueous[46, 53] AA gives rise to a (2 × 1) overlayer on the (1 ×

1) terminated surface with a saturation coverage of half a monolayer (ML) with respect to surface Ti_{5c} sites. AA has been reported to adsorb on R_{110} in a dissociative bi-dentate manner with both oxygens (i.e. C=O and C-OH) binding to two adjacent Ti_{5c} atoms with loss of the H.[52] The proton is thought to bond to the adjacent O_{2c} atom as a bridging OH species (OH_{br}).[1] Similarly, the adsorption of TMAA on R_{110} occurs in a dissociative bi-dentate manner and forms a (2 × 1) overlayer on the (1 × 1) terminated surface.[48, 54, 55] Motivated by the need to understand the photo-chemistry (photo-catalysis) of TiO_2, R_{110} with adsorbed AA and TMAA has been subjected to photo-active (i.e. UV) illumination. In UHV, UV illumination has been reported to cause little or no change to the R_{110}/AA system, however, AA desorption under UV illumination can be induced in the presence of ~5 $\times 10^{-8}$ mbar O_2.[56] In contrast, UV illumination of the R_{110}/TMAA system is capable of inducing TMAA desorption in UHV in the absence of O_2.[55]

Other than R_{110}, AA adsorption has also been probed on R_{011} single crystal[47], an A_{101} single crystal[49] and A_{001} thin films[51] with STM at saturation coverage, however, research on these systems is limited and focussed on measuring surfaces after dosing AA from the gas phase in UHV. As is the case with R_{110}, the acetate species is understood to adsorb largely in a dissociative bi-dentate manner. On R_{011} (2 × 1), AA adsorbs as 1D acetate clusters that run along the troughs in the $[01\bar{1}]$ direction with adsorption predicted by DFT to be a combination of associative mono-dentate and dissociative bi-dentate in the clusters. On A_{101}, AA adsorption at room temperature is reported to display no long range order, however, adsorption at elevated temperatures (420 K) leads to a partially ordered (2 × 1) overlayer which corresponds to dissociative bi-dentate adsorption. Lastly, exposure of A_{001} (1 × 4) thin films[51] to AA have been reported to generate a (4 × 2) overlayer of acetate molecules.

6.2 Experimental Procedure

A_{101} and R_{100} single crystals were mounted on a Ta plate with Ta clips and degassed in UHV. Surfaces were prepared with cycles of Ar^+ sputtering ($P_{Ar} = 8 \times 10^{-5}$ mbar, 1 kV, 10 μA cm^{-2}, 10 minutes) and annealing (A_{101}: ≤ 1023 K, R_{100} (1 × 1): ≤ 973 K and R_{100} $(1 \times 3)^{MF}$: ≤ 1273 K). Low energy electron diffraction (LEED) and Auger electron spectroscopy (AES) were used to ensure an ordered and contaminant free surface (below the detection limits of AES) for STM measurements. STM measurements were made at room temperature on an *Omicron* AFM/STM instrument (see Figure 3.2) with a base pressure of ~1×10^{-10} mbar. STM was performed in constant current mode with electrochemically etched tungsten tips that were degassed in UHV and conditioned during scanning with voltage pulses and high bias scans (up to ±10 V). Surfaces were imaged by tunneling into empty states using positive sample bias voltages in the range of +1 to +1.6 V. Figures 6.10 and 6.11 are adapted, with permission, from previous work[57] in the Thornton Group.

AA and TMAA (*Sigma Aldrich*) were dosed into the UHV system via a high precision leak valve (see Section 3.2.4 for more details). The AA and TMAA was placed inside a glass vial and purified with numerous freeze-pump-thaw cycles. In this paper, exposures are quoted in langmuirs where one Langmuir (L) equates to 1.33×10^{-6} mbar s. Surface ML coverages are given with respect to the number of surface unit cells of R_{100} (1 × 1) which corresponds to a density of 7.4 nm^{-2}. AA and TMA were dosed onto the surface at chamber pressures of 1×10^{-8} mbar. Surface electron irradiation was performed at 3 keV with a commercial UHV high energy electron gun (*Thermo LEG62*) (see Section 3.2.3 for more details) at ~1×10^{-9} mbar.

6.3 Results and Discussion

6.3.1 Electron Irradiation and STM Tip Manipulation of Anatase TiO_2 (101)

In this section, STM tip pulses (+10 V_s, >50 nA, 200 ms ramped at 2×10^{-3} V μs^{-1}) have been employed to create regions that we argue to be R_{100} on electron irradiated A_{101}. Previous work in the Thornton group shows that STM tip manipulation of as-prepared A_{101} does not yield any ordered non-A_{101} structures. Hence, A_{101} underwent high energy electron irradiation at 3 keV to induce surface destabilisation (increasing surface energy) for purposes of easing the transition from anatase to rutile. High energy electron irradiation has been previously utilised on R_{110} surface to destabilise the surface where STM tip manipulation of these surfaces can induce surface reconstructions.[36] The choice of using the (101) face of anatase is because it is the most stable and abundant anatase termination as well as being the most well investigated.

a. High Energy Electron Irradiation of Anatase TiO_2 (101)

Figure 6.5 - 6.7 shows the evolution of an as-prepared A_{101} surface as it is successively electron irradiated at 3 keV (see Section 3.2.3) without surface re-preparation (the structure and appearance of as-prepared A_{101} surfaces is shown in Figure 4.3). Figure 6.5, 6.6 and 6.7 show the A_{101} surface 15, 25 and 35 minutes after electron irradiation, respectively. As is seen in Figure 6.4 (a, b), 6.5 (a, b) and 6.6 (a, b), the 'terrace resolution' images of the surface are increasingly losing their characteristic trapezoidal structure. However, the 'atomically resolved' images (see Figure 6.4 (c), 6.5 (c) and 6.6 (c)) indicate that the surface continues to maintain its characteristic sphere-like features (see Figure

4.3) that represent the A_{101} (1 × 1) termination. These regions are highlighted with white dashed circles in the respective STM images.

Generally, the electron irradiated surface exhibits pitting with the appearance of 'nano-cracks' that get larger as the duration of electron irradiation is increased. The formation of 'nano-cracks' on electron irradiated TiO_2 surfaces has been previously reported.[36] Their appearance can provide an insight of the manner in which electron irradiation de-stabilises and roughens the A_{101} surface. The 'nano-cracks' possess depths of ~3.5 to ~4.0 Å that is in good agreement with the monatomic step height of A_{101}, suggesting that an entire surface layer has been removed.[58, 59] This is perhaps best observed in Figure 6.5 (d and e) where evidence of the A_{101} (1 × 1) termination can be observed inside the 'nano-cracks' exposing the underlying structure which exhibits the A_{101} (1 × 1) termination. The out-of-phase rows observed inside the nano-crack is characteristic of steps on A_{101}.[58] In parallel to STM, LEED measurements of the electron irradiated surface were also obtained. As expected from the STM images, the intensity of the diffraction spots in LEED get increasingly weak as the duration of electron irradiation is increased. Nonetheless, a LEED pattern for A_{101} (1 × 1) is observable.

The mechanism of surface roughening and 'nano-crack' formation due to electron irradiation can be explained by O^+ ejection via an Auger decay process.[34, 36, 60-62] This would ultimately induce the under-saturated Ti atoms to migrate and thus allow for the formation of the 'nano-cracks'. Post-electron irradiation, the surface also exhibits numerous clustered (amorphous) features that are circled in black in Figures 6.4 (c), 6.5 (c) and 6.6 (c). These features are reminiscent of TiO_x clusters formed on numerous as-prepared TiO_2 surfaces and can be considered to be TiO_x and TiO_xC_y clusters that are compensating for the O^+ loss and subsequent reduction of the crystal.[34, 63]

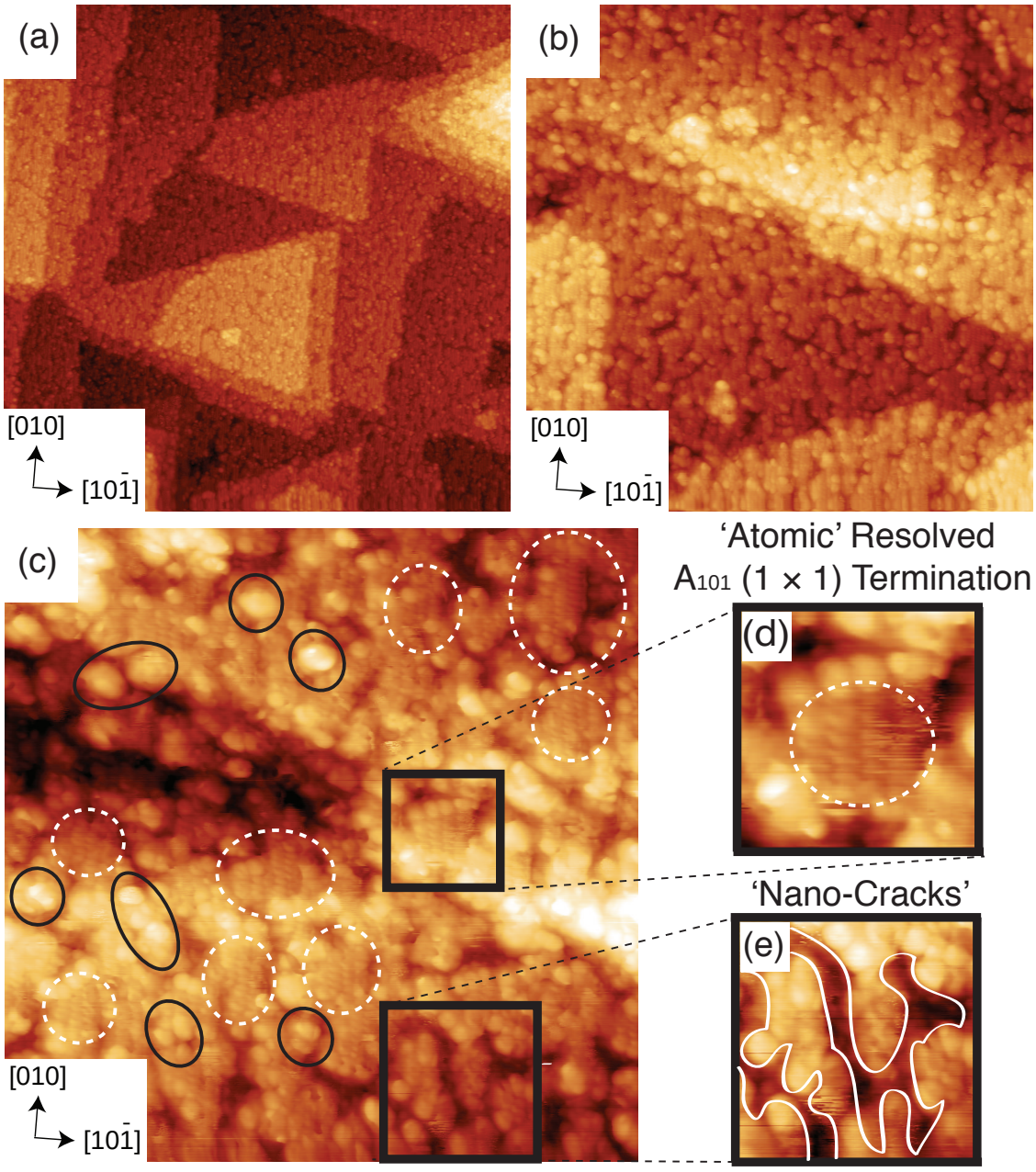

Figure 6.4: (a) 100 × 100 nm^2, (b) 50 × 50 nm^2 and (c) 25 × 25 nm^2 STM images (V_s = +1.6 V, I_t = 0.1 nA) of A_{101} after 15 mins electron irradiation at 3 keV. (d) 4 × 4 nm^2 zoom-in of black boxed region connected with dotted black line in '(c)' highlighting 'atomic' resolved A_{101} (1 × 1) termination. (e) 6 × 6 nm^2 zoom-in of black boxed region connected with dotted black line in '(c)' highlighting 'nano-cracks' on the surface. The nano-cracks are highlighted in (e) encapsulated by a solid white line. 'Atomically' resolved A_{101} (1 × 1) termination regions on the surface are highlighted with dashed white ovals. Amorphous regions are highlighted with black lined ovals.

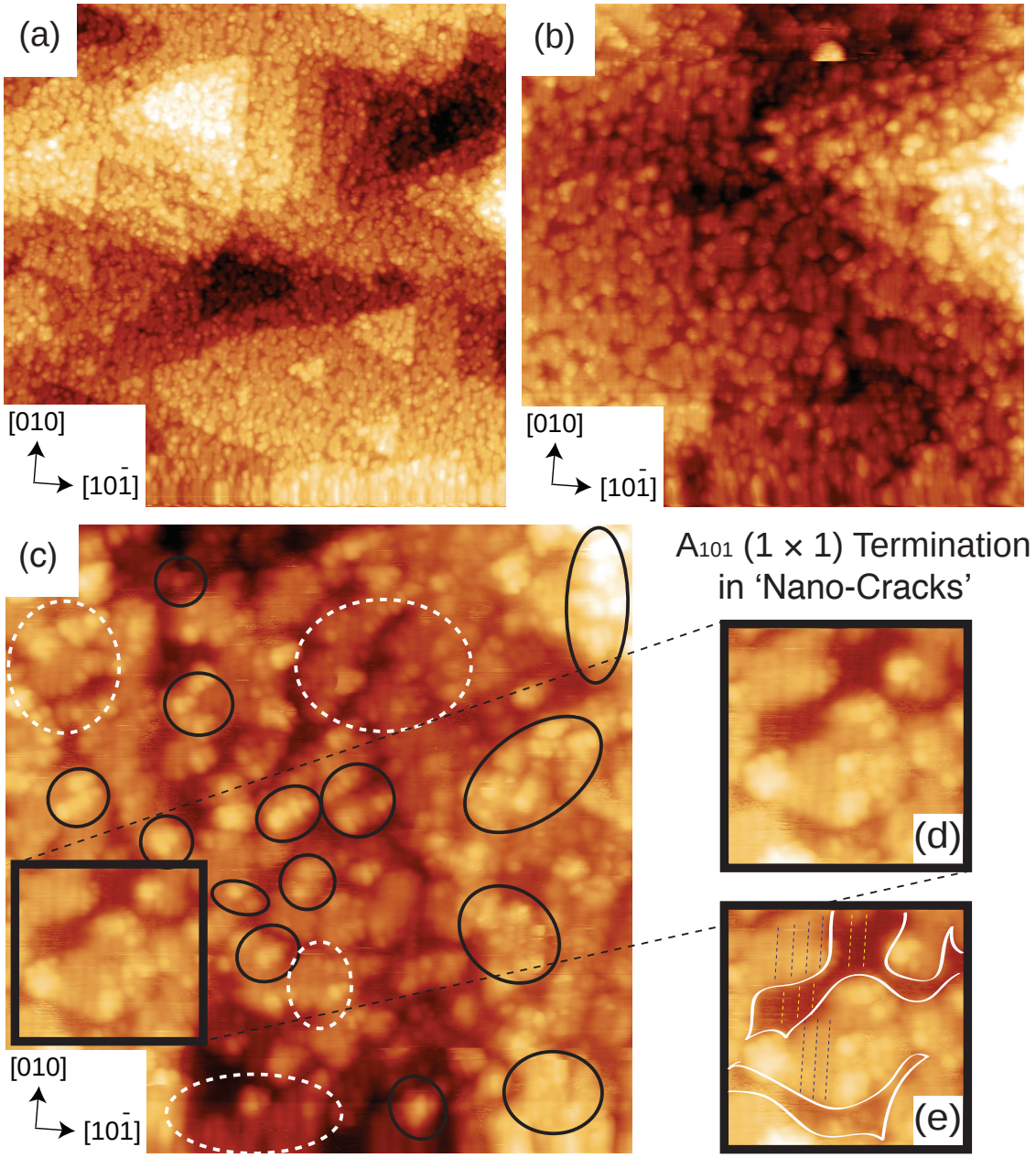

Figure 6.5: (a) 100 × 100 nm^2, (b) 50 × 50 nm^2 and (c) 25 × 25 nm^2 STM images (V_s = +1.6 V, I_t = 0.1 nA) of A_{101} after 25 mins electron irradiation at 3 keV (successive to Figure 6.4). (d) 7.5 × 7.5 nm^2 zoom-in of black boxed region connected with dotted black line in '(c)' highlighting 'row' resolved A_{101} (1 × 1) termination on the surface and inside 'nano-cracks'. (e) Copy of '(d)' with 'nano-cracks' highlighted encapsulated by a solid white line with dashed blue line highlighting surface 'atomic' rows in [010] direction and dashed yellow line highlighting rows in [010] direction inside 'nano-cracks'. 'Atomically' resolved A_{101} (1 × 1) termination regions on the surface are highlighted with dashed white ovals. Amorphous regions are highlighted with black lined ovals.

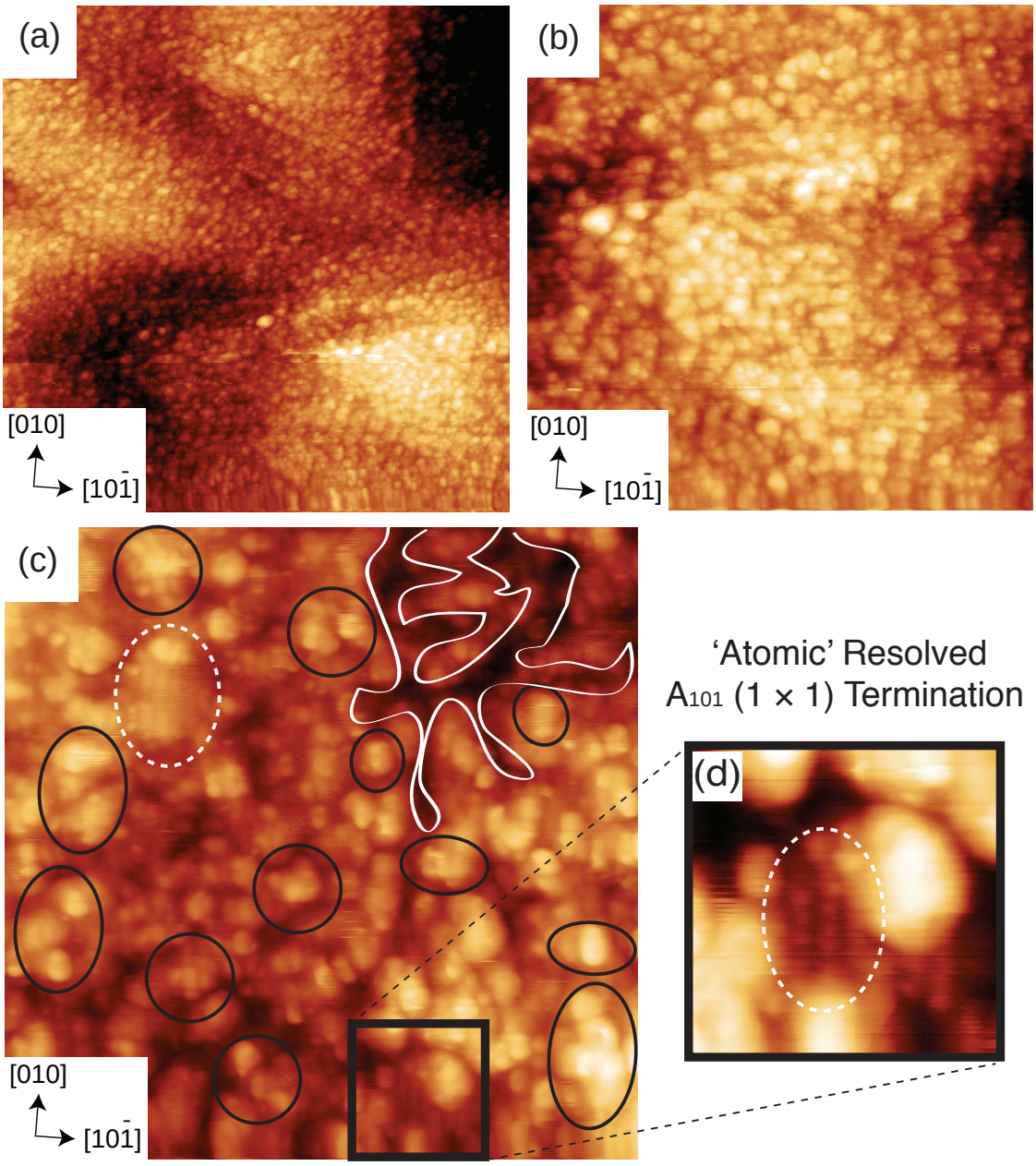

Figure 6.6: (a) 100 × 100 nm^2, (b) 50 × 50 nm^2 and (c) 25 × 25 nm^2 STM images (V_s = +1.6 V, I_t = 0.1 nA) of A_{101} after 35 mins electron irradiation at 3 keV (successive to Figure 6.5). (d) 5 × 5 nm^2 zoom-in of black boxed region connected with dotted black line in '(c)' highlighting 'atomically' resolved A_{101} (1 × 1) termination on the surface. 'Atomically' resolved A_{101} (1 × 1) termination regions on the surface are highlighted with dashed white ovals. Amorphous regions are highlighted with black lined ovals.

b. STM Tip Manipulation: Rutile TiO_2 (100) on Electron Irradiated Anatase TiO_2 (101)

STM tip pulsing (+10 V, >50 nA, 200 ms) gives rise to a mound structure with a distinct shape (see Figure 6.7). The formation of this feature is attributed to the electric field induced with the tip, the injection of electrons at local sites, localised heating by electrons and/or mechanical tip/surface contact. All pulsed surfaces were electron irradiated for 35 min at 3 keV (see Section 3.2.3) prior to STM tip manipulation (10 V, >50 nA, 200 ms). We utilise this technique in an attempt to induce an anatase to rutile phase transition.

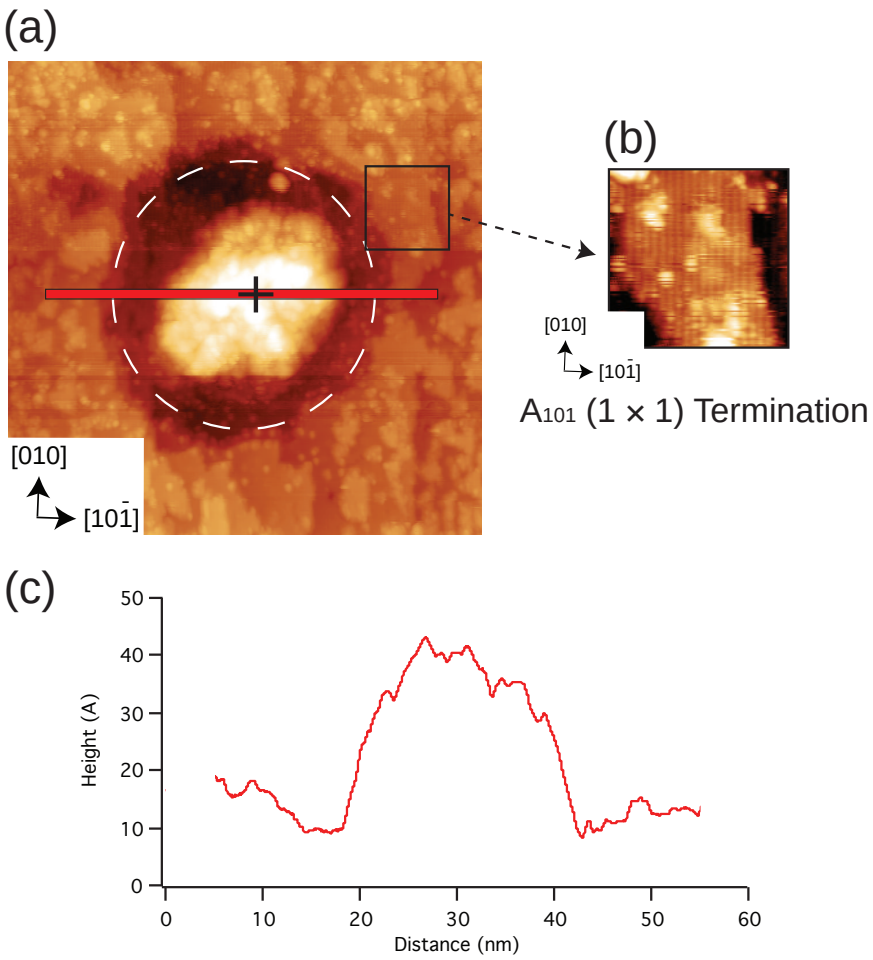

Figure 6.7: (a) 60 × 60 nm^2 STM image (V_s = +1.6 V, I_t = 0.1 nA) of a 'mound' structure created after STM tip pulsing (+10 V, >50 nA, 200 ms) of electron irradiated A_{101}. The shape and structure varies with each STM pulse. The white dashed circle denotes the 'mound' created by STM tip pulsing. (b) A region outside the dashed white circle where the STM tip pulsing has exposed the A_{101} surface. (c) Line profile of black line in '(a)' depicting the shape of the mound. The '+' represents the pulse epicentre.

Figure 6.8, shows the formation of an ordered region on electron irradiated A_{101} via STM tip pulsing. The spacing of the ordered region is observed at 3.1 Å × 4.7 Å (see Figure 6.9). As is seen in Figure 6.8 (e and f), the out-of-phase shift in rows indicates the existence of a step edge. This phenomena is commonly associated with TiO_2 surfaces as is also observed for R_{100} (see Figure 6.8 (h)).[1, 2, 58] This step edge has a height of ~2.5 Å (see Figure 6.8 (g)). On the basis of the ordered region spacing and step-height, we assign this surface as R_{100} (1 × 1), which has a surface cell of 2.96 Å × 4.59 Å (see Figure 6.16) and a step height of 2.7 Å (see Figure 6.8 (h)). For TiO_2 surfaces, the separation of 3 Å along the row is only characteristic of rutile surfaces - in particular the (110), (100) and (010) terminations. The separation between rows for R_{110} (1 × 1) is 6.49 Å whereas for R_{100} (1 × 1) and rutile TiO_2 (010) (R_{010}) (1 × 1) it is 4.59 Å. Hence, this ordered region could be assigned as R_{100} (1 × 1) or R_{010} (1 × 1). R_{010} is a rare and unstable termination of rutile with no experimental surface science being performed on it to date. On this basis, R_{100} (1 × 1) is a more likely candidate for the ordered structure in the pulsed region.

STM tip manipulation of electron irradiated A_{101} also resulted in the creation of an ordered region that was additionally probed with AA (see Figure 6.10 and 6.11). The spacing of the ordered region is observed at 3.1 Å × 14.2 Å (see Figure 6.10), where details observed between the rows and shape of the line profile of the ordered structure in the pulsed region (see Figure 6.2 (b)) is reminiscent of R_{100} $(1 \times 3)^{ß}$ - a termination with a surface cell of 2.96 Å × 13.77 Å. This, rather interestingly, is a reconstruction of the R_{100} (1 × 1) structure proposed in the pulsed region shown in Figure 6.8 and 6.9. Additionally, this ordered region was dosed with AA (as a probe molecule) which at saturation coverage gives rise to a (×2) periodicity of adsorbed AA along the rows (see Figure 6.11 (d-f)). Room temperature AA dosing on A_{101}[49] and R_{011}[47] has largely been shown to create dis-ordered over layers. On the contrary, AA has been widely reported to

form a (2 × 1) overlayer on R_{110}. In Section 5.3.2, AA adsorption on single crystal R_{100} illustrates that AA binds in a dissociative bidentate manner on the (1 × 1) and $(1 \times 3)^{MF}$ termination giving rise to an overlayer that possesses a (×2) periodicity in the [001] direction (i.e. along the rows). On the basis of this, we believe that R_{100} $(1 \times 3)^{ß}$ is also likely to generate a overlayer that possesses a (×2) periodicity in the [001] direction. Although our assignment of the pulsed region as R_{100} $(1 \times 3)^{ß}$ is based on the shape of the STM line profile (see Figure 6.10), the subsequent dosing of AA on the region and the emergence of the (×2) periodicity in the [001] direction lends further evidence of at least a potential R_{100} (1 × 3) termination.

Thus far, two ordered regions on electron irradiated surfaces have been suggested that have been assigned as R_{100} (1 × 1) (see Figure 6.8 and 6.9) and as R_{100} $(1 \times 3)^{ß}$ or $(1 \times 3)^{MF}$ (see Figure 6.10 and 6.11). From this we propose that, with the current evidence, R_{100} can be preferentially grown on A_{101}. Additionally, Figure 6.12 And 6.13 illustrates further ordered regions (created via STM tip pulsing on electron irradiated A_{101}) that have a row spacing of 8.8 ± 0.8 Å and 14.0 ± 0.8 Å, respectively. The surface structure with row spacing of 8.8 Å poses an interesting structure. On single crystal R_{100}, the formation of R_{100} (1 × 2) has not been reported. However, thin films of TiO_2 grown on Au (111) has been reported to yield a R_{100} (1 × 2) termination with a row spacing of 9 Å although a structure has not yet been proposed.[9] Based on the aforementioned formation of R_{100} on A_{101}, we assign the pulsed region with row spacing of 8.8 Å to R_{100} (1 × 2). Similarly, the surface structure with row spacing of 14.0 ± 0.8 Å (see Figure 6.13) can be assigned to R_{100} (1 × 3) where the specific form of (1 × 3) is unclear.

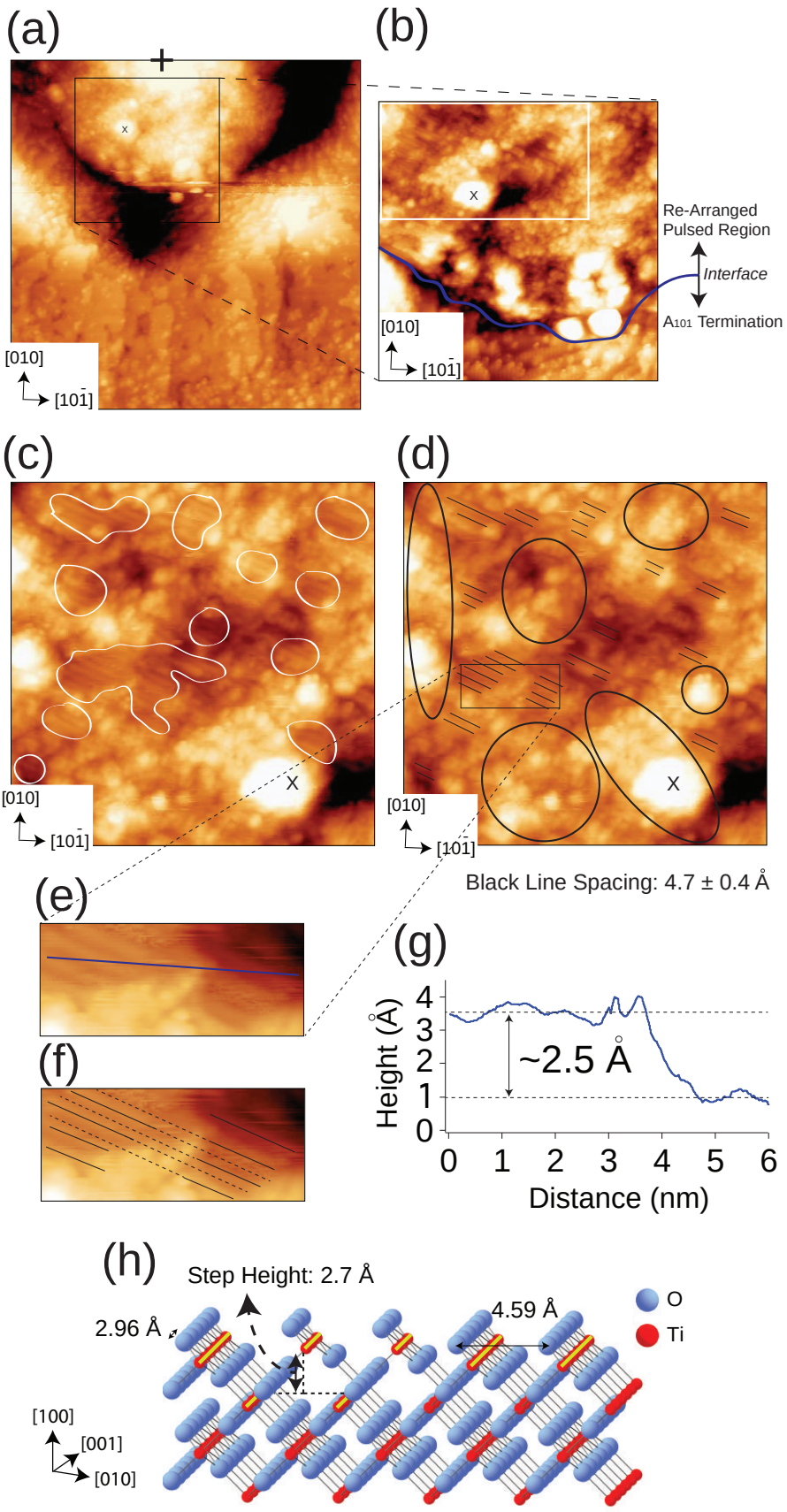

Figure 6.8: STM tip pulsing (+10 V_s, >50 nA, 200 ms ramped at 2×10^{-3} V μs^{-1}) on electron irradiated A_{101} to form a proposed region of R_{100} (1 × 1). (a) 75 × 75 nm^2 STM image (V_s = +1.6 V, I_t = 0.1 nA) of pulsed region ('+': pulse epicentre). (b) 31 × 31 nm^2

STM image (V_s = +1.6 V, I_t = 0.1 nA) indicating the A_{101} / pulsed region interface - the white box shows order created by the pulse. (c) 21 × 21 nm^2 STM image (V_s = +1.6 V, I_t = 0.1 nA) with order (in pulsed region) encircled by a white line. (d) Replica of '(c)' where black lines cover the re-arranged rows and black ovals highlight disordered regions. (e and f) Zoom-in of '(d)' illustrating a step edge. In '(e)', the blue line represents the line profile in '(g)'. In (f), the solid and dashed black lines represent surface rows and the out of phase shift of rows associated with a step-edge, respectively. (h) Ball and stick model of R_{100} (1 × 1) representing its step edge/height - yellow lines represent rows in STM. The black × (a-d) is for reference. The black + represents the pulse epicentre.

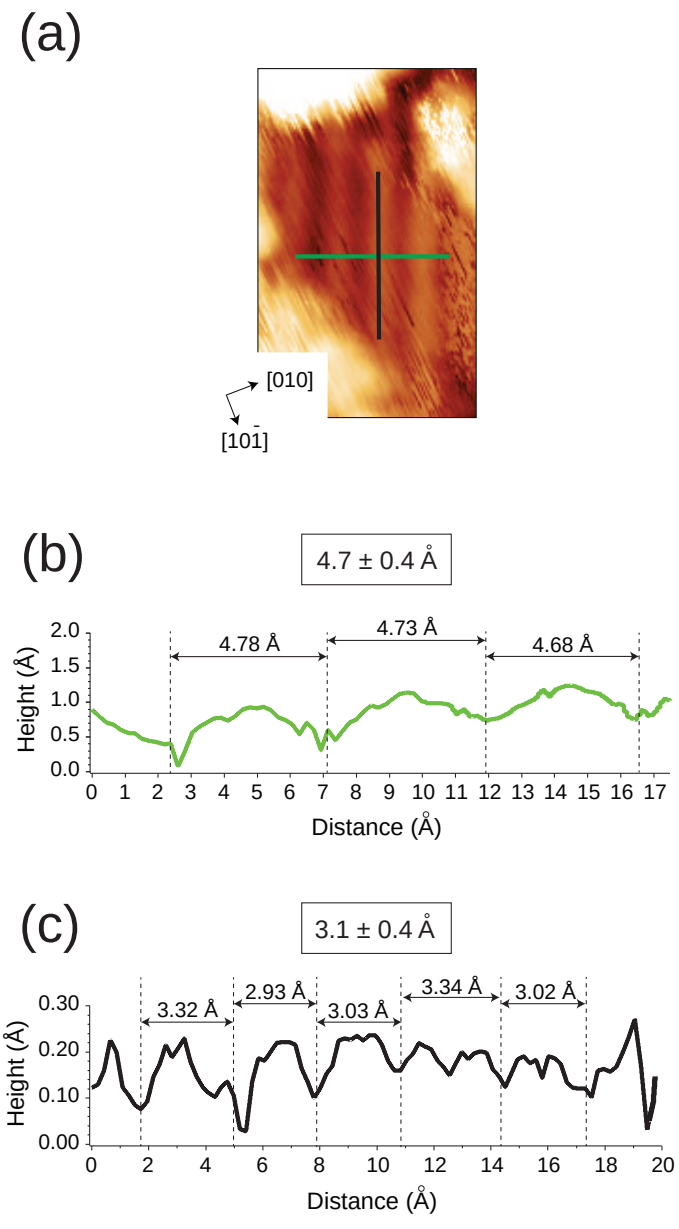

Figure 6.9: STM tip pulsing (+10 V, >50 nA, 200 ms) on electron irradiated A_{101} to form a proposed region of R_{100} (1 × 1). (a) 2.5 × 4.0 nm^2 STM image (V_s = +1.6 V, I_t = 0.1 nA) of an ordered region created by the pulse. The green line represents the line profile depicted in (b). The black line represents the line profile depicted in (c).

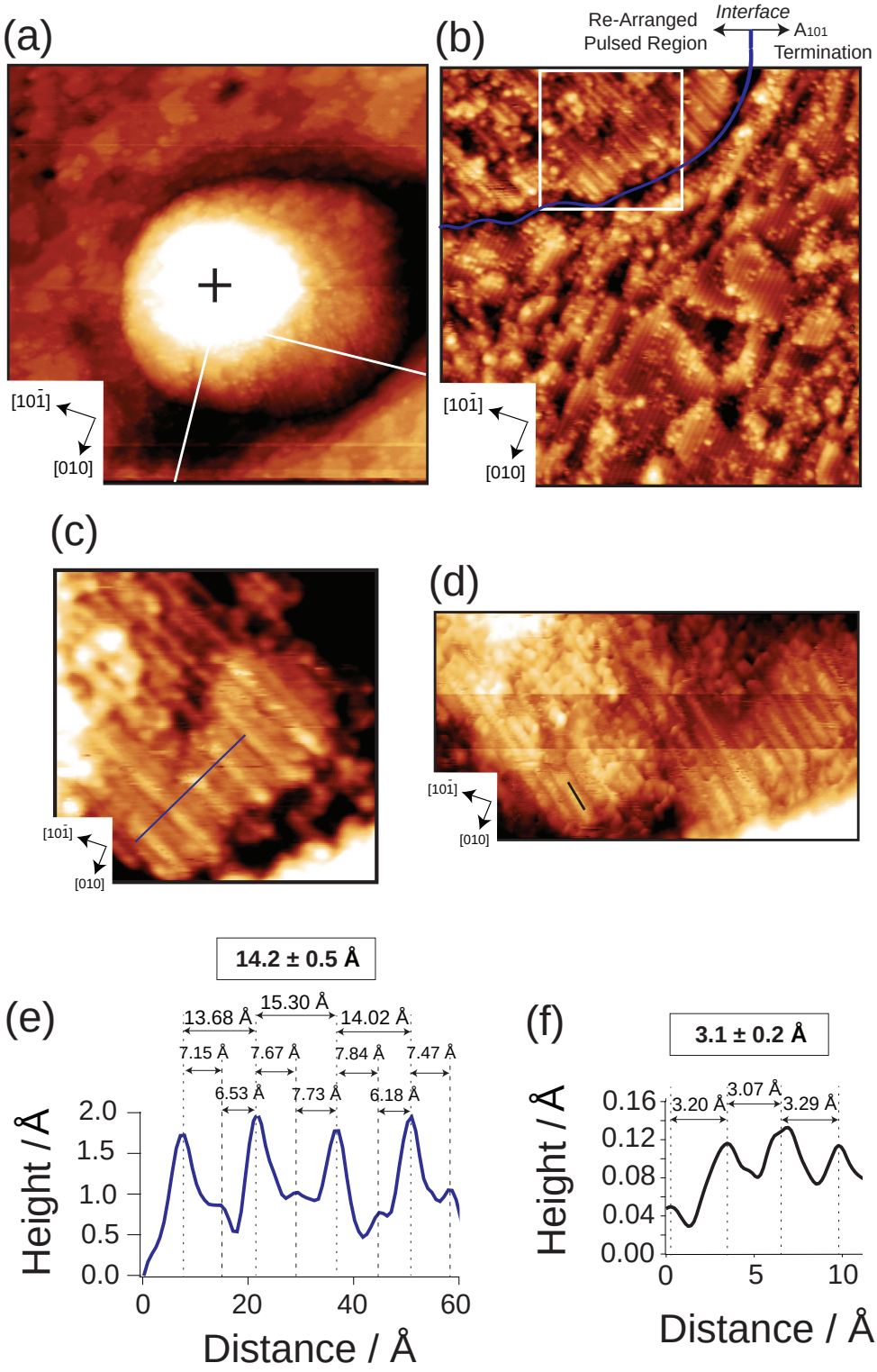

Figure 6.10: STM tip pulsing (+10 V, 50 nA, 200 ms) on electron irradiated A_{101} to form a proposed region of R_{100} $(1 \times 3)^{ß}$. (a) 69 × 71 nm^2 STM image (V_s = +1.6 V, I_t = 0.1 nA) of pulsed region ('+': pulse epicentre). (b) 38 × 39 nm^2 STM image (V_s = +1.6 V, I_t = 0.1 nA) indicating the A_{101} / pulsed region interface. (c) 12.5 × 12.5 nm^2 and (d) 22 × 12 nm^2 STM image (V_s = +1.6 V, I_t = 0.1 nA) showing order in the pulsed region. (e and f) Line profiles corresponding to blue and black line in '(c)' and '(d)', respectively. The black + represents the pulse epicentre. Adapted from previous work in Thornton Group.[57]

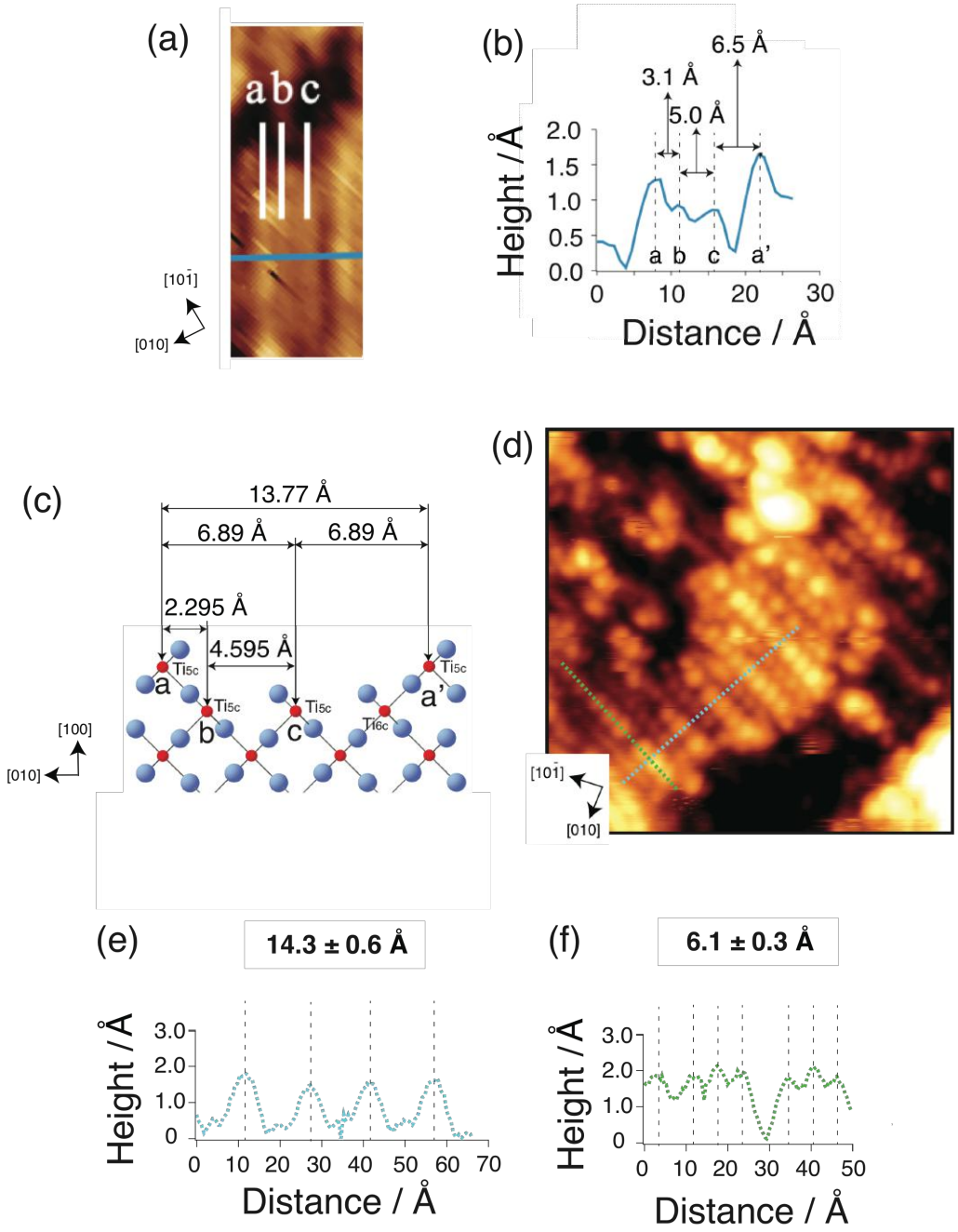

Figure 6.11: STM tip pulsing (+ 10 V, >50 nA, 200 ms) on electron irradiated A_{101} to form a proposed region of R_{100} $(1 \times 3)^{ß}$. (a) STM image (V_s = +1.6 V, I_t = 0.1 nA) of order in the pulsed region with its line profile and model in (b) and (c), respectively. (d) 14 × 14 nm^2 STM image (V_s = +1.6 V, I_t = 0.1 nA) of pulsed region after saturation coverage of AA. Line profiles (e and f) show an ordered overlayer with a (×2) periodicity along the rows as is seen in line profile (f). Adapted from previous work in Thornton Group.[57]

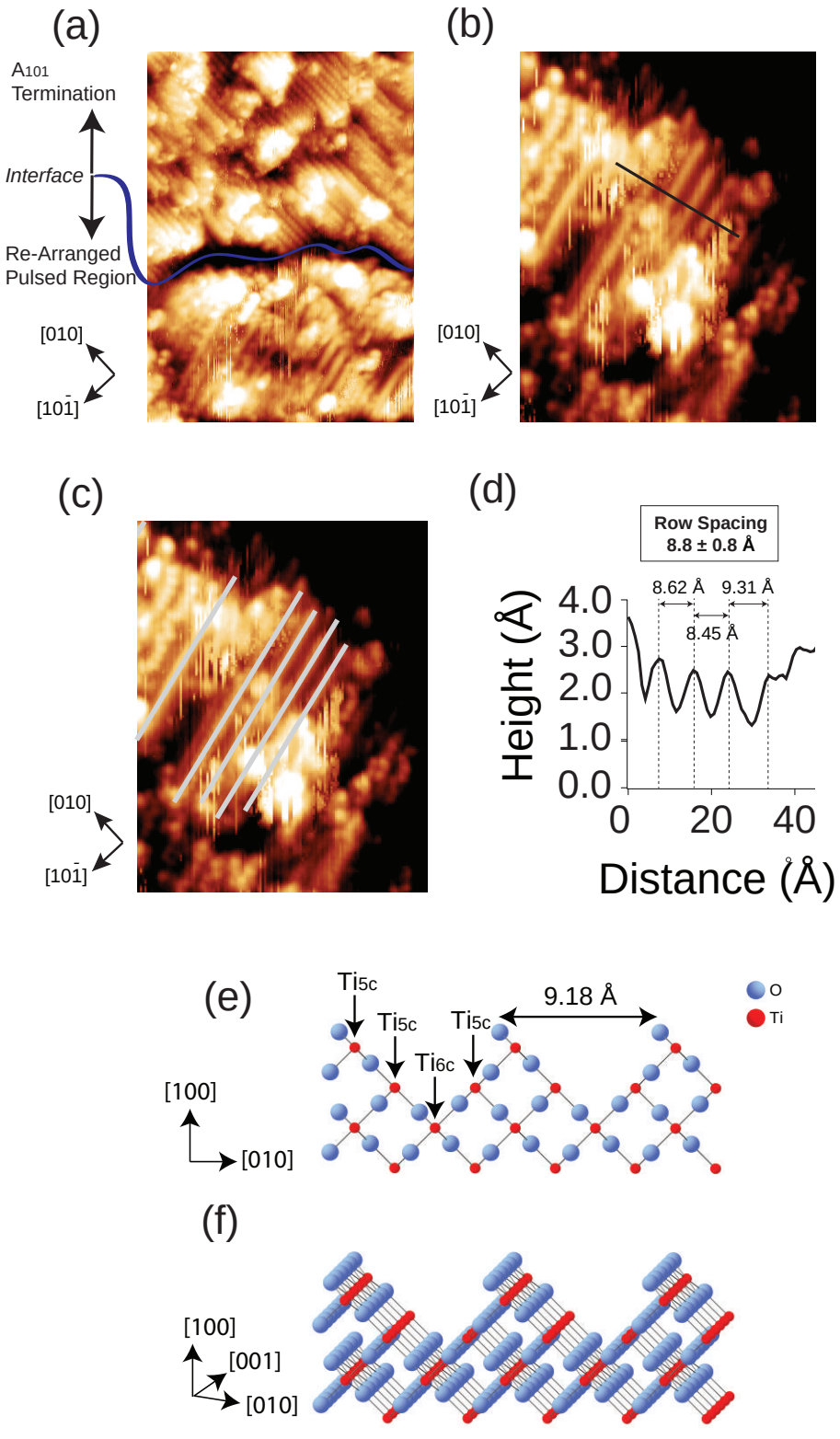

Figure 6.12: STM tip pulsing (+ 10 V, >50 nA, 200 ms) on electron irradiated A_{101} to form a proposed region of R_{100} (1 × 2). (a) 17 × 24 nm^2 STM image (V_s = +1.6 V, I_t = 0.1 nA) of pulsed region indicating the A_{101} / pulsed region interface. (b and c) 10.6 × 13.5 nm^2 STM image (V_s = +1.6 V, I_t = 0.1 nA) showing order (highlighted by grey lines in (c)) in the pulsed region. The line profile of the black line in '(b)' highlights the row spacing. (e and f) Proposed model for the R_{100} (1 × 2) surface.

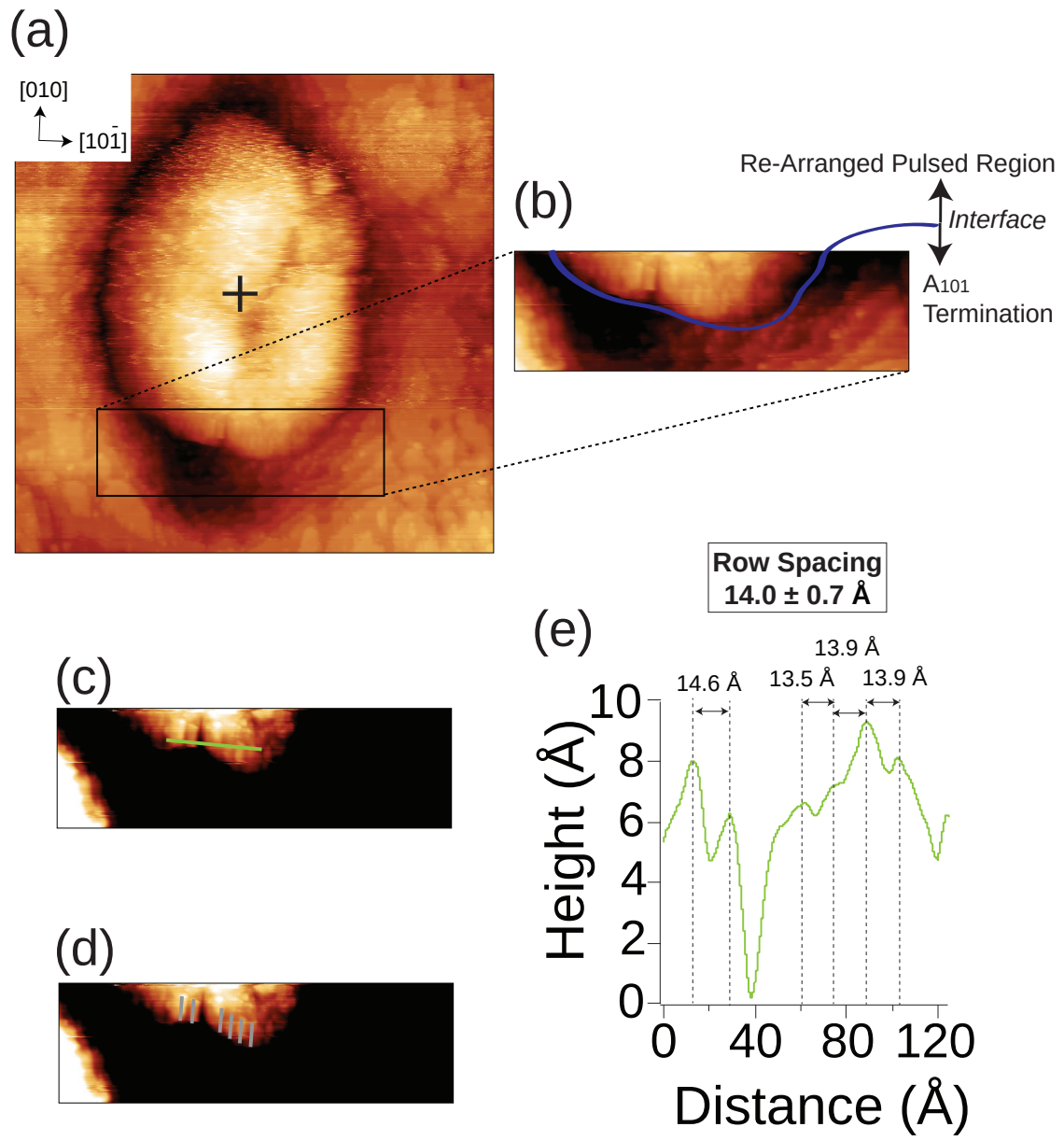

Figure 6.13: STM tip pulsing (+ 10 V, >50 nA, 200 ms) on electron irradiated A_{101} to form a proposed region of R_{100} (1 × 3). (a) 90 × 90 nm^2 STM image (V_s = +1.6 V, I_t = 0.1 nA) of pulsed region ('+': pulse epicentre). (b-d) 50 × 15 nm^2 STM images (V_s = +1.6 V, I_t = 0.1 nA) showing the (b) A_{101} / pulsed region interface, (c) Green line represents the line profile shown in (e). (d) Grey lines indicating the ordered rows. The black + represents the pulse epicentre.

The presented structures in the pulsed region indicate that R_{100} can be preferentially grown on electron irradiated A_{101} via STM tip manipulation. We propose the formation of an R_{100} thin film on single crystal A_{101}. Thin film TiO_2 growth is known to be dependent on the underlying substrate. For example, thin films of TiO_2 on $SrTiO_3$ (001) preferentially gives rise to A_{001} as opposed to R_{110} or A_{101}, where the former is the most thermodynamically stable and abundant TiO_2 face, and the latter is considered the most stable anatase TiO_2 face.[50, 51] Alternatively, W (100) – O (2 × 1) gives rise to thin films of R_{110}.[64] A_{001} thin films grown on $LaAlO_3$ (001) or $SrTiO_3$ (001) present evidence of R_{100} nucleation at surface defect sites.[27, 28]

Before considering rutile growth on anatase, let us first consider why STM tip manipulation does not re-arrange the Ti and O atoms to re-generate A_{101}. The preferred growth of TiO_2 should adopt a similar geometry to the A_{101} substrate. STM tip pulsing of as-prepared A_{101} results in only amorphous regions being created whilst STM tip pulsing of electron irradiated A_{101} results in the creation of ordered regions that we assign to R_{100} - a phenomenon that can be explained in thermodynamic terms. On the as-prepared surface, STM tip manipulation provides sufficient energy to destabilise the surface, however, the pulsed region is unable to overcome the transition barrier to rutile and hence results in an amorphous region being created where surface atoms have insufficient energy to revert to A_{101} (1 × 1). However, the outer regions of the pulsed area maintain A_{101} (1 × 1). An electron irradiated A_{101} surface is destabilised (with increased surface energy) such that STM tip pulsing allows for the surface atoms to overcome the irreversible anatase to rutile transition with greater ease than on the as-prepared surface. Thus, ordered and amorphous regions are created at or near the tip pulse epicentre whereas A_{101} (1 × 1) is observed beyond this.

Theoretical calculations[4] of the rutile/anatase interface where R_{100} in the [010] direction is aligned parallel and perpendicular to the A_{101} [$\bar{1}$01] direction presents favourable adhesion energies of 1.5 J m^{-2} and percentage mismatches of 1%. These calculations indicate that R_{100} growth on A_{101} is possible and favourable. The formation of different reconstructions of R_{100} in the pulsed regions requires us to consider the behaviour of rutile surfaces. UHV prepared R_{011} exhibits a radical reconstruction in UHV where the surface yields a (2 × 1) termination.[65] Alternatively, R_{110} and R_{100} have been shown to exhibit a (1 × 1) termination. The formation of R_{110} (1 × 2) and R_{100} (1 × 3)^{MF} occurs after high annealing temperatures (> 1300 K) or after numerous cycles of Ar^+ sputtering and annealing (> 1000 K) and is largely based on the oxygen density of the crystal.[2] Annealing induces oxygen ejection from the crystal that in turn induces the surface to reconstruct. On this principle, the termination of the R_{100} ordered regions is attributed to the local density of oxygen atoms. STM tip manipulation provides the surface atoms sufficient energy to re-order, however, the form of ordering would be dependent on the local (in STM terms) ratio of Ti and O atoms. In other words, the formation of a specific R_{100} termination depends on the number and type of atoms that are within the sphere of influence of the STM tip pulsing.

Considering the interface structure between the A_{101} and ordered structure in the pulsed region, our STM evidence suggests the existence of a disordered (amorphous) layer between the two structure that is a few Å thick. This is largely consistent with DFT calculations which broadly predict the existence of a disordered interface.[4, 29-31] On a similar note, the growth of R_{100} on A_{101} is likely to possess an amorphous interface a few Å thick. It is expected that this amorphous layer determines the direction of the R_{100} rows. As is seen in Figures 6.08 - 6.13, the row direction for the ordered regions (with respect to the A_{101} [010] direction) differs for each scenario.

c. Annealing High Energy Electron Irradiated Anatase TiO_2 (101)

A_{101} has been exclusively discussed to possess a (1 × 1) termination with no reports suggesting the existence of a surface reconstruction. After annealing up to 850 K for 10 min, electron irradiated R_{110} (1 × 1) has been shown to re-construct to give a (1 × 2) termination.[36] On this principle, the 3 keV (35 min) electron irradiated A_{101} surface was annealed to 850 K for 10 min (see Figure 6.14 (a)) and subsequently to 1000 K for 10 min (see Figure 6.14 (b)) to probe if electron irradiation induced oxygen deficiency can lead to an A_{101} reconstruction.

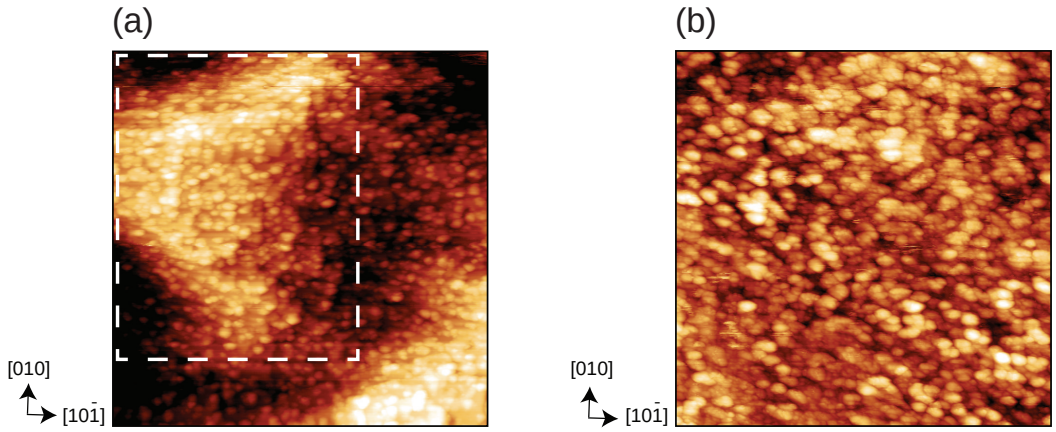

Figure 6.14: 75 × 75 nm^2 STM image (V_s = +1.6 V, I_t = 0.1 nA) of electron irradiated A_{101} after 35 min electron irradiation at 3 keV (see Section 3.2.3) and annealing at (a) 850 K for 10 min followed by annealing at (b) 1000 K for 10 min. White dashed box in (a) highlights a region where characteristic trapezoidal A_{101} terraces are faintly observable.

Annealing the surface to 850 K for 10 min resulted in an increased roughening of the surface such that it was no longer possible to obtain atomically resolved images of the surface. Nonetheless, it was possible to obtain terrace resolution images of the surface where it is possible to observe faint remnants of the characteristic trapezoidal terraces of A_{101}. Annealing the surface for a further 10 min at 1000 K results in the creation of an increasingly amorphous surface where it is no longer possible to observe surface terraces.

The surface appears to be covered in agglomerated amorphous regions. No evidence of an A_{101} surface reconstruction was observed. This corroborates the literature where A_{101} is not known to exhibit any surface reconstructions.

d. Summary

In this presented work, we present evidence of the formation of a R_{100}/A_{101} interface created via the STM tip manipulation of electron irradiated A_{101}. Our findings indicate that R_{100} can be preferentially grown on A_{101}, where the termination of the R_{100} is dependent on the local ratio of Ti : O atoms. Characterisation of the electron irradiated A_{101} surface indicates surface roughening where the surface possesses nano-cracks and exhibits numerous amorphous clusters. Nonetheless, atomically resolved regions of A_{101} (1 × 1) are continued to be observed with STM. STM tip pulsing of electron irradiated A_{101} gives rise to a mound on the surface, in whose immediate vicinity, regions of order are observed. These ordered regions have row spacing of ~4.5 Å, ~9.0 Å and ~13.5 Å which we assign to R_{100} (1 × 1), R_{100} (1 × 2) and R_{100} (1 × 3), respectively and are typically created in ~1/100 tip pulses. See Figure 6.15 for a summary of created ordered regions.

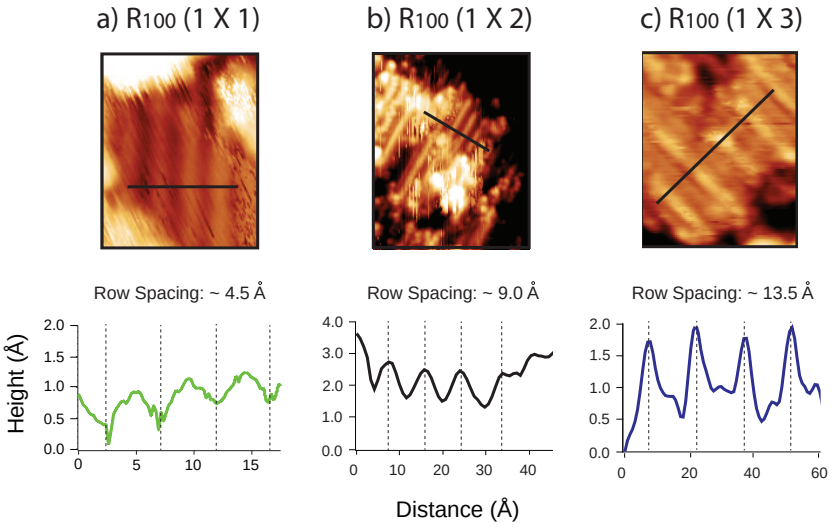

Figure 6.15: Summary showing three ordered regions created via STM tip pulsing (+ 10 V, >50 nA, 200 ms) on electron irradiated A_{101}.

6.3.2 Rutile TiO_2 (100) and its Interface with Acetate Molecules

The adsorption and photo-activity of AA and TMAA on various TiO_2 surface has received much experimental attention - in particular with STM (see Section 6.1.2.d). However, an STM perspective of AA and TMAA adsorption on R_{100} is thus far lacking. Experimental findings of carboxylic acid adsorption on R_{100} are limited.[66] In this section, an STM perspective of AA and TMAA adsorption on R_{100} (1 × 1) and $(1 \times 3)^{MF}$ is presented.

a. As-Prepared Rutile TiO_2 (100)

STM of rutile TiO_2 surfaces has largely focussed on R_{110} and R_{011}.[1] On the contrary, STM of R_{100} is less well pronounced due to the relatively more difficult preparation procedure and complex set of terminations. To this extent, we will briefly discuss our preparation procedure for preparing the (1 × 1) and $(1 \times 3)^{MF}$ terminations. UHV preparation of R_{100} (1 × 1) and $(1 \times 3)^{MF}$ are largely temperature dependent where the density of oxygen vacancies dictates surface reconstruction - a behaviour that is reproduced on other rutile faces such R_{110} where oxygen deficiency results in a (1 × 2) termination followed by a (1 × 2) cross-linked termination.[1, 2]

Starting from a non-reduced R_{100} single crystal, Ar^+ sputtering and annealing (<973 K) cycles gives rise to R_{100} (1 × 1). Previously, oxygen annealing has also been discussed to allow for R_{100} (1 × 1) however such surfaces, as of yet, have not been characterised by STM.[67] As UHV annealing induces the crystal reduction, repeated Ar^+ sputtering and annealing (973 K) will eventually induce a surface reconstruction - as is the case with R_{110}. Figure 6.16 illustrates a ball and stick model and STM images of the R_{100} (1 × 1) surface. The surface consists of bright and dark rows with a separation of 4.59 Å in the [010] direction and 2.96 Å in the [001] direction.

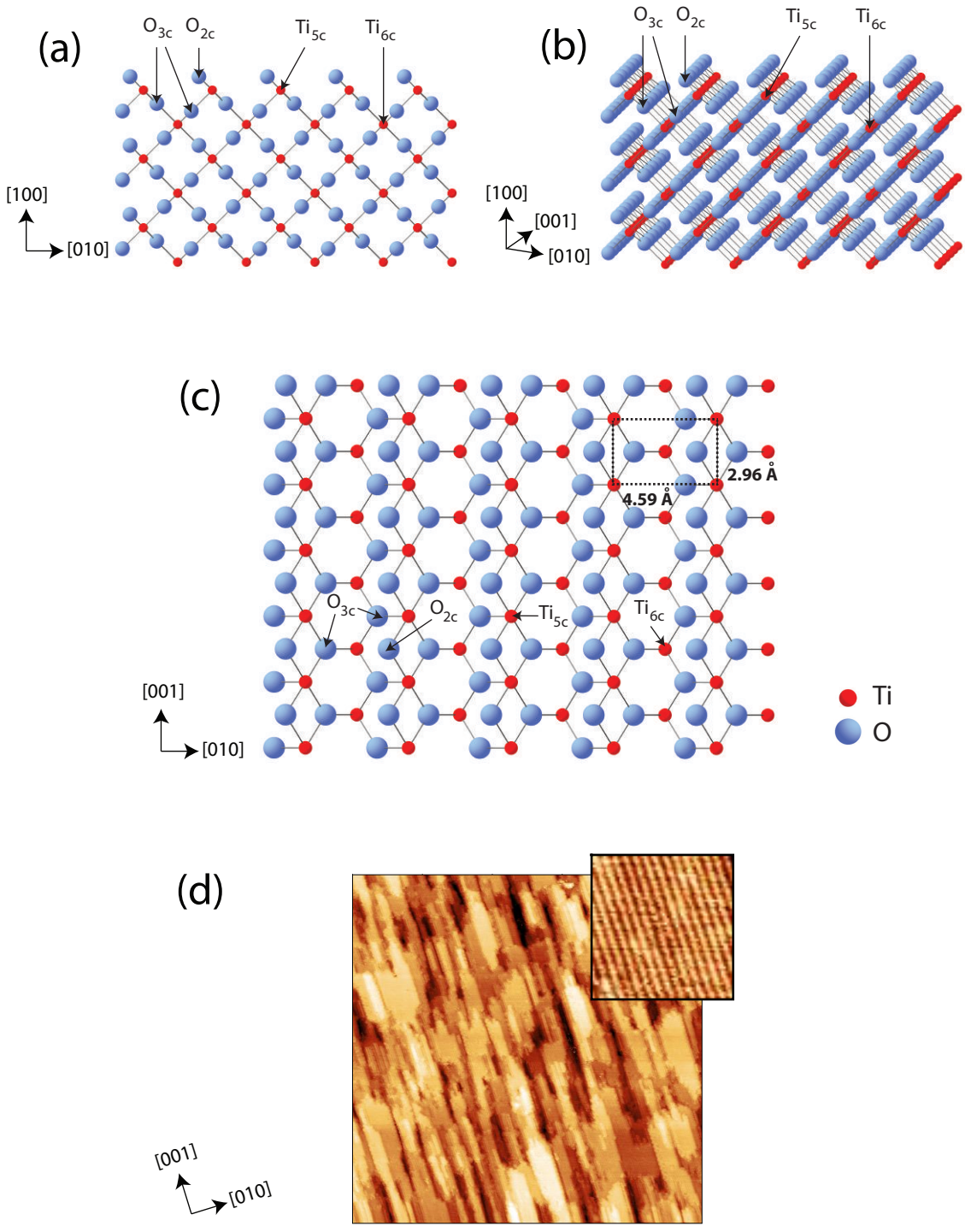

Figure 6.16: Ball and stick illustration depicting the R_{100} (1 × 1) surface via different view-points with surface atoms Ti_{6c}, Ti_{5c}, O_{3c} and O_{2c} labelled. (a) Side view of surface. (b) Tilted view of surface with respect to (a). (c) Aerial view of surface with surface unit cell in black dashed box. (d) 100 × 100 nm^2 STM image of R_{100} (1 × 1) (V_s = +1.6 V, I_t = 0.1 nA) with inset (6 × 6 nm^2) illustrating 'atomically resolved' features.

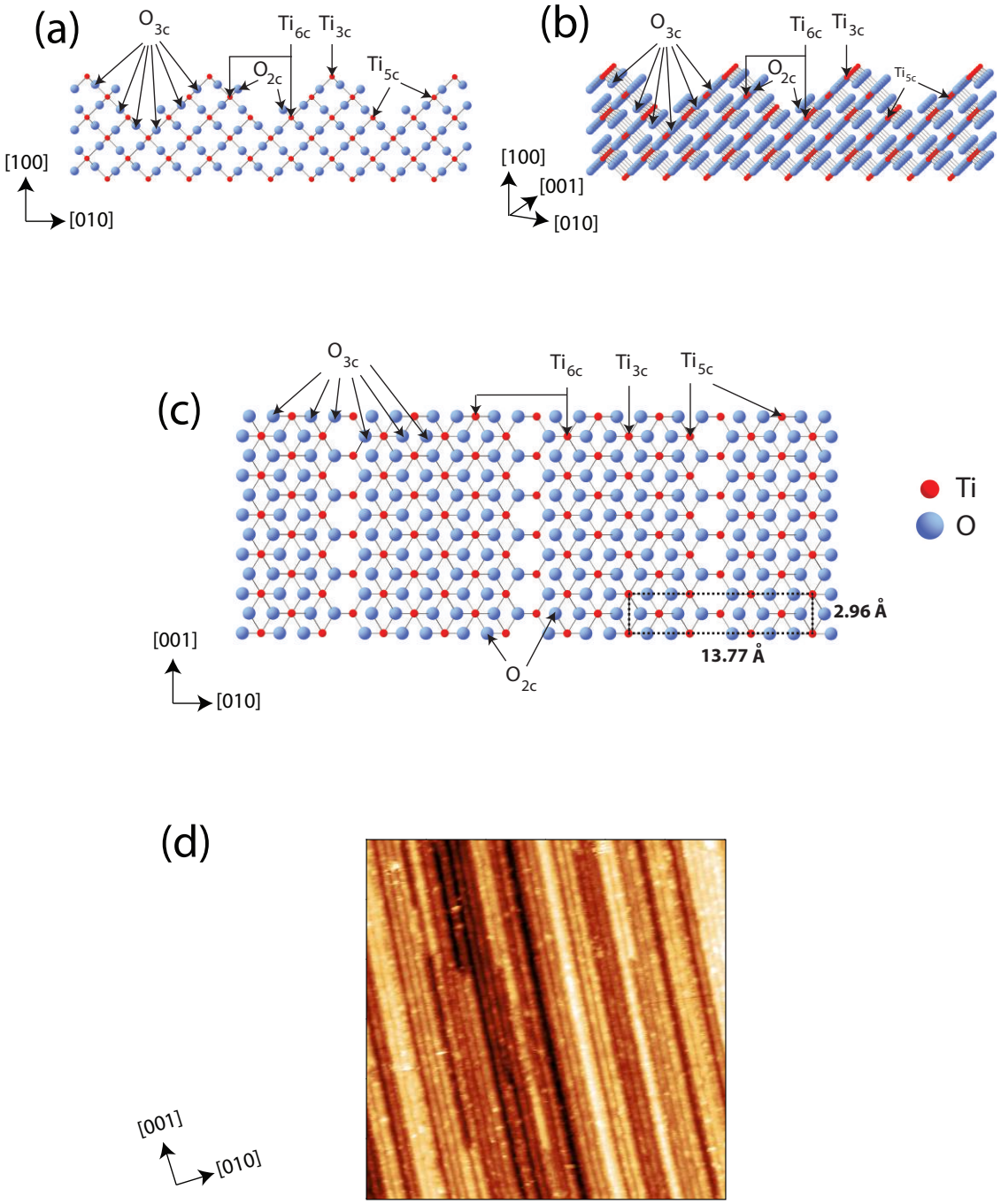

Figure 6.17: Ball and stick illustration depicting the R_{100} $(1 \times 3)^{MF}$ surface via different view-points with surface atoms Ti_{6c}, Ti_{5c}, Ti_{3c}, O_{3c} and O_{2c} labelled. (a) Side view of surface. (b) Tilted view of surface with respect to (a). (c) Aerial view of surface with surface unit cell in black dashed box. (d) 50×50 nm^2 STM image of R_{100} $(1 \times 3)^{MF}$ (V_s = +1.6 V, I_t = 0.1 nA).

The R_{100} $(1 \times 3)^{MF}$ can be prepared by Ar^+ sputtering and annealing the surface to > 1273 K for prolonged periods. In UHV, this induces an R_{100} $(1 \times 3)^{MF}$ surface which is considered the easiest of all R_{100} terminations to prepare and is hence the most widely investigated. Figure 6.17 illustrates a ball and stick model and STM images of the R_{100} $(1 \times 3)^{MF}$ surface. STM of these surface yields thick strands running along the [001] directions with a spacing of 13.77 Å and a spacing of 2.96 Å in the [001] direction. At annealing temperatures of 1273 K, the surface is $(1 \times 3)^{MF}$ with little or none of the 'intermediate', $(1 \times 3)^{\alpha}$ and R_{100} $(1 \times 3)^{ß}$ (see Section 6.1.2.c) terminations occurring. As 'intermediate' reconstructions, these phases are not stable at 1273 K.

b. Acetate Adsorption on Rutile TiO_2 (100) (1 × 1)

Figure 6.18 presents three possible acetate binding geometries on R_{100} (1 × 1) - dissociative bi-dentate adsorption, associative adsorption in geometry I (G-I) and associative adsorption in geometry II (G-II). Dissociative adsorption involves AA/TMAA dissociating by losing the proton on the OH group. Subsequently, each O atom on the AA/TMAA, adsorbs to a Ti_{5c} atom (see Figure 6.18 (a-c)). Associative adsorption consists of adsorption without dissociation such that the AA/TMAA O atom adsorbs to a Ti_{5c} site whereas the OH species forms a hydrogen bond with the O_{2c}. The geometry of the AA/TMAA molecule determines the adsorption as G-I (see Figure 6.18 (d-f)) or G-II (see Figure 6.18 (g-i)).

Figure 6.19 (a) illustrates STM images obtained for the R_{100} (1 × 1) and AA interface at saturation coverage. Figure 6.19 (a) shows that the adsorbed AA molecules presents an ordered overlayer on R_{100} (1 × 1) with a spacing in the [001] direction of 5.8 ± 0.2 Å and a spacing of 4.5 ± 0.1 Å in the [010] direction and a coverage of 0.37 ± 0.02 ML. Given the R_{100} (1 × 1) surface cell dimensions of 2.96 Å × 4.59 Å, the overlayer is adjudged to

maintain a (2 × 1) periodicity. Dissociatively adsorbed AA molecules have been reported to give rise to a (2 × 1) overlayer on R_{110} at room temperature in UHV[1, 2] and at the solid/liquid interface.[46, 53] Additionally, dissociatively adsorbed AA (bi-dentate adsorption) gives rise to a locally ordered (2 × 1) overlayer on A_{101} when dosing AA on the surface at 420 K.[49] At saturation coverage, G-I and G-II associative mono-dentate adsorption is expected to create a (1 × 1) overlayer on R_{100} whereas dissociative bi-dentate adsorption is expected to create a (2 × 1) overlayer of AA - as is widely observed on TiO_2 surfaces. Hence, the formation of a (2 × 1) overlayer (see Figure 6.19) indicates dissociative bi-dentate AA adsorption - as is seen on R_{110}[1, 2, 46, 53], A_{101}[49] and A_{001}[51].

Figure 6.19 (e and f) highlight defects in the (2 × 1) AA overlayer with a corresponding ball and stick model describing the nature of the defect. Such defects in the overlayer can occur due to underlying surface defects. The adsorbed AA can be adjudged to be bound strongly to the surface (as is expected with bi-dentate dissociative adsorption) as successive scans of the surface indicate little or no changes in the overlayer structure (immobile overlayer) on the scale of a few hours. STM tip manipulation has been widely utilised on R_{110}[1] and A_{101}[41] to induce chemical reactions and desorption of adsorbed species. Similarly, STM tip pulsing of the overlayer indicated little or no change at tip pulses up to +6 V. This further highlights the nature of the strong bonding between the surface and AA.

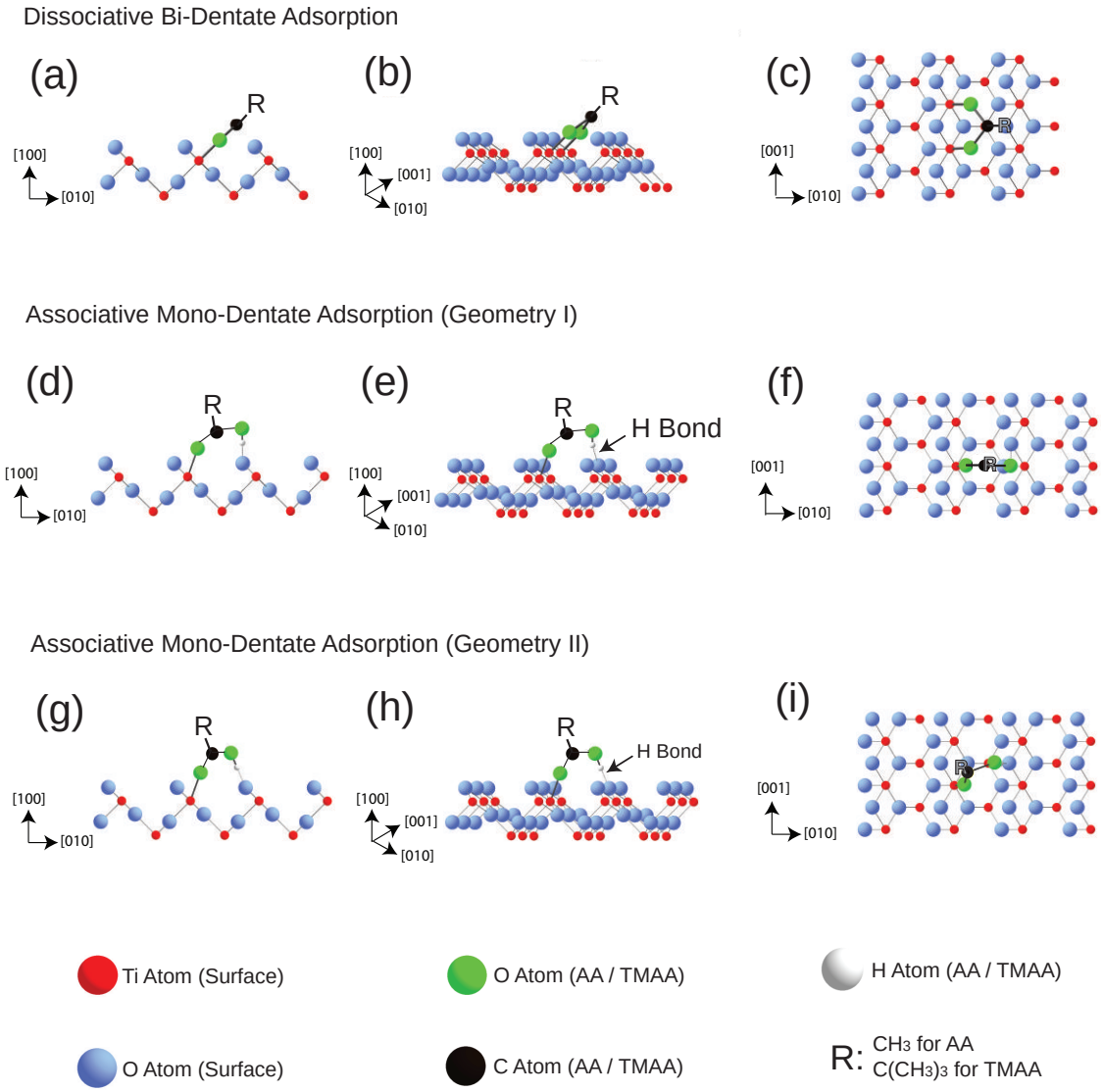

Figure 6.18: Ball and stick illustration depicting adsorption geometries of AA and TMAA on the R_{100} (1 × 1). (a, b and c) Different viewpoints depicting AA and TMAA adsorption in a dissociative bi-dentate manner. (d, e and f) Different viewpoints depicting AA and TMAA adsorption in an associative mono-dentate (G-I) manner. (g, h and i) Different viewpoints depicting AA and TMAA adsorption in an associative mono-dentate (G-II) manner.

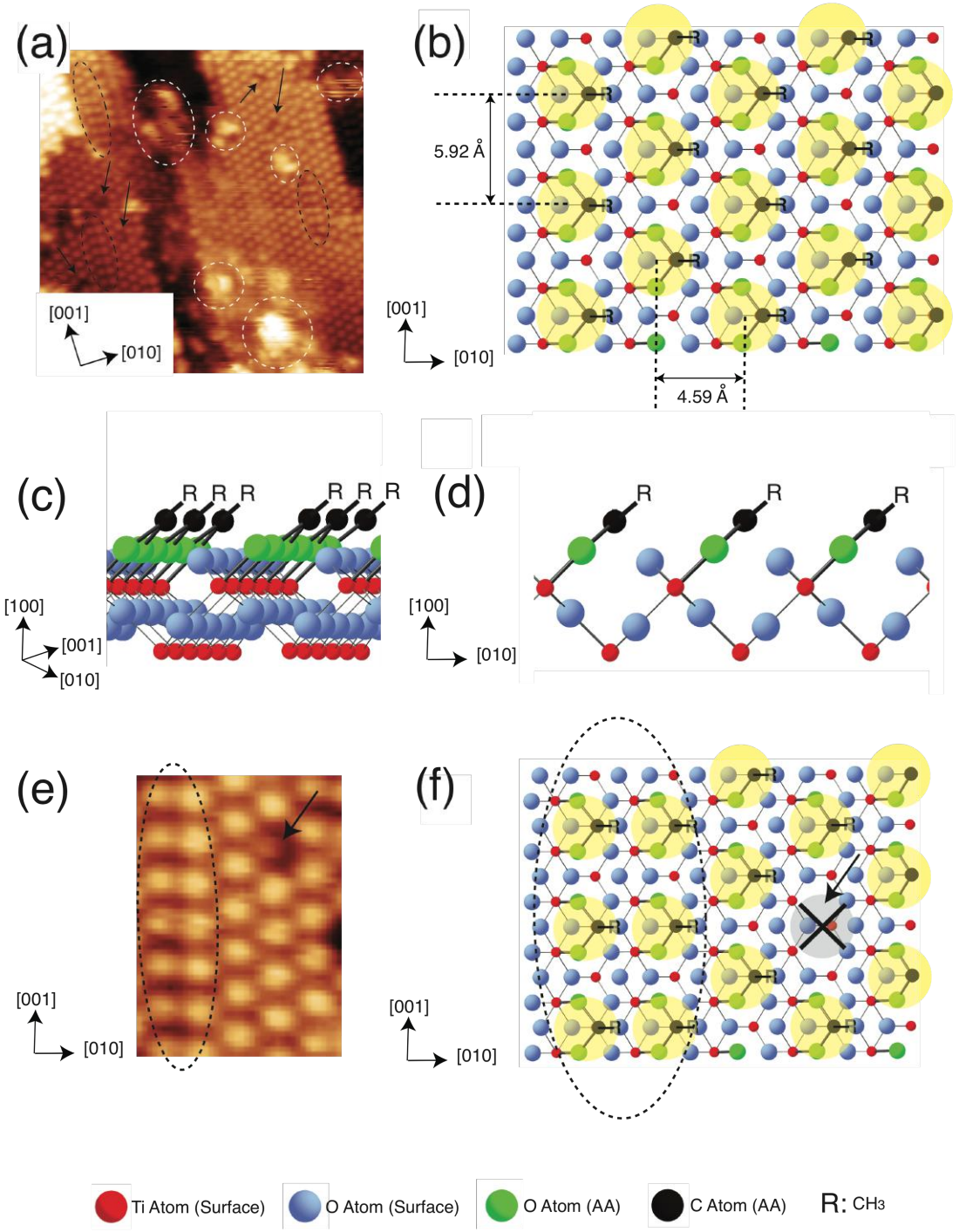

Figure 6.19: (a) 15 × 15 nm^2 STM image of R_{100} (1 × 1) (V_s = +1.6 V, I_t = 0.1 nA) after saturation coverage of AA (1 - 2 L AA exposure). (b) Ball and stick model with yellow circles highlighted the formation of the (2 × 1) overlayer observed in '(a)'. (c and d) Different viewpoints of '(b)'. (e) 2.4 × 3.4 nm^2 STM image (V_s = +1.6 V, I_t = 0.1 nA) of defects in the (2 × 1) AA overlayer. (f) Ball and stick model with yellow circles highlighted the formation of the defects in the (2 × 1) overlayer observed in '(e)'. Dashed black ovals highlight regions with a break in the zig-zag periodicity in the [010] direction. Black arrows point to regions with absent AA adsorbate. Dashed white oval refer to amorphous regions likely caused by AA agglomeration around surface defective regions.

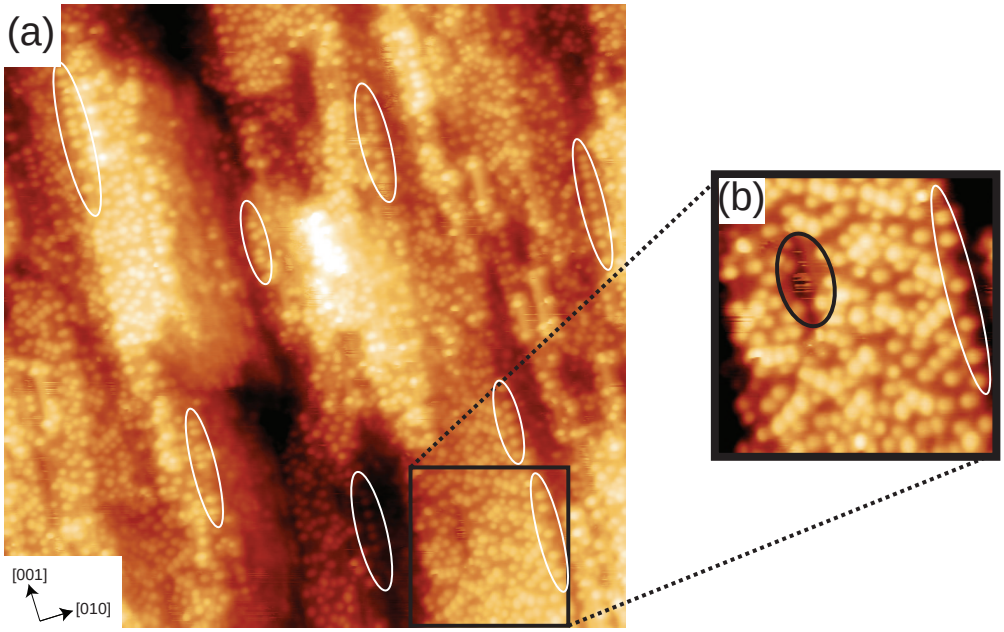

Figure 6.20: (a) 40 × 40 nm^2 and (b) 10 × 10 nm^2 STM image of R_{100} (1 × 1) (V_s = +1.6 V, I_t = 0.1 nA) after saturation coverage of TMAA (1 - 2 L TMAA exposure). White ovals depict linear chains of TMAA forming in the [001] direction. Black oval highlights a defect region with minimal TMAA adsorption.

Figure 6.20 illustrates STM images obtained for the R_{100} (1 × 1) and TMAA interface at saturation coverage where the adsorbate binds to the surface in a disordered manner at a coverage of 0.27 ± 0.04 ML. The disordered nature of TMAA adsorption on R_{100} (1 × 1) is in stark contrast to that observed with AA (see Figure 6.19). Interestingly, AA and TMAA adsorption on R_{110} (1 × 1) both form a (2 × 1) overlayer. However, this behaviour appears not to be reproduced by R_{100} (1 × 1) and can be considered to be due to the smaller surface cell of R_{100} (2.96 Å × 4.59 Å) when compared to R_{110} (2.96 Å × 6.49 Å). Thus steric effects associated with the tri-methyl group on TMAA prevents the formation of an ordered overlayer making a disordered overlayer more favourable. The binding of TMAA on R_{100} (1 × 1) is unclear. From AA on R_{100} (1 × 1) (see Figure 6.19), dissociative bi-dentate adsorption would be predicted. However, the disordered nature of the overlayer suggests a mixed associative and dissociative adsorption. As is the case with the R_{100} (1

× 1) / AA interface, the adsorbed TMAA molecules are largely immobile over successive scans on the scale of a few hours. Although the adsorption of TMAA on R_{100} is largely disordered there are certain regions (encircled in white ovals in Figure 6.20) that highlight the existence of linear chains of TMAA that exhibit quasi-order in the [001] direction. This ordering is exclusively observed at the step edges and can be attributed to there being less steric hindrance at the step edge.

c. Acetate Adsorption on Rutile TiO_2 (100) $(1 \times 3)^{MF}$

Figure 6.21 presents three possible acetate binding geometries on R_{100} $(1 \times 3)^{MF}$ - dissociative bi-dentate adsorption, associative adsorption in G-I and associative adsorption in G-II. As is the case with R_{100} (1 × 1) (see Figure 6.18), dissociative adsorption yields bi-dentate adsorption whilst associative adsorption yields mono-dentate adsorption where the geometry of the AA/TMAA molecule determines the adsorption as G-I (see Figure 6.21 (d-f)) or G-II (see Figure 6.21 (g-i)).

Figure 6.22 illustrates STM images of R_{100} $(1 \times 3)^{MF}$ exposed to AA at saturation coverage. This gives rise to a surface AA coverage of 0.19 ± 0.03 ML. As is seen in Figure 6.22 (b), the bound AA molecule exhibits partial local order on the surface where regions of order are encircled in white ovals. The local ordered nature of the adsorbed AA indicates that the surface is expected to exhibit mixed associative and dissociative adsorption. The order is largely seen in the [001] directions which, as was seen with the R_{100} (1 × 1) / AA interface, gives rise to a (×2) periodicity in the [001] direction with periodicity in the [010] direction remaining unchanged. AA order in the [010] direction is largely lacking and can largely be attributed to the positioning of the three adsorption sites (see Figure 6.22 (a)) such that successful adsorption at all three sites (or even two sites) is rare due to steric affects.

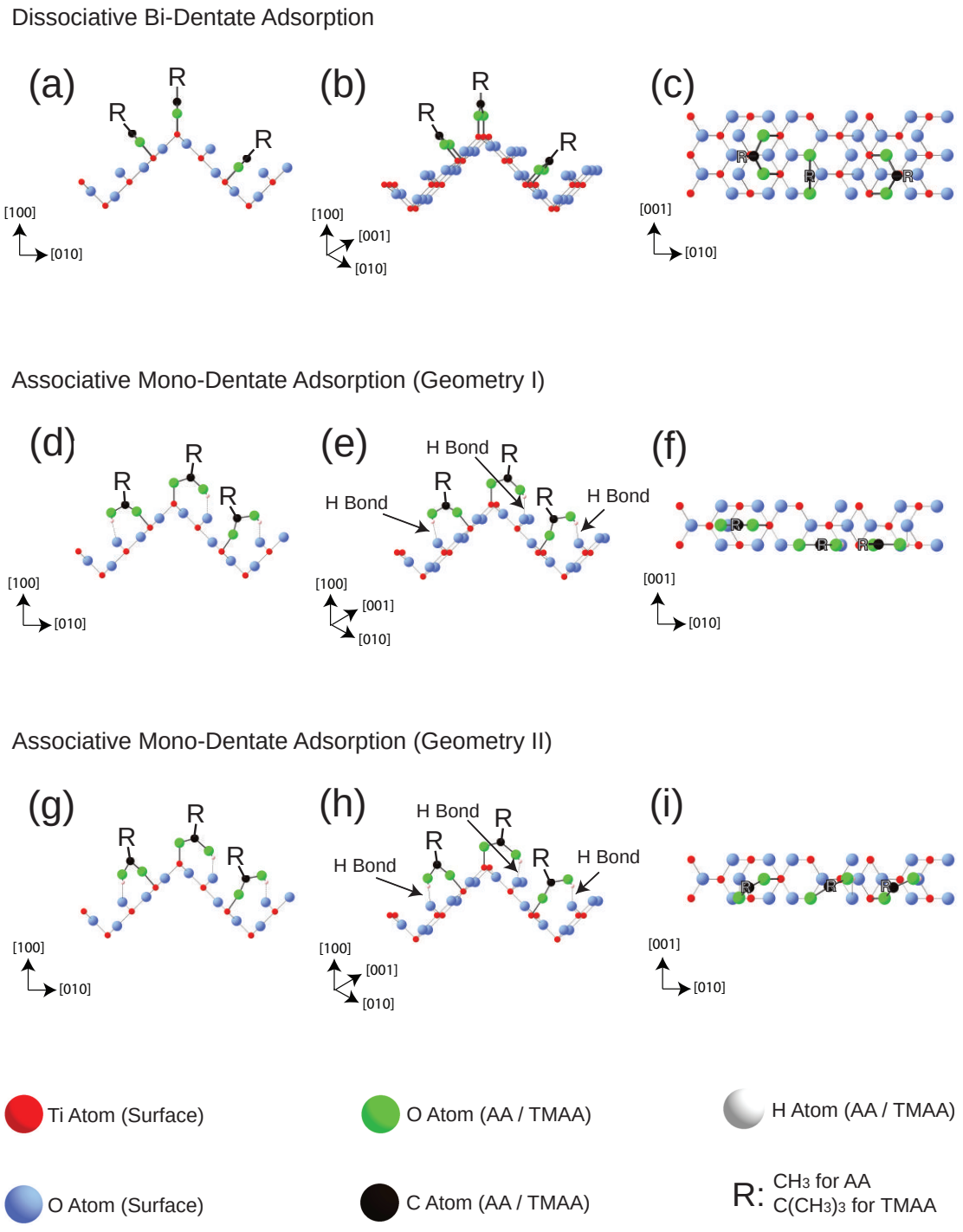

Figure 6.21: Ball and stick illustration depicting adsorption geometries of AA and TMAA on the R_{100} $(1 \times 3)^{MF}$. (a, b and c) Different viewpoints depicting AA and TMAA adsorption in a dissociative bi-dentate manner. (d, e and f) Different viewpoints depicting AA and TMAA adsorption in an associative mono-dentate (G-I) manner. (g, h and i) Different viewpoints depicting AA and TMAA adsorption in an associative mono-dentate (G-II) manner.

Figure 6.22 (c and d) gives a pictorial representation of an instance where AA binds to sites A, B and C. The labelled STM image and ball and stick model suggest that adsorption of AA in the ordered region adopts dissociative bi-dentate adsorption and conversely a (×2) periodicity in the [001] direction. As was seen with the R_{100} (1 × 1) / AA interface, the adsorbed AA molecules in the ordered overlayer are largely immobile with little or no changes in the overlayer structure on the scale of a few hours.

Figure 6.23 illustrates STM images of R_{100} $(1 \times 3)^{MF}$ exposed to TMAA at saturation coverage. This gives rise to a surface TMAA coverage of 0.15 ± 0.04 ML. As was seen with the R_{100} (1 × 1) / TMAA interface (see Figure 6.20), the adsorption of TMAA is largely disordered (marked with white ovals), however, partial order or linear chains can be observed in the [001] direction at the step edges and can be attributed to there being less steric hindrance at the step edge. Interestingly the surface further consists of non-linear chains of TMAA (see Figure 6.23 (b-d)). As was seen with the R_{100} (1 × 1) / TMAA interface (see Figure 6.20), the disordered nature of TMAA adsorption can be attributed to the bulky tri-methyl group that prevents the formation of a relatively more ordered overlayer. Additionally, as was seen for the R_{100} $(1 \times 3)^{MF}$ / AA interface (see Figure 6.22), steric hindrance factors associated with adsorption sites is also expected to prevent TMAA adsorption at all surface sites. Hence, the ML coverage obtained for both AA and TMAA adsorption is lower on R_{100} $(1 \times 3)^{MF}$ when compared to R_{100} (1 × 1). The disordered nature of the adsorbed TMAA indicates mixed associative and dissociative adsorption. The adsorbed TMAA presents little or no change over successive STM images on the scale of a few hours, thus suggesting strong surface adsorption.

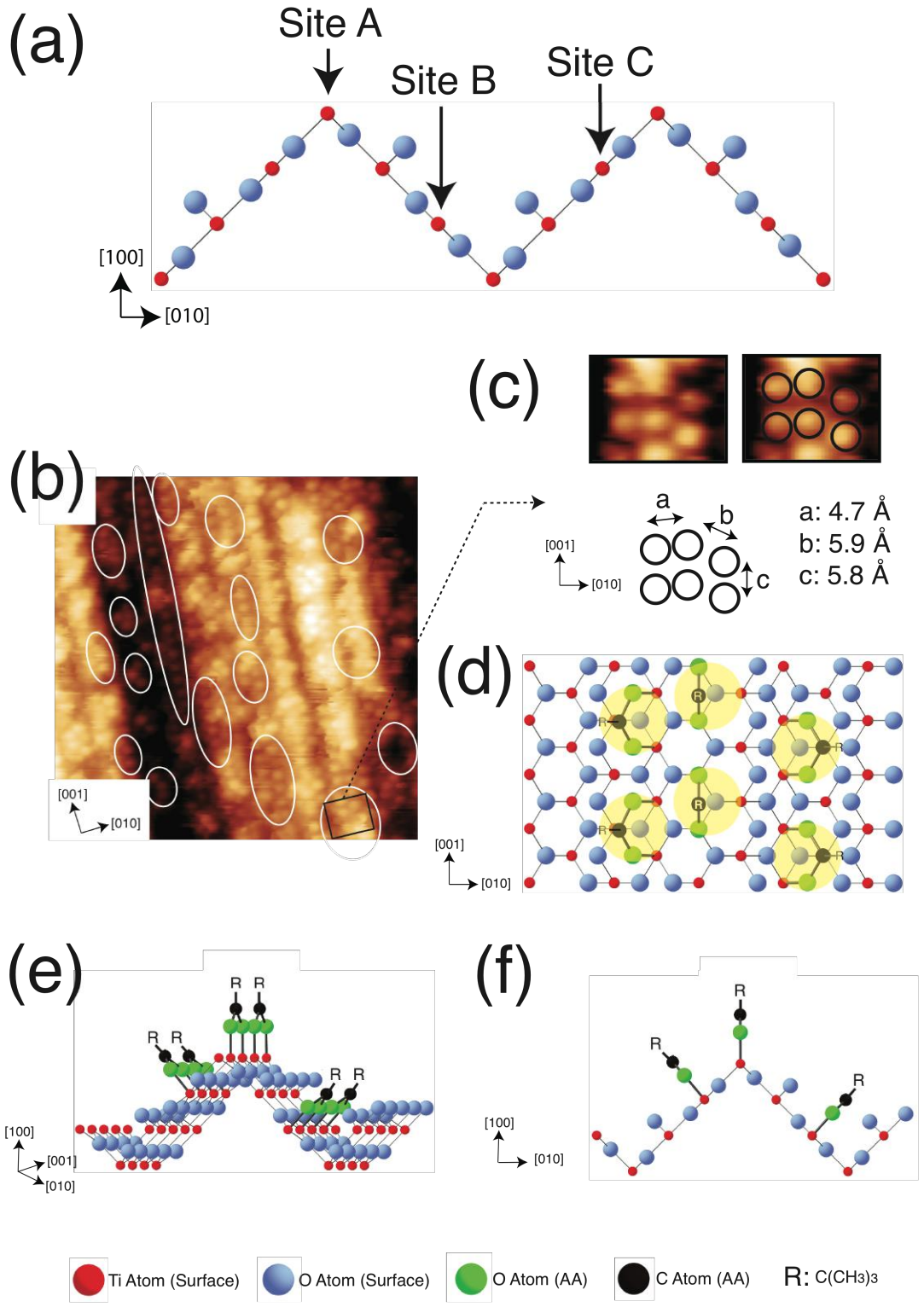

Figure 6.22: (a) Ball and stick model of R_{100} $(1 \times 3)^{MF}$ with three AA adsorption sites labelled. (b) 15 × 15 nm^2 STM image of R_{100} $(1 \times 3)^{MF}$ (V_s = +1.6 V, I_t = 0.1 nA) after saturation coverage of AA (1 - 2 L AA exposure) with (c) showing a 2.0 × 1.5 nm^2 STM image where black circles highlight the adsorbed AA. (d) Ball and stick model with yellow circles highlighted the formation of the AA arrangement seen in '(c)'. (e and f) Different viewpoints of '(d)'. White ovals refer to regions with local ordering of the AA.

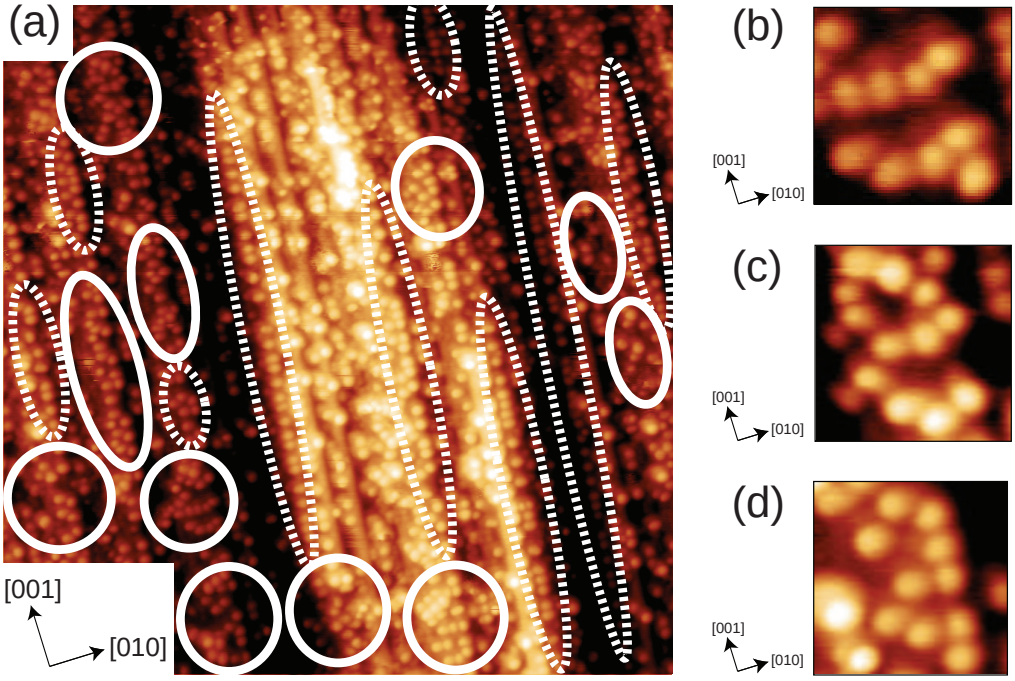

Figure 6.23: (a) 35 × 35 nm^2 STM image of R_{100} (1 × 3)^{MF} (V_s = +1.6 V, I_t = 0.1 nA) after saturation coverage of TMAA (1 - 2 L TMAA exposure). White oval highlights regions of adsorbed TMAA in a disordered manner. White dashed ovals depict linear chains of TMAA forming in the [001] direction. (b) 2.5 × 2.5 nm^2 (c, d) 3.0 × 3.0 nm^2 STM images highlighting regions with disordered TMAA adsorption where adsorption appears to form non-linear chains of TMAA molecules.

d. Summary

Single crystals of R_{100} (1 × 1) and R_{100} (1 × 3)^{MF} have been prepared and dosed with AA and TMAA at saturation coverage to probe the manner in which the species adsorb on the surface. AA adsorption on R_{100} (1 × 1) gives rise to a (2 × 1) overlayer with dissociative bi-dentate adsorption expected. AA adsorption on R_{100} (1 × 3)^{MF} also gives rise to a (×2) periodicity in the [001] direction with local ordering observed on the surface. The ordered regions are expected to maintain dissociative bi-dentate adsorption whilst adsorption in the non-ordered region is predicted to be mixed associative and dissociative. TMAA adsorption on R_{100} (1 × 1) and R_{100} (1 × 3)^{MF} is largely disordered with regions of quasi-

order observed in the [001] direction. This disorder is explained by the tri-methyl group on TMAA which induces steric effects. Adsorption is expected to be largely mixed associative and dissociative due to the disordered manner of adsorption.

6.4 Conclusions and Future Work

Surface science of TiO_2 has largely been restricted to single crystals or thin films of a single TiO_2 phase. Mixed phase rutile and anatase TiO_2 have been experimentally shown to exhibit greater photo-catalytic activity than single phase TiO_2 where the photo-catalytic activity is understood to be most potent at the anatase/rutile interface. We present evidence of utilising STM tip manipulation to generate an R_{100} / A_{101} interface. Thin films of different R_{100} reconstructions can be grown on electron irradiated A_{101}. STM tip pulses (+10 V, >50 nA, 200 ms) on electron irradiated A_{101} (destabilised surface) can be used to induce an anatase to rutile phase transition. STM tip pulsing of electron irradiated A_{101} gives rise to ordered regions with a row spacing of ~4.5 Å, ~9.0 Å and ~13.5 Å. These spacing are in good agreement for R_{100} (1 × 1), R_{100} (1 × 2), R_{100} (1 × 3) leading us to believe that our ordered structures are different terminations of R_{100}. On the latter termination, AA was dosed on the surface and yielded a (×2) periodicity along the rows. Complementing this work, single crystal R_{100} (1 × 1) and R_{100} (1 × 3)^{MF} were prepared and their interface with AA and TMAA probed. AA adsorption on R_{100} (1 × 1) and R_{100} (1 × 3)^{MF} gives rise to a (×2) periodicity in the [001] direction (i.e. along the rows). This behaviour of R_{100} (1 × 1) and R_{100} (1 × 3)^{MF} with respect to AA indicates that AA is a useful probe to identify R_{100} surfaces. TMAA adsorption on single crystal R_{100} (1 × 1) and R_{100} (1 × 3)^{MF} suggests largely disordered adsorption, however, TMAA is an excellent photo-active molecule and will be central to future experiments pertaining to the dosing of photo-active molecules at the R_{100} / A_{101} interface followed by illuminating the surface with UV light to probe photo-activity at the interface. Additionally, future work will include scanning tunneling spectroscopy (STS) and the use of different anatase terminations for STM tip manipulation to probe the rutile / anatase interface.

6.5 References

1. C. L. Pang, R. Lindsay and G. Thornton, *Chemical Society Reviews*, 2008, **37**, 2328-2353.
2. C. L. Pang, R. Lindsay and G. Thornton, *Chemical Reviews*, 2013, **113**, 3887-3948.
3. Y. Mi and Y. X. Weng, *Scientific Reports*, 2015, **5**, 11482.
4. N. A. Deskins, S. Kerisit, K. M. Rosso and M. Dupuis, *Journal of Physical Chemistry C*, 2007, **111**, 9290-9298.
5. U. Diebold, *Surface Science Reports*, 2003, **48**, 53-229.
6. P. J. Hardman, G. N. Raikar, C. A. Muryn, G. Vanderlaan, P. L. Wincott, G. Thornton, D. W. Bullett and P. Dale, *Physical Review B*, 1994, **49**, 7170-7177.
7. H. Raza, C. L. Pang, S. A. Haycock and G. Thornton, *Physical Review Letters*, 1999, **82**, 5265-5268.
8. J. Muscat, N. M. Harrison and G. Thornton, *Physical Review B*, 1999, **59**, 2320-2326.
9. D. V. Potapenko, J. Hrbek and R. M. Osgood, *Acs Nano*, 2008, **2**, 1353-1362.
10. P. W. Murray, F. M. Leibsle, C. A. Muryn, H. J. Fisher, C. F. J. Flipse and G. Thornton, *Physical Review Letters*, 1994, **72**, 689-692.
11. P. Zschack, J. B. Cohen and Y. W. Chung, *Surface Science*, 1992, **262**, 395-408.
12. Y. W. Chung, W. J. Lo and G. A. Somorjai, *Surface Science*, 1977, **64**, 588-602.
13. Z. Klusek, A. Bustakiewicz and P. K. Datta, *Surface Science*, 2006, **600**, 1619-1623.
14. O. Warschkow, Y. Wang, A. Subramanian, M. Asta and L. D. Marks, *Physical Review Letters*, 2008, **100**, 086102.
15. T. Ohno, K. Sarukawa, K. Tokieda and M. Matsumura, *Journal of Catalysis*, 2001, **203**, 82-86.
16. D. O. Scanlon, C. W. Dunnill, J. Buckeridge, S. A. Shevlin, A. J. Logsdail, S. M. Woodley, C. R. A. Catlow, M. J. Powell, R. G. Palgrave, I. P. Parkin, G. W. Watson, T. W. Keal, P. Sherwood, A. Walsh and A. A. Sokol, *Nature Materials*, 2013, **12**, 798-801.
17. T. Miyagi, M. Kamei, T. Mitsuhashi, T. Ishigaki and A. Yamazaki, *Chemical Physics Letters*, 2004, **390**, 399-402.
18. X. R. Zhang, Y. H. Lin, D. Q. He, J. F. Zhang, Z. Y. Fan and T. F. Xie, *Chemical Physics Letters*, 2011, **504**, 71-75.
19. D. C. Hurum, A. G. Agrios, S. E. Crist, K. A. Gray, T. Rajh and M. C. Thurnauer, *Journal of Electron Spectroscopy and Related Phenomena*, 2006, **150**, 155-163.
20. D. C. Hurum, A. G. Agrios, K. A. Gray, T. Rajh and M. C. Thurnauer, *Journal of Physical Chemistry B*, 2003, **107**, 4545-4549.
21. D. C. Hurum, K. A. Gray, T. Rajh and M. C. Thurnauer, *Journal of Physical Chemistry B*, 2005, **109**, 977-980.
22. S. Leytner and J. T. Hupp, *Chemical Physics Letters*, 2000, **330**, 231-236.
23. D. A. H. Hanaor and C. C. Sorrell, *Journal of Materials Science*, 2011, **46**, 855-874.
24. K. Okada, N. Yamamoto, Y. Kameshima, A. Yasumori and K. J. D. MacKenzie, *Journal of the American Ceramic Society*, 2001, **84**, 1591-1596.
25. H. Shin, H. S. Jung, K. S. Hong and J. K. Lee, *Journal of Solid State Chemistry*, 2005, **178**, 15-21.
26. A. Matthews, *American Mineralogist*, 1976, **61**, 419-424.
27. R. Shao, C. M. Wang, D. E. McCready, T. C. Droubay and S. A. Chambers, *Surface Science*, 2007, **601**, 1582-1589.
28. G. Xiong, R. Shao, T. C. Droubay, A. G. Joly, K. M. Beck, S. A. Chambers and W. P. Hess, *Advanced Functional Materials*, 2007, **17**, 2133-2138.
29. M. Nolan, N. A. Deskins, K. C. Schwartzenberg and K. A. Gray, *Journal of Physical Chemistry C*, 2016, **120**, 1808-1815.
30. M. G. Ju, G. X. Sun, J. J. Wang, Q. Q. Meng and W. Z. Liang, *Acs Applied Materials & Interfaces*, 2014, **6**, 12885-12892.

31. J. Kullgren, H. A. Huy, B. Aradi, T. Frauenheim and P. Deak, *Physica Status Solidi-Rapid Research Letters*, 2014, **8**, 566-570.
32. S. C. Zhu, S. H. Xie and Z. P. Liu, *Journal of the American Chemical Society*, 2015, **137**, 11532-11539.
33. O. Bikondoa, C. L. Pang, R. Ithnin, C. A. Muryn, H. Onishi and G. Thornton, *Nature Materials*, 2006, **5**, 189-192.
34. C. L. Pang, O. Bikondoa, D. S. Humphrey, A. C. Papageorgiou, G. Cabailh, R. Ithnin, Q. Chen, C. A. Muryn, H. Onishi and G. Thornton, *Nanotechnology*, 2006, **17**, 5397-5405.
35. A. Mellor, D. Humphrey, C. M. Yim, C. L. Pang, H. Idriss and G. Thornton, *Journal of Physical Chemistry C*, 2017, **121**, 24721-24725.
36. D. S. Humphrey, C. L. Pang, Q. Chen and G. Thornton, unpublished work.
37. Z. Klusek, A. Busiakiewicz, P. K. Datta, R. Schmidt, W. Kozlowski, P. Kowalczyk, P. Dabrowski and W. Olejniczak, *Surface Science*, 2007, **601**, 1513-1520.
38. R. E. Tanner, M. R. Castell and G. A. D. Briggs, *Surface Science*, 1998, **412-13**, 672-681.
39. A. Berko and E. Krivan, *Journal of Vacuum Science & Technology B*, 1997, **15**, 25-31.
40. M. Setvin, M. Schmid and U. Diebold, *Physical Review B*, 2015, **91**, 195403.
41. M. Setvin, B. Daniel, U. Aschauer, W. Hou, Y. F. Li, M. Schmid, A. Selloni and U. Diebold, *Physical Chemistry Chemical Physics*, 2014, **16**, 21524-21530.
42. H. Raza, C. L. Pang, S. A. Haycock and G. Thornton, *Applied Surface Science*, 1999, **140**, 271-275.
43. P. W. Murray, F. M. Leibsle, C. A. Muryn, H. J. Fisher, C. F. J. Flipse and G. Thornton, *Surface Science*, 1994, **321**, 217-228.
44. P. J. Hardman, N. S. Prakash, C. A. Muryn, G. N. Raikar, A. G. Thomas, A. F. Prime, G. Thornton and R. J. Blake, *Physical Review B*, 1993, **47**, 16056-16059.
45. A. G. Thomas and K. L. Syres, *Chemical Society Reviews*, 2012, **41**, 4207-4217.
46. D. C. Grinter, T. Woolcot, C. L. Pang and G. Thornton, *Journal of Physical Chemistry Letters*, 2014, **5**, 4265-4269.
47. J. G. Tao, T. Luttrell, J. Bylsma and M. Batzill, *Journal of Physical Chemistry C*, 2011, **115**, 3434-3442.
48. M. A. Henderson, J. M. White, H. Uetsuka and H. Onishi, *Journal of Catalysis*, 2006, **238**, 153-164.
49. D. C. Grinter, M. Nicotra and G. Thornton, *Journal of Physical Chemistry C*, 2012, **116**, 11643-11651.
50. R. E. Tanner, A. Sasahara, Y. Liang, E. I. Altman and H. Onishi, *Journal of Physical Chemistry B*, 2002, **106**, 8211-8222.
51. R. E. Tanner, Y. Liang and E. I. Altman, *Surface Science*, 2002, **506**, 251-271.
52. Q. Guo, I. Cocks and E. M. Williams, *Journal of Chemical Physics*, 1997, **106**, 2924-2931.
53. H. Hussain, X. Torrelles, G. Cabailh, P. Rajput, R. Lindsay, O. Bikondoa, M. Tillotson, R. Grau-Crespo, J. Zegenhagen and G. Thornton, *Journal of Physical Chemistry C*, 2016, **120**, 7586-7590.
54. M. A. Henderson, J. M. White, H. Uetsuka and H. Onishi, *Journal of the American Chemical Society*, 2003, **125**, 14974-14975.
55. J. M. White and M. A. Henderson, *Journal of Physical Chemistry B*, 2005, **109**, 12417-12430.
56. H. Idriss, P. Legare and G. Maire, *Surface Science*, 2002, **515**, 413-420.
57. G. T. Harrison, PhD Thesis, University College London, 2016.
58. J. P. W. Treacy, H. Hussain, X. Torrelles, D. C. Grinter, G. Cabailh, O. Bikondoa, C. Nicklin, S. Selcuk, A. Selloni, R. Lindsay and G. Thornton, *Physical Review B*, 2017, **95**.
59. W. Hebenstreit, N. Ruzycki, G. S. Herman, Y. Gao and U. Diebold, *Physical Review B*, 2000, **62**, R16334-R16336.
60. P. J. Feibelman and M. L. Knotek, *Physical Review B*, 1978, **18**, 6531-6539.

61. M. L. Knotek and P. J. Feibelman, *Physical Review Letters*, 1978, **40**, 964-967.
62. J. Lee, Z. Zhang and J. T. Yates, *Physical Review B*, 2009, **79**, 081408.
63. L. I. Vergara, M. C. G. Passeggi and J. Ferron, *Thin Solid Films*, 2007, **515**, 8365-8370.
64. G. T. Harrison, M. C. Spadaro, C. L. Pang, D. C. Grinter, C. M. Yim, P. Luches and G. Thornton, *Materials Science and Technology*, 2016, **32**, 203-208.
65. X. Torrelles, G. Cabailh, R. Lindsay, O. Bikondoa, J. Roy, J. Zegenhagen, G. Teobaldi, W. A. Hofer and G. Thornton, *Physical Review Letters*, 2008, **101**, 185501.
66. M. A. Henderson, *Journal of Physical Chemistry*, 1995, **99**, 15253-15261.
67. H. Raza, S. P. Harte, C. A. Muryn, P. L. Wincott, G. Thornton, R. Casanova and A. Rodriguez, *Surface Science*, 1996, **366**, 519-530.

Chapter 7

Concluding Remarks and Future Work

This thesis investigates titanium dioxide (TiO_2) to provide a nano-scale understanding of its surfaces and interfaces relevant to photocatalysis under a variety of experimental conditions ranging from ultra-high vacuum (UHV) to ambient pressure. Additionally, a droplet cell experimental apparatus has been implemented at Beamline I07 at Diamond Light Source to promote solid/liquid interface research. The development and implementation of the set-up is discussed in Section 3.5.3.

In Chapter 4, we look to understand the anatase TiO_2 (101) (A_{101}) and water interface in order to explore the nano-scale behaviour of photocatalytic water splitting on TiO_2. In UHV, at 298 K, A_{101} is widely considered to be inert with respect to water adsorption. In UHV, at 298 K, rutile TiO_2 (110) (R_{110}) possesses surface oxygen vacancies (V_o) that can split residual water in vacuum to generate bridging OH (OH_{br}) species. On the contrary, this phenomenon was not considered to occur on A_{101} as its V_o reside in the subsurface/bulk rather than the surface. Hence, at 298 K, we use electron irradiation to create meta-stable V_o and investigate their ability to dissociate residual water in vacuum to create OH_{br} species. Previous spectroscopic work in the Thornton Group suggests that this method is capable of generating OH species. In our scanning tunnelling microscopy (STM) findings we present evidence of these species being OH_{br}. Moving out of UHV, we also present an ambient pressure surface X-ray diffraction (SXRD) investigation of the aqueous interface of A_{101}. We present an *in situ* investigation of the A_{101} interface with an ultra-thin water film (10 ±2 monolayers) and bulk water. Our findings illustrate that both interfaces contain a 25:75 mixture of molecular H_2O and terminal OH (OH_t) bound to titanium atoms along with bridging OH species in the contact layer. This is in complete contrast to the inert character of room temperature A_{101} in ultra-high vacuum. A key difference between the ultra-thin and bulk water interfaces is that in the latter, water in the second layer is also ordered. These molecules are hydrogen bonded to the contact

layer, modifying the bond angles. Our findings on A_{101} are a critical step towards understanding the aqueous interface of A_{101}. Looking to the future, probing the aqueous interface of A_{101} with UV illumination as well as its interface with electrolyte solutions is a promising avenue to pursue with the aim of obtaining an atomic scale perspective of photocatalysis on A_{101}.

In Chapter 5, we aim to provide an understanding of the interface of R_{110} with electrolyte solutions. Understanding the preferred adsorption sites on R_{110} under electrolyte solutions is a major step in determining the nano-scale interface evolution of electrocatalytic process on TiO_2. In the first instance, we present the first *in-situ* STM images of R_{110} under electrolyte solutions (0.1 M NaOH and 0.1 M HCl). Our presented STM findings give evidence of surface order at the solid/liquid interface with surface rows being observed. Additionally, preliminary electrochemical STM images of R_{110} give evidence of surface terraces being maintained. In essence, our findings open up the use of STM to probe R_{110} and electrolyte interfaces - a research area which has largely been overlooked in favour of STM in UHV conditions. In parallel, *in-situ* SXRD data for the interface of R_{110} with the 0.1 M NaOH and 0.1 M HCl are also presented. Our findings indicate that Na adsorption is favoured at the surface tetra-dentate site. The adsorption of Cl is favoured at the surface Ti site. Findings presented in this chapter focus on developing an understanding of TiO_2 submerged in electrolyte solutions. Looking to the future, given the lack of research in this field, there are numerous avenues to pursue. Initially, probing R_{110} and other TiO_2 terminations with various electrolyte solutions would be a direct continuation of the current work. Next, probing the electrochemical interface of R_{110} would be a significant step forward in understanding the nano-scale electrochemical interfaces of R_{110} in relation to catalysis. The next practical steps from an electrochemical perspective is to explore different concentrations of NaOH and HCl to better understand

its interaction with R_{110}. In addition, more electrolytes should also be explored to further expand the electrolyte choice for future electrochemical experiments. In terms of electrochemistry, the first electrochemical procedures to pursue should be a basic and standard electrochemical process such as the electrochemical redox reaction of ferrocene. Lastly, for electrochemical STM, a variety of noble metal tips should be explored to determine which tip material is best suited to a given electrolyte. The use of W tips (typically used in UHV STM) was explored extensively with electrochemical STM of R_{110}, however, these tips were found to deteriorate under solution with a life time of ~15 min. This necessitates the need to explore a variety of resistant tip materials (i.e. noble metals).

In Chapter 6, we return our focus to UHV studies of TiO_2. We focus on the anatase/rutile and rutile TiO_2 (100) (R_{100})/acetate interface. The most potent TiO_2 photocatalyst consists of a 3:1 ratio of anatase and rutile nanoparticles (Degussa P-25®). The anatase/rutile interface is predicted to play a major role in photocatalysis, however experimental surface scientists have largely probed single crystal and thin film TiO_2 surfaces. In this chapter we aim to utilise STM tip manipulation to convert anatase to the thermodynamically more stable rutile. STM tip manipulation of electron irradiated (destabilised) A_{101} results in ordered regions of being created where the interface between the two appears disordered. The row spacing of the newly created ordered regions is observed at ~4.5 Å, ~9.0 Å and ~13.5 Å. These spacing are in good agreement for R_{100} (1 × 1), R_{100} (1 × 2), R_{100} (1 × 3) leading us to believe that the ordered structures are different terminations of R_{100}. One of the ordered regions created (assigned as R_{100} (1 × 3)) was additionally probed with acetic acid (AA) where the adsorbed species gives rise to a (×2) periodicity in the [001] direction (i.e. along the rows). Complementary to this work, the interface of single crystal R_{100} (1 × 1) and R_{100} (1 × 3) were probed with AA and tri-methyl acetic acid (TMAA). Our

findings indicate that the adsorption of AA gives rise to a (×2) periodicity in the [001] direction (i.e. along the rows) on R_{100} (1 × 1) and R_{100} (1 × 3) which suggests dissociative bi-dentate adsorption that ultimately gives rise to the (×2) periodicity. TMAA adsorption is largely disordered with some quasi-order observed at step-edges presumably caused by there being less steric hindrance at the step edge. Looking to the future, an interesting avenue to pursue would be to utilise STM tip manipulation to generate an anatase/rutile interface, dose it with a photo-active molecule (such as AA or TMAA) and lastly expose the surface to UV illumination to probe the photo-activity at the anatase/rutile interface. Additionally, utilising different anatase substrate for STM tip manipulation would be an exciting avenue to pursue to better understand the anatase / rutile interface.